Jets from supermassive black holes: from cosmic to human timescales

Proefschrift

ter verkrijging van de graad van doctor
aan de Radboud Universiteit Nijmegen
op gezag van de rector magnificus prof. mr. S.C.J.J. Kortmann,
volgens besluit van het college van decanen
in het openbaar te verdedigen op
dinsdag 2 september 2014
om 14:30 uur precies

door

Sjoert van Velzen

geboren op 28 augustus 1984
te Amsterdam

Promotor:	Prof. dr. H.D.E. Falcke
Copromotor:	Dr. E.G. Körding
Manuscriptcommissie:	Prof. dr. E.A. Cator
	Prof. dr. G.R. Farrar (New York University, USA)
	Prof. dr. P.J. Groot
	Prof. dr. H.J.A. Röttgering (Universiteit Leiden)
	Prof. dr. F.W.M. Verbunt

Jets from supermassive black holes
Thesis, Radboud University Nijmegen
Illustrated; with bibliographic information and Dutch summary
Cover design by Studio BAR. Image credit: NRAO/AUI

ISBN: 978-90-9028465-1

Was het even blauw? Misschien
een deel. Nevel verflauwt. Meer
toch als wat wij kennen: geel.

Enig contour? Een andere kleur
schommelt door wat leeg
lijkt heen. Wellicht om geur

verkleurt het rood tot groen.
Of door de klank – want vlug
daarna: alles in 't vermiljoen

K. Schippers

Contents

Chapter 1

Introduction

Not everything that falls towards a black hole will be lost forever behind the event horizon. Just before crossing this point-of-no-return, some particles can escape the black hole by latching onto a high-speed outflow. These narrow outflows are known as jets, and while they are a common feature of astrophysical objects, we do not know how they are produced.

The first jet was discovered in an optical image of the biggest galaxy in the constellation Virgo, Messier 87 (Curtis 1918). We now know that this jet originates from the supermassive black hole at the center of this galaxy (Fig. 1.1). The most extreme jets are gamma-ray bursts, which are likely powered by gas falling onto a newly formed black hole after the collapse of a massive star. However a black hole is not a necessary requirement for producing a jet: neutron stars that accrete[1] gas from a donor star also consistently show relativistic outflows and accreting white dwarfs follow the same pattern. Even objects as mundane as protostars, which accrete from a protoplanetary disk, show collimated outflows piercing out of the dusty clouds that enshroud them (Fig. 1.1).

We can formulate the following rule of thumb: whenever an astrophysical object is gathering mass via an accretion disk, jets will at some point appear. These jets can carry angular momentum away from the accretion disk, allowing material to get closer to the central object. So we may think of an accretion disk plus a jet as a coupled system, their relation is symbiotic.

Even though jets are common and have been studied for decades, we still have no consistent theory of how or when they are produced. This thesis provides new clues to solve this puzzle by approaching the problem on two different timescales: jets from supermassive black holes that evolve on cosmic timescales (millions of years or more) and newborn jets that evolve on human timescale (up to few tens of years). Below, I introduce the main topics of this thesis (black holes, accretion disks, quasars and stellar tidal disruption flares) in some detail.

[1] *Accretion* refers to the accumulation of mass from an outside source.

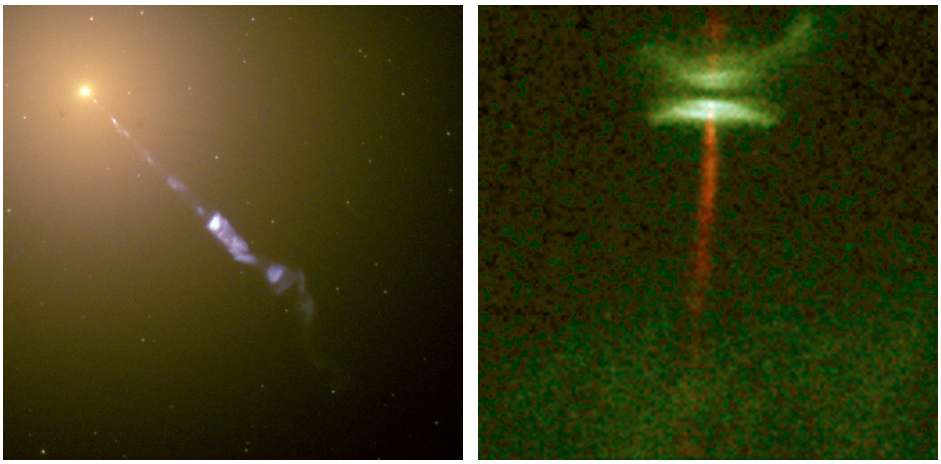

FIGURE 1.1: Optical images of jets as observed using the Hubble Space Telescope. Left: the jet that originates from the supermassive black hole at the center of the elliptical galaxy Messier 87. The length of the jet in this image about 1.5 kpc (5×10^{19} meter). Right: jet produced by the accretion disk around the Herbig-Haro star HH 30. The star itself is not visible due to obscuration by inner parts of the dusty disk. The protostellar jet in this image is about 700 AU long (1×10^{14} meter). Credit: NASA, STScI.

1.1 Black holes in theoretical physics

Before discussing the properties of jets, we need to introduce the theoretical concept of a black hole. From a classical point of view, a black hole is simply an object whose escape velocity is greater than the speed of light (c). So for a sphere of mass M we have

$$R_{\text{classical}} = \frac{2GM}{c^2} \quad , \tag{1.1}$$

with G the gravitational constant. This idea of a black hole was formulated already by the end of the 18th century (Michell 1784; Laplace 1799). Yet to fully appreciate the concept of a black hole we need to understand space and time itself, i.e., we need General Relativity (GR). The field equations of GR equate the local curvature of spacetime to the local energy density. The solution to the Einstein field equations at a radial distance r from a spherical (non-charged, non-rotating) mass can be expressed as

$$c^2 d\tau^2 = \left(1 - \frac{R_s}{r}\right) c^2 dt^2 - \left(1 - \frac{R_s}{r}\right)^{-1} dr^2 \tag{1.2}$$

(Schwarzschild 1916), where τ is the proper time and t the coordinate time. The Schwarzschild radius is defined as

$$R_s \equiv \frac{2GM}{c^2} \quad , \tag{1.3}$$

which happens to be identical to the classical radius of a black hole as derived from the Newtonian escape velocity (Eq. 1.1). The Schwarzschild metric (Eq. 1.2) tells us how to measure distances in spacetime and thus how particles move. At $r = 0$ and $r = R_s$ the metric diverges (the latter is, in fact, a coordinate singularity, i.e., by choosing a different coordinate system it can be shown that the metric is regular at $r = R_s$). An astronaut traveling towards a black hole can cross the Schwarzschild radius in a finite amount of proper time, yet an outside observer will never observe the crossing; the astronaut would appear frozen on the horizon (although this image is not detectable due to the gravitational redshift). We thus arrive at the concept of an event horizon at $r = R_s$. A black hole is an object whose surface is formed by an event horizon.

The nature of the singularity at $r = 0$, or the state of the matter inside a black hole are currently open questions in theoretical physics. An important result to help understand black holes is the no-hair theorem. According to this theorem, black holes are uniquely described by their mass, charge, and spin —they have no "hair" that can be pulled to probe the state of material inside the horizon. From the no-hair theorem one may conclude that black holes are not very different from elementary particles (e.g., electrons), since these are also described by just three quanta. However, our understanding of black holes within the framework of quantum field theory (QFT), the theory of elementary particles, is far from complete. For example, Hawking radiation, which is a solid prediction of QFT applied to black holes, appears to contradict the Equivalence Principle of GR (Almheiri et al. 2013). To solve this problem we will need a theory of quantum gravity, which many argue to be the "Holy Grail" of theoretical physics.

While black holes remain an elusive concept for theoretical physicists, they are a daily reality for astronomers. Black holes are out there. We wish to understand how they formed, how they interact with their environment, and indeed, how they create jets. To reach these goals we can be (almost)[2] agnostic about what quantum gravity has to say about the interior of the horizon.

In the following sections I will present the astrophysical evidence for the existence of black holes, but in order to appreciate this evidence, we first need to discuss accretion disks.

1.2 Accretion disks

To understand observations of black holes and jets, one needs to understand accretion disks. In this section we therefore review the basics of accretion theory and summarize

[2]The timescale for black hole evaporation via Hawking radiation is $\sim G^2M^3/\hbar c^4$. For a solar mass black hole this exceeds the age of the universe by more than sixty orders of magnitude. Hence the quantum properties of known black holes are not likely to be relevant in our current universe —although surprises may be possible (e.g., Rovelli & Vidotto 2014).

the main results —for a much more extensive discussion of accretion disks see the (enjoyable) review by Abramowicz & Fragile (2013).

Consider a spherical cloud of material with mass m and some (small) amount of angular momentum that is falling towards a central object. We will assume this central object is a black hole, but most of the results presented below are valid for any type of central mass. Due to conservation of angular momentum, the collapse is only uninhibited along the axis of rotation and the cloud will thus turn into a disk. Viscous stress in the disk can transfer angular momentum outward, allowing accretion to take place. When our cloud is accreted all the way to the Schwarzschild radius, it will have lost $\sim 0.1mc^2$ of its gravitational potential energy. This explains why black hole accretion disks can be extremely luminous: they provide the most efficient method to extract rest-mass energy from matter.

To first order, accretion disks can be modeled as a superposition of blackbody emitters, with the local temperature given by the local dissipation rate,

$$L(r)\,dr \sim \frac{GM\dot{m}}{2r}\,dr = 4\pi\, r\sigma_{\rm SB}T_{\rm disk}^4\,dr \quad . \tag{1.4}$$

With M the mass of the central object, $\dot{m}$ the accretion rate, r the radius in the disk, and $\sigma_{\rm SB}$ the Stefan-Boltzmann constant.

The smallest radius of the toy disk model we are considering here is given by the innermost stable circular orbit (ISCO). The ISCO depends on the angular momentum (J) of the black hole, which is often expressed using a dimensionless spin parameter

$$a \equiv \frac{cJ}{GM} \quad . \tag{1.5}$$

For a non-rotating black hole ($a = 0$), the ISCO is at found at $r = 3R_s$, while for maximal spin ($a = 1$) the ISCO of a particle in a prograde orbit is at $r = R_s$. For the latter case, where the disk extends all the way to the horizon, Eq. 1.4 yields an accretion disk efficiency $\eta \equiv L/\dot{m}c^2 = 0.25$. Using the proper GR calculation, we find $\eta = 0.057$ (for $a = 0$), $\eta = 0.42$ (for $a = 1$).

An upper limit to the accretion rate follows by considering the pressure that photons exert via Thomson scattering. Above the Eddington luminosity,

$$L_{\rm Edd} = 1.3 \times 10^{38}\frac{M}{M_\odot}\,{\rm erg\,s^{-1}} \tag{1.6}$$

the force of radiation exceeds the gravitational force ($M_\odot$ denotes one solar mass). This yields a maximum accretion rate (assuming photon pressure acts in the radial direction only):

$$\dot{m}_{\rm Edd} = \frac{L_{\rm Edd}}{\eta c^2} = \frac{2\times10^{-9}}{\eta}\frac{M}{M_\odot}M_\odot\,{\rm yr^{-1}} \quad . \tag{1.7}$$

We can now estimate the typical temperature of an accretion disk radiating at $f_{\rm Edd}$ of the Eddington luminosity:

$$\bar{T}_{\rm disk} \sim \left(\frac{f_{\rm Edd} L_{\rm Edd}}{2\pi\sigma_{\rm SB} R_s^2} \right)^{1/4} \quad K \tag{1.8}$$

$$= 5 \times 10^7 \left(f_{\rm Edd} \frac{M_\odot}{M} \right)^{1/4} \quad K \quad . \tag{1.9}$$

The spectral energy distribution (SED) of a black hole with a mass of 10 $M_\odot$ that accretes close to the Eddington limit and radiates away all of the available gravitational energy peaks in the X-ray regime of the electromagnetic spectrum.

We have not yet discussed the origin of the viscous stress that must act to decrease the angular momentum of the particles that are accreted. The origin of this viscosity is not fully understood (due to the low density in the disk, normal molecular viscosity is far too weak). The best candidate is the magneto-rotational instability, which leads to turbulence and thus acts as an effective viscosity. Shakura & Sunyaev (1973) showed that a successful method to solve the fluid equations of accretion disks is to couple the viscosity coefficient (ν_*) to the scale height of the disk (H) and the sound speed (c_S) using a dimensionless constant α:

$$\nu_* = \alpha H c_S \quad . \tag{1.10}$$

The Shakura–Sunyaev analytic model is valid for optically thick disks that are geometrically thin ($H/R \ll 1$); it has been very successful in reproducing the observed properties of objects accreting at $f_{\rm Edd} \sim 0.1$.

Shakura–Sunyaev disks are, by construction, radiatively efficient, but as the accretion rate decreases this assumption is not likely to remain valid. When the density in the disk decreases, the optical depth can fall below unity and the disk is no longer able to radiate the energy that is dissipated by viscosity. The disk will thus become very hot and puffs up ($H/R > 1$) most of the gravitational energy is now advected into the black hole. The change from a radiatively efficient thin disk to an advection dominated accretion flow (ADAF; Narayan & Yi 1994; Abramowicz et al. 1995) can be thought of as a phase transition (e.g., liquid water to water vapor). The critical accretion rate for this transition is predicted to be $\alpha^2 \dot{m}_{\rm Edd}$ (Narayan & Yi 1995). The emission mechanism of ADAFs and other hot accretion flows (for a recent review see Yuan & Narayan 2014) is non-thermal and the luminosity scales as $L \propto \dot{m}^{2-3}$.

The requirements for a thin disk will also be broken when the luminosity is close to the Eddington limit, because the accretion disk is unable to cool sufficiently via thermal radiation. Abramowicz et al. (1988) showed that we obtain a slim disk ($H/R < 1$); in this type of accretion flow, the contribution of advective cooling increases with accretion rate. Since the criterion for a thin disk that is thermally

stable decreases with radius (Chen et al. 1995), an accretion flow could consist of both an ADAF for the inner part and a radiatively efficient disk at larger radii (e.g., Yuan & Narayan 2004). However it remains unclear how to connect the outer thin disk to the inner hot flow.

In summary, from qualitative arguments we deduced the existence of two modes of accretion: an optically thick disk that can cool efficiently via thermal radiation (with a spectrum that is approximately given by Eq. 1.4, or more accurately by the Shakura–Sunyaev solution) and the radiatively inefficient ADAF (with a non-thermal spectrum). The transition between these modes depends on the viscosity of the disk and the accretion rate; the ADAF typically appears at $\dot{m} \lesssim 10^{-2}\dot{m}_{\rm Edd}$. In the next two sections we compare the properties of the two accretion modes with the observed properties of active black holes.

1.3 Stellar mass black holes

While the main aim of this thesis is understanding accretion disks and jets from supermassive black holes (with $M_{\rm BH} = 10^{6-10} M_\odot$), it will prove to be instructive to first review the properties of Galactic black holes (with $M_{\rm BH} \sim 10\ M_\odot$). At a fixed gravitational distance from the black hole, the orbital timescale is proportional to mass, $t \propto r^{3/2}(GM)^{-1/2} \propto M$. By studying Galactic black holes we could thus see the evolution of supermassive black holes fast-forwarded by a factor 10^{5-8}. The validity of this scale-invariant view of accretion —one of the main themes of this thesis— is discussed later in Section 1.7.1.

1.3.1 Gravitational collapse

Stellar mass black holes are a natural outcome of the evolution of massive stars. When nuclear fusion has produced an iron core, further fusion becomes endothermic. With no energy source available, the star must collapse. If the contracting stellar core is less massive than 1.44 $M_\odot$, the Chandrasekhar (1931) mass, degeneracy pressure of the electrons halts the gravitational collapse and we obtain a white dwarf. For stellar remnants that exceed the Chandrasekhar limit, neutron degeneracy pressure can balance the gravitational force up to a theoretical maximum mass of about 2.5 $M_\odot$ (Oppenheimer & Volkoff 1939; Lattimer 2012); for higher mass, the formation of a black hole appears to be inevitable. Indeed the highest neutron star mass observed to date is $2.01 \pm 0.04\ M_\odot$ (Antoniadis et al. 2013). Since stars lose mass as they age, the minimum initial mass of a star that will end its life as a black hole is 15–20 $M_\odot$.

The electromagnetic force is much stronger than the gravitational force, thus preventing the accumulation of net charge during gravitational collapse. Hence astrophysical black holes are considered to be neutral. Spinning black holes, on the other hand, are anticipated if angular momentum is conserved during the collapse —if the progenitor star was rotating, so should the black hole.

In summary, spinning black holes of $\sim 10 M_\odot$ are anticipated as the end product of the evolution of massive stars. These high-mass stars are relatively rare, but not uncommon; about one hundred million black holes are estimated to exist in our Galaxy today (e.g., Shapiro & Teukolsky 1983). Below I review the properties of a subset of Galactic black holes, namely those that are a member of a binary system.

1.3.2 X-ray binaries

Stellar mass black holes can be discovered when they are accreting from a companion star. From Eq. 1.9 we see that for $M_{\rm BH} \sim 10\ M_\odot$, the peak of the spectral energy distribution (SED) of a radiatively efficient accretion disk is at X-ray frequencies. This explains why accreting stellar mass black holes are known as black hole X-ray binaries (for a review see Remillard & McClintock 2006).

A remarkable property of black hole binaries becomes clear when we track the X-ray spectrum during an outburst[3], an example is shown in Fig. 1.2. Before the outburst, the X-ray count rate is low —some black hole binaries are not even detected in this quiescent phase— and the X-ray SED is hard. In this *hard state*, X-ray binaries show steady and compact jets (Fender 2001), with a moderate bulk Lorentz factor ($\Gamma < 1.4$). This jet could in fact be responsible for some of the observed X-ray flux in the hard state (Markoff et al. 2001). As the X-ray luminosity increases, so does the radio luminosity of the jet (Corbel et al. 2003), while the X-ray hardness remains constant. This situation, an increasing count rate at a constant hardness ratio, continues up to a maximum luminosity. At this point we observe a rapid change in the X-ray SED: a blackbody spectrum appears, we have entered the *soft state*.

During the transition to the soft state (also known as the intermediate state), a powerful radio flare is produced (Mirabel & Rodríguez 1994), which can be resolved into distinct components with relativistic motions ($\Gamma > 2$). Once in the soft sate, the X-ray binary will not show any jet activity, the jet appears to be quenched (Tananbaum et al. 1972; Russell et al. 2011).

At their maximum luminosity, some X-ray binaries make multiple transitions from hard to soft and back again, with repeated ejections of transient jets. As the outburst decays, the source moves back to the hard state and the steady flat-spectrum jet appears again. The soft-to-hard transition is typically observed at a few percent of the Eddington luminosity (Maccarone 2003), while the hard-to-soft transition can occur close to the Eddington luminosity as well (e.g., Steiner et al. 2013).

The consistent spectral changes of black hole binaries as a function of luminosity are direct evidence for the existence of two accretion modes: the soft state is explained by emission from a radiatively efficient disk, while the low-luminosity part of the hard

[3]The outbursts we consider here are triggered by an instability in the matter that has built up at the edge of the disk, leading to a rapid increase of the viscosity (Meyer & Meyer-Hofmeister 1981). So the accretion rate during an outburst can vastly exceed the rate of Roche lobe overflow.

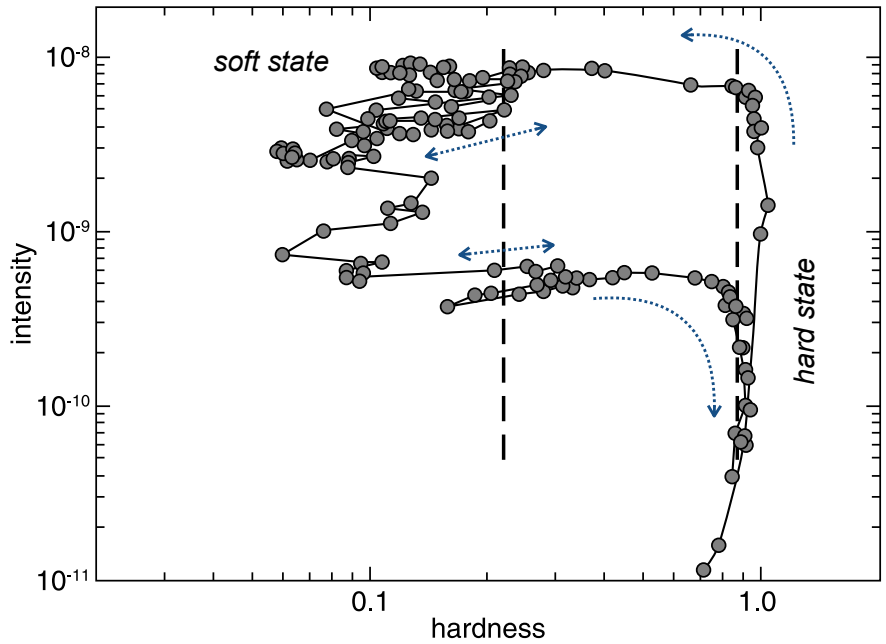

FIGURE 1.2: An example hardness-intensity diagram for an outburst of the Galactic black hole X-ray binary GX 339–4. The duration of the outburst is about one year and is sampled with a roughly constant cadence. The arrows indicate how the source moves through the diagram. The hardness is given by the 6-10 keV flux over the 3-6 keV flux; the X-ray intensity is measured over the full range (3-10 keV, in $\mathrm{erg\,s^{-1}\,cm^{-2}}$). Figure adapted from Meyer-Hofmeister et al. (2009), based on data of Dunn et al. (2008) as obtained with the Rossi X-ray Timing Explorer.

state corresponds to an ADAF, or a "jet-dominated advective system" (Körding et al. 2006b). We have arrived at a unified model for the radio and X-ray properties of black hole binaries (Fender et al. 2004), with jet production and destruction occurring during the transition between these states. Neutron star X-ray binaries show the same behavior (Migliari & Fender 2006) and transients jets have also been observed when accreting white dwarfs change spectral state during a nova outburst (Körding et al. 2008a).

An important distinction between black hole accretion disks and disks around other compact objects (neutron stars, white dwarfs), is that the latter have a surface where accreted material can pile up. Neutron star X-ray binaries can be identified by powerful X-ray bursts —although we sometimes have to wait 25 years before seeing one (e.g., Linares et al. 2010). The lack of flares from (candidate) black hole X-ray binaries is very strong[4] evidence that the central compact object in these systems has

[4]We have to note that electromagnetic observations can never provide a watertight prove for the existence of black holes. Exotic objects with a size of $1 + \epsilon$ times the Schwarzschild radius (e.g.,

an event horizon (Narayan & McClintock 2008).

1.4 Supermassive black holes

Just like their stellar mass cousins, supermassive black holes are most easy to spot when they are accreting. From Eq. 1.9 we can estimate that the SED of an accreting black hole of $M_{\rm BH} = 10^9\ M_\odot$ peaks at $\nu \sim 10^{16}$ Hz, not very different from the colors of young stars. Accreting supermassive black holes were initially called quasi-stellar radio sources, because they were identified as radio sources with star-like optical counterparts. The label quasi-stellar radio source was later replaced by a more catchy name: *quasar*.

The first quasars were identified in searches for optical counterparts to point sources of the 3rd Cambridge radio survey (Matthews & Sandage 1963). After Schmidt (1963) realized that the optical spectrum 3C 273 can be explained if all the lines are redshifted by $\Delta\lambda/\lambda_0 = 0.158$, it became clear that quasars are of extra-galactic origin and thus extremely luminous. While not each galaxy hosts a quasar, it seems natural to assume that all galaxies went through a quasar phase and as a result have a supermassive black hole at their center (Lynden-Bell 1969; Soltan 1982).

An important breakthrough in the study of supermassive black holes followed from Hubble Space Telescope measurements of the surface brightness profiles of nearby galaxies. Dynamical models for the ensemble properties of the stellar orbits in these galaxies could only reproduce these profiles after including a "central massive object" (Magorrian et al. 1998). The authors suggested that every galaxy hosts a supermassive black hole at its center, with a mass that is a fixed fraction of the stellar mass in the bulge. Subsequent observations have confirmed this picture (for a review see Kormendy & Ho 2013) and have shown that the velocity dispersion of the stars in the bulge (σ) correlates with the mass of the black hole (the M-σ relation: Gebhardt et al. 2000; Ferrarese & Merritt 2000).

The evidence for extra-galactic supermassive black holes obtained by modeling the surface brightness profiles of galaxies is already very compelling, but at the center of the Milky Way we can do even better: here we can resolve the orbits of individual stars. Measuring the orbits of these so-called S-stars through the dust that obscures the Galactic center is challenging, but not impossible (e.g., Eckart & Genzel 1996; Ghez et al. 2005). By applying Kepler's law we find a mass of $(4.3 \pm 0.4) \times 10^6\ M_\odot$ within 0.0006 pc (Schödel et al. 2002; Gillessen et al. 2009). This measurement implies a matter density that can, in principle, be reached with a cluster of neutron stars, but such a system would be dynamically unstable and evaporate within a million years (Maoz 1998). The only sensible explanation for the high velocity of the S-stars is a

gravastars; Mazur & Mottola 2001) can remain unseen due to the gravitational redshift when $\epsilon \ll 1$ (Abramowicz et al. 2002).

supermassive black hole. The mass of our Galactic center black hole fits nicely onto the M-σ relation found for the extra-galactic supermassive black holes.

The idea that each galaxy hosts a supermassive black hole at its center is now widely (if not uniformly) accepted. Accreting supermassive black holes are referred to as active galactic nuclei (AGN). Quasars are the most powerful AGN, they outshine their host galaxy. Below we discuss AGN subtypes in a bit more detail.

1.4.1 Obscuration and unification

Based on their optical spectrum, AGN can be divided into two classes: type-1 and type-2 AGN (also called Seyfert 1/Seyfert 2 when the AGN is not a quasar). Type-1 AGN show narrow emission lines and broad ($\sim 10^3\,\mathrm{km\,s^{-1}}$) emission lines. The broad lines (typically Hα and other lines in the Balmer series) are variable in strength on $\sim$day timescales and thus originate from a few light days of the black hole. Spectra of type-2 AGN are defined by the lack of broad lines. Among the narrow lines are forbidden transitions (e.g., [OIII]), these lines show no signs of variability. They therefore must originate from a low-density region, relatively far from the black hole (a few tens to hundreds of light years).

Key to AGN unification is the idea that type-1 AGN show the intrinsic spectrum of the accretion disk, while our view of type-2 AGN is modified by obscuration. This implies that the narrow lines must be ionized by disk radiation that was not emitted into our line of sight. Type-1 and type-2 AGN are then unified with one parameter: the orientation of the obscuring structure (the "dusty torus") with respect to our line of sight. The observation of broad lines in the polarized emission (i.e., light that has been scattered into our line of sight) of type-2 AGN (Antonucci & Miller 1985) has convinced many that the orientation-based unification model is correct.

1.4.2 A story of feedback

The observed correlation between the mass of the central black hole and a number of galaxy properties (e.g., velocity dispersion or bulge mass) has led to the idea that AGN may influence the evolution of their host. Radiation pressure and winds from the accretion disk can heat and push gas out of galaxies (Silk & Rees 1998), which will halt the formation of new stars (for a review see Fabian 2012). This negative feedback loop can start after a merger of two galaxies, which boosts the gas supply for the AGN, turning it into a quasar. The quasar-mode feedback (Kauffmann & Haehnelt 2000) likely explains why the most massive galaxies all appear to be "red and dead" (Bower et al. 2006). Jets from AGN can provide feedback on both the galactic and inter-galactic level. Mechanical feedback from jets could stop massive cooling flows (Fabian 1994) from accreting onto the galaxy (McNamara & Nulsen 2012).

A simple, but attractive story of the co-evolution of black holes and galaxies has emerged. After the quasar has grown powerful enough to shut itself down by pushing

out the gas via radiation pressure and winds, the accretion rate drops to below 1% of the Eddington limit. As we have seen in our discussion of stellar mass black holes, steady jets emerge at low accretion rate. So after the quasar phase, jets from a radiatively inefficient accretion flow will keep the gas hot and thus "maintain" the passive state of the black hole (e.g., Churazov et al. 2005).

While it appears very plausible that AGN feedback plays a role in galaxy evolution, the details still have to be worked out. In the last few years, galaxy-wide winds that are driven by black hole accretion have been identified (e.g., Nesvadba et al. 2008; Dunn et al. 2010). However, the observations of winds in non-active galaxies (e.g., Schawinski et al. 2009) bring into question the idea that quasar feedback is an essential phase of galaxy evolution.

1.5 The appearance of jets

At the end of the last section, arguments were given that jets from AGN may influence the cosmological evolution of their host galaxy. In this section, I will discuss the observational signature and the evolution of the jets themselves. We start at the base of the jet and from there follow its path through the galaxy.

1.5.1 The base of the jet and the radio core

Since we do not have a consistent picture of their formation (see next section), it is somewhat problematic to define where jets start. For now, we simply state that somewhere in the accretion flow, plasma is ejected into symmetric nozzles and gets accelerated. We assume that the supersonic jet can freely expand sideways due to its pressure, resulting in a conical geometry (Blandford & Königl 1979). At some point downstream in the jet, electrons are accelerated (a likely mechanism is diffusive shock acceleration, via internal shocks; Bell 1978) and the jet starts to emit synchrotron radiation. This point is known as the radio core.

If we assume that the energy in the relativistic electrons is in equipartition with the energy of the magnetic field, the field decays with r^{-1}, and the location where the jet becomes optically thin to synchrotron self-absorption should follow $r_{\rm ssa} \propto \nu^{-1}$. This scaling has been confirmed by using very long baseline interferometry (VLBI) to measure the shift of the location of the radio core with frequency (for a recent example see Hada et al. 2011), which is a major triumph for the conical equipartition jet model. In NGC 4258, the observed offset of the radio core with respect to the dynamical center of the accretion disk (measured via maser emission) also confirms the predictions of the conical jet model (Herrnstein et al. 1997).

At higher frequencies we look deeper into the jet, yielding a higher synchrotron emissivity but a smaller emission volume. The net effect is that an unresolved conical jet core has a flat spectrum: $L_\nu \propto \nu^0$. The radio luminosity, in the rest-frame of the

jet, is given by

$$L_\nu = N_{\rm eq} \left(\frac{q_j L_{\rm disk}}{10^{46} {\rm erg\,s^{-1}}} \right)^{17/12} {\rm erg\,s^{-1}Hz^{-1}} \quad (1.11)$$

(Falcke & Biermann 1995). Here $q_j \equiv Q_{\rm jet}/L_{\rm disk}$ is the jet-disk coupling parameter (the evidence for this linear coupling is discussed in Section 1.6.1). Observations of the mechanical jet power derived from X-ray cavities (Allen et al. 2006) imply $q_j \approx 0.2$, (Körding et al. 2008b, Chapter 4) —however see Russell et al. (2013b) for a critique of the cavity method. The normalization of Eq. 1.11, $N_{\rm eq}$, depends on the details of equipartition and is predicted in the range $N_{\rm eq} = 10^{31.5-33}$ (Falcke & Biermann 1995). Observations of quasars (Falcke et al. 1995b, Chapter 5) and X-ray binaries (Körding et al. 2006b) both yield $N_{\rm eq} \approx 1 \times 10^{33}$ (normalized for $q_j = 0.2$).

The high-frequency turnover of the SED of the core occurs when the innermost part of the jet becomes optically thin. For stellar mass black holes, the observed turnover places the start of particle acceleration within $\sim 10^2$ gravitational radii from the nozzle (Markoff et al. 2001), implying that the base of the jet is close to the inner part of the accretion flow.

We may conclude that our understanding of the low-frequency synchrotron emission from the core of the jet is fairly complete. The open questions concern the particle acceleration mechanism, and most importantly the particle content of the jet. The latter is hard to measure since the observed synchrotron emission is due to electrons only. Close to the base, jets could consist of an electron-positron plasma, or contain an equal number of electrons and protons. Discriminating these two models using current observations is difficult. For example, the γ-ray emission of jets can be explained by both inverse Compton scattered photons (the leptonic model) or decay of π^0 particles produced by accelerated protons (the hadronic model). A measurement of the neutrino emission would be the best way to differentiate the two types of jet composition, since neutrinos can only be produced in the hadronic model.

1.5.2 Propagation: lobes and hotspots

The conical jet model that we discussed in the previous section breaks down when the jet can no longer freely expand. The jet will slam into the interstellar medium, creating a bow shock. The shocked interstellar medium creates a hot cocoon around the jet, which can help to keep the jet collimated (Bromberg et al. 2011). The jet material is decelerated at the reverse shock; here the compressed magnetic field allows efficient type-I Fermi acceleration, explaining why the location where the jet terminates is often visible as a synchrotron hotspot.

The head of the jet propagates by pushing at the matter in front of it. For young AGN jets, with a size of $\sim 10^2$ parsec, the typical hotspot velocity is $0.3c$, as measured from multi-epoch VLBI observations (Taylor et al. 2000). Jets from AGN can grow to scales much larger than their host galaxy. When they reach $\sim 10^2$ kpc, large lobes become a prominent feature of their radio morphology. The lobes are filled with hot

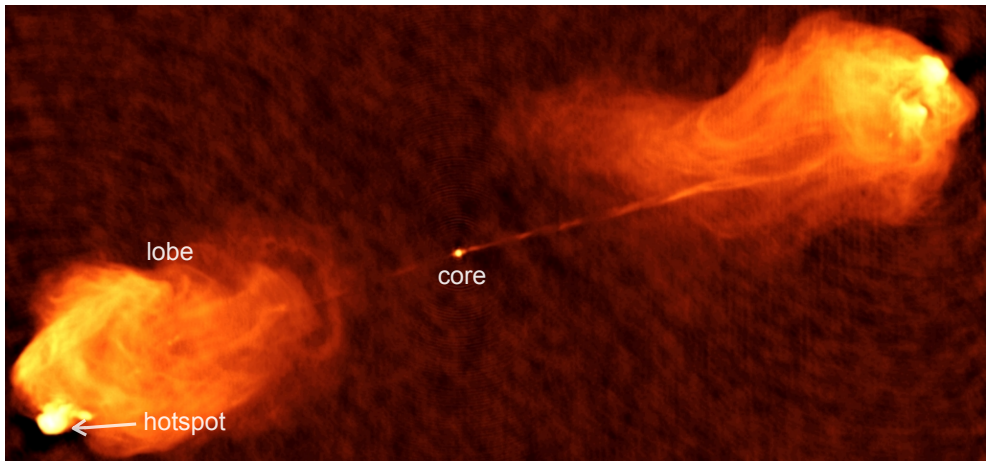

FIGURE 1.3: Radio image (5 GHz) of the FR II radio galaxy Cygnus A as observed in 1983 using the Very Large Array. The separation between the hotspots is about 150 kpc. Image courtesy of NRAO/AUI.

plasma that was accelerated in (or near) the hotspots, as evidenced by the steeper spectrum of the lobes downstream from the hotspot (Carilli et al. 1991). Based on the age derived from the synchrotron spectrum, we find a typical (extra-galactic) hotspot advance speed of $0.1c$ (Liu, Pooley, & Riley 1992).

The radio morphology of AGN jets is correlated with their luminosity (Fanaroff & Riley 1974). The most powerful sources are referred to as FR IIs (see Fig 1.3 for a famous example). They can be identified by their prominent hotspots and strong bow shocks, which yield an edge-brightened radio morphology. In radio maps of FR I sources, on the other hand, the jet emission is more prominent and hotspots are weak or not visible at all. The jets of FR I radio galaxies are clearly less powerful and thus get disrupted by the interaction with their environment. The observation that the luminosity threshold for obtaining an FR II morphology increases with host galaxy mass (Ledlow & Owen 1996) is consistent with this picture, since higher-mass galaxies are found in denser environments.

1.6 Theories of jet production

We now arrive at the frontier of jet physics: the launching and acceleration mechanism. Below I will review the two competing theories of jet production: disk-powered jets versus spin-powered jets. While these theories were written down over thirty years ago, we have yet to find conclusive evidence that allows us to decide which is right.

1.6.1 Disk-powered

Blandford & Payne (1982) proposed that matter can be ejected from the accretion disk with the help of poloidal magnetic fields. These poloidal fields remain frozen in the disk and along some field lines the centrifugal force will be larger than the gravitational force. Since the plasma follows the poloidal field, "like beads on wire" (Blandford & Payne 1982), it can be accelerated outwards. This mechanism alone is not sufficient to create a narrow jet, the ejected matter still has a strong equatorial component and somehow needs to be collimated. A thick disk can provide pressure for collimation close to the black hole, plus magnetic fields may also do the trick. When the outflowing magnetic field stops co-rotating with the disk, each rotation of the part of the line that is still anchored in the disk will increase the toroidal field strength. Collimation could also be established by the poloidal fields of the disk (Spruit et al. 1997).

In the Blandford–Payne mechanism, the jet power is extracted from the angular momentum of the disk, thus establishing a jet-disk symbiosis. Support for a disk-driven jet is the linear relation between accretion power and jet power, observed for both AGN (Rawlings & Saunders 1991; Falcke et al. 1995b; Serjeant et al. 1998; Willott et al. 1999) and (albeit more indirectly) in X-ray binaries (Klein-Wolt et al. 2002; Körding et al. 2006a).

A second attractive feature of the Blandford–Payne jet launching mechanism is its universality. The mechanism works not only for jets from black holes, but also for white dwarfs and stars: "all you need is an accretion disk" (and poloidal magnetic fields). An objection that is commonly raised, mostly motivated by simulations of jets (e.g., McKinney 2005), is that a pure magneto-hydrodynamical (MHD) launching mechanism is not powerful enough to create jets with high Lorentz factors ($\Gamma > 2$).

1.6.2 Spin-powered

A rotating black hole has free energy (Penrose 1969), which can be extracted from its ergosphere[5]. Blandford & Znajek (1977) realized that via magnetic torques the Penrose process can be used to power an electromagnetic (Poynting flux) jet at the cost of angular momentum of the black hole. The power of the jet is proportional to the dimensionless spin parameter (a, Eq. 1.5) and the magnetic flux at the horizon (Φ_B):

$$Q_{\rm BZ} \propto a^2 \Phi_B^2 \quad (a \lesssim 1) \quad . \tag{1.12}$$

The Blandford–Znajek mechanism thus requires magnetic field lines that thread the black hole event horizon and ergosphere. Spacetime dragging will twist these field lines in to a helical structure which can accelerate plasma along the black hole spin axis. The disk is not relevant for the jet power and only serves as a current sheet for fields

[5]The ergosphere is a consequence of spacetime dragging; it is defined to be the surface around the black hole where a particle has to travel at the speed of light to appear stationary for an observer at infinity.

near the black hole. That last point, however, also presents a theoretical weakness of the spin-powered jet model. Since the field around the horizon is a continuation of the field in the disk, the strength of the Blandford–Znajek process is limited (Ghosh & Abramowicz 1997), and could be much weaker than the electromagnetic energy extracted from the accretion disk (Livio et al. 1999). Also, loading the black hole with more power than is available from its rotational energy is calculated to terminate the Blandford-Znajek mechanism (Globus & Levinson 2013).

The coupling between spin and jet power has appealed to many authors since it allows for a wide range of jet powers at a given accretion rate. In the so-called spin-paradigm, the distribution of jet power of AGN follows from the distribution of black hole spin (Rees et al. 1982; Wilson & Colbert 1995; Sikora et al. 2007). As $a \to 1$, the jet-spin coupling steepens, hence high-spin may effectively act as a threshold for AGN with detectable radio jets (Tchekhovskoy et al. 2010).

Observations of black holes in X-ray binaries can be used to test the Blandford–Znajek mechanism, since their spin can be estimated by modeling the SED of the accretion disk in the soft state. (The inner part of the disk is set by the ISCO, which depends on spin, see McClintock et al. (2013) for a review.) Interestingly, a quadratic correlation between the radio power of the ballistic jet emitted during the hard-to-soft transition and the spin parameter has been reported (Narayan & McClintock 2012). However, other authors report no evidence for such a correlation (Fender et al. 2010).

In the disk-driven model, the jet axis is perpendicular to the inner part of the accretion disk, while Blandford–Znajek jets follow the spin axis of the black hole. If the inner part of the disk is tilted with respect to the black hole spin vector, it will precess around its angular momentum vector (Lense & Thirring 1918). Viscosity can communicate this pressure outwards through the disk, causing the inner disk to quickly align with the plane of the black hole (Bardeen & Petterson 1975). However, it was recently shown that this alignment requires a sufficiently large viscosity coefficient to keep the disk together (Nixon et al. 2012). For AGN, changes to black hole angular momentum are on a timescale of 10^{7-8} yr (e.g., Volonteri et al. 2007), so jets precessing on a much shorter timescale can be interpreted as evidence that the accretion disk, and not the standard Blandford-Znajek mechanism, is driving the jet (Nixon & King 2013). Complex ('S shaped') radio morphologies (e.g., in Mrk 6; Kharb et al. 2006) and a change of the position angle of the jet core (e.g., in M 81; Martí-Vidal et al. 2011), can be interpreted as signs of jet precession. But these observations are far from conclusive (e.g., the jet precession period of the core in M 81 is ten thousand times faster than precession period deduced from the radio morphology of Mrk 6).

1.6.3 Hybrid models and simulations

It is important to keep in mind that a coupling between jet power and magnetic field strength does not directly imply a coupling between jet power and accretion rate. While matter can pass through the horizon, the no-hair theorem forbids magnetic

fields from "sticking out". The fields will not be accreted into the black hole causing a pile-up close to the horizon. At first sight, this presents a major challenge for the spin-powered jet model: how to explain the observed linear relation between accretion rate and jet power? A potential solution is to let the magnetic flux at the horizon increase until the black hole is saturated with magnetic flux. This could yield a magnetic barrier that temporarily halts accretion into the black hole. These so-called magnetically arrested disks (MADs; Narayan et al. 2003) produce a very strong jet, with a linear coupling between accretion rate and jet power:

$$Q_{\rm MAD} \sim \dot{m}c^2a^2 \quad (a > 0.5) \quad . \tag{1.13}$$

The MAD scenario has been reproduced in GR MHD simulations of radiatively inefficient flows (Tchekhovskoy, Narayan, & McKinney 2011), although these require a continuous input of large-scale poloidally-dominated magnetic fields. When spin is not important ($a \to 0$), simulations show a MAD jet efficiency of a few percent (Igumenshchev 2008).

An alternative way to obtain a coupling between jet power and accretion rate, while also keeping a role for black hole spin, is to consider the effect of frame dragging on the Blandford–Payne mechanism (Punsly & Coroniti 1990). The calculations by Meier (2001) for such a hybrid model show that the jet power scales linearly with $\dot{m}$ and (roughly) quadratic with the angular momentum of the black hole.

A different kind of hybrid model is the two-component or spine-sheath jet (Sol et al. 1989; Hawley & Krolik 2006). Close to the black hole, the spine of the jet is dominated by Poynting flux and is created by the Blandford–Znajek mechanism, while the slower moving sheath contains baryons that were launched from the disk. This model could explain how BL Lac jets produce TeV photons while in VLBI observations their radio knots hardly move (Ghisellini, Tavecchio, & Chiaberge 2005).

Finally, we stress that both the spin-driven and disk-powered jet models require poloidal fields to be present in the inner parts of the disk. The magneto-rotational instability may not be able to generate a poloidal component that is large enough to sustain a persistent relativistic jet (Beckwith et al. 2008). In order words, launching a jet in a computer simulation (e.g., Fig. 1.4) currently requires specific initial conditions: a large-scale field with suppressed higher moments (McKinney & Blandford 2009). Whether such fields are accreted by astrophysical black holes is uncertain.

1.7 Jets in AGN

In the previous section we discussed *how* jets are launched. We now focus on *when* the launch happens and how long a single jet episode lasts. This question is relevant for AGN only, since the timing of X-ray binary jets is already described in a unified model (Sec. 1.3.2). Hence to understand how AGN jets are triggered, we can also

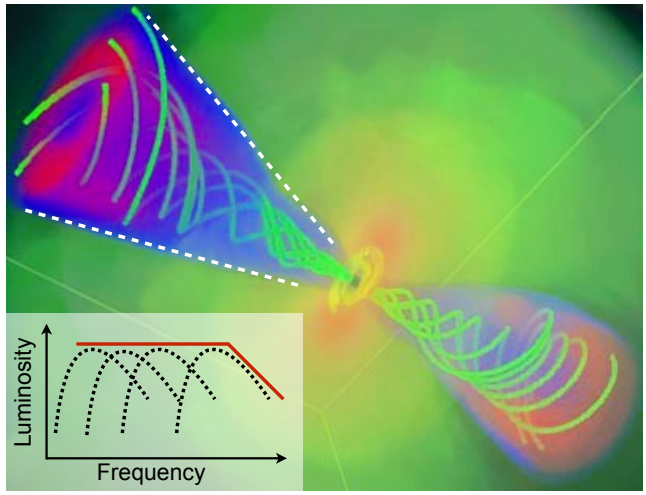

FIGURE 1.4: Snapshot from a simulation by McKinney & Blandford (2009), showing a jet launched by the Blandford–Znajek mechanism. The size of the simulation box is 10^3 gravitational radii, the inner ± 100 radii are shown here. The orange/green colors indicate high/low density material of the accretion disk and wind; the red/blue colors indicate a high/low Lorentz factor of the jet. The green lines show the magnetic field threading the black hole. The inset shows the flat spectrum that results from integrating the synchrotron spectrum of a conical jet with equipartition between magnetic fields and relativistic electrons; the highest energy synchrotron emission originates from the innermost part of the jet. We note that in the simulation shown here, the jet is magnetically-dominated, it contains virtually no particles and thus emits very little synchrotron radiation.

try to answer the following question: are AGN scaled-up versions of black hole X-ray binaries?

1.7.1 Analogy with X-ray binaries

Evidence that accretion is scale-invariant follows from the fundamental plane of black hole activity (Merloni, Heinz, & di Matteo 2003; Falcke, Körding, & Markoff 2004a). For sources at low accretion rate, the radio luminosity and X-ray luminosity follow a single power-law, $L_{\rm X} \propto L_{\rm Radio}^{1.4} M_{\rm BH}^{0.9}$, over eight (!) orders of magnitude in black hole mass; from X-ray binaries in the hard state, to the Galactic center black hole (Sgr A*), to low-luminosity AGN, and finally, to blazars (Plotkin et al. 2012). The mass term ($M_{\rm BH}^{0.9}$) is needed to account for the fact that the X-ray SED is not scale-invariant (e.g., the frequency where the spectrum becomes optically thin increases with mass). The origin of the X-ray emission could be optically thin synchrotron emission from the jet (Falcke et al. 2004a) or emission from the hot accretion flow (Merloni et al. 2003). For an ADAF scaling of $L_{\rm X} \propto \dot{m}^2$, Eq. 1.11 shows that the latter scenario implies a linear jet-disk relation ($Q_{\rm jet} \propto \dot{m}$). The scale-invariant model of accretion is

also supported by the observed rms-flux relation for the emission of the accretion disk, which is similar for both AGN, X-ray binaries, and white dwarfs (Uttley & McHardy 2001; Scaringi et al. 2012).

An obvious difference between Galactic black holes and supermassive black holes is the source of their fuel. While X-ray binaries receive a relatively steady mass input from their donor star, the feeding of AGN could change on a timescale that is similar to the duration of an accretion-state transition. Furthermore, the gas supply for supermassive blacks is more heterogeneous; the angular momentum and temperature of the gas depend on its origin (e.g., heated cluster gas, cold gas from stellar winds or galaxy mergers). This suggests that the role of the galaxy environment needs to be taken into account to understand AGN jets. Indeed, optically-selected AGN are more often hosted by galaxies with young stellar populations (Kauffmann et al. 2003). At low redshift, nearly all radio jets are hosted by massive elliptical galaxies. This could be due to accretion-state changes (i.e., at a fixed accretion rate, only massive black holes yield a jet-producing accretion flow) or due to environment.

1.7.2 Results from large surveys

Population studies are often used to find evidence for distinct accretion states in AGN. A key observation was made by Ho (1999), who reported that low-luminosity AGN (LLAGN) "look strikingly different compared to the standard energy spectrum of luminous Seyfert galaxies and QSOs"; LLAGN are much fainter at optical and UV wavelengths, they lack the so-called blue bump that is characteristic of radiatively efficient AGN. Radio follow-up observations revealed that most LLAGN show a compact flat-spectrum jet (Nagar et al. 2000). These observations support the idea that LLAGN are similar to X-ray binaries in the hard sate: a radiatively inefficient accretion flow with a steady jet that dominates the electromagnetic output of the system (Falcke 2001).

The advent of large surveys has enabled a new approach to study AGN. The Sloan Digital Sky Survey (SDSS; York et al. 2000) has imaged a large part of the northern sky (14,555 square degree, in 5 filters, to $m_r = 22.5$) augmented by massive spectroscopic follow-up. Now in its tenth data release, SDSS has produced almost 2 million galaxy spectra and over 300,000 quasar spectra (Ahn et al. 2014). This optical data is often combined with Faint Images of the Radio Sky at Twenty centimeters (FIRST; Becker, White, & Helfand 1995), to yield large samples of galaxies/AGN/quasars that show radio emission.

By combining SDSS and FIRST with X-ray data (from *ROSAT*), Körding, Jester, & Fender (2006b) constructed an AGN-equivalent of the hardness intensity diagram. The LLAGN were observed to fall on the hard-state branch while radio-loud quasars occupy the upper region (the high-soft and intermediate branch), suggesting that multiple AGN sample the track of a single XRB outburst. A similar conclusion was reached by Best & Heckman (2012), who used the SDSS spectra to divide radio

galaxies into 'high-excitation' and 'low-excitation' sources (high-excitation sources basically have stronger forbidden lines relatively to Hα, see Laing et al. 1994). The high-excitation radio galaxies show a stronger cosmological evolution and are found at higher Eddington ratios. The authors concluded that high-excitation spectra are explained by radiatively efficient disks, while low-excitation radio galaxies are fueled by hot gas via radiatively inefficient flows.

Jets from quasars are perhaps the most challenging topic to address with current observations. Based on a direct analogy with X-ray binaries, one would expect that jets in most quasars are quenched. Only during the hard-to-soft transition quasars briefly ($\sim 10^{6-7}$ yr) have powerful jets, which would explain why only a fraction of quasars are observed to be radio-loud (Nipoti, Blundell, & Binney 2005). The radio emission of the radio-quiet quasars, however, is difficult to interpret since it could be due to weak jets (Falcke et al. 1996), star formation (Condon et al. 2013), or winds from the accretion disk (Stocke et al. 1992; Zakamska & Greene 2014). The subject is complicated further by the lack of consensus on the radio-loudness distribution; claims of bi-modality (Strittmatter et al. 1980; Kellermann et al. 1989; Falcke et al. 1996; Xu et al. 1999) are followed by counter claims (Condon et al. 1981; White et al. 2000; Ivezić et al. 2002; Singal et al. 2013). Some of this discrepancy can be explained by source selection, e.g., most studies use only one frequency and include point sources, which smears out the radio-loudness distribution due to Doppler boosting of flat-spectrum radio cores.

Perhaps the best way to test the analogy between the transient X-ray binary jets and radio-loud quasars is to look for signs of intermittency of jets from quasars. Galaxies with a double-double radio morphology (i.e., a pair of double radio sources with a common center; Schoenmakers et al. 2000) show that jet intermittency on relatively short timescales ($\sim 10^7$ yr) is possible. Double-double radio galaxies are rare, but this type of morphology is observable for only a brief period of the source lifetime. Hence it remains unclear if episodic/intermittent jet activity is a common feature of AGN.

1.8 Tidal disruption flares

In the previous section we discussed when AGN jets are launched, concluding that current observations suggest that they are similar to X-ray binaries, with jet production coupled to the mode of accretion. Critically testing this idea remains difficult because nearly all supermassive black holes evolve on timescales much longer than the baseline of our observations. The exception are black holes that are caught in the act of tidally disrupting a star.

A stellar tidal disruption event happens when a star passes within a few tens of gravitational radii of a supermassive black hole; within the tidal disruption radius,

$$R_r \approx 25 R_s \left(\frac{M_{\rm BH}}{10^6 M_\odot} \right)^{-2/3} \tag{1.14}$$

the star is disrupted due to the tidal effect of gravity. About half of the star remains bound to the black hole and after a time

$$t_{\rm fb} \approx 0.11 \left(\frac{M_{\rm BH}}{10^6 M_\odot} \right)^{1/2} \ {\rm yr} \quad , \tag{1.15}$$

this debris returns to the pericenter at a rate of $\dot{m}_{\rm fb} \propto (t/t_{\rm fb})^{-5/3}$ (Rees 1988). For a black hole with a mass of $M_{\rm BH} \sim 10^6 M_\odot$ the fallback rate initially exceeds the Eddington limit, yet after ~ 10 years $\dot{m}_{\rm fb} < 1\% \dot{m}_{\rm Edd}$. This implies we may anticipate an accretion state change, and thus observe a jet for every disrupted star.

The first tidal disruption flare (TDF) candidates were discovered using soft X-ray (0.1–2.5 keV) observations of *ROSAT* (see Komossa 2002), which measured the thermal emission of the stellar debris. Later, the *GALEX* mission allowed the selection of TDF candidates at UV wavelengths, yielding four strong candidates (Gezari et al. 2009b, 2012). The discovery of TDFs using an optical survey is presented in Chapter 6 of this thesis.

Recently, two stellar disruption events with relativistic jets were discovered, implying that the debris can circularize into some type of accretion disk after the disruption. Both events were discovered as γ-ray transients by the Burst Alert Telescope (BAT) of *Swift* and both showed a transient radio counterpart (Zauderer et al. 2011; Cenko et al. 2012b). Interestingly, the X-ray light curve of the best sampled relativistic TDF, Swift 1644+57, shows a very steep drop when the estimated fallback rate crosses the Eddington limit (Zauderer et al. 2013), suggesting that the jet has switched off due to a state change of the accretion flow (i.e., from a slim advection dominated flow to a thin disk).

Besides new probes of jet physics, stellar tidal disruptions are interesting for at least three other reasons.

First, TDFs are arguably our only tool to study non-active black holes beyond the Local Universe —at least until eLISA comes online. Since $t_{\rm fb}$ is proportional to the mass of the black hole (Eq. 1.15), a measurement of the fallback rate could provide a handle to measure this mass (Lodato, King, & Pringle 2009; Guillochon & Ramirez-Ruiz 2013).

Second, the frequency of stellar disruptions depends on the phase space distribution of stellar orbits, so the rate of TDFs can be used to learn about the gravitational potential of galaxies. Since the merger of two galaxies is expected to enhance the disruption rate, both due to mixing of the two nuclear star clusters (Wegg & Nate-Bode

2011) and the recoil of the merged black holes (Stone & Loeb 2011), the detection of multiple flares can be used to identify gravitational wave sources for eLISA.

Finally, using stars as test particles, TDFs can yield dynamical evidence for the existence of an event horizon. Because we can only observe disruptions that happen outside this horizon, the TDF rate will be strongly suppressed above a critical mass of $M_{\rm BH} \approx 10^8\,M_\odot$ (Hills 1975). This critical mass is larger for higher spin (Kesden 2012), so in principle a sample of TDFs can be used to measure the spin distribution of dormant supermassive black holes.

So far, none of the thermal (optical/UV/soft X-ray) TDF candidates show evidence for jets. The SED of the two relativistic TDFs discovered by *Swift*, on the other hand, shows no sign of thermal emission. So we have yet to discover the "missing link" between jetted and thermal TDFs, i.e., a disrupted star that yields detectable emission from both an accretion disk and a jet.

1.9 This thesis

In this thesis we study the properties of jets from supermassive black holes, with the ultimate goal of understanding how and when jets are launched.

We start with radio jets in the Local Universe. A new all-sky inventory of these sources is presented in Chapter 2. We use this sample to investigate the influence of the galaxy environment on jets. In Chapter 3, we investigate the hypothesis that the jets of local radio galaxies are responsible for the observed flux of ultra-high energy cosmic rays. This could inform us on the efficiency of the particle acceleration mechanism in jets and radio lobes. For Chapters 4 & 5 we move to higher redshift ($z \sim 1$) to study FR II radio galaxies. We first use the correlation between disk power and lobe radio luminosity to test the Blandford–Znajek mechanism (Ch. 4). In Chapter 5, we present the first attempt to predict the areal density of FR IIs from the number density of known quasars.

The second part of the thesis deals with accretion on a timescale of a few years, namely stellar tidal disruption flares. We first present a successful search for these rare events (Ch. 6) and use Monte Carlo simulations to compute the rate of disruptions (Ch. 7). We then present a new model for the radio emission of jets from tidal disruption (Ch. 8) and predict the event rate for radio transient surveys. In Chapter 9, we close the scientific circle by testing these predictions using new radio observations.

Part I:
Cosmic timescales

Chapter 2

Radio galaxies of the Local Universe

Sjoert van Velzen, Heino Falcke, Pim Schellart, Nils Nierstenhöfer,
and Karl-Heinz Kampert
2012, Astronomy & Astrophysics, 544, A18

Abstract

To understand the feedback of black holes on their environment or the acceleration of ultra-high energy cosmic rays in the present cosmic epoch, a systematic, all-sky inventory of radio galaxies in the Local Universe is needed. Here we present the first catalog of radio-emitting galaxies that meets these requirements. Our catalog allows the selection of volume-limited subsamples containing all low-power radio galaxies, similar to the prototypical low-power radio galaxies Cen A or M87, within some hundred Mpc. It is constructed by matching radio emission from the NVSS and SUMSS surveys to galaxies of the 2MASS Redshift Survey (2MRS) using an image-level algorithm that properly treats the extended structure of radio sources. The sample contains 575 radio-emitting galaxies with a flux greater than 213 mJy at 1.4 GHz. Over 30% of the galaxies in our catalog are not contained in existing large-area extra-galactic radio samples. We compute the optical and radio luminosity functions and the fraction of radio galaxies as a function of galaxy luminosity. We find that the local galaxy density in a sphere of 2 Mpc centered on the radio galaxies is 1.7 times higher than around non-radio galaxies of the same luminosity and morphology. This significant enhancement suggests a causal relation between external galaxy properties, such as environment or merger history, and the formation of powerful jets in the present universe. Since the enhancement is observed with respect to galaxies of the same luminosity and Hubble type, it is not primarily driven by black hole mass. Our automated matching procedure is found to select radio-emitting galaxies with high efficiency (99%) and purity (91%), which is key for future processing of deeper, larger samples.

2.1 Introduction

The final episode in the history of black hole accretion and galaxy formation takes place in our cosmic backyard, the Local Universe. A large sample of nearby radio galaxies may thus be considered an important anchor point for theories of black hole growth and downsizing (e.g., Alexander & Hickox 2012) and can be used to study feedback from radio jets (Fabian et al. 2003; Mathews & Brighenti 2003) on the environments of their host galaxies.

Nearby radio galaxies allow one to study a regime of fainter jets and thus, assuming standard jet-disk coupling (Rawlings & Saunders 1991; Falcke & Biermann 1995), lower rates of accretion onto the black hole. At these low rates, the mode of accretion (Narayan & Yi 1995) may switch to a 'jet-dominated mode' or 'radio mode' (Falcke, Körding, & Markoff 2004a), similar to the 'low-hard state' of X-ray binaries (Fender, Belloni, & Gallo 2004), implying that radio surveys are an ideal tool to find active black holes in this regime. Large samples of radio-loud active galactic nuclei (AGN) provide increasing evidence that two different modes of accretion onto super-massive black holes indeed exist (Ghisellini & Celotti 2001; Körding et al. 2006b; Ghisellini et al. 2011; Wu et al. 2011; Best & Heckman 2012).

The first catalogs of extra-galactic radio sources were constructed by gathering a (heterogeneous) set of optical follow-up observations (Schmidt 1968; Véron & Véron 1974; Kuehr et al. 1981; Laing et al. 1983; Jones & McAdam 1992). With the advent of wide-field optical surveys and deep radio surveys with high angular resolution, it has become possible to match cataloged sources at both wavelengths, and thus systematically construct large catalogs of radio sources with distance information (Condon et al. 2002; Ivezić et al. 2002; Best et al. 2005b; Sadler et al. 2007; Mauch & Sadler 2007; Kimball & Ivezić 2008; Donoso et al. 2009; Brown et al. 2011). Such catalogs have played a key role in the study of star formation, AGN, and the interplay between them.

While at intermediate to large redshifts ($z \gtrsim 0.1$) one can survey a limited area of the sky to obtain a representative slice of the extra-galactic volume, studies of the Local Universe require full-sky coverage (i.e., 4π solid angle) to map the anisotropy of the matter distribution. None of the modern catalogs of active black holes meet this requirement.

With the recent release of the 2MASS redshift survey (2MRS; Huchra et al. 2012), currently the deepest all-sky redshift survey, it has become possible to construct an extra-galactic radio catalog that covers 90% of the volume of the Local Universe. Indeed we made this our goal: obtain a complete, all-sky catalog of galaxies that emit at radio wavelengths. We have constructed this catalog in the most systematic way possible to ensure that the selections effects are well-defined (opposed to compiling a list of known radio sources from the literature). Since the radio galaxies of our catalog are a subset of normal galaxies and, by construction, the sample is the largest of its kind, it present a powerful tool for a statistical study of the relation between black

hole activity and galaxy environment.

Our primary motivation for building an all-sky radio catalog is to obtain a volume-limited sample of galaxies that could be powerful enough to accelerate ultra-high energy cosmic rays (UHECRs, charged particles with an energy in excess of 5×10^{19} eV) and study the magnetic field and energetics of these sources. For this study, full-sky coverage is key because interactions with photons of the cosmic microwave background limit the distance an UHECR can travel to about 100 Mpc, the so-called, GZK horizon (Greisen 1966; Zatsepin & Kuz'min 1966); if the sources of UHECRs are rare ($< 10^{-5}$ Mpc^{-3}), the full-sky has to be searched to obtain a sizable sample.

A good candidate source of UHECRs is Cen A: this radio galaxy may just be powerful enough to accelerate protons up to the ultra-high energy scale (for a recent review see Biermann & de Souza 2012). Since Cen A is the nearest and one of the best studied radio galaxies, it provides a good anchor for the rest of the catalog; the flux of Cen A at 100 Mpc (~ 1 Jy at 1 GHz and $K = 11$) is comfortably within the limits of existing surveys. Our main goal can thus be summarized in one sentence: *find all radio galaxies within 100 Mpc that are as a luminous as Cen A*. Since Cen A is relatively faint at optical wavelengths, this requirement actually allows us to find most typical radio galaxies within 200 Mpc.

In this chapter, we focus on the construction and properties of the radio-bright sample[1]. In Section 2.2 we discuss our matching algorithm and we compare our sample to existing radio catalogs. In the third section we present the number counts (Sec. 2.3.1), the cross-correlation of our radio galaxies with the local matter distribution (Sec. 2.3.2), and the luminosity functions (Sec. 2.3.3). We close with a discussion in Section 2.4.

2.2 Catalog construction

As explained in the introduction, we wish to obtain a flux-limited, all-sky catalog of extra-galactic radio sources, from which a volume-limited sample can be derived. In this section we discuss the construction of this catalog. First, we will describe the input (Sec. 2.2.1), followed by a detailed discussion of the matching algorithm (Sec. 2.2.2). In Section 2.2.3 we present the columns our catalog. We assess the completeness in Section 2.2.4 and probability for random matches in Section 2.2.5. A comparison to existing extra-galactic radio catalogs is presented in Section 2.2.6. Finally, we briefly discuss some newly identified radio-emitting galaxies in Section 2.2.7.

[1]The master catalog (described in Table 1) and the catalog listing all radio matches per galaxy, are available in electronic form at the CDS via `http://cdsweb.u-strasbg.fr/cgi-bin/qcat?J/A+A/` or at `http://ragolu.science.ru.nl`.

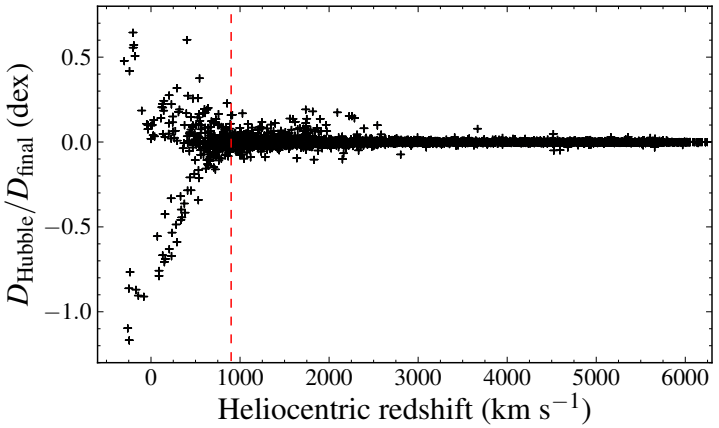

FIGURE 2.1: The difference between the Hubble distance, after our correction for peculiar velocity ($D_{\rm Hubble}$), and the final distance ($D_{\rm final}$). The latter is the inverse-variance weighted mean of $D_{\rm Hubble}$ and median redshift-independent distance from NED-D. The fractional uncertainty on the Hubble distance decreases with redshift, hence the convergence to zero difference. The dashed line indicates the redshift cut that is applied in the computation of the luminosity functions and clustering (Sec. 2.3).

2.2.1 Input

In the following paragraphs we discuss the input for our catalog: the 2MASS Redshift Survey (2MRS), the NRAO VLA Sky Survey (NVSS), and the Sydney University Molonglo Sky Survey (SUMSS).

2.2.1.1 Redshift survey

To be able to select a volume-limited sample of radio sources, we need a measurement of the distance to each source. Currently, the deepest all-sky redshift survey is the 2MRS (Huchra et al. 2012), which covers essentially the entire extra-galactic sky accessible at optical wavelengths (91% of the full-sky). The targets of this survey are galaxies from the 2 Micron All-Sky Survey (2MASS; Skrutskie et al. 2006), contained in the extended source catalog (Jarrett et al. 2000; Jarrett 2004), selected with the following requirements:

- $K_s < 11.75$ and detected in the H-band
- $E(B-V) < 1$
- $|b| > 5°$ for $30° < l < 330°$; $|b| > 8°$ otherwise.

Where $E(B-V)$ is the extinction from the maps of Schlegel et al. (1998); l and b are the Galactic longitude and latitude, respectively. K_s is the isophotal magnitude (measured in an elliptical aperture defined at the 20 mag per square arcsecond

isophote). The K-band is centered at $\lambda \approx 2.2\,\mu m$, the near infrared (NIR) part of the electromagnetic spectrum.

The 2MRS cuts select 44,599 galaxies from 2MASS; the current catalog contains redshifts for 97.6% of these. The median redshift is 0.028, 90% of the sample is contained within $z < 0.052$. We applied no cuts on the 2MRS catalog.

Some care has to be taken when converting redshifts of nearby-galaxies to distances using the Hubble law. We adopt the approach used by Blanton et al. (2005) for the construction of the NYU Value-Added Galaxy Catalog. First, we shift to the Local Group barycenter using the heliocentric velocity determination of Yahil et al. (1977). In this frame we estimate the most likely distance and its uncertainly using the model of the local velocity field of Willick et al. (1997) based on the IRAS 1.2 Jy redshift survey (Fisher et al. 1995). We adopt $H_0 = 72\,\mathrm{km\,s^{-1}}$ and $\Omega_m = 0.3$, $\Omega_\Lambda = 0.7$ to convert the peculiar-velocity corrected redshifts to a distance.

For galaxies with a radial velocity (measured in Local Group barycenter) below $6,000\,\mathrm{km\,s^{-1}}$ we attempt to improve the Hubble law distance using published redshift-independent distances (e.g., Cepheids, Supernova Type Ia, Tully-Fisher relation) as listed in NED-D[2]. For 3351 galaxies (8%) we compute the inverse variance weighted mean distance modulus from our peculiar-velocity corrected Hubble distance and the median redshift-independent distance modulus. The corrections to the luminosity distances derived solely from the Hubble law are modest, -0.0006 ± 0.07 dex in the mean. Corrections larger than 0.5 dex are observed only for galaxies with a Local Group barycenter radial velocity smaller than 187 $\mathrm{km\,s^{-1}}$ (Fig. 2.1). For the radio-emitting galaxies in our final sample (Sec. 2.2.2.3), the coverage of NED-D is 100% below 250 $\mathrm{km\,s^{-1}}$, so the uncertainty on the radio luminosity due to peculiar velocities is not significant.

2.2.1.2 Radio catalogs

No single radio survey covers the full sky, we thus have to combine multiple surveys. To avoid sky-dependent selection effects, these surveys have to be similar in depth, frequency and resolution. With these requirements only one set of radio surveys remains[3]: NVSS (Condon et al. 1998) and SUMSS (Bock et al. 1999; Mauch et al. 2003), covering the Northern and Southern Hemisphere, respectively.

The NVSS catalog is derived from images obtained with the VLA in D and DnC configurations at 1.4 GHz and covers the sky north of declination $-40°$ (75% of the full-sky). The size of the point-spread-function (PSF) of these images is $45''$ FWHM and the astrometric accuracy is better than 1" for $F_\nu > 15$ mJy. The typical rms

[2] `http://ned.ipac.caltech.edu/Library/Distances/` (v5.1) compiled by I. Steer and B. F. Madore.

[3] Other radio surveys such as FIRST (Becker et al. 1995) or AT20G (Murphy et al. 2010), could be considered more suitable for matching to optical catalogs of galaxies. However this set of surveys does not meet our requirement of covering the entire sky at a similar frequency.

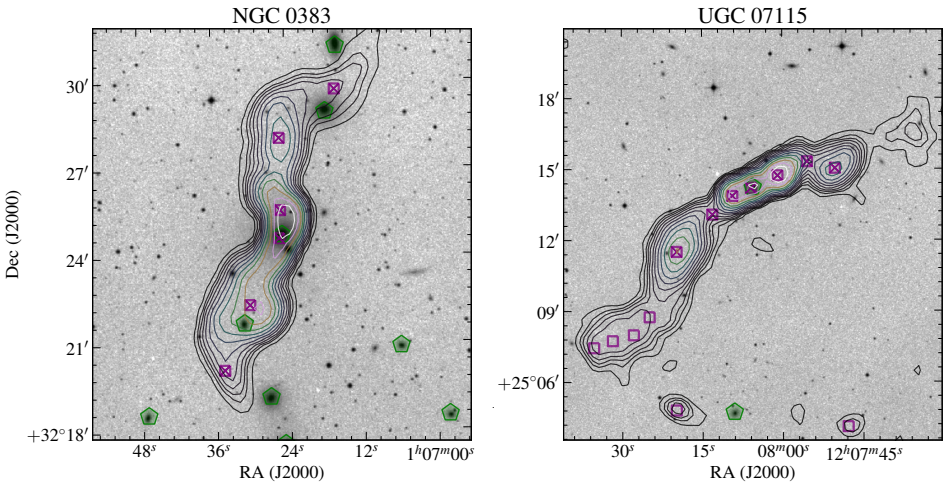

FIGURE 2.2: Two examples to illustrate the challenges that arise when matching optical images with a resolution of ~ 2" to radio images with a resolution of 45". The contours show the radio emission from NVSS; 2MRS galaxies are labeled with green pentagons. The entries of the NVSS catalog are shown by purple squares, we see that both jets are decomposed into multiple elliptical Gaussians (6 for NGC 383 and 11 for UGC 7115). The radio entries matched to this galaxy by the angular distance requirement (Eq. 2.1) are labeled with crosses. For UGC 07115, the remaining four jet components are included after applying a friends-of-friends algorithm (Sec. 2.2.2.1).

brightness fluctuations in the NVSS images are 0.45 mJy/beam and the completeness limit is about 2.5 mJy.

The SUMSS catalog is constructed from data obtained with MOST (Molonglo Observatory Synthesis Telescope; Mills 1981; Robertson 1991) at 843 MHz. The resolution of the SUMSS images is 43" FWHM. The typical astrometric accuracy in right ascension is $2-3$" at 10 mJy and 1" above 20 mJy; position uncertainties in declination (δ) are typically a factor of $\csc(|\delta|)$ higher than in right ascension. The rms noise level of the SUMSS images is ~ 1 mJy/beam, the completeness limit is about 10 mJy. The survey covers the sky south of declination $-30°$ with $|b| > 10°$. The sky below $|b| = 10°$ that is not in the NVSS footprint is covered by MGPS-2 (The second epoch Molonglo Galactic Plane Survey; Murphy et al. 2007) which is the Galactic counterpart to SUMSS. The MGPS-2 catalog, however, currently only contains compact sources which makes it unsuited for our matching algorithm. We therefore removed the $|b| < 10$ region for $\delta < -40$, reducing the area covered by our catalog from 91% to 88%.

It is important to realize that both the SUMSS and NVSS catalog are constructed by fitting elliptical Gaussians to the radio maps. Each entry in the catalog is a separate Gaussian with a measured major/minor axis and integrated flux. Extended

radio sources are often broken up into multiple Gaussians, hence a single astrophysical object is not necessarily represented by a single entry in the radio catalogs.

2.2.1.3 Flux limit

As explained in the introduction, our primarily goal to obtain a volume limited sample of radio galaxies as bright as Cen A. We use the flux of Cen A at the distance that contains 95% of the galaxies in 2MRS to find a conservative value for the radio flux limit. Using $F_{1400} = 1330$ Jy for all the radio emission of Cen A (Cooper et al. 1965) at 1.4 GHz and a spectral index[4] $\alpha = -0.6$, we obtain the following flux limits: $F_{1400} > 213$, $F_{843} > 289$ mJy for NVSS, SUMSS. We apply these limits to the sum of the integrated radio flux of all Gaussians that are matched to a galaxy. Extending these flux limits to the completeness limits of the radio surveys (~ 10 mJy) will be the subject of future work.

2.2.2 Matching

The next step is to match the radio surveys to the redshift survey to find radio-emitting galaxies. Our aim is to automate the matching as much as possible. This reduces (or at least parametrizes) human bias and substitutes expensive man-hours with cheap cpu-time. Since this is our first attempt at fully automated cross-wavelength matching, we will also inspect all matches manually.

Two challenges have to be met: (i) the FWHM of the PSF of the radio images is over an order of magnitude greater than the NIR images, (ii) many radio sources are resolved and will appear in the radio catalogs as multiple entries which can be offset from the galaxy by several arcminutes (e.g., giant radio galaxies). Our approach to this problem is to proceed in two steps: first we match on the catalog-level (Sec. 2.2.2.1), then we assess these matches at the image-level (Sec. 2.2.2.2). We designed the first step to be "generous", i.e., all potential matches should be found, at the cost of a large background of false identifications. At the image-level this background is often trivially rejected.

In a nutshell, our matching pipeline is based on the assumption that the galaxy is source or origin of the radio emission, but we allow this emission to be displaced and even disconnected from the galaxy; it is optimized to recover radio emission from both starforming galaxies, and systems with more complicated or asymmetric morphologies such as FR II galaxies or "head-tail" sources.

2.2.2.1 Catalog-level matching

We use the size of the radio source and the angular distance between this source and the galaxy to define the first matching criterion:

$$d_i < N_{\rm lim} \times {\rm FWHM}_i \quad {\rm OR} \quad d_i < d_{\rm lim} \quad , \tag{2.1}$$

[4]We define the spectral index, α, by $F_\nu \propto \nu^\alpha$.

where d_i is angular distance between the ith radio entry and the galaxy center and FWHM_i is the deconvolved major axis of the radio Gaussian. We adopted the following cuts: $N_{\mathrm{lim}} = 3$ and $d_{\mathrm{lim}} = 2'$. In Section 2.2.4 we verify that these settings are indeed generous enough.

For the coordinate matching we use `k3match`, a new[5] and efficient implementation of 3 dimensional binary tree search. It can find matches between two sets of points on a sphere in $O(N \log(N))$ time as opposed to the $O(N^2)$ time needed for a brute force search (Schellart 2013).

In some cases, the requirement set by Eq. 2.1 will miss a small fraction of the radio emission (e.g., UGC 7115 in Fig. 2.2: the start of the jet is matched to the galaxy, but the rest of the radio emission, extending 6' further out, is not). This problem is solved by extending the matches using a friend-of-friend algorithm. We add a new radio entry to the group of matches if $d_{ij} < \max(N_{\mathrm{lim}} \times \mathrm{FWHM}_i, d_{\mathrm{lim}})$, with d_{ij} the angular distance between the current radio match i and the potential new entry j (i.e., a link length equivalent to Eq. 2.1), and we repeat this procedure until no new matches are found. This approach successfully recovers the entire structure of nearly all extended radio sources (as demonstrated by the images in Appendix 2.A).

For each galaxy, the total radio emission is simply given by the sum of the integrated flux of all the components that are matched to the galaxy. Using Eq. 2.1 we obtain 1273 galaxies with a total radio flux above our flux limit (Sec. 2.2.1.3), with a total of 8452 matches between galaxies and entries in the radio catalogs. The generous criteria used at this stage are required to match galaxies with displaced radio counterparts, but they inevitably yield false matches; we discuss the rejection of these false matches in the following section.

2.2.2.2 Image-level rejection

We now proceed to remove false matches from the set of 1273 galaxies from the catalog-level matching (Sec. 2.2.2.1) using the information contained in the pixels of the radio images. We stress that in nearly all cases these false matches are trivially identified (e.g., the left panel of Fig. 2.2, in this field all galaxies are matched to the radio emission, but the source of this emission is undoubtedly the central galaxy, NGC 0383). The only challenge is to parametrize the judgment of a trained astronomer[6]. Again our approach is to use the galaxy as a starting point to identify (disconnected) radio emission as originating from a single source (e.g., IC 2722 in Fig. 2.14).

Our algorithm consists of the following steps (in Fig. 2.3 we show two examples).

1. Make a cut-out of the radio image centered at the coordinates of the galaxy. The width of this image (I) is set by the maximum angular distance between

[5] k3match is available under GNU General Public License at `pschella.github.com/k3match`

[6] This is a classical problem of Computer Vision; it may likely be solved more efficiently using tools from this field.

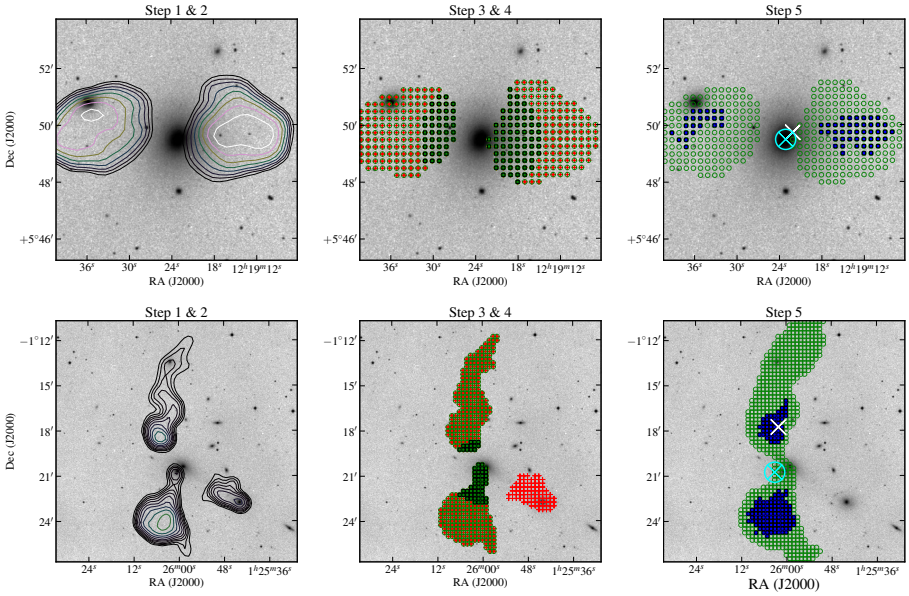

FIGURE 2.3: The image-level matching algorithm at work (top: UGC 7360, bottom: NGC 0547). In step 1 & 2 we determine the size of the frame and draw contours. In step 3 we find the pixels above the value of the outer contour (labeled with red plusses) and in step 4 we link these pixels to the optical center of the galaxy (green squares). In step 5, we find the pixels that are connected to the group obtained in the previous step (shown by green circles), these define the radio emission matched to this galaxy. Finally we measure the geometrical center (white cross) and the flux-weighted center (cyan circled cross). For the latter, we use only the pixels that contain 80% of the total flux of the group (labeled with blue squares).

the galaxy and the radio sources matched to this galaxy.

2. Draw contours on this sub image. The level of the lowest contour is given by $\max(\sigma(I)/7, 3\times\sigma(I_{50}))$, where $\sigma(I)$ is the standard deviation of the pixels of the image obtained in the previous step and I_{50} is subset of this image containing the pixels below the median of the image.

3. Find all pixels contained by lowest contours that are within max(FWHM$_i$, 30") of the location of the galaxy, where FWHM$_i$ is the deconvolved major axis of the radio sources matched to this galaxy. If no pixels are found, we reject this galaxy. Most galaxies are rejected at this step since they are not connected to the radio contours (e.g., left panel of Fig. 2.2). Radio sources that consist of two lobes (FR II morphologies) are not rejected because the galaxy connects the two lobes (e.g., UGC 7360 in Fig. 2.3).

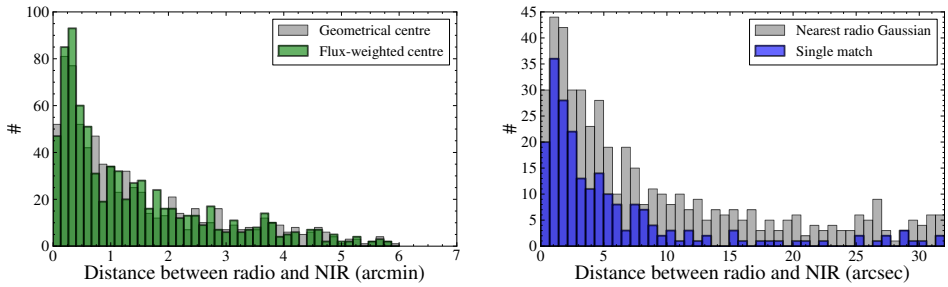

FIGURE 2.4: Histogram of angular distance between the NIR center of the galaxy (i.e., 2MRS coordinates) and different measure of the center for the radio emission for the candidate matches from the catalog cuts (Eq. 2.1). Left: the geometrical center (Eq. 2.2) and the flux-weighted center (Eq. 2.3). Right: the minimum angular distance between the galaxy and any of the matched radio sources for galaxies with a single match (thick blue line) and multiple matches (thin gray line).

4. Find all pixels within the lowest contour that are connected to pixels of the previous step. Any radio matches outside this group are rejected. This step removes unrelated radio emission that has been matched at the catalog-level (e.g., the head-tail source that was initially matched to NGC 0547, Fig. 2.3).

5. If more than one elliptical Gaussian from the radio catalogs is matched to a galaxy, we try to estimate the center of the radio emission. We compute the geometrical center by minimizing

$$d_i = \sum_j d_{ij} \quad , \tag{2.2}$$

where d_{ij} is distance between pixel i and j and the sum runs over all pixels in the group (i.e., pixels obtained in step 4). We also compute a flux-weighted center by minimizing

$$d_i = \max(d_{ij} w_{ij}) \quad , \tag{2.3}$$

where the weight w_{ij} is unity for the pixels that contain 80% of the total flux in the group and zero otherwise. The geometrical method (Eq. 2.2) yields a robust measurement of the center for radio sources that have at least one symmetry axis that intersects the location of the galaxy, while the flux-weighted center gives a better estimate for radio sources with two bright spots at equal distance to the galaxy.

Step 3 rejects 412 galaxies that are not close enough to the outer contour of the radio emission. After removing unrelated radio emission in Step 4, we al left with 769 galaxies above the radio flux limit.

To define our final sample, we use a cut on the angular distance of the galaxy to the geometrical and the flux-weighted center. Since these measures of the center are not alway appropriate (e.g., for head-tail sources), we also consider the minimum angular distance between the galaxy and the radio matches as well as the minimum angular distance between the galaxy and the second-highest contour (if the galaxy is within this contour we set this distance to zero). In Fig. 2.4 we show the distribution of these distances. Based on these distributions, we adopt the following criteria for galaxies with multiple radio matches:

$$d \quad < \quad \begin{cases} 1.2' & \text{to geometrical center} \\ 1.2' & \text{to flux-weighted center} \\ 15" & \text{to second highest contour} \\ 8" & \text{to nearest radio catalog entry} \end{cases} \tag{2.4}$$

Galaxies with multiple radio matches should pass *at least one* of these angular distance criteria. For galaxies with a single radio match, the flux-weighted or geometrical center should not be used. Instead, we require at least one of the following two criteria:

$$d \quad < \quad \begin{cases} 8" & \text{to radio catalog entry} \\ 0" & \text{to second highest contour} \end{cases} \tag{2.5}$$

The second of these two requirements implies that the coordinates of the galaxy are *within* the second highest radio contour. For point sources this requirement is superfluous (the galaxy always lies within the highest contour). For extended radio emission, however, the galaxy can be within the second highest contour while the distance to the radio catalog entry is $> 8"$.

The image-level cuts (Eqs. 2.4 & 2.5) reject 119 galaxies; 78 sources are flagged for manual inspection because more than one galaxy is matched to the same radio source. Besides these 78 ambiguous matches, we will also inspect the rejected and accepted matches to measure how well our image-level algorithm is performing.

2.2.2.3 Manual inspection & classification

The sample obtained after the catalog-level matching (Eq. 2.1) is small enough to inspect all matches. We stress that, at this point, we do not add new sources to the sample, the only goal is to identify spurious or ambiguous results from the automatic matching pipeline.

For 51 galaxies the radio emission matched to the galaxy by the image-level algorithm (Sec. 2.2.2.2) was rejected after human inspection, hence the purity of the sample after our fully automated image-level matching procedure is 91%. Some of these initially accepted matches are very hard to classify or reject automatically (e.g., blended sources or, very rarely, Galactic emission), but most are due to artifacts in the radio images. We found that in only six cases, our image-level cuts (Eqs. 2.5 &

2.4) rejected a galaxy while at inspection we found this to be genuine match, implying an efficiency of 99%.

The sources above the flux limit (Sec. 2.2.1.3) that remain after manual inspection comprise the final sample: 575 radio-emitting galaxies. Using the morphology of the radio emission, we classify these into four categories, the number of sources in each class is given in brackets.

- *Point Sources (97)*: a single, unresolved radio source.
- *Starforming galaxies (52)*: extended radio emission that coincides with the extended NIR emission from the galaxy.
- *Jets & Lobes (407)*: resolved radio emission beyond the NIR image of the galaxy that appears to originate from the center of galaxy. We did not attempt to subdivide this sample using the Fanaroff & Riley (1974) classification scheme because most sources with an FR II morphology would not be classified as such based on their radio luminosity.
- *Unknown (19)*: if none of the above classes apply. These sources are *not* removed from our sample because they formally pass our image-level cuts (Eqs. 2.5 & 2.4). Yet their morphology suggests that the radio emission is not associated with the host galaxies. Users of the catalog may decide to remove the sources in this class.

We stress that these classes are based on morphology only, they are not complete (i.e., some starforming galaxies or jets are classified as point sources because the radio emission is not resolved).

2.2.3 Catalog columns

We combine the properties of the 575 galaxies of our final sample into a single master catalog; the columns of this catalog are described in Table 2.1. Since for some applications it is useful to have acces to the individual radio matches per galaxy, we also provide a basic catalog, listing all matched radio Gaussians per galaxy.

2.2.4 Completeness

The 575 galaxies of our master catalog are a subset of the potential matches obtained from the catalog parameters (Sec. 2.2.2.1). We can check if the latter sample was large enough by comparing the minium angular distance between the radio Gaussians and the galaxies to the cuts that we have adopted. In Fig. 2.5 we see that the catalog selection is not limiting the size of the final sample, because all galaxies are well within one of the two requirements placed by Eq. 2.1.

We also confirm that the small difference in frequency between NVSS (1.4 GHz) and SUMSS (843 MHz) does not lead to a noticeable selection effect: the number

Column	Units	Description	Source
`2MASX`		Target name of the object from 2MRS database	2MRS
`NED_id`		NED id of galaxy	NED
`ra`	deg	Right Ascension of galaxy	2MRS
`dec`	deg	Declination of galaxy	2MRS
`l`	deg	Galactic longitude	2MRS
`b`	deg	Galactic latitude	2MRS
`Kmag`	AB	K-band isophotal magnitude, corrected for Galactic extinction	2MRS
`Kmag_err`	AB	uncertainty on `K`	2MRS
`z`		Heliocentric redshift	2MRS
`zdist`		Peculiar-velocity corrected redshift	2.2.1.1
`zdist_err`		Uncertainty on `z_dist`	2.2.1.1
`D`	Mpc	Inverse-variance weighted mean of distance from NED-D and peculiar velocity corrected Hubble distance ($h = 0.72$)	2.2.1.1
`D_err`	Mpc	Uncertainty on the former row	2.2.1.1
`gal_type`		Galaxy morphology: -9 to 9, encodes Hubble sequence, 98 if galaxy has never been examined (Huchra et al. 2012, Table A8)	2MRS
`n_nvss`	#	Number of radio Gaussians matched to galaxy (after manual inspection)	NVSS
`n_sumss`	#	Number of radio Gaussians matched to galaxy (after manual inspection)	SUMSS
`F1400`	mJy	Sum of integrated flux at 1.4 GHz of all radio matches (zero if `n_nvss=0`)	NVSS
`F1400_err`	mJy	Uncertainty on the former row	NVSS
`F843`	mJy	Sum of integrated flux at 843 MHz of all radio matches (zeros if `n_sumss=0`)	SUMSS
`F843_err`	mJy	Uncertainty on the former row	SUMSS
`Fsyn`	mJy	Flux at 1.1 GHz, obtained from 1.4 GHz or 843 MHz flux using $\alpha = -0.6$	N/S[a]
`Lsyn`	erg/s	νL_ν at 1.1 GHz	N/S[a]
`sum_ma`	deg	Sum of deconvolved FWHM of the major axis of all matched radio Gaussians	N/S[a]
`max_ma`	deg	Largest deconvolved major axis FWHM of all matched radio sources	N/S[a]
`lim_ma`	bool	Limit flag on major axis (=0 if source is resolved)	N/S[b]
`max_dist_to_gal`	deg	Maximum angular distance between the galaxy and the radio matches	N/S
`min_dist_to_gal`	deg	Minimum distance between the galaxy and the radio matches	N/S
`contour_dist`	deg	Angular distance to the second-highest radio contour (or zero if inside contour)	2.2.2.2
`geo_cen_ra`	deg	RA of the geometrical center	Eq. 2.2[c]
`geo_cen_dec`	deg	Decl. of the geometrical center	Eq. 2.2[c]
`flux_cen_ra`	deg	RA of the flux-weighted center	Eq. 2.3[c]
`flux_cen_dec`	deg	Decl. of the flux-weighted center	Eq. 2.3[c]
`class`		Classification based on morphology: `p`=*Point Sources*, `g`=*Starforming galaxies*, `j`=*Jets & Lobes*, `u`=*Unknown*	2.2.2.3

TABLE 2.1: Columns of the master catalog. [a]when both NVSS and SUMSS matches are available, we the pick the largest value. [b]when both NVSS and SUMSS data is available, we raise the major axis limit flag if the source is not resolved in both catalogs. [c]when both NVSS and SUMSS matches are available, we use the mean.

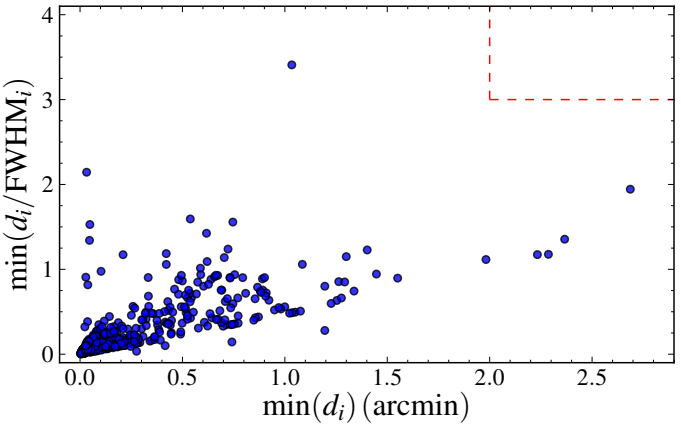

FIGURE 2.5: The minium angular distance between the radio matches and center of the galaxy (d_i) and the minimum of this distance weighted by the major axis (d_i/FWHM$_i$) for the 575 galaxies of our master catalog. These parameters were used to select the sample of potential radio emitting galaxies (Eq. 2.1). We see that our cuts, $d_i < \max(2', 3 \times \text{FWHM}_i)$ (dashed lines), are not limiting the number of galaxies in the final sample.

of NVSS sources over the number of SUMSS sources is 3.65, which is very close to fraction of the area (within the 2MRS footprint) probed by these surveys, 3.74.

Since we manually inspected all matches obtained from the catalog-level selection (Sec. 2.2.2.1), the completeness of our master catalog is primarily determined by the completeness of the input catalogs. As discussed in Section 2.2.1, the completeness of NVSS and SUMSS is nearing 100% at our flux limits and the completeness of 2MRS is 97.6%. However, at the radio flux limit of our catalog, the systematic uncertainty on the total flux of sources with a complex radio morphology slightly decreases the completeness; a few sources may be missing from our final sample because our estimate of the total flux is below the true value of the total flux. This is not a serious limitation since most complex sources have been described in the literature which allows us to improve the estimate of their total flux (see Section 2.2.6).

2.2.5 Probability of random matches

To estimate the contamination due to background radio sources we shuffle the R.A. of the 2MRS galaxy catalog to obtain a randomized, uniform sample. The catalog-level cuts (Eq. 2.1) yield 233 galaxies with a total of 1332 matches to the radio catalogs. Our image-level algorithm rejects 218 of these, leaving only 15 galaxies. After checking this sample for imaging artifacts, we are left with 13 sources that genuinely passed the image-level cuts (Eqs. 2.4 & 2.5). Two of the 13 matches with the randomized 2MRS catalog are radio sources that have already been unambiguously identified as

local radio-emitting galaxies using the original 2MRS data, hence these should not be included in the estimate of the number of background matches.

All of the matches of the shuffled galaxy sample are to extended radio sources; most are background double sources whose geometrical center is within 1.2 arcminutes of the galaxy. As expected, they are classified into the *Unknown* morphological class (Sec. 2.2.2.3). To conclude, the expected number of background matches for extended radio sources in our catalog is ≈ 11, or 2% contamination. This number is of the same order as the number of galaxies in our catalog that have an unclassifiable radio morphology, confirming that most of these are very likely to be random matches.

2.2.6 Comparison to other catalogs

We now compare our sample of 575 radio-emitting galaxies with some well-known catalogs of extra-galactic radio sources.

First, we consider the Kuehr et al. (1981) catalog, which is essentially complete for sources with $F_{5000} > 1$ Jy at 5 GHz and covers roughly the whole sky excluding $|b| < 10°$. Three radio galaxies with $z < 0.05$ from this catalog are not found in our final sample: NGC 1265 ($K = 12.4$, $z = 0.025$), ESO 252-GA018 ($K = 12.0$, $z = 0.034$), and NGC 7385 ($K = 13.3$, $z = 0.026$). The K-band flux of these galaxies is *below* the flux limit of 2MRS ($K < 11.75$), hence by construction they are not included in our final sample. We shall not add these three galaxies to our final sample by hand because this would dramatically complicate the selection function —they would need to be excluded to obtain a well-defined volume-limited sample. We can also test the completeness of the Kuehr et al. (1981) catalog using our list of final sources. We limit our sample using the completeness limit of the Kuehr catalog $F_{5000} > 1$ Jy, converted to NVSS and SUMSS using $\alpha = -0.6$ and restrict to at $|b| > 10$, to find 16 radio-emitting galaxies that are not listed in Kuehr et al. (1981).

Next, we compare our catalog to that of Condon, Cotton, & Broderick (2002), obtained by a careful manual selection of UGC galaxies that are detected in NVSS. We restrict this catalog using our K-band and radio flux limits to 131 sources and find that five of these are not contained in our final sample. All five are nearby ($z < 0.0017$) starforming galaxies whose very extended, low surface brightness radio emission has not been fully included in the NVSS catalog, causing them to fall (just) below our flux limit. For the main science goal of this work ("find all local radio galaxies"), these five galaxies are irrelevant.

We also compare the total flux measured at 1.4 GHz by Condon et al. (2002) by a re-analysis of the NVSS images to our estimate using the sum of the fitted elliptical Gaussian listed in the NVSS catalogs. The flux they report is on average 0.04 ± 0.13 dex, higher than our work. Six radio galaxies show an offset larger than 0.3 dex: NGC 0315, NGC 891, IC 342 NGC 5127, NGC 6946, and NGC 7236. For NGC 0315, this is due a hotspot in the jet that has been missed by the friends-of-friends algorithm. The missing flux for the other sources is due to their complex radio

morphology that is not entirely captured by the superposition of elliptical Gaussians. For these six cases, we use the total flux reported by Condon et al. (2002) as final value for the flux in our catalog, this reduces the the flux offset of the other 125 sources that are common to both catalogs to 0.010 ± 0.06 dex.

We should also compare our catalog to that of Jones & McAdam (1992), 193 southern extra-galactic radio sources with a flux density greater than 0.4 Jy and a size greater than 0.5'. After restricting this catalog to galaxies detected in 2MRS, we find three sources that are not in our final sample: WKK 4452, ESO 137-G006 and ESO 137-G00. All three, however, are detected below $|b| < 10$, which is outside the footprint of SUMSS (and thus outside the footprint of our catalog). In a future release, we will complete our coverage of the southern sky below $|b| = 10$ using the MGPS-2 images and these radio galaxies will be included.

We find a mean ratio between the 843 MHz flux measured by Jones & McAdam (1992) and this work of 0.015 ± 0.17 dex. Only Fornax A showed an offset greater than 0.3 dex, which is due the complex morphology of this source. For this galaxy, we use the total flux measured by Jones & McAdam (1992) as final value for the flux in our catalog (this reduces the flux offset to -0.014 ± 0.1 dex). We also manually adjusted our catalog flux of Cen A to the total flux (i.e., inner and outer lobes) as measured by Cooper et al. (1965).

Of the 575 radio sources in our final sample, 209 are *not* contained in the union of the three catalogs described above, plus the catalog of radio sources in the 6dFGS survey (Mauch & Sadler 2007) and the collection of known extra-galactic radio sources and AGN of Véron & Véron (1974); Véron-Cetty & Véron (2006).

2.2.7 Newly found radio galaxies

In the previous paragraph we found that over 30% of the galaxies in our sample are not contained in existing large-area samples of extra-galactic radio sources or AGN. Some of these have been identified as such by surveys that cover a smaller area of the sky, but in many cases this work is the first to classify these galaxies as radio emitting. Below we discuss some notable examples of these genuinely new identifications. We also list some sources that have been identified as (candidate) extra-galactic sources (e.g., based on their radio morphology or radio spectrum) by earlier work, but for which this work is the first to provide a redshift of the galaxy. The NED name of the galaxy can be used to find the images of these sources in Appendix 2.A.

- J00112171+5231437 blended point source or head-tail source, member of a cluster that contains a radio relic (van Weeren et al. 2011).
- NGC 0349 jet over 5' long, non-detection in the CRATES catalog of flat-spectrum radio sources (Healey et al. 2007).
- J03204016+2727485 complex geometry, multiple hotspots?

- J03212595+1806093 large (5′) radio galaxy, shows both lobe emission and strong central emission.
- NGC 1477 complex morphology, strong emission from galaxy center and faint lobes, contained in the CRATES catalog (Healey et al. 2007).
- J05444416+1648501 extended jet emission, observed but not detected at VLBI scales: VERA 22 GHz flux < 0.1 Jy (Petrov et al. 2007).
- J06120351-3257472 large source with a triple morphology (detected in both NVSS and SUMSS), galaxy is member of a rich cluster (Dressler 1980).
- J07331844-3654533 two large lobes ($\sim 10^2$ kpc), detected in both NVSS and MGPS-2.
- J11032753-4657471 large surface brightness difference between the two lobes.
- IC 2722 "relaxed FR II", looks like central engine has turned off.
- ESO 505- G 014 spectacular narrow and long (10') jet.
- J13595556-1056266 clearly extended jet emission, detected by Chandra (Evans et al. 2010).
- J16103572-0511173 jet morphology, but galaxy is not exactly at the center of the radio emission.
- J16390277-6505079 complex morphology, seems to show a hot spot displaced from current jet axis. Galaxy is located in the Great Attractor region (Radburn-Smith et al. 2006).
- J17050125-2445099 two lobes and core emission, located in the Ophiuchus cluster (Hasegawa et al. 2000).
- J17124278-2435477 complex morphology, located in the Ophiuchus cluster.
- J17131541-2502266 two lobes, with $\nu L_\nu = 2{\times}10^{41}\,\mathrm{erg\,s^{-1}}$, this is one of brightest radio sources within 125 Mpc. It was identified as a potential double source (with unknown redshift) by Slee, Siegman, & Mulhall (1982).
- J19264081+4123284 head-tail source.
- J19300192-1509191 resolved radio emission, most likely central jet emission. Detected by ROSAT (Voges et al. 1999), radio, X-ray and optical (without redshift) matched by Bauer et al. (2000).
- J20430830-5059054 resolved radio emission, morphological class not clear.
- J21492796-6429194 slightly resolved, identified as radio source in the direction of the Abell cluster (i.e., without redshift) by van Weeren et al. (2011).
- J22380121+4107363 two non-axisymmetric lobes.
- MCG -05-55-032 wide-angle morphology, classified as a point source in the CRATES catalog (Healey et al. 2007).

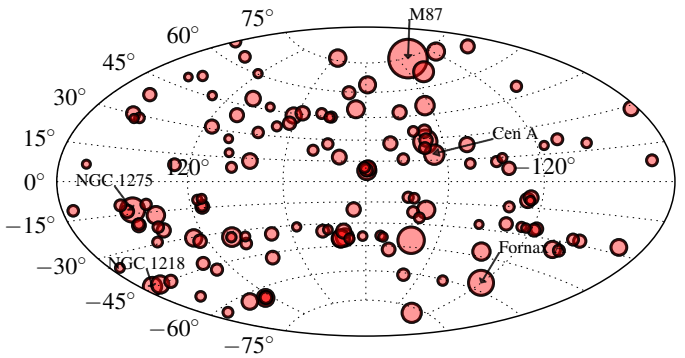

FIGURE 2.6: Map in Galactic coordinates with the radio galaxies of the volume-limited sample ($z < 0.03$). The area of the circles is proportional to the radio flux of the source. The location of some famous sources is indicated (M87 and NGC 1275 are the brightest members of the Virgo and Perseus cluster, respectively).

2.3 Analysis

The 575 radio-emitting galaxies we identified in the previous section are a subset of a much larger flux-limited sample of "normal" galaxies, which allows for detailed comparison of both classes. In section we will work with two samples of radio galaxies. We define sample A, the volume-limited sample that is used to measure the Hubble type abundance (Sec. 2.3.1) and clustering (Sec. 2.3.2) of radio galaxies. And we define sample B, which is limited only by the radio luminosity of the galaxy, to compute the luminosity functions (Sec. 2.3.3).

2.3.1 Number counts in a volume-limited sample

Our master catalog is limited by both the flux limit of the redshift survey and the radio flux limit we imposed. To obtain a volume-limited sample, we thus have to make a cut on both the K-band luminosity and the radio luminosity. We shall restrict our sample to $z = 0.03$, or comoving distance of 130 Mpc; the corresponding minimum K-band luminosity is $M_K = -23.78$, this limit is just high enough to select all galaxies with a K-band luminosity equal to Cen A ($M_K = -23.8$). Applying this distance and NIR luminosity cut to 2MRS yields 10964 galaxies; our master catalog is reduced from 575 to 153 galaxies. The flux limit applied to the radio catalogs was $F_{1400} > 213$ mJy, $F_{843} > 289$ mJy for NVSS, SUMSS, respectively. Hence for $z < 0.03$, our catalog contains all sources with a radio luminosity greater than $\nu L_\nu = 5.8 \times 10^{39}\,\mathrm{erg\,s^{-1}}$ at 1.4 GHz and $\nu L_\nu = 4.8 \times 10^{39}\,\mathrm{erg\,s^{-1}}$ at 843 MHz (or $L_{1400} > 4.2 \times 10^{23}\,\mathrm{W\,Hz^{-1}}$, $L_{843} > 5.6 \times 10^{23}\,\mathrm{W\,Hz^{-1}}$). Applying this radio luminosity requirement selects 461 galaxies of which 74 are below $z = 0.03$, all of these also obey the cut in K-band luminosity. None of these radio-emitting galaxies are morphologically classified as *Starforming*. In the following we shall refer to this set of 74 sources within $z = 0.03$

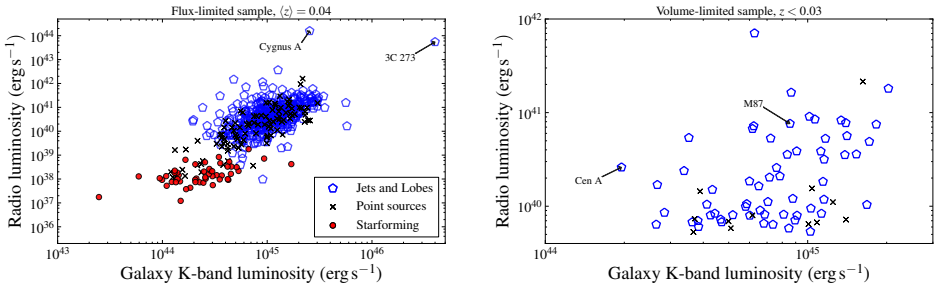

FIGURE 2.7: The K-band and 1 GHz luminosity (νL_ν) for all extra-galactic radio sources in our sample (left) and a volume-limited sample (right). Most sources that are morphologically classified as AGN (i.e., the *Jets and Lobes* class) are more luminous than $\nu L_\nu = 10^{39}$ erg s^{-1}. Our volume-limited sample shows that the galaxy NIR luminosity and radio luminosity are not strongly correlated.

as sample A: the volume-limited sample of radio galaxies.

If we restrict sample A to galaxies with a radio luminosity that is greater or equal than Cen A ($\nu L_\nu = 2.6 \times 10^{40}$ erg s^{-1} at 1 GHz), only 24 radio galaxies within $z = 0.03$ remain.

In Fig. 2.6 we show a map in Galactic coordinates with the location of the 74 radio galaxies of sample A. The radio and K-band luminosity of both the full flux-limited sample and volume-limited sample are shown in Fig. 2.7. The 74 radio galaxies comprise 0.65% of all galaxies in the volume-limited sample; in Fig. 2.8 we show this fraction as a function of distance to the barycenter of the Local Group.

Using the 2MRS morphological galaxy classification for sources with $K < 11.25$, we find the following Hubble type fractions for our volume-limited sample of radio galaxies: 47% Ellipticals, 47% S0 galaxies, and 3% Spirals. For the $\sim 10^4$ normal galaxies within $z = 0.03$ the E, S0 and S fractions are 14%, 31%, and 54%; for massive normal galaxies with $M_K < -25$, these fraction are 26%, 40%, and 33%. To allow a direct comparison to the galaxy morphology distribution of radio galaxies, we compute the Hubble type fractions of non-radio galaxies in bins of absolute K-band magnitude and we compute the mean fraction weighted by the number of radio galaxies in each luminosity bin. We thus find the Hubble type fractions for non-active galaxies drawn from the observed mass distribution of radio galaxies: 27%, 38%, and 34% (E, S0, and S).

2.3.2 Clustering of radio galaxies

Our sample of radio galaxies is a subset of an all-sky redshift survey, allowing us to study the clustering of radio galaxies with respect to the matter distribution. We use the volume-limited sample of radio galaxies within $z = 0.03$ (sample A, defined in Section 2.3.1) and we restrict to $z > 0.003$, yielding 73

radio galaxies. In Fig. 2.9 we show a "top view" of this volume-limited sample;

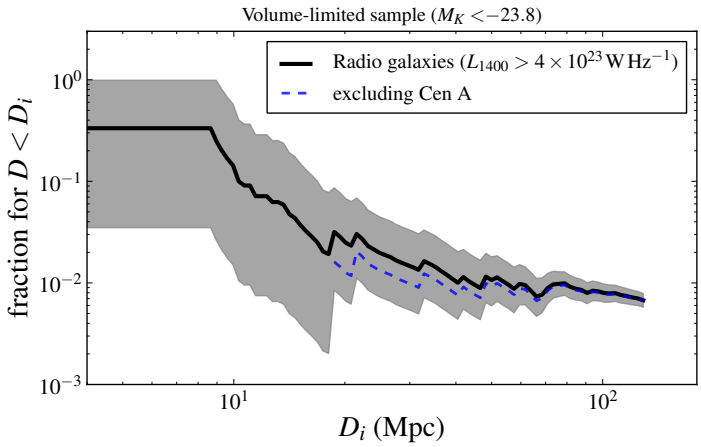

FIGURE 2.8: The fraction of radio galaxies in the volume-limited sample (sample A, defined in Section 2.3.1) as a function of distance to the local group barycenter. The gray area shows the 90% CL, based on Poisson statistics for the number of observed radio galaxies. Since our sample probes over 90% of the volume, this uncertainty reflects the cosmic variance, rather than the statistical significance of this observation. Cen A remains the only radio galaxy up to 16 Mpc, where M 87 joins the ranks (at this distance, the number of normal galaxies in the volume-limited sample is 62).

more than 50% of the radio galaxies are within the contour that encompasses half of the normal galaxy sample, an obvious sign of enhanced clustering. We quantify this clustering by counting the number of pairs between radio galaxies and normal 2MRS galaxies as a function of comoving distance, $\rho_{\rm RG}(d)$, i.e., the total galaxy count within a comoving distance d of each radio galaxy. We compare this to the number of pairs for random subsets of 73 non-radio galaxies of the volume-limited sample, $\rho_{\rm matter}(d)$. In the top panel of Fig. 2.10 we show $\rho_{\rm RG}/\langle\rho_{\rm matter}\rangle - 1$: a highly significant excess of clustering with respect to the normal galaxy distribution is clear.

Clustering is well-known to correlate with galaxy mass and morphology (e.g., Dressler 1980; Bamford et al. 2009) and the majority of the radio galaxies in our sample have massive, early-type hosts. Hence galaxy luminosity and morphology are confounding factors in the analysis of radio galaxy clustering. One can remove the clustering due to host mass by computing the density excess with respect to the radio-loud galaxy mass distribution. We thus measure $\langle\rho_{\rm matter*}\rangle$ by drawing random subsets of non-radio galaxies from the observed K-band luminosity distribution of radio galaxies. We show the result in the middle panel of Fig. 2.10; while the amplitude of the excess decreases, it remains highly significant. By forcing the random subsets of non-radio galaxies to have, on average, the same Hubble type (E, S0, or S) abundance as the radio galaxies we also correct the density excess for clustering due to morphology. We find that the galaxy number density around our sample of radio galaxies remains enhanced by a factor of 1.7 at 2 Mpc (Fig. 2.10 bottom panel); the

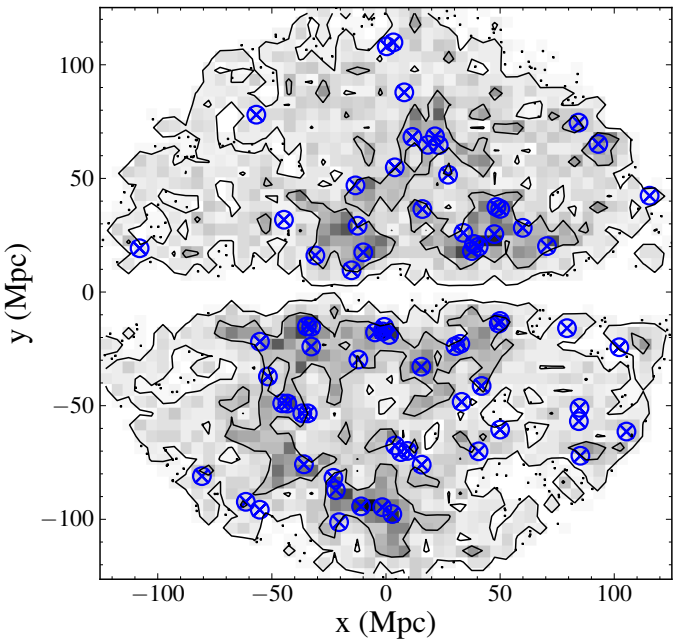

FIGURE 2.9: Projected density of the volume-limited sample of $\sim 10^4$ galaxies ($z < 0.03$) along $b = l = 0$ in Galactic coordinates. The contour encompass 95% and 50% of the sample. The lack for sources around $y = 0$ is due to the disk of the Milky Way. One clearly sees that the radio galaxies in our volume-limited sample (blue circled crosses) reside in regions of high galaxy density.

probability that this enhancement is observed for a set of non-radio galaxies with the same luminosity and Hubble type distribution as the radio galaxies is less than 0.3%.

The brightest galaxy of a cluster is often found to be radio-loud (Matthews, Morgan, & Schmidt 1964; Burns 1990) and this will contribute to the observed density excess of radio galaxies. We therefore perform a simple test to find the brightest cluster galaxies and estimate this contribution. First, we define a cluster or group as a collection of more than 5 galaxies from the volume-limited sample ($M_K < 23.8$) that can be connected by 3 Mpc strings (i.e., a friends-of-friends cluster finding algorithm with a comoving link length of 3 Mpc). Of the 73 radio galaxies from sample A that we use here, 32 are in such groups. Of these, 18 are the brightest member of their group (or cluster). After removing these galaxies, the enhanced clustering (corrected for mass and morphology of the host galaxies) of the remaining 55 radio galaxies falls between the 2σ-level and the 3σ-level for all distances we consider; at 2 Mpc, the fractional density excess is 50%.

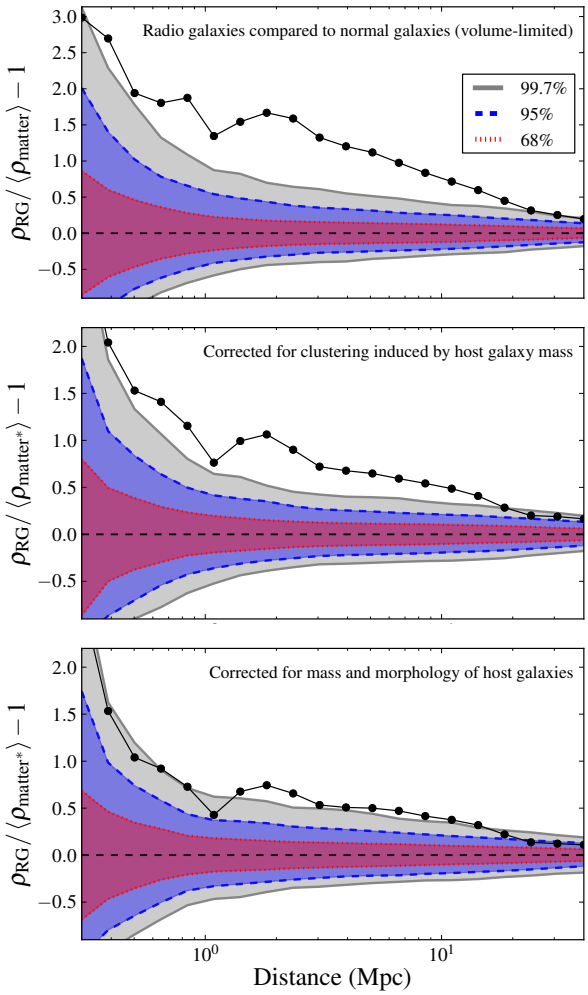

FIGURE 2.10: The fractional density excess of radio galaxies in the volume-limited sample (defined in Section 2.3.1). Top: the excess with respect to a volume-limited sample of non-radio galaxies (i.e., $z < 0.03$ and $M_K < -23.78$). Middle: the excess with respect to normal galaxies drawn from the K-band luminosity function of radio galaxies. Bottom: the fractional density excess corrected for clustering induced by the morphological type of the host galaxies *and* their luminosity. Even after correcting for the clustering of their massive and predominantly early-type hosts, radio-loud jets are observed to occur in regions of high galaxy density.

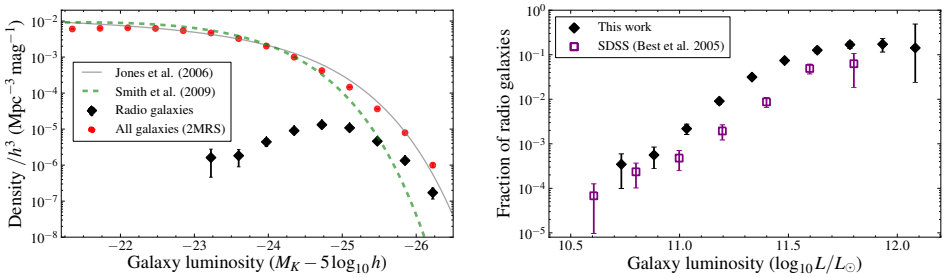

FIGURE 2.11: Left: the K-band luminosity function for powerful radio galaxies (sample B: $L > 10^{24}\,\mathrm{W\,Hz^{-1}}$) and normal galaxies. We also show Schechter function fits to galaxies from the UKIDSS Large Area Survey (Smith et al. 2009) and the 6dF Galaxy Survey (Jones et al. 2006). The number density of powerful radio galaxies peaks at an absolute K-band magnitude of -25.5 (using $h = 0.72$). Right: the fraction of radio galaxies as a function of galaxy luminosity. We see at rapid increase from zero for $L < 5 \times 10^{10}\ L_\odot$ to $\sim 20\%$ for the brightest galaxies. We also show the fraction of radio-loud AGN (with the same minimum radio luminosity) in SDSS (Best et al. 2005a), converted to the K-band luminosity using a mean mass-to-light ratio $M/L_K = 0.8$ (Bell et al. 2003).

2.3.3 Luminosity function

In this section, we use the $1/V_{\rm max}$ method (e.g., Schmidt 1968), to obtain the number density of radio galaxies and normal galaxies as a function of luminosity. The $1/V_{\rm max}$ method allows one to compute this density without applying a hard distance limit (such as the $z < 0.03$ limit that was used to define sample A in Section 2.3.1). In this section, we define sample B: a set of powerful radio galaxies with $L_{1400} > 10^{24}\,\mathrm{W\,Hz^{-1}}$. As before, we also require a minimum redshift $z > 0.003$ and exclude the sources with unknown morphology, because these are most likely random matches. The luminosity and minimum redshift cut have been picked to aid a comparison to previous work. These cuts leave 527 radio-emitting galaxies, with a median redshift of 0.042, and 401 powerful radio galaxies with a median redshift of 0.052.

We find $\langle V/V_{\rm max}\rangle = 0.494 \pm 0.012$ and $\langle V/V_{\rm max}\rangle = 0.496 \pm 0.014$ for all radio-emitting galaxies and the powerful radio galaxies, respectively, which shows that density evolution with redshift or distance-dependent selection effects are not a significant influence on the derived radio source densities.

In Fig. 2.11 we show the K-band luminosity function. One clearly sees that the powerful radio galaxies reside in the most luminous hosts and their density peaks at $M_K \approx -25.5$. The fraction of radio galaxies is a strong function of galaxy luminosity. No radio galaxies with $L_{1400} > 10^{24}\,\mathrm{W\,Hz^{-1}}$ are found for $M_K > -23.7$ and the fraction rises rapidly to an asymptotic value of 0.25 for the most massive galaxies. We also compute the luminosity function of normal galaxies which agrees reasonably well with Schechter functions that have been derived from the UKIDSS Large Area

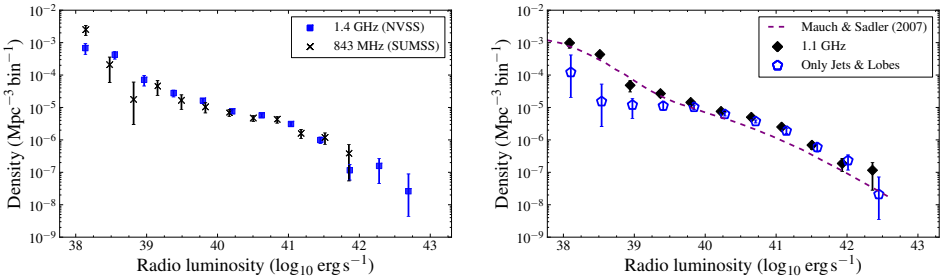

FIGURE 2.12: The radio luminosity (νL_ν) function of extra-galactic radio sources at different frequencies. Right: 1.4 GHz from NVSS ($\delta > -40$) and 843 MHz from SUMSS ($\delta < -30$, $|b| > 10$). Left: the 1.1 GHz sample includes sources from both surveys by scaling to this frequency using the mean spectral index of $\alpha = -0.6$. For $\nu L_\nu > 10^{39}$ erg s^{-1}, the luminosity function for radio galaxies with a jet or lobe morphology (open diamonds) is similar to the full sample, while below this scale the contribution from starforming galaxies becomes clear.

Survey (Smith et al. 2009) and the 6dF Galaxy Survey (Jones et al. 2006) (except at the bright end, which is a known issue with Schechter functions).

Recalling that the radio-emitting galaxies in our catalog originate from NVSS (at 1.4 GHz) and/or SUMSS (at 843 MHz), we first compute the luminosity function for each survey separately (Fig. 2.12, left panel). We find that, as expected, the luminosity functions from NVSS and SUMSS are nearly identical. To increase the statistical power, we combine both surveys by scaling the flux to 1.1 GHz using the mean spectral index of $\alpha = -0.6$ (Fig. 2.12, right panel). We find that the luminosity function of radio-emitting galaxies with a jet or lobe morphology agrees well with the results of the entire sample, except below $\nu L_\nu = 10^{39}$ erg s^{-1}. Below this luminosity, the contribution of starforming galaxies starts to dominate (e.g., Condon et al. 2002). At 10^{41} erg s^{-1} our estimate of the number density is a factor 2–3 above the 1.4 GHz luminosity function derived form 2661 radio-loud AGN at $0.003 < z < 0.3$ (Mauch & Sadler 2007). Below, we suggest an explanation for this difference.

2.4 Conclusions & Discussion

Our conclusions can be summarized as follows.

1. A new extra-galactic radio catalog covering 88% of the celestial sphere has been constructed. The catalog contains all galaxies brighter than $K = 11.75$ that show radio emission at $F_{1400} > 213$ mJy or $F_{843} > 289$ mJy; it contains 575 sources. Over 30% of these radio-emitting galaxies are not contained in existing large-area catalogs.

2. Our matching algorithm identifies extra-galactic radio sources with 99% efficiency and 91% purity. All matches have been inspected manually to remove imaging artifacts and blended sources. The contamination due to background radio sources in the final sample is 2%; the *Unknown* morphological class contains 19 potential random matches.

3. For a volume-limited sample within $z = 0.03$ (130 Mpc), we find 27 galaxies with a radio and K-band luminosity greater or equal to Cen A, which is 0.2% of all 2MRS galaxies within the same volume.

4. No obvious correlation between galaxy luminosity and total radio power is observed (Fig. 2.7).

5. The K-band luminosity function of radio galaxies peaks at $M_K = -25.5$ or a luminous mass of $\sim 10^{11}\ M_\odot$ (Fig. 2.11).

6. Of radio galaxies within $z = 0.03$, 94% are of the E/S0 Hubble type; this higher than the fraction of bright ($M_K < -25$) normal galaxies that are of this morphological class (66%) or the E/S0 fraction of non-active galaxies scaled to the same K-band luminosity distribution as the radio galaxies (65%).

7. The fraction of radio galaxies as a function of K-band luminosity rises asymptotically to 20% (Fig. 2.11).

8. We have computed the fractional density excess of radio galaxies in a volume-limited sample as a function of distance from the radio galaxies. Radio galaxies are significantly more clustered than normal galaxies; in a sphere of 2 Mpc centered on the radio galaxies, the galaxy density is 2.7 times greater than around normal galaxies (Fig. 2.10 top panel).

9. After correcting the latter result for the extra clustering induced by the mass and Hubble type of the radio galaxies, the density excess remains significant ($> 3\sigma$): at 2 Mpc the density around radio galaxies is 1.7 times higher than around non-radio galaxies with the same mass and galaxy morphology distribution (Fig. 2.10 bottom panel).

The observation that radio-loud AGN are found in the most massive galaxies is well-known. Indeed, the median absolute K-band magnitude of radio galaxies in the NVSS-6dFGS sample (Mauch & Sadler 2007) of $M_K = -25.4$ is in excellent agreement with our results. The radio luminosity where the density of AGN overtakes that of starforming galaxies ($\nu L_\nu = 10^{39}\ \mathrm{erg\,s^{-1}}$) agrees with radio luminosity functions from other surveys at similar redshift (Condon et al. 2002; Mauch & Sadler 2007).

The decreasing fraction of radio galaxies with distance (Fig. 2.8) appears at odds with the cosmological trend of increasing AGN activity to $z \sim 2$ (e.g., Hopkins et al. 2007), yet most observers in other galaxies would find the same. Because radio galaxies

are found in high density regions and the average astronomer lives in a galaxy inside a cluster, the local fraction of radio galaxies is typically observed to be higher than the cosmic average.

For a standard mass-to-light ratio in the K-band, $M/L_K \sim 1$, we find that the fraction of galaxies with a radio luminosity greater than $L = 10^{24}$ W Hz^{-1} is a factor 5 larger than the fraction of AGN with the same minimum radio luminosity in SDSS (Best et al. 2005a, 2007). We also find a factor 2–3 higher number density of radio sources at $\nu L_\nu = 10^{41}$ erg s^{-1} (or 10^{25} W Hz^{-1}) compared to the NVSS-6dFGS sample (Mauch & Sadler 2007). If we restrict our sample to sources detected beyond 200 Mpc (leaving 237 radio galaxies), while keeping $V_{\rm max}$ of each source fixed, these two discrepancies disappear. Hence a large-scale local overdensity of radio galaxies or a distance dependent selection effect are the most likely explanations for the larger radio galaxy density derived from our sample. We note that Mauch & Sadler (2007) find $\langle V/V_{\rm max}\rangle = 0.532 \pm 0.006$ for their radio-loud AGN; this significant offset from 0.5 implies evolution (or selection bias) is present in their sample.

The conclusion of Ledlow & Owen (1995) that the number of radio galaxies detected in Abell clusters simply scales with the number of galaxies surveyed, appears incompatible with our detection of enhanced clustering of radio galaxies with respect to normal galaxies. Our clustering detection, however, is in agreement with more recent work at intermediate redshift ($z \gtrsim 0.1$). Using the SDSS galaxy sample, Kauffmann et al. (2008) found a factor ≈ 2 increase for the galaxy counts in a projected radius of 300 kpc around radio-loud AGN compared to radio-quiet AGN; Donoso et al. (2010) found that the projected cross-correlation at 2 Mpc between radio-loud AGN and luminous red galaxies (LRG) is 25% stronger than the auto-correlation of the radio-quiet LRG. Tasse et al. (2008a) compared the environment of the host galaxies of powerful radio sources ($L_{1400} \gtrsim 10^{24}$ W Hz^{-1}) in the XMM-LSS field (Tasse et al. 2008b) to normal galaxies of the same mass and redshift. For $M > 10^{10.5}\ M_\odot$ their photometric-redshift-based density estimator finds an overdensity at 450 kpc, close to the distance where the enhanced clustering of radio galaxies in our sample exceeds the 3σ-level.

The enhanced density around radio galaxies suggests a causal relation between galaxy environment and jet power. Since this excess is measured with respect to galaxies of the same mass and morphological type, the mechanism behind this relation is not primarily driven by black hole mass. The gas cooling out of the hot atmospheres of the host galaxies is often suggested as a potential mechanism to turn on radio-loud jets (Burns 1990; Best et al. 2005a). An interesting future application is to compare the luminosity of the core of the jet, which will be measured by a VLBA 8 GHz survey of 2MASS galaxies (Condon et al. 2011), to the large scale radio emission contained in our catalog. This will allow a study of jet power as a function of black hole mass — the latter can be estimated using the luminosity and Hubble type of the galaxy (e.g., Caramete & Biermann 2011).

The automated image-level matching presented here could be considered an improvement to the manual classification that has been used to construct similar samples in the past. For future studies of existing extra-galactic catalogs (e.g., the 2MASS Extended Source Catalog) as well as upcoming radio surveys (e.g., LOFAR, ASKAP), automated cross-wavelength identification will be key to manage the large number of sources.

Acknowledgments
SvV would like to thank M. R. Blanton, E. Körding, R. Plotkin, H. Röttgering, and R. van Weeren for useful discussions. In addition, we would like to thank the referee for the swift reply and the useful comments. HF acknowledges funding from the European Research Council (ERC) Advanced Grant. KHK acknowledges funding from the German Ministry of Education and Research (BMBF).

This research has made use of the NASA/IPAC Extragalactic Database (NED) which is operated by the Jet Propulsion Laboratory, California Institute of Technology, under contract with the National Aeronautics and Space Administration. This research has also made use of the SIMBAD database, operated at CDS, Strasbourg, France. The Two Micron All Sky Survey is a joint project of the University of Massachusetts and the Infrared Processing and Analysis Center/California Institute of Technology, funded by the National Aeronautics and Space Administration and the National Science Foundation. The Digitized Sky Survey was produced at the Space Telescope Science Institute under U.S. Government grant NAG W-2166. The images of these surveys are based on photographic data obtained using the Oschin Schmidt Telescope on Palomar Mountain and the UK Schmidt Telescope. The plates were processed into the present compressed digital form with the permission of these institutions.

The density contours in Fig. 2.9 were created with `bovy_plot`. All plots with celestial coordinates were produced with `APLpy`.

2.A Example images

Here we show images of examples of newly identified radio-emitting galaxies discussed in Section 2.2.7. For the images of all 575 radio-emitting galaxies in our sample we refer to the online catalog, `http://ragolu.science.ru.nl/hcat.html`. The following legend applies to all images:

- Green pentagram: 2MRS galaxy.
- Green cross (×): center of the frame (i.e., galaxy in question).
- Purple square (□): SUMSS/NVSS catalog source.
- Purple cross (×): matched catalog source by image-level algorithm.
- Purple plus (+): manually accepted match.
- Large magenta cross: geometrical center of radio emission.
- Large red circled cross: flux-weighted center of radio emission.

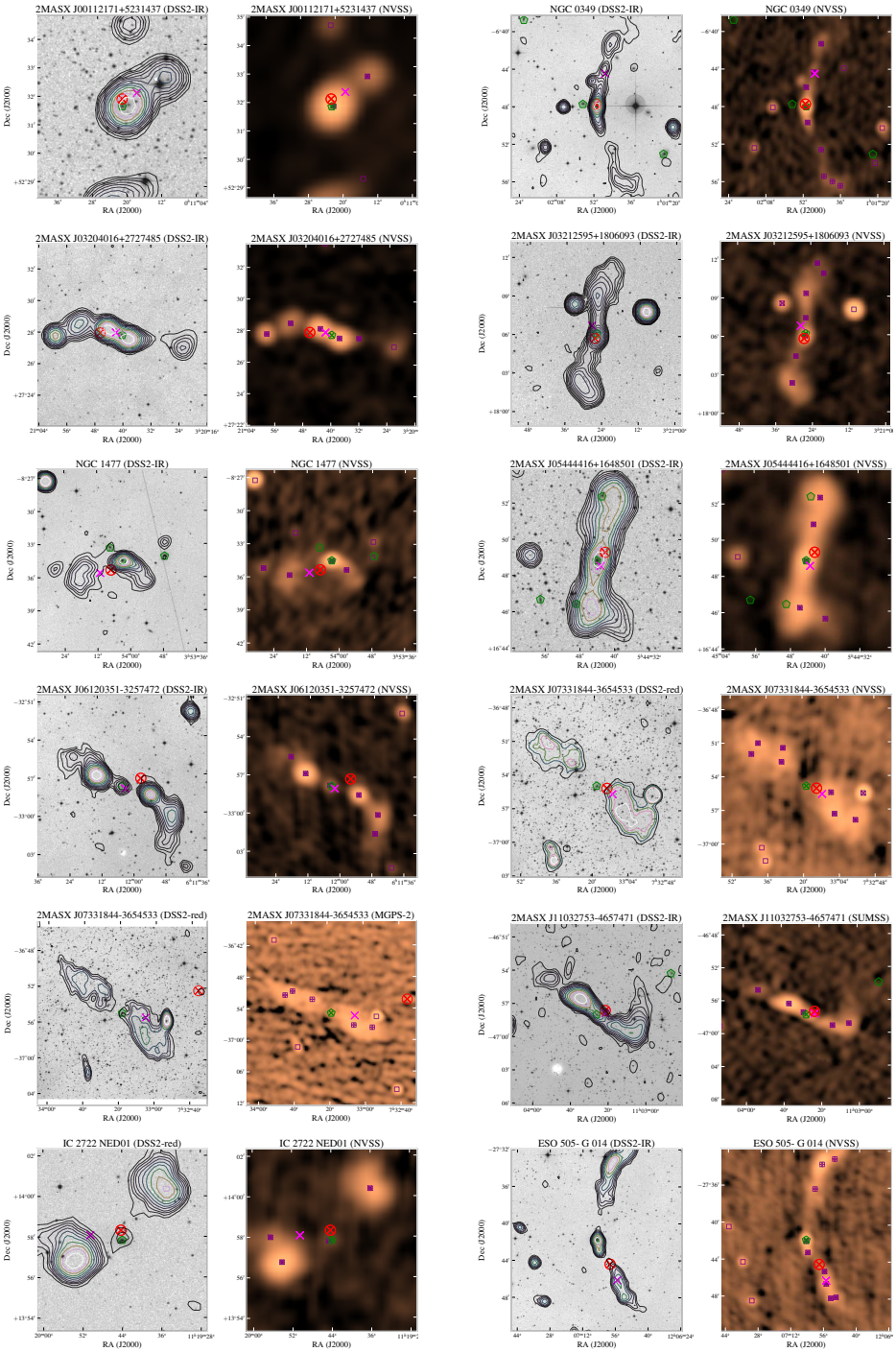

FIGURE 2.13: Examples of newly identified radio-emitting galaxies.

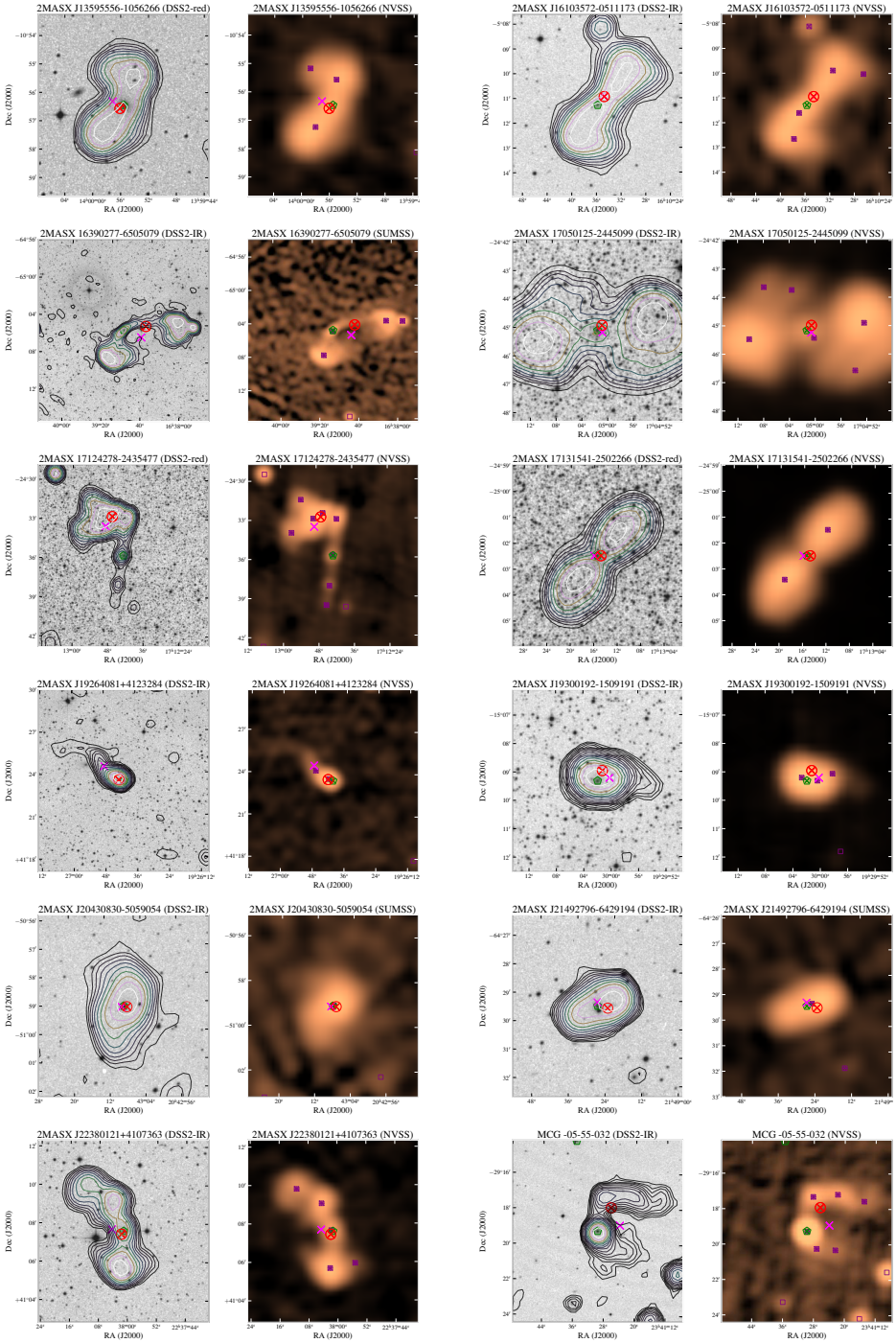

FIGURE 2.14: Examples of newly identified radio-emitting galaxies.

Chapter 3

Local radio galaxies as the source of ultra-high energy cosmic rays

Sjoert van Velzen, Heino Falcke, and Jörg Hörandel
Auger Collaboration internal (GAP) note: 2012-081

Abstract

Radio galaxies are a longstanding candidate source of ultra-high energy cosmic rays (UHECRs). Observations of the lobes of the prototypical radio galaxy Centaurus A indicate that this source could be large and luminous enough to accelerate charged particles to the ultra-high energy scale. We therefore wish to find all galaxies like Cen A within the GZK horizon ($\sim 10^2$ Mpc) and compare this sample with the angular distribution of UHECRs. To this end, we used a new catalog of radio-emitting galaxies covering the entire extra-galactic sky. We construct an empirical Hillas diagram to identify all radio galaxies with lobes that are large enough to contain ultra-high energy (UHE) protons. We find that the total energy injected per unit volume by the jets that are powering these lobes is sufficient to explain the observed UHECR flux. After correcting for the cosmic rays that could be due to Cen A, we find that the cross-correlation of radio galaxies with UHECRs is not significantly stronger than the cross-correlation of UHECRs with the local matter distribution. Finally, we show that when the deflections due to intergalactic magnetic fields to $E > 60$ EeV protons are small ($< 10^\circ$), the hypothesis that all UHECRs are protons with radio galaxies as their source is ruled-out.

3.1 Introduction

Ultra-high energy cosmic rays are charged particles with an energy in excess of $\sim 5 \times 10^{19}$ eV. Interactions with photons of the cosmic microwave background limits the typical distance an UHECR can travel to about 100 Mpc, the GZK horizon (Greisen 1966; Zatsepin & Kuz'min 1966). This horizon should yield an exponential suppression to the energy spectrum, which has indeed been observed by the Pierre Auger observatory (Abraham et al. 2008) and the High Resolution Fly's Eye experiment (Abbasi et al. 2008).

The origin of UHECRs remains elusive. Traditional candidates are AGN or radio galaxies (Ginzburg & Syrovatskii 1963), but transient sources such as gamma-ray burst (Waxman 1995a) or accretion events onto supermassive black holes (Farrar & Gruzinov 2009) have also been proposed. The gamma-ray burst model is challenged by recent results from the ICECUBE collaboration, who obtained upper limits on the flux of neutrinos from gamma-ray burst (Abbasi et al. 2012).

A correlation between UHECRs and AGN from the VCV catalog (Véron-Cetty & Véron 2006) on an angular scale of 1° has been reported (The Pierre Auger Collaboration 2007), but this result is difficult to interpret since the VCV catalog is biased and incomplete. In an updated the analysis (The Pierre Auger Collaboration 2010b), the significance of the correlation with VCV AGN has decreased to about 3-σ. The region around the nearest radio galaxy Centaurus A shows an apparent overdensity of UHECRs. Since Cen A itself sits at the center of an overdensity of galaxies (the Centaurus supercluster which lies in the super-galactic plane), this excess is again difficult to interpret.

What further complicates the search for the origin of UHECRs is the lack of information on their composition. For energies in the range $E = [10^{18}, 10^{19.5}]$ eV, measurements of the depth of the particle shower maximum suggest that the fraction of protons decreases with energy (The Pierre Auger Collaboration 2010a). If all UHECRs are iron particles, the large ($> 20°$) magnetic deflections due to Galactic and inter-galactic fields, imply that the arrival direction distribution should be largely isotropic (which appears to be incompatible with the correlation of UHECRs and VCV AGN).

3.1.1 Radio galaxies

In this work we focus on the hypothesis that radio galaxies are the source of UHECRs. The jets of radio galaxies carry energy of the accretion disk away from the black hole, creating lobes filled relativistic electrons that emit synchrotron radiation. The magnitude of the magnetic field (B) in these lobes can be estimated from their observed radio luminosity (L_ν) and radius (R). For any synchrotron-emitting source, the lowest total energy is obtain when the energy density of the magnetic fields (U_B) is in equipartition with the relativistic particles that are emitting the radiation (U_e).

Using this minimum energy argument, we find

$$B = \left(\frac{L_\nu/\epsilon}{10^{31}\,\mathrm{erg\,s^{-1}Hz^{-1}}}\right)^{2/7} \left(\frac{R}{100\ \mathrm{kpc}}\right)^{-6/7} \left(\frac{\nu}{\mathrm{GHz}}\right)^{1/7} \mu\mathrm{G} \tag{3.1}$$

(e.g., Pacholczyk 1970). Here we used the standard assumptions: an electron energy distribution with a power law index $p = 2$ and a minimum electron energy of 5 MeV, and $\epsilon \equiv U_e/U_B$. X-ray observations of the lobes of FR II radio galaxies (Croston et al. 2005) yield a magnetic field that is close to equipartition, i.e., $\epsilon \approx 1$. For simplicity, we will use $\epsilon = 1$ throughout this work. We can combine Eq. 3.1 with the Hillas requirement (Hillas 1984),

$$\frac{R}{100\ \mathrm{kpc}}\frac{B}{\mu G} > E_{20}Z^{-1} \quad , \tag{3.2}$$

where Z is the atomic number and we expressed the energy of the cosmic ray as $E_{20} \equiv E/10^{20}\,\mathrm{eV}$, to find

$$L_\nu > 10^{31}\,\epsilon \left(\frac{E_{20}}{Z}\right)^{7/2} \left(\frac{R}{100\ \mathrm{kpc}}\right)^{-1/2} \left(\frac{\nu}{\mathrm{GHz}}\right)^{-1/2} \mathrm{erg\,s^{-1}Hz^{-1}}. \tag{3.3}$$

This is the minimum luminosity of a synchrotron emitting blob to confine cosmic rays of rigidity E_{20}/Z.

Applying Eq. 3.3 to the well-known 3C and B2 extra-galactic radio catalogs (Hardcastle 2010) reveals why radio galaxies are a popular candidate source of UHECRs: many of the sources in these catalogs are luminous and large enough to contain ultra-high energy protons. These flux-limited catalogs, however, contain mostly radio galaxies far beyond the GZK horizon. To study the sources of *observed* UHECRs, we need a catalog of all nearby radio galaxies. Some authors argue that the nearest radio galaxy, Centaurus A, is the source of *all* UHECR (Biermann & de Souza 2012). We thus wish to find all galaxies like Cen A within the GZK horizon.

Motivated by the study of ultra-high energy accelerators, a new sample of local radio-emitting galaxies was recently constructed (Chapter 2; van Velzen et al. 2012). The essential properties of the catalog are as follows.

1. **Full-sky**: the coverage is 11 sr (essentially the entire accessible extra-galactic sky).

2. **Complete**: all radio galaxies that are as bright as Cen A are contained for $z < 0.03$ (125 Mpc).

3. **Systematic**: the radio-emitting galaxies are a well-defined subset of a larger galaxy sample, namely the 2MASS Redshift Survey (2MRS; Huchra et al. 2012).

We will use the new radio galaxy catalog to derive an empirical Hillas diagram (Sec. 3.2.1). We then estimate the total energy injected by radio jets into the GZK volume (Sec. 3.2.2), and finally we present the cross-correlation of radio galaxies with UHECRs (Sec. 3.2.3). In Section 3.3 we summarize the results and we close with a discussion (Sec. 3.4).

3.2 Analysis

3.2.1 Empirical Hillas diagram

In this section we apply the well-known size and magnetic field requirements for particle acceleration (Eq. 3.3) to a full-sky sample of radio-emitting galaxies. For this analysis, it is important to note the cataloged information of a given radio galaxy is a set of elliptical Gaussians that were fitted to the radio image. Extended radio sources can comprise of physically distinct components (i.e., two lobes and two jets). We therefore apply the size and magnetic field requirement separately to all components. For the radius (R) of the component we use 0.5 times the deconvolved full-width-half-maximum (FWHM); if the component is not resolved, we use the upper limit on its size as given by the resolution of the radio telescope (45 arcsec FWHM).

In Fig. 3.1 we show the luminosity and size of the region of the radio-emitting galaxies with the largest value of $B \times R$, since this determines the maximum cosmic ray energy. We see that only a handful of radio-emitting galaxies within 100 Mpc are large and luminous enough to (potentially) accelerate protons to $E = 10^{20}$ eV. These seven source are: Cen A, UGC 1841, NGC 1128, NGC 1275, NGC 3862, NGC 4782, and CGCG 114-025.

We stress that our approach will overestimate the maximum attainable cosmic ray energy for sources that are not resolved or near the resolution of the radio survey (e.g., NGC 1275, NGC 3862). For these galaxies, the emission of the core of jet contributes to the luminosity and thus increases our magnetic field estimate (Eq. 3.1). Because the size of this core is at least three orders of magnitude smaller than the upper limit on the radius we derive from the resolution of the radio survey, the value of $B \times R$ is overestimated.

3.2.2 Magnetic fields and energy injection

The total energy in magnetic fields (U_B) can be used to estimate the power of the jet (Q_j) that has created this region: $Q_j \sim (1+\epsilon)U_B/t_d$, with t_d the dynamical time. Here we make an order of magnitude estimate of the jet power by assuming that each radio component is a spherical region that is uniformly filled with magnetic fields, $U_B = 1/6\, B^2 R^3$; we estimate the dynamical time using the distance of the region to the galaxy center (d) over the mean velocity of the jet (v_j). To avoid $d \to 0$ for radio galaxies that are not resolved into multiple components, we use FWHM/2 to yield a lower limit on d. The jet velocity is fixed at $v_j = 0.1c$; this velocity is at the upper

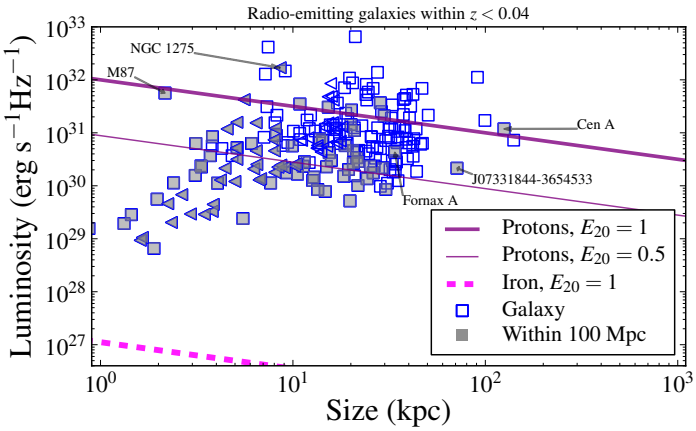

FIGURE 3.1: The radio luminosity and size of radio-emitting galaxies within $z = 0.04$ (or a co-moving distance of 170 Mpc), for the region with the largest value of $B \times R$. For components that are not resolved, we use the upper limit on R given by the resolution of the radio survey (at 50 Mpc this corresponds to 10 kpc). The minimum luminosity and size that are needed to contain cosmic rays (Eq. 3.3) are shown. Only a handful of sources within the GZK volume are above the limit for protons of 10^{20} eV, while all sources are large enough to contain iron nuclei of this energy.

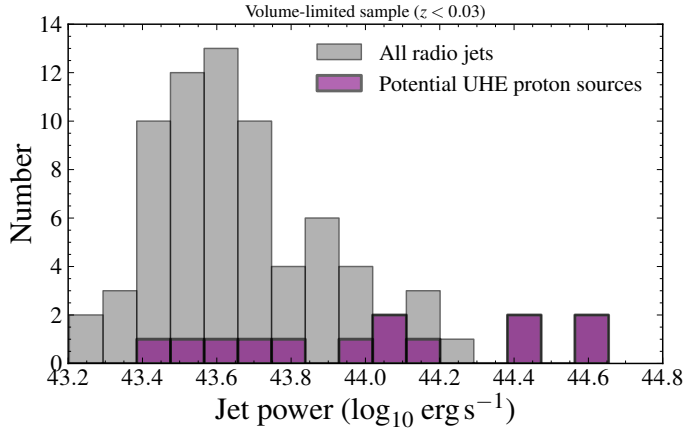

FIGURE 3.2: Distribution of jet power for a volume-limited sample of radio galaxies. The jet power follows from the total magnetic energy over the dynamical time (Eq. 3.4). For the 'Potential UHE proton sources', this sum runs only over components that are large and luminous enough to accelerate protons to $E = 10^{20}$ eV.

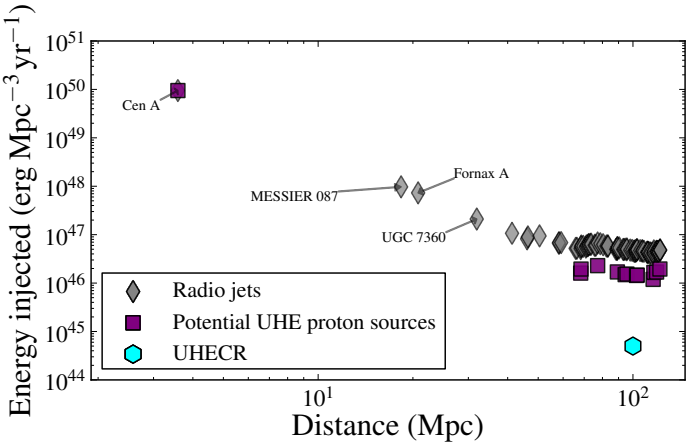

FIGURE 3.3: The energy injected into the sphere spanned by the distance between us and the source, for a volume-limited sample of radio galaxies. Because the Milky Way is situated in an overdensity of galaxies, and thus an even stronger overdensity of radio galaxies, the energy injected per unit volume increases to smaller distances. We see that the energy injected into protons with $E > 10^{19.5}$ eV (Waxman 1995a; Berezinsky 2008; Katz et al. 2009), is two orders of magnitude less than the energy that is available from radio galaxies.

end of the observed hot spot propagation speeds (Liu et al. 1992) and thus yields a generous estimate of the time-averaged jet power. For a given component of the radio galaxy we obtain,

$$Q_{j,\mathrm{comp}} = 5 \times 10^{43}\,(1+\epsilon) \left(\frac{L_\nu/\epsilon}{10^{31}\mathrm{erg\,s^{-1}Hz^{-1}}}\right)^{4/7} \left(\frac{R}{100\ \mathrm{kpc}}\right)^{9/7} \left(\frac{d}{100\ \mathrm{kpc}}\right)^{-1} \left(\frac{\nu}{\mathrm{GHz}}\right)^{4/7} \mathrm{erg\,s^{-1}} \quad . \tag{3.4}$$

To estimate the single jet energy (Q_j), we sum $Q_{j,\mathrm{comp}}$ of all radio-emitting components of the galaxy divide by 2. In Fig. 3.2 we show the distribution of jet powers for a volume-limited sample (sample A of van Velzen et al. (2012), i.e., a minimum luminosity of $\nu L_\nu > 5\times10^{39}\,\mathrm{erg\,s^{-1}}$ within 125 Mpc). The energy injected per unit volume follows by summing $2Q_j$; for sources within 100 Mpc we obtain $5\times10^{46}\,\mathrm{erg\,Mpc^{-3}yr^{-1}}$. If we restrict the sum of $Q_{j,\mathrm{comp}}$ to components that are large and luminous enough to contain protons of 10^{20} eV (Eq. 3.3), fewer galaxies contribute, resulting in a factor 2 decrease of the total injected energy.

In Fig. 3.3 we show the energy injected by radio galaxies as a function of their distance to the Milky Way and the energy injected into UHECRs. The latter is estimated by fitting the observed flux of these particles to a theoretical injection spectrum. For protons with energies larger than $\sim 10^{19.5}$ eV, values in the literature

range between $(3-6)\times 10^{44}\,\mathrm{erg\,Mpc^{-3}yr^{-1}}$ (Waxman 1995a; Berezinsky 2008; Katz et al. 2009). This is two orders of magnitude below the energy injected by radio galaxies within 100 Mpc.

3.2.3 Cross correlation

In this section we present the cross-correlation between UHECRs and volume-limited samples of galaxies. Since the radio galaxies are a subset of a large (10^4) volume-limited sample of "normal" galaxies, we can measure the strength of the correlation with respect to the matter content of the Local Universe. We will use the sample of 69 cosmic rays with energies $E > 55$ EeV detected by Auger between 2004 and 2009 (The Pierre Auger Collaboration 2010b, hereafter Auger10).

We first consider a volume-limited sample of normal galaxies within $z = 0.03$ (125 Mpc), which consists of all galaxies with an IR luminosity greater than $M_K = -23.8$. Following Auger10, we compute the number of CR-galaxy pairs for different maximum separation angles, $n_g(d)$, and we compare this to the isotropic expectation, $\langle n_g^{\rm iso}(d)\rangle$. We obtain $\langle n_g^{\rm iso}\rangle$ from the average number of pairs for 69 cosmic rays that follow the geometrical exposure (Sommers 2001) of the Auger observatory. In Fig. 3.4(a) we show the fractional excess of pairs, $n_p(d)/\langle n_p^{\rm iso}(d)\rangle - 1$.

We now repeat the above analysis for a volume-limited sample of radio galaxies to find the relative excess of pairs with respect to an isotropic CR distribution. In Fig. 3.4(b) we show the result using all 24 radio galaxies within $z = 0.03$ that are as luminous as Cen A; a significant correlation is clearly visible at 15°–30°. In Fig. 3.4(c) we compare this signal to the mean excess of pairs for samples of 24 non-radio galaxies. At all angular scales, the correlation between radio-galaxies and cosmic rays is significantly stronger than the correlation with normal galaxies; at 15°–20° the correlation signal of the radio galaxies exceeds the matter distribution by 3-σ.

To estimate how much of the correlation between radio galaxies and UHECRs can be explained by the Cen A region, we computed the mean excess of pairs for samples of 23 non-radio galaxies plus Cen A. By adding Cen A to the random samples of non-radio galaxies, we obtain a measure of the correlation signal that is exclusive to the Cen A region. In Fig. 3.4(d) we see that the excess of pairs between UHECRs and radio galaxies is at most a factor two above signal from Cen A, which is a 2-σ increase with respect to the fluctuations due to sampling of the matter distribution.

3.3 Results

We have investigated the properties of a complete sample of radio galaxies in the context of UHECR acceleration.

- We compared the luminosity and size to the minimum requirements for particle acceleration (Fig. 3.1). We find only seven galaxies within the 100 Mpc have regions that could be large and luminous enough to contain protons with an

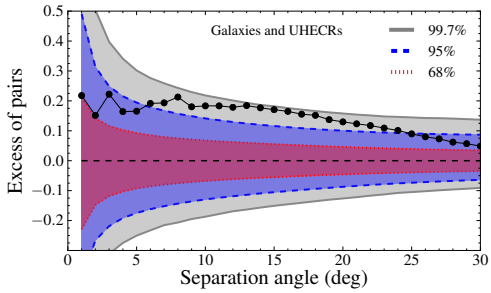

(a) UHECRs and normal galaxies

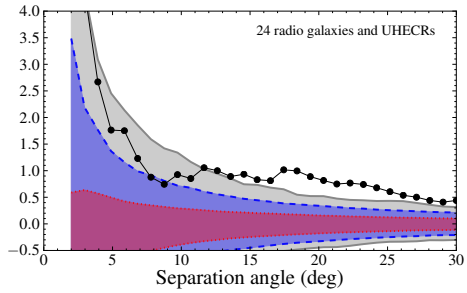

(b) UHECRs and radio galaxies (volume-limited)

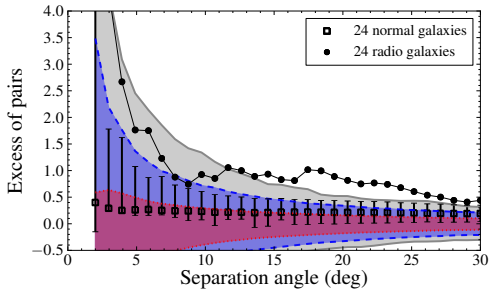

(c) Comparing to 24 normal galaxies

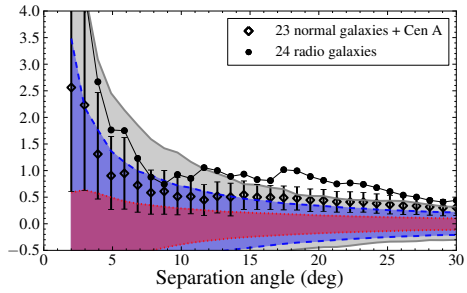

(d) Comparing to 23 normal galaxies, plus Cen A

FIGURE 3.4: (a) The cross-correlation between a volume-limited sample of galaxies ($z < 0.03$, $M_K < -23.8$) and 69 Auger UHECRs with $E > 55$ EeV (The Pierre Auger Collaboration 2010a). We show the relative excess of CR-galaxy pairs with respect to an isotropic CR distribution as observed by the Auger Surface Detectors. (b) The cross-correlation for a volume-limited sample ($z < 0.03$) of 24 galaxies with a radio luminosity greater or equal to Cen A. The third figure (c) is identical to (b), but we also show the mean cross correlation for random samples of 24 non-radio galaxies. Error bars show the uncertainty (68% CL) due to sampling the galaxy distribution. The last figure (d) is identical to the previous two figures, except that we compare to random samples 23 non-radio galaxies, plus Cen A.

energy of 10^{20} eV, yielding a rather low density of 2×10^{-6} Mpc^{-3}. However all radio-emitting galaxies in our sample appear large enough to contain UHE iron nuclei.

- The total energy injected by radio galaxies (with a minimum radio luminosity of $\nu L_\nu > 5 \times 10^{39}\,\mathrm{erg\,s^{-1}}$) is $5 \times 10^{46}\,\mathrm{erg\,Mpc^{-3}yr^{-1}}$ within 100 Mpc. If we restrict to jets that are associated with lobes that are large enough to contain protons of 10^{20} eV, the total injected energy is a factor 2 lower. This estimate is two orders of magnitude above the energy that is injected into UHECRr (Fig. 3.3).

- The number of pairs between the 24 radio galaxies that are as luminous as Cen A and Auger UHECRs is significantly enhanced with respect to the distribution of normal galaxies, Fig. 3.4(c), but a large fraction of the correlation is driven by the region around Cen A, Fig. 3.4(d).

3.4 Discussion

Our estimate of the energy injected by radio galaxies is two orders of magnitude above the estimated energy in UHECRs within the GZK volume. Hence radio galaxies appear to inject sufficient energy into the Local Universe to explain the observed UHECR flux. We note that while our estimate of the jet energy was generous, it is not likely to overestimate the power by a factor $\sim 10^2$. In fact, our estimates of Q_j are consistent with the relation between radio luminosity and mechanical jet power determined using the X-ray cavities in the hot gas of galaxy groups/clusters (Cavagnolo et al. 2010).

The most luminous jets in the GZK volume have a power of $10^{44.5}\,\mathrm{erg\,s^{-1}}$ (Fig. 3.2). We can compare this to the lower limit on the Poynting luminosity,

$$L_B \sim \frac{1}{6} c B^2 R^2 \Gamma^4 \gtrsim 10^{45} \left(\Gamma \frac{E_{20}}{Z}\right)^2 \mathrm{erg\,s^{-1}} \tag{3.5}$$

(Waxman 1995b; Farrar & Gruzinov 2009), with Γ the Lorentz factor of the jet, to find that steady jets in the Local Universe can only accelerate particles with $Z > 2E_{20}\Gamma$. In other words, the time-averaged jet power of AGN in the Local Universe is not sufficient to accelerate protons to the highest cosmic-ray energies. A similar conclusion has been made based on the power of the accretion disks of nearby AGN (Zaw et al. 2009). If all observed UHECRs are protons, long-lived jets in the Local Universe can not be their sources —jets from variable sources, such as gamma-ray burst (Waxman 1995a) or giant AGN flares (Farrar & Gruzinov 2009), are better candidates. We note that, iron nuclei of $E = 10^{20}$ eV, only require $L_B > \Gamma^2\ 10^{42}\ \mathrm{erg\,s^{-1}}$; for $\Gamma \leq 3$, this lower limit is consistent with the measured jet power of all AGN jets in our volume-limited sample.

While none of the radio jets in the Local Universe appear powerful enough to accelerate ultra-high energy protons, the magnitude of the equipartition magnetic field of the lobes that have been created by these jets, is, in some cases, strong enough to contain these particles (Fig. 3.1). This apparent contradiction is explained by the large volume of the lobes; for an adiabatically expanding sphere of magnetic energy we have $B \times R \propto R^{1/3}$.

In summary, our analysis shows that lobes of radio galaxies remain potential sources of UHECRs. The lobes contain sufficient energy to be compatible with the observed cosmic ray flux at the highest energies, even if only 1% of the total energy is given to these particles. Only a few radio galaxies in the Local Universe have lobes

that are large enough to contain UHE protons, while iron nuclei of 10^{20} eV could be contained by virtually all galaxies with radio lobes.

Since the potential accelerators are sparse, the current lower limit on the density of potential UHECR sources, based on the observed number of UHECR pairs, could be sufficient to rule out the proton-only hypothesis. Deflections of $E = 60$ EeV protons due to Galactic magnetic fields are $< 10^\circ$ for most parts of the sky (Jansson & Farrar 2012). For an angular smearing of 20°, the lower bound on the density of sources that produce $E > 60$ EeV cosmic rays is 1×10^{-5} Mpc^{-3}, assuming uniform intensity of the sources (The Pierre Auger Collaboration 2013). This lower bound exceeds our density of potential UHE proton sources by an order of magnitude. Hence only if the inter-galactic magnetic fields are strong enough to lead to $> 20^\circ$ deflections, radio galaxies remain a potential source of UHE protons.

Chapter 4

The contribution of spin to jet-disk coupling in black holes

Sjoert van Velzen & Heino Falcke

2013, Astronomy & Astrophysics Letters, 557, L7

Abstract

The spin of supermassive black holes could power jets from active galactic nuclei (AGN), although direct observational evidence for this conjecture is sparse. The accretion disk luminosity and jet power, on the other hand, have long been observed to follow a linear correlation. If jet power is coupled to black hole spin, deviations from the jet-disk correlation for a sample of AGN can be used to probe the dispersion of the spin parameter within this sample. To apply this idea, we matched double-lobed radio sources from the FIRST survey (1.4 GHz) to spectroscopically confirmed quasars from SDSS. We obtain 763 FR-II quasars with a median redshift of $z = 1.2$. A tight correlation between the optical luminosity of the accretion disk and the lobe radio luminosity is observed. We estimate that 5-20% of the bolometric disk luminosity is converted to jet power. Most of the scatter to the optical-radio correlation is due to environment; deviations from jet-disk coupling due to internal factors (e.g., spin) contribute at most 0.2 dex. Under the assumption that the Blandford-Znajek mechanism operates in AGN, we obtain an upper limit of 0.1 dex to the dispersion of the product of the spin and the magnetic flux threading the horizon. If black hole spin determines the AGN jet efficiency, then our observations imply that all FR-II quasars have very similar spin. In addition, the quasar spin distribution needs to have a wide gap to explain the radio-quiet population. The alternative, and perhaps more likely, interpretation of the tight jet-disk correlation is that black hole spin is not relevant for powering AGN jets.

4.1 Introduction

Accreting astrophysical objects often produce jets; outflows are commonly observed to escape from active black holes, neutron stars, white dwarfs, and young stellar objects. For all but the last, their velocities are (at least mildy) relativistic (Reipurth & Bally 2001; Körding et al. 2008a; Mirabel & Rodríguez 1999). Despite a wealth of observations, the launch mechanism of jets has so far remained elusive.

Some authors argue that all disk-jet systems can be described in a scale-invariant framework (e.g., Falcke et al. 1999; McHardy et al. 2006; Migliari & Fender 2006; Körding et al. 2006b). Jets from black holes, on the other hand, are often considered a separate class, since these are the only objects where General Relativity can have a major influence on the dynamics. In particular, it has often been conjectured that black hole spin is the dominant parameter in determining jet power, because space-time dragging can twist magnetic field lines (Blandford & Znajek 1977). In the Blandford-Znajek mechanism, jet power is coupled to the dimensionless spin parameter (a) and the magnetic flux (Φ_B) that threads the horizon: $Q_j \propto a^2\Phi_B^2$.

Evidence for spin-powered jets has recently been claimed for stellar mass black holes in X-ray binaries. Narayan & McClintock (2012) observed a correlation between the 5 GHz radio luminosity of the transient ballistic jet, which is launched during the accretion state transition when the accretion rate is close to the Eddington limit (Fender et al. 2004), and the spin parameter of the black hole. Fender, Gallo, & Russell (2010), on the other hand, reported no evidence for a correlation between spin and a number of measurements that probe jet power. The discrepancy between these two results (e.g., Russell et al. 2013a versus Steiner et al. 2013) could be due to source selection.

The spin of supermassive black holes is often invoked to explain why only about 10% of quasars are radio-loud (Kellermann et al. 1989; Xu et al. 1999; Baloković et al. 2012): only rapidly spinning black holes produce powerful jets (e.g., Rees et al. 1982; Wilson & Colbert 1995; Moderski et al. 1998; Sikora et al. 2007). In this is so-called spin-paradigm, the observed radio loudness maps to the supermassive black hole spin distribution. This distribution can be estimated by modeling black hole growth from accretion. If an accretion episode is long enough, maximum spin ($a \approx 1$) is expected because the inner parts of the accretion disk are forced to rotate in the equatorial plane of the black hole (Bardeen & Petterson 1975). Simulations of spin evolution that include both accretion and black hole coalescence (Hughes & Blandford 2003; Gammie et al. 2004; Volonteri et al. 2007) typically yield a smooth distribution, i.e., no gap between the high-spin ($a > 0.9$) systems and the rest of the population. Alternatively, the low number of radio-loud quasars can be explained by intermittent jet production due to state changes of the accretion disk (Merloni et al. 2003; Nipoti et al. 2005). A hot accretion flow may be required to accumulate sufficient magnetic flux near the black hole horizon (Beckwith et al. 2008; Sikora & Begelman 2013).

A direct measurement of the spin of supermassive black holes can be obtained when

the broad iron fluorescence line is detected at high signal-to-noise, with simultaneous broadband X-ray coverage to constrain line distortions due to absorption (Risaliti et al. 2013). Hence this is currently possible only for a restricted class of (nearby) AGN.

To study supermassive black hole spin for large populations, we propose to use the well-known correlation between jet power and disk luminosity. Jet-disk coupling has been observed using emission from the compact radio core (Falcke & Biermann 1995), the extended radio lobes (Rawlings & Saunders 1991), and the power in X-ray cavities (Allen et al. 2006); these observations can be used to show that a constant fraction of about 10% of the disk luminosity is injected into the jet (Falcke et al. 1995b; Körding et al. 2008b).

Since mass will disappear into the black hole while magnetic fields can pile up at the horizon, a linear coupling of accretion rate and jet power is not a natural result of the standard Bandford-Znajek mechanism. However, in the magnetically arrested disk (MAD; Narayan et al. 2003) scenario, black holes that are saturated with magnetic flux obey $Q_j = \eta_{\rm MAD}\dot{m}c^2$, with $\eta_{\rm MAD} = 140\%$ for $a = 0.99$ (Tchekhovskoy et al. 2011).

In this chapter, we will show that the scatter to the radio-optical correlation for a sample of AGN can be used to constrain the dispersion of black hole spin, or any other internal parameter that couples to jet power. Our approach is different from previous radio-based studies (e.g., Nemmen et al. 2007; Daly 2009), which aimed to reproduce the observed jet power within the spin paradigm. Since Doppler boosting of the compact radio core of the jet smears out the radio-loudness distribution (Falcke et al. 1996), we will only use the radio emission of the lobes of FR II (Fanaroff & Riley 1974) sources. These lobes emit isotropically and can thus be used to obtain an orientation-independent measurement of the jet power. If accretion onto compact objects is scale-invariant, radio-loud quasars can be considered (e.g., Körding et al. 2006b) to be the supermassive analogy of the ballistic jets that are launched when X-ray binaries switch between accretion states. Recalling that a correlation between radio luminosity and black hole spin has been reported only for these jets (Narayan & McClintock 2012), FR II quasars are arguably the most promising class of AGN to show the effects of spin on jet power.

We adopt the following cosmological parameters $h = 0.70$, $\Omega_{\rm M} = 0.3$, $\Omega_\Lambda = 0.7$.

4.2 Selection of FR II quasars

The radio emission of FR II sources is dominated by two edge-brightened lobes that are separated by $\sim 10^2$ kpc. These sources are easy to identify in images of the radio sky; a surveys with a resolution a 10 arcsec can resolve pairs with a projected separation 100 kpc throughout the entire universe.

A presented in great detail in Chapter 5, a large sample of FR IIs can be obtained

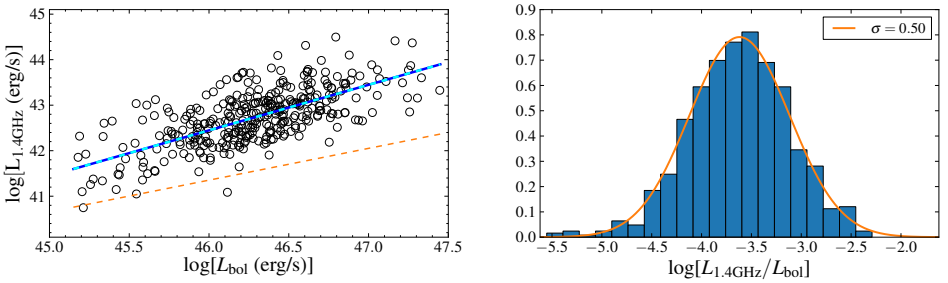

FIGURE 4.1: Left: we observe a linear correlation between the lobe radio luminosity and the bolometric quasar luminosity (solid blue+cyan line). The dashed orange line shows the correlation that one would obtain if all the radio sources clustered at the detection threshold (Eq. 4.1). Our observations are sensitive to outliers of the correlation of 1 dex. Right: the residuals of the correlation are well-described by a Gaussian distribution with $\sigma = 0.50 \pm 0.01$ dex.

by simply searching for source pairs in catalogs of radio surveys. We use the catalog radio sources at 1.4 GHz from FIRST (Faint Images of the Radio Sky at Twenty-centimeters; Becker et al. 1995). These images have a resolution of 5 arcsec FWHM and cover $\sim 10^4$ deg^2 to a limiting peak flux of 1 mJy. We selected all pairs within a separation 10" $< d <$ 60", yielding 89,214 candidate FR IIs.

To assess the potential of constraining black hole spin with radio observations, we have to consider the flux limit of our FR II sample. To detect an extended source requires higher signal-to-noise than for a point source, so the limit on the integrated flux is a function of source compactness. Since we search for source pairs, our flux limit also depends on the lobe-lobe flux ratio. We thus obtain the following expression for the lower limit on the sum of the integrated flux of the two lobes

$$S_{\nu,\mathrm{lim}} = 1 \text{ mJy} \times \max(S_{\mathrm{int}}/S_{\mathrm{peak}}) \times (1 + f_{\mathrm{lobe-lobe}}) \quad . \tag{4.1}$$

Here $\max(S_{\mathrm{int}}/S_{\mathrm{peak}})$ is the largest value of the inverse compactness ratio of the two lobes (its median value is 1.8), and $f_{\mathrm{lobe-lobe}}$ denotes the absolute value of the lobe-lobe flux ratio. Since the lobe-lobe flux ratio peaks at unity, the median flux limit is 4 mJy.

We matched the centers of our radio-selected FR IIs to spectroscopically identified quasars (Richards et al. 2002; Schneider et al. 2007) in the Sloan Digital Sky Survey (SDSS). We use the Seventh Data Release (DR7; Abazajian et al. 2009) edition of the catalog (Schneider et al. 2010), consisting of 105,783 quasars with $M_i < -22$. For the match radius we use $d/4$, with d the lobe-lobe separation (this ensures that the quasar is located between the two lobes). We obtain 763 FR II quasars, the contribution of random matches is only 1.6±0.5%, because the areal density of both the radio doubles and quasars is relatively sparse. The median redshift is $z = 1.16$; the median mass

and Eddington ratio of the FR II quasars is $10^{9.2}$ $M_\odot$ and 8%, respectively (Shen et al. 2011).

Next, we use the luminosity and frequency dependent bolometric correction of Hopkins, Richards, & Hernquist (2007) to convert the i-band flux to the bolometric quasar luminosity ($L_{\rm bol}$). The K correction for the rest-frame radio luminosity is obtained using the mean spectral index of the lobes ($\alpha = -0.9$). We obtain a linear relation between bolometric disk luminosity and the 1.4 GHz (rest-frame) lobe luminosity (Fig. 4.1, left) with $\langle \log L_{\rm bol}/L_{1.4{\rm GHz}} \rangle = -3.6$. The residuals of this correlation follow a normal distribution with $\sigma_{\rm optical-radio} = 0.50 \pm 0.01$ dex, as obtained using an unbinned maximum likelihood fit (Fig. 4.1, right). We also observed a highly significant flux-flux correlation (the p-value for a Kendall's tau rank analysis is 10^{-33}), showing that our optical-radio correlation is not induced by Malmquist bias.

The observed optical-radio correlation is consistent with the Willott et al. (1999) minimal energy argument for synchrotron emission, $Q_j \propto L_{\rm bol}^{6/7} f^{3/2}$. For a fudge factor that is typical for FR II sources, $f = 10$ (Blundell & Rawlings 2000), we find that on average about 20% of the bolometric quasar luminosity ends up in the jet, $q_j \equiv Q_j/L_{\rm bol} = 0.17$. Recently, Godfrey & Shabala (2013) presented a method to measure jet power from the hotspot properties. These authors obtain $Q_j \propto L^{0.8} D^{0.58}$, with D the source size (Shabala & Godfrey 2013). For this model, the median jet-disk coupling parameter is $q_j = 0.08$ (Fig. 4.2, left).

4.3 Measuring the spin contribution

In the previous section we obtained a sample of 763 FR II quasars and found a linear relation between the lobe radio luminosity and the bolometric disk luminosity. The residuals to this correlation can be modeled with four separated Gaussian distributions:

$$\sigma^2_{\rm radio-optical} = \sigma^2_{\rm data} + \sigma^2_{\rm environ} + \sigma^2_{\rm delay} + \sigma^2_{\rm internal} = 0.50 \text{ dex}. \qquad (4.2)$$

Below we present a lower limit for the first three external effects, allowing us to obtain an upper limit to $\sigma_{\rm internal}$.

The scatter due to the measurement uncertainty ($\sigma_{\rm data}$) is dominated by the dispersion in the bolometric correction that we applied to the optical luminosity. For quasars observed at optical wavelengths, this dispersion is measured to be 0.15 dex (Hopkins et al. 2007).

From symmetry arguments, we can assume that two jets from one black hole carry equal kinetic energy, hence the lobe-lobe flux ratio can be used to obtain a lower limit on the effect of the local environmental on differences in the radio luminosity ($\sigma_{\rm environ}$). The lobe-lobe flux ratio can be modeled with a Gaussian distribution with $\sigma = 0.39$ dex. Under the conservative assumption that the quasar-to-quasar fluctuations in environment are similar to the fluctuations probed by two jets from one quasar, we obtain $\sigma_{\rm environ} > 0.39$ dex.

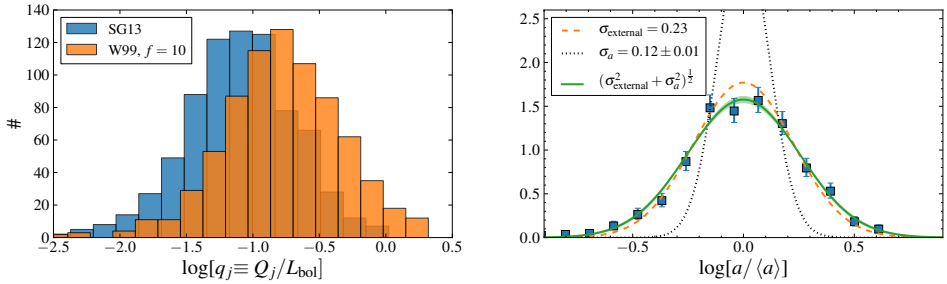

FIGURE 4.2: Left: the jet-disk coupling parameter for two different models of synchrotron emission by the lobes. The Willott et al. (1999, W99) model is based on minimum energy arguments; the median jet power in this model is $q_j = 0.2$. For the Shabala & Godfrey (2013, SG13) scaling we obtain $q_j \approx 0.1$. Right: The dispersion of black hole spin as obtained from the residuals to the radio-optical correlation. Here we adopt the Blandford-Znajek mechanism to change coordinates, $L_{1.4\rm GHz} \propto Q_j \propto \Phi_B^2 a^2$. The lower limit on the external factors (dashed orange line) provides a reasonable description of the data. Hence the contribution due to spin or magnetic flux is constrained to a narrow range (black dotted line).

The radio emission is delayed and smeared with respect to our optical view of the quasar, since it takes time for the energy produced near the black hole to reach the lobes. Evolution of the quasars during this $\sim 10^6$ yr delay will also introduce scatter to the optical-radio correlation. The longest baselines of optical quasar light curves reach 50 yr (in the observer's frame); a structure function analysis reveals 0.28 mag variability for this time scale (MacLeod et al. 2012). We thus obtain the very conservative lower limit, $\sigma_{\rm delay} > 0.11$ dex. We note that for quasars with a radio luminosity that is a factor ten below the radio-optical correlation (Fig. 4.1, left), we find a median core-to-lobe ratio of 1.4. Only 6% of all FR II quasars in our sample have such strong cores, providing evidence that the largest outliers to the optical-radio correlation are due to a delay between the newly activated disk luminosity and the lobe radio luminosity.

The three measurements discussed above can be combined to find a strict lower limit on the external contributions to deviations from jet-disk coupling, $\sigma_{\rm external} > 0.45$ dex. We now obtain an upper limit for the remaining contribution by processes that could influence the jet power, $\sigma_{\rm internal} = 0.24 \pm 0.03$ dex. Adopting the standard Blandford-Znajek mechanism, this translates into an upper limit on the dispersion of the product of black holes spin and magnetic flux, $\sigma_{\rm BZ} < 0.12$ dex (Fig. 4.2, right).

4.4 Discussion

Using a large sample of FR II quasars at $z \sim 1$, we obtained a tight correlation between the luminosity of the radio lobes and the accertion disk. After correcting for

the environment and other external factors that contribute to the scatter around this correlation, we find that factors that are internal to the black hole can change the jet power by at most 0.24 dex. For jets powered by a Blandford-Znajek mechanism, $Q_j \propto \Phi_B^2 a^2$, this implies $\sigma_{\rm BZ} < 0.12$.

Most of the SDSS quasars are not detected as FR II radio sources in the FIRST survey (de Vries et al. 2006; White et al. 2007). Adopting the spin paradigm, this would imply that the spin of the radio-quiet quasars is at least a factor of three lower than the mean spin of the FR II quasars. The typical value for this spin-reduced jet power is 2×10^{38} W; this is much larger than the median FR II jet power (e.g., Antognini et al. 2012), hence such radio-quiet quasars would not be missing from our sample because their jets are too weak to obtain an FR II morphology. We also note that the spin-alignment time of quasars (e.g., Volonteri et al. 2007) is at least an order of magnitude longer than the typical lifetime of powerful FR IIs (Carilli et al. 1991), so our radio selection is not biased to high spin black holes.

Our results appear to be at odds with the analysis of X-ray binaries by Narayan & McClintock (2012), who observed a correlation between radio luminosity and black hole spin that spans three orders of magnitude. If radio-loud quasars also follow this correlation, the small scatter to the optical-radio correlation implies that these supermassive black holes all have a similar spin parameter. We consider a narrow distribution of black hole spin for radio-loud quasars, plus a wide gap to explain the radio-quiet quasars, an unnatural result of black hole evolution. Since spin-up and spin-down are both expected to occur during the growth of a black hole, one generically obtains a smooth distribution for the spin parameter.

For quasars at $z \sim 1$, massive accretion events triggered by major mergers may yield a high ($a > 0.6$) mean spin, with modest scatter (Volonteri et al. 2013). In this scenario, which is consistent with our upper limit on the dispersion of spin for FR IIs, jet-spin coupling via the Blandford-Znajek mechanism clearly fails to explain why the majority of quasars are radio-quiet. To explain our observations within the spin paradigm, one is forced to adopt a very strong jet-spin coupling, such that high spin effectively acts as a threshold for jet production (Tchekhovskoy et al. 2010). In this case, however, one would expect an asymmetric distribution of residuals, which is not observed (Fig. 4.1).

In the MAD scenario, introduced on page 67, jet power is independent of magnetic flux and is proportional to the accretion rate. Hence for $a = 1$ this model would naturally predict linear jet-disk coupling with no scatter due to internal parameters. Unfortunately, the predicted MAD jet efficiency ($\eta_{\rm MAD} \approx 1.4\, a^2$) for maximally spinning black holes is two orders of magnitude higher than the observed mean efficiency of the FR II quasars (Fig. 4.2, left): $Q_j \approx 0.1 L_{\rm bol} \approx 10^{-2} \dot{m} c^2$.

We thus conclude that the observed radio-optical correlation supports a tight jet-disk coupling (Rawlings & Saunders 1991; Falcke & Biermann 1995) and suggest that the power output from the inner part of the accretion disk dominates over the power

extracted from the black hole by the Blandford-Znajek mechanism (Livio et al. 1999). Spin, or in fact any other internal parameter that can vary from quasar to quasar, is not a dominant parameter for powering jets. This leaves intermittent jet production due to state changes of the accretion disk as the best explanation for the radio loudness distribution of quasars.

Acknowledgments

We would like the thank the referee, Demos Kazanas, for the swift reply. We are grateful to P. L. Biermann, J. Dexter, T. M. Heckman, J. Hlavacek-Larrondo, E. Körding, J. H. Krolik, J. E. McClintock, B. D. Metzger, R. Narayan, R. S. Nemmen, H. Röttering, B. S. Sathyaprakash, M. Sikora, J. F. Steiner, R. L. White, and N. L. Zakamska for useful discussions.

This work was supported by an ERC Advanced Grant (n. 227610). The National Radio Astronomy Observatory is a facility of the National Science Foundation operated under cooperative agreement by Associated Universities, Inc. Funding for the SDSS and SDSS-II has been provided by the Alfred P. Sloan Foundation, the Participating Institutions, the National Science Foundation, the U.S. Department of Energy, the National Aeronautics and Space Administration, the Japanese Monbukagakusho, the Max Planck Society, and the Higher Education Funding Council for England.

Chapter 5

Nature and evolution of powerful radio galaxies at $z \sim 1$ and their link with the quasar luminosity function

Sjoert van Velzen, Heino Falcke, and Elmar Körding

2014, Monthly Notices of the Royal Astronomical Society, submitted

Abstract

Current wide-area radio surveys are dominated by active galactic nuclei, yet many of these sources have no identified optical counterparts. Here we investigate whether one can constrain the nature and properties of these sources, using Fanaroff-Riley type II (FR II) radio galaxies as probes. These sources are easy to identify since the angular separation of their lobes remains almost constant at some tens of arcseconds for $z > 1$. Using a simple algorithm applied to the FIRST survey, we obtain the largest FR II sample to date, containing over 10^4 double-lobed sources. A subset of 459 sources is matched to SDSS quasars. This sample yields a statistically meaningful description of the fraction of quasars with lobes as a function of redshift and luminosity. This relation is combined with the bolometric quasar luminosity function, as derived from surveys at IR to hard X-ray frequencies, and a disk-lobe correlation to obtain a robust prediction for the density of FR IIs on the radio sky. We find that the observed density can be explained by the population of known quasars, implying that the majority of powerful jets originate from a radiatively efficient accretion flow with a linear jet-disk coupling. Finally, we show that high-redshift jets are more often quenched within 100 kpc, suggesting a higher efficiency of jet-induced feedback into their host galaxies.

5.1 Introduction

This year marks the fortieth anniversary of the famous publication by Fanaroff & Riley (1974), reporting that the morphology of extra-galactic radio sources is correlated with their luminosity. The powerful FR II radio galaxies are edge-brightened; their radio output is dominated by two lobes with a hotspot at a typical separation of a few hundred kpc (Mullin et al. 2008). The fainter FR I sources, on the other hand, show a radial decrease of radio intensity and often have disrupted, non-symmetric morphologies.

With radio lobes we can probe powerful active nuclei that are obscured at higher frequencies. The lobes of FR II radio sources can be used as calorimeters of the kinetic jet luminosity (Scheuer 1974; Falle 1991; Kaiser & Alexander 1997; Willott et al. 1999), which allows us to test theories of black hole jet formation (e.g., Rawlings & Saunders 1991). FR II radio sources are also interesting since they single out galaxies at an important epoch of their evolution. Feedback during the quasar-phase (Kauffmann & Haehnelt 2000; Churazov et al. 2005; Hopkins et al. 2006) most likely explains why the most massive galaxies are "red and dead" (Bower et al. 2006; Croton et al. 2006). This AGN feedback (for reviews see Cattaneo et al. 2009; Fabian 2012; McNamara & Nulsen 2012; Alexander & Hickox 2012) can be exercised by winds from the accretion disk or by the relativistic jet (e.g., Morganti et al. 2013). Jets from quasars are particularly interesting since they can carry large amounts of energy up to a distance of ~ 1 Mpc, thus expanding the black hole's influence to the scale of galaxy groups (Fabian 2012).

Since stellar mass black holes consistently show powerful jets during a state change of the accretion disk at high luminosity (Fender et al. 2004), a scale-invariant view of black hole accretion (Falcke et al. 1999; McHardy et al. 2006) tells us that all quasars will host powerful jets for some part of their lifetime (Nipoti et al. 2005; Körding et al. 2008b). The radio lobes of these FR II quasars are bright; the sensitivity of current radio surveys is sufficient to detect the most powerful sources (such as Cygnus A) at the earliest possible cosmological epoch ($z \sim 10$). To tap this potential of radio surveys, we need a robust method of source identification (e.g., we wish to avoid mixing up low-redshift starforming galaxies with high-redshift blazars). This selection can be done using the radio spectrum, information from higher frequency (e.g., optical/IR) observations, or the radio morphology.

In this work, we apply a simple morphological selection method to the catalog obtained from Faint Images of the Radio Sky at Twenty-cm (FIRST; Becker, White, & Helfand 1995) to collect double-lobed radio sources. We obtain a relatively clean sample of over ten thousand supermassive black holes with powerful jets. To derive the areal density of these sources (i.e., the number per unit area on the sky), we postulate that they must be coupled to the quasar luminosity function —after all, jets are ultimately powered by accretion. Indeed there exists a well-known (near) linear correlation between the accretion disk luminosity and the power of the compact radio

core (Falcke & Biermann 1995) or the radio luminosity of the lobes (Rawlings & Saunders 1991; Willott et al. 1999). This correlation is the beating heart of our method; we will assume that all double-lobed radio sources obey a single relation between disk power and lobe radio luminosity and we demonstrate that our observations support this assumption.

Previous work on the radio source population has been focused on: (*i*) the luminosity function of radio galaxies and radio-loud quasars (e.g., Dunlop & Peacock 1990; Willott et al. 2001), (*ii*) estimating the kinetic jet luminosity function using a model for the conversion of jet power to radio emission (Körding et al. 2008b; Kapińska et al. 2012; Mocz et al. 2013), or (*iii*) a parametric redshift-dependent model of the source counts (Condon 1984; Massardi et al. 2010).

5.1.1 FR II radio sources

The division in radio luminosity between FR I and FR II sources is nominally placed at $L_{1.4\mathrm{GHz}} \sim 10^{25}\,\mathrm{W\,Hz^{-1}}$ (Fanaroff & Riley 1974), although recent observations have found FR IIs at lower luminosity (e.g., Antognini, Bird, & Martini 2012), implying that the transition from FR I to FR II happens gradually with luminosity (e.g., Singal & Rajpurohit 2012). The typical FR I/II transition luminosity increases with host galaxy mass (Ledlow & Owen 1996), which provides strong evidence that the Fanaroff-Riley classification separates jets based on their ability to drill through the gas in their environment: FR I jets are not powerful enough and get disrupted (see Kaiser & Best 2007, and references therein).

Contrary to radio emission from the compact core of the jet, which is subject to relativistic Doppler boosting, the observed lobe luminosity is independent of the jet inclination. Radio lobes can be used as calorimeters of jet power (Godfrey & Shabala 2013), which makes them useful to test theories of jet formation. For example, we recently used the correlation between the optical disk luminosity and lobe radio luminosity to constrain the importance of the Blandford & Znajek (1977) mechanism for powering quasar jets (van Velzen & Falcke 2013).

The observation that radio morphology and power are correlated was derived from images of the 3C survey (MacDonald et al. 1968; Mackay 1971). Since then, the number of identified FR II sources has grown with subsequent revisions and extensions of the 3C catalog (Laing et al. 1983; Blundell et al. 1999) and other radio surveys (e.g., Schoenmakers et al. 2001). Other methods of finding FR II quasars or radio galaxies include (targeted) radio observations of galaxy clusters (Owen et al. 1993; Croft et al. 2007; Antognini et al. 2012), and more recently, cross-matching of large area optical and radio surveys (Ivezić et al. 2002; Best et al. 2005b; de Vries et al. 2006; Kimball & Ivezić 2008; Hodge et al. 2009; Singal et al. 2013; Condon et al. 2013). Most of these authors used FIRST and the Sloan Digital Sky Survey (SDSS; York et al. 2000).

To identify a pair of astronomical sources with a projected separation of 100 kpc

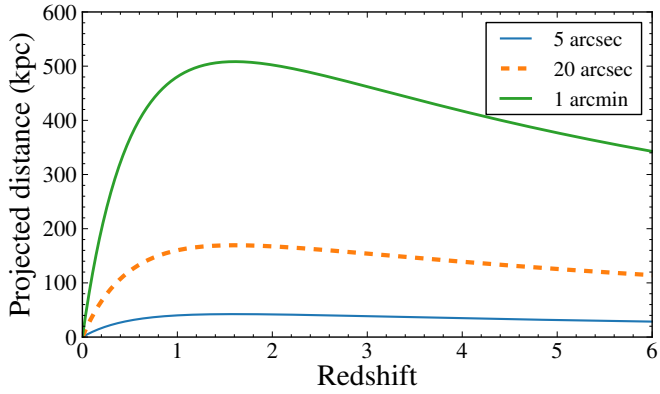

FIGURE 5.1: Physical separation for a fixed angular distance as a function of redshift. A survey with a resolution better than 5 arcsec can resolve sources with a projected separation > 50 kpc throughout the entire universe. In our search for double-lobed radio sources we used a maximum angular distance of 1 arcmin, corresponding to a maximum projected physical size of ≈ 500 kpc.

in a survey with a resolution of 1 arcmin, one is limited to $z < 0.1$. With a resolution of 10 arcsec, however, the pair can be resolved throughout the entire universe (Fig. 5.1). The FIRST survey covers $\sim 10^4$ deg^2 with a resolution of 5 arcsec FWHM to a limiting peak flux of 1 mJy. This combination of depth, large area, and high resolution implies that the images of the FIRST survey are fruitful fields to search for powerful jets at moderate to high redshift.

The difference between the existing FR II research, as summarized above, and the work presented here is that we shall not rely on information from other wavelengths for the construction of our FR II sample, instead we employ a simple, fully automated and purely morphological criterion to compile the largest possible FR II sample. We note that Kimball et al. (2011) have manually classified SDSS quasars that match to FIRST sources (finding 387 'Lobe' and 619 'Triple' sources), but this advanced classification is not available for the fast majority of FIRST sources that have no matching SDSS quasars. Proctor (2011) has applied a combination of human identification and supervised pattern recognition software to the FIRST images to provide morphological annotations, but this method was optimized for identifying different bent types (e.g., wide-angle tail) and does not provide a measurement of the flux of the core or the lobes (nor does it provide an estimate for the background due to chance associations).

Finally, we emphasize that in this work we focus on a subset of radio-loud quasars, namely those with large (> 100 kpc) radio lobes. This frees us from the controversy around the radio-loudness distribution, which has been claimed to be bi-modal

(Strittmatter et al. 1980; Kellermann et al. 1989; Falcke et al. 1996; Xu et al. 1999) or continuous (Condon et al. 1981; White et al. 2000; Ivezić et al. 2002; Singal et al. 2013). This discrepancy is mostly due to the treatment of radio emission on galaxy scales (< 10 kpc), which can be due to star formation (e.g., Condon et al. 2013), winds from the accretion disk (Stocke et al. 1992; Zakamska & Greene 2014), or compact/extended jets (e.g., Falcke et al. 1996). In this work we remove the emission on galactic scales, allowing us to measure only the jet-induced radio output.

5.1.2 Short guide to this chapter

We can summarize the method and the scientific aim of this work in one sentence: *obtain a large sample of FR II radio sources from the FIRST survey, study their properties, and reproduce their areal density by combining the bolometric quasar luminosity function with linear jet-disk coupling.*

Readers with very limited time can skip straight to Fig. 5.8, which displays the main result of this work. To obtain a good overview of the data selection, read Table 5.1. The summary of our method is given in Section 5.4.1.

Throughout this chapter, we work with the following cosmology, $h = 0.70$, $\Omega_m = 0.3$, $\Omega_\Lambda = 0.7$.

5.2 Source selection

In this section we first present the details of our FR II selection algorithm[1]. The method has a few parameters which need to be adjusted to the properties of the survey and the desired purity and completeness of the resulting candidate FR II sample. Here we discuss the optimal choice of these parameters in the context of the FIRST survey, but we stress that our algorithm can be applied to other radio catalogs as well. We used the 12FEB16 version of the FIRST catalog, containing 946,464 sources in 1.05×10^4 deg^2.

5.2.1 Automatic identification of double-lobed radio sources

An FR II radio source at $z \sim 1$ observed with 5 arcsec resolution will often simply appear as two point sources. They are readily spotted by eye, but given the large area of the FIRST survey and the even larger size of upcoming SKA surveys, we want to be able to identify them automatically. The essence of our approach is to simply search for pairs of sources. We need to account for two exceptions: (*i*) images of FR IIs at GHz frequencies can also contain unresolved emission from the compact core of the jet, and (*ii*) some lobes are resolved into separate components (i.e., multiple elliptical Gaussians are fitted to the observed brightness). The aim of our lobe-finding algorithm is to retrieve all cataloged components that are part of a

[1]The development of this algorithm was motivated by the large density of small doubles that appeared in the first wide-field, high-resolution LOFAR images at 150 MHz (Orrù et al., in prep).

double-lobed source and separate the two lobes from the core. We proceed in five steps:

1. Match all entries in the catalog to each other, with a maximum radius $d_{\max}$. For this computationally expensive step we use `k3match`, a very efficient coordinate matching algorithm (van Velzen et al. 2012; Schellart 2013). In the following steps we refer to the collection of all matches as a group.

2. Find the symmetry axis of the group by fitting a straight line to the coordinates of the sources, weighted by their flux.

3. Reject members of the group that are more than $d_{\rm rej}$ from the best-fit line and redo the fit for the symmetry axis.

4. Use the center of the line that describes the symmetry axis to define the center of the group. We thus assume that the origin of the twin jet system is near this geometrical center. The core flux is given by the sum of the flux of all group members within $d_{\rm core}$ of the center.

5. Project the (remaining) group members onto the symmetry axis. The sources that fall North of the center make the northern lobe and vice versa. The lobe-lobe separation (d) is given by the largest angular distance between the group members.

This FR II detection algorithm thus has three parameters, $d_{\max}$, $d_{\rm rej}$, and $d_{\rm core}$, we discuss these below.

The maximum separation of the two lobes ($d_{\max}$) needs to be smaller than the typical separation of single sources. Otherwise too many true FR IIs are rejected because the initial group contains an unrelated bright source which results in a wrong measurement of the symmetry axis, leading to rejection in step 3. Furthermore, a larger value of $d_{\max}$ implies a larger background of random matches between unrated sources (see Fig. 5.2). We found that for the FIRST survey, the background due to random matches starts to become important for $d > 1$' (Fig. 5.2). We therefore adopted $d_{\max} = 1'$. This cut implies we can identify lobes with a maximum separation of 500 kpc at $z = 1$ (Fig. 5.1).

Of the FIRST sources that pass our maximum distance criterion, 10% consisted of more than two Gaussian components and are thus processed further —steps 2 to 4— to reject unrelated sources and separate the core flux from the lobe flux. The maximum angular distance from the symmetry axis ($d_{\rm rej}$) needs to be larger than the resolution of the survey because extended lobes can be resolved into multiple Gaussian components. The angular distance that is used to identify the core emission ($d_{\rm core}$) should be similar to the resolution of the survey because the radio core is unresolved. We reject unrelated components using $d_{\rm rej} = 10$" and identified core emission using $d_{\rm core} = 5$". After applying these criteria we are left with 115,889 candidate FR IIs, the lobe flux and separation is plotted in Fig. 5.2 (left panel).

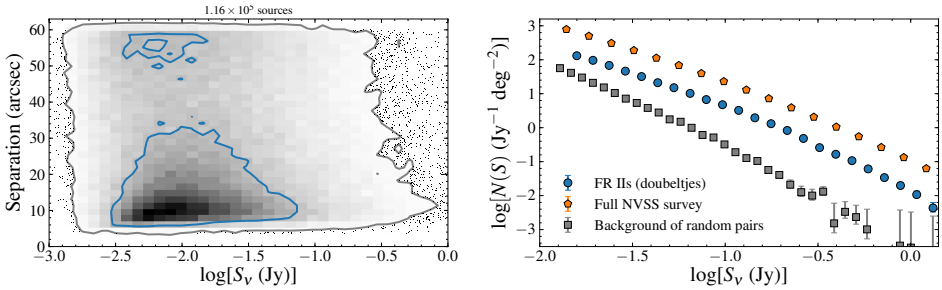

FIGURE 5.2: Left: 115,889 candidate FR II sources selected from the FIRST survey. We show the sum of the integrated flux of the lobes (S_ν) and their angular separation. Contour encompass 50% and 99% of the population. As the separation approaches 1 arcmin, the background of random matches starts to dominate over the population of true FR IIs. Right: the source count using 24,973 doubeltjes that remain after applying the quality cuts (Table 5.1). We also show the counts for a sample of random doubeltjes, obtained by applying the same selection criteria to a uniform distribution of source coordinates, and for the full catalog of the NVSS survey.

5.2.2 Flux limit and quality cuts

In the previous section we obtained a long list of double and triple radio sources. We now apply a series of quality criteria to this sample to obtain a well-defined, flux-limited sample of FR IIs.

The lower limit for the peak flux (F_p) of sources in the FIRST catalog is 1 mJy (White et al. 1997). Yet a turnover in the number counts as a function of integrated flux (F_i) can be seen at $F_i \approx 3$ mJy. This is due to extended sources that are not detected because their peak flux falls below the detection threshold. Double-lobed sources can also be missed because the flux of one of the lobes is below the flux limit. We thus obtain the following flux limit for the sum of the integrated flux of the two lobes:

$$S_{\nu,\mathrm{lim}} = 1 \text{ mJy} \times F_i/F_p(1 + f_{l/l}) \quad . \tag{5.1}$$

The median lobe-lobe flux ratio is unity and the median of F_i/F_p is 1.4 (see Fig. 5.3), yielding a typical flux limit of $S_{\nu,\mathrm{lim}} \approx 3$ mJy. Based on the distribution of F_i/F_p and $f_{l/l}$ we find that for $S_\nu > 11.9$, less than 1% of sources are missing because one of the lobes is not detected. We therefore adopt $S_{\nu,\mathrm{lim}} = 12$ as our flux limit. To suppress the background due to random matches we remove sources with extreme flux ratio's: $F_i/F_p > 5$ and $f_{l/l} > 10$.

Finally, we have to apply one more important quality cut. While the resolution of the FIRST surveys implies that double-lobed sources can be resolved for $d > 8$" (Fig. 5.2), we found that sources with a core require $d > 18$" (for lower separations the core and lobes start to blend). We wish to avoid a bias for FR IIs without a core and thus require a lower limit to the lobe-lobe separation of $d_{\mathrm{min}} = 18''$.

Cut	# left	Explanation
$d_{\max} = 1'$	115,889	Maximum angular separation of the lobes.
$S_\nu > 12$ mJy	59,192	Flux limit for a complete sample (applied to the sum of the integrated flux of the lobes).
$d_{\min} = 18$"	35,851	Minimum angular separation.
$f_{l/l} < 10$	30,021	Upper/lower limit on the ratio of the integrated flux of the two lobes.
$F_i/F_p < 5$	24,973	Integrated flux over the core flux (applied to each lobe).

TABLE 5.1: Cuts for a well-defined sample of FR II radio sources.

Applying all quality cuts (Table 5.1) and the flux limit leaves 24,973 FR II sources. We will sometimes refer to these as *doubeltjes*, as derived from the Dutch word for small double[2]. The areal density of the doubeltjes at $S_\nu > 12$ mJy is 2.4 deg^{-2}. In the right panel of Fig. 5.2 we show the areal density as a function of flux.

5.2.3 Correction for missing flux

The UV coverage that was used for the FIRST survey (VLA B-configuration) implies that some of the extended lobe flux will be "resolved out" (i.e., the radio interferometer acts as a high-pass filter). We compared the flux of our doubeltjes to the flux measured from the lower resolution images of NVSS (NRAO VLA Sky Survey; Condon et al. 1998, obtained with VLA D- and DnC-configurations). Since we selected relatively compact sources, the median flux difference between the NVSS flux and the FIRST flux is only 0.05 dex. We measured this flux ratio as a function of the FIRST flux of the lobes and found $S_{\nu,\mathrm{corrected}} = 0.983\, S_\nu^{0.951}$ (with S_ν in Jy). Hereafter we use the lobe flux that is corrected for missing flux using this function.

5.2.4 Background subtraction

The last step before we can analyze our sample of doubeltjes is to estimate and subtract the background of random, unrelated matches. To this end we generate a homogeneous source distribution with fluxes drawn from the FIRST catalog and repeat our lobe-finding algorithm (Sec. 5.2.1) and apply our quality cuts (Sec. 5.2.2). Because sources with high flux are rare, the fractional contribution of the background is very small for $S_\nu > 100$ mJy (see Fig. 5.2). The areal density of background matches for $S_\nu > 12$ mJy is 0.5 deg^{-2}. Our method of identifying random pairs slightly underestimates the true background since the sources are clustered. By counting how many SDSS quasars that match to a single FIRST source (see below) are identified as doubles by our algorithm we obtain an upper limit to the mean background of 4%.

[2]The first high-resolution images of LOFAR showed that the low-frequency radio sky is teeming with small doubles. We called them doubeltjes to emphasizes the difference with 'Classic Doubles', which usually refers to well-resolved lobes with a separation of several arcminutes.

After correcting for random matches, we find that, about 20% of NVSS sources with $S_\nu \sim 10^2$ mJy are identified as doubeltjes. In the interval $S_\nu = [10, 100]$ mJy, the background-corrected fraction of NVSS sources that are doubeltjes increases with increasing flux.

5.2.5 Comparison to the CONFIG sample

The Combined NVSS-FIRST Galaxies (CoNFIG; Gendre & Wall 2008; Gendre et al. 2010) sample is constructed by manual classification of subsets of NVSS sources. The most relevant subset for this work is the so-called CONFIG-4 sample which is complete to $S_\nu = 50$ mJy and covers 64 deg^2. This sample contains 92 identified FR IIs. Of these manually identified doubles, 90% are retrieved by our lobe-finding algorithm. Of the nine sources that we miss, six have $d > 1$' and three have $d < 10$". As explained in Section 5.2.2 we applied a cut on the minimum lobe-lobe separation ($d_{\rm min} = 18$") to avoid a selection bias for FR IIs without a core. If we apply our quality cuts to the CONFIG-4 sample, we recover 100% of their manually identified FR II sources.

5.3 Redshift-independent properties of $\sim 10^4$ FR IIs

In the previous section we obtained a well-defined sample of radio sources with an FR II morphology by collecting pairs with similar flux. In Fig. 5.3 we present the basic properties of these doubeltjes: the flux ratio of the lobes, compactness ratio of both lobes, the core-to-lobe ratio, and the 1400-325 MHz spectral index.

To measure the spectral index we used radio sources of the Westerbork Northern Sky Survey (WENSS, Rengelink et al. 1997) that are within 20" of the center of our FR IIs. The images of WENSS have a resolution of 54" $\times$ 54"/ sin(dec) FWHM, thus all of the FR IIs in our sample are matched to a single WENSS source. This implies that the derived spectral index of sources with a detected core is slightly too steep (because the WENSS flux contains both the lobes and the core). The median spectral index of all sources is $\alpha = -0.85$; if we restrict to sources without a detected core, we find $\alpha = -0.82$. We also computed the spectral index using data from NVSS, which has a resolution similar to WENSS, finding a median spectral index of $\alpha = -0.81$. When we compute the spectral index using 74 MHz data from the VLA Low-frequency Sky Survey Redux (VLSSr; Lane et al. 2014) we find $\alpha = -0.85$.

5.3.1 $\sim 10^2$ FR IIs matched to quasars

The next step is to match our sample of double-lobed radio sources to known quasars. The sample of spectroscopically identified quasars from SDSS (Richards et al. 2002; Schneider et al. 2007) is most suited for this task since, by design, the sky coverage of FIRST almost fully overlaps with the SDSS footprint.

We use the Seventh Data Release (DR7; Abazajian et al. 2009) edition of the SDSS quasar catalog (Schneider et al. 2010), consisting of 105,783 quasars with $M_i < -22$.

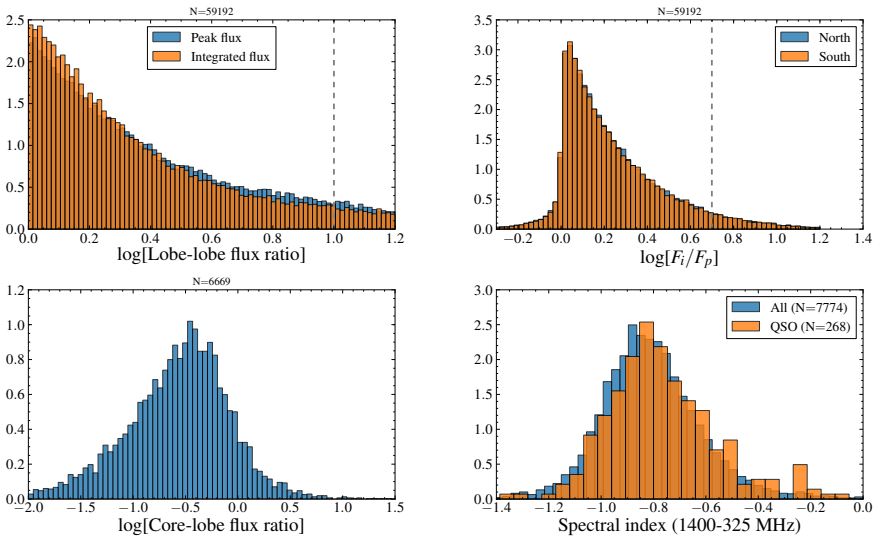

FIGURE 5.3: Top left: The flux ratio of the two lobes. Top right: the ratio of the integrated flux to the peak flux (for each lobe). Formally, this ratio has to be greater or equal to unity, but for faint sources the FIRST detection algorithm can yield a peak flux that is higher than the integrated flux. Bottom left: the core flux over the sum of the flux of both lobes (we show only the sources with a detected core). Bottom right: the spectral index using the WENSS (325 MHz) and NVSS (1.4 GHz) flux. For the first three plots we show the doubeltjes sample before applying the quality cuts (Table 5.1), otherwise these histograms would be truncated at the dashed line. For the bottom right panel, we show the sample after the quality cuts have been applied. All histograms are normalized (i.e., the integral over the binned parameter is equal to one).

We also included the 87,810 quasars from DR9, the Baryon Oscillation Spectroscopic Survey (BOSS; Dawson et al. 2013) quasar catalog (Ross et al. 2012; Pâris et al. 2012), which probes deeper than DR9 and includes more quasars at $z > 2$. The majority of the SDSS quasars were selected for spectroscopic follow-up based on their optical colors, but information from other wavelengths was also used. We selected only SDSS DR7 quasars that were targeted based on their optical properties, leaving 77,319 sources. For the BOSS quasars we restricted the sample using the `UNIFORM>0` requirement, leaving 42,433 objects. For the DR7 quasars that have been re-observed by BOSS, we used the latest redshift determination (i.e., `Z_VI` from the BOSS catalog). Our final combined SDSS/BOSS quasar sample consists of 11,7174 unique sources. Since BOSS is part of SDSS-III (Eisenstein et al. 2011), we hereafter refer to this sample simply as the SDSS quasar sample.

At the 5" resolution of the FIRST survey, most quasars are unresolved, double-lobed morphologies are rare (de Vries et al. 2006; Kimball et al. 2011). To demonstrate

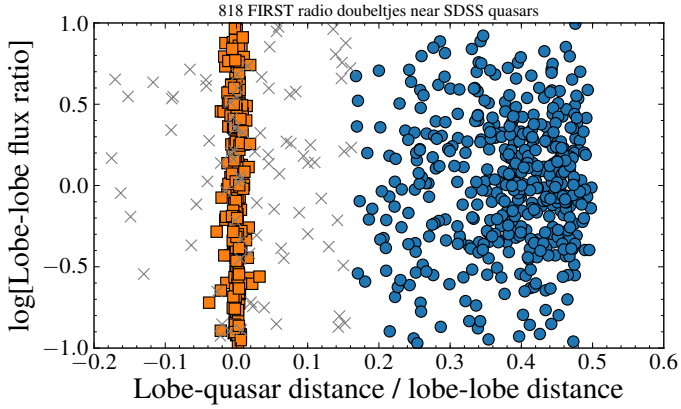

FIGURE 5.4: The distance between the quasar and the lobe (Eq. 5.2), divided by the lobe-lobe separation, versus the lobe-lobe flux ratio. A negative distance implies that the quasar is found outside the lobes. Our sample of FR II quasars (Eq. 5.3) is labeled with blue circles. We see a clear overdensity of quasars near the center of the lobes. Radio sources with a lobe-quasar distance less than 1" are labeled with orange squares. These are radio quasars that have been misidentified as doubles due to a nearby, but unrelated radio source. These misidentifications occur for 4% of all quasars that are matched within 1" of a single FIRST source.

this, we first match our quasar catalog to the centers of our FR IIs using a match radius of 30" (half of the maximum lobe-lobe separation). Since the center of the FR II is simply given by the geometrical center of the two lobes, the quasar-lobe separation can be written as

$$D_{\mathrm{quasar-lobe}} = d/2 - s \tag{5.2}$$

with d the lobe-lobe distance and s the separation between the quasar and the FR II center. When $D_{\mathrm{quasar-lobe}} < 0$, the quasar is located outside the circle that connects the two lobes. In Fig. 5.4 we show $D_{\mathrm{quasar-lobe}}$ normalized by the lobe-lobe separation. We find that some quasars which are radio point sources are misidentified as FR IIs by our algorithm. Of the 5863 FIRST sources that are within 1" of a SDSS quasar, 4% have $D_{\mathrm{quasar-lobe}} < 1$". This confirms that the background due to matches between unrelated FIRST sources is low (Sec. 5.2.4).

Based on the observed distribution of lobe-quasar distances (Fig. 5.4), we adopt the following criterion to define the FR II quasar sample

$$s < d/3 \quad . \tag{5.3}$$

This requirement yields 459 double-lobed radio quasars.

If we shuffle the Declination of the SDSS quasars we find on average 9.9 matches,

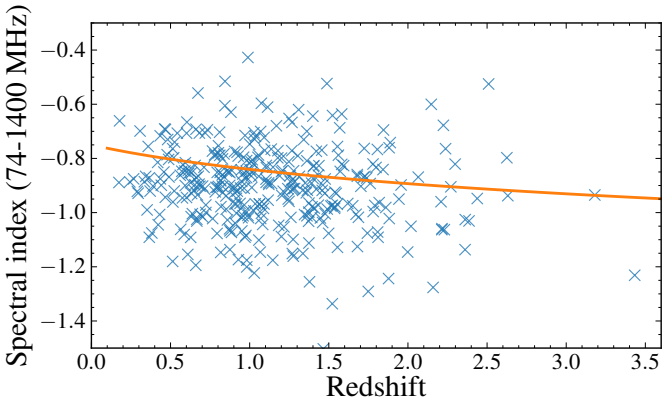

FIGURE 5.5: Redshift and spectral index for the FR II quasars that are detected in VLSSr. The curve shows the relation found by Ker et al. (2012) using a dataset that is independent from ours.

so the probability of a chance association of a quasar with a radio source pair using Eq. 5.3 is 2.2%. When we make no quality cuts to the doubeltjes sample and we use all SDSS quasars, the number of matches is 1109, with an average of 1.7% random associations.

The median projected separation of the lobes of the SDSS quasars is 261 kpc; the largest and smallest separation is 55 kpc and 497 kpc, respectively. The highest redshift of the FR II quasars is 3.4 and the median redshift is 1.06 (for the parent sample of quasars the maximum and median redshift are 5.46 and 1.83, respectively). Using the virial mass estimates of Shen et al. (2011), which are available for all SDSS quasars from DR7, we find a median black hole mass of $10^{9.2}\,M_{\odot}$ for the FR II quasars (for a recent study of the radio-loud fraction of SDSS quasars as a function of black hole mass, see Kratzer & Richards 2014). We find a weak correlation between redshift and the spectral index measured between 74 MHz and 1.4 GHz, $\alpha \propto (-0.11 \pm 0.04) \times \log[1+z]$ (Fig. 5.5).

To study the properties of the SDSS FR II quasars it will prove valuable to have a second quasar sample selected at different wavelength. We therefore applied the elegant color selection proposed by Stern et al. (2012), $W2 > 15$ and $W1 - W2 > 0.8$ (Vega magnitudes), to data from the Wide-field Infrared Survey Explorer (WISE; Wright et al. 2010) All-Sky Release. This mid-IR requirement selects powerful AGN with high purity ($\approx 90\%$). We find 1546 WISE quasars at the centers of our FR IIs (Eq. 5.3). Thanks to the lower optical depth at IR frequencies, the WISE sample contains more obscured AGN compared to optical/UV selection (e.g., Lusso et al. 2013), but not all radio-selected AGN are retrieved (Gürkan et al. 2014).

Recalling that the main aim of this work is to test if the areal density of radio pairs can be obtained from the quasar luminosity function, the following two sections

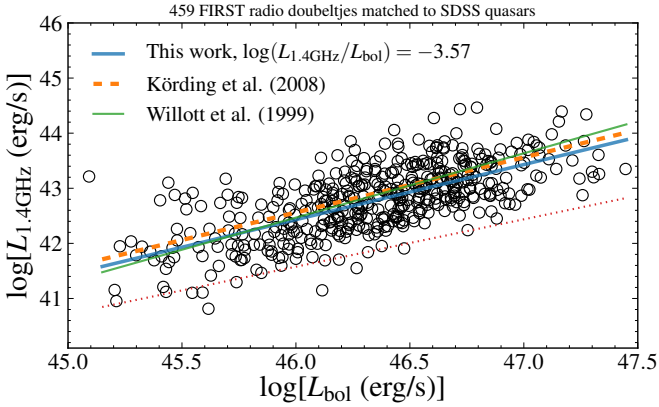

FIGURE 5.6: We observe a linear correlation between the radio luminosity of the lobes (νL_ν at 1.4 GHz in the rest-frame) and the bolometric quasar luminosity (obtained from the i-band magnitude). The scatter of $L_{1.4\mathrm{GHz}}/L_{\mathrm{bol}}$ is 0.47 dex (rms). Our normalization is consistent with the results of Körding et al. (2008b), who matched SDSS quasars to point sources at 74 MHz. Furthermore, the well-known minimum-energy relation between jet power (Q_j) and lobe radio luminosity (Willott et al. 1999) combined with standard jet-disk coupling ($Q_j/L_{\mathrm{bol}} = 0.2$) is also consistent with our observations. The red dotted line show the correlation that would be obtained if all quasars clustered at the flux limit of the radio survey.

focus on two properties of the FR II quasars that are needed to reach this goal: the efficiency factor for turning accretion power into lobe radio luminosity and the fraction of quasars that are found in our FR II sample.

5.3.1.1 Optical-radio correlation

A linear coupling between the power of the accretion disk (L_{bol}) and the power of the jet (Q_j) has been observed using radio emission from the compact jet core (Falcke & Biermann 1995) and the extended lobes (Rawlings & Saunders 1991). Willott et al. (1999) used the 3CRR and 7C radio samples to measure a correlation between the 151 MHz luminosity and the [OII] line luminosity of the central source. The two radio samples span over a decade in flux, and thus it was incontrovertibly shown that the disk luminosity predominantly correlates with radio luminosity, not redshift (Willott et al. 1999).

In this work, we use the i-band luminosity of the quasars as a proxy for disk power. The luminosity- and frequency-dependent bolometric correction of Hopkins, Richards, & Hernquist (2007) is used to convert the rest-frame optical luminosity of the quasars to their bolometric luminosity. The K-correction for the rest-frame radio luminosity is obtained using the mean spectral index of our sample ($\alpha = -0.85$). As expected based on the previous work summarized above, we find a linear relation

between disk and lobe luminosity (Fig. 5.6). The normalization is:

$$\epsilon_r \equiv \log L_{1.4\mathrm{GHz}}/L_{\mathrm{bol}} = -3.57 \pm 0.47 \quad . \tag{5.4}$$

This linear correlation is not induced by the finite flux limit of the surveys that we used. First of all, we observe a significant flux-flux correlation: the p-value of the Spearman rank correlation coefficient between the i-band flux and the 1.4 GHz flux is 10^{-15} (a Kentall's tau analysis yields the same significance level). Furthermore, the Spearman partial rank correlation (e.g., Macklin 1982) was used to check the significance of the L_{bol}-$L_{1.4\mathrm{GHz}}$ correlation, in the presence of the z-L_{bol} correlation. We found $p = 10^{-12}$ for this partial correlation analysis, confirming once more that the disk-lobe correlation is not is not induced by an underlying correlation between redshift and luminosity.

The depth of the FIRST data allows us to measure outliers to the disk-lobe correlation of about 1 dex (Fig. 5.6). Indeed the median flux of the radio-selected FR IIs is 26 mJy, while the median flux of the FR II quasars is 80 mJy. As shown in van Velzen & Falcke (2013) the residuals to the disk-lobe correlation follow a Gaussian distribution and are dominated by environmental effects (i.e., the conversion of jet power to radio luminosity) rather than internal processes (i.e., fluctuating jet power at a fixed accretion rate). We stress once more that the observed correlation presented here applies only to double-lobed radio sources and is therefore not incompatible with the much broader radio-loudness distribution of SDSS quasars and single FIRST sources (e.g., Singal et al. 2013).

Our measurement of ϵ_r is consistent with minimal energy arguments for synchrotron emission as presented in Willott et al. (1999), $Q_j \propto L_{1.4\mathrm{GHZ}}^{6/7} f^{3/2}$. For a fudge factor that is typical for FR II sources, $f = 10$ (Blundell & Rawlings 2000; Godfrey & Shabala 2013), our observations imply that about 20% of the bolometric quasar luminosity ends up in the jet, $q_j \approx 0.2$. The empirical correlation between 74 MHz luminosity and L_{bol}, as measured by Körding et al. (2008b) using the DR5 version of the SDSS quasar catalog and sources from VLSS (Cohen et al. 2007), is in excellent agreement with our result (Fig. 5.6).

5.3.1.2 FR II fraction

The last property that we need to investigate is the fraction of quasars that are identified by our lobe-finding algorithm (Sec. 5.2.1) and pass the quality cuts (Sec. 5.2.2). This FR II fraction (f_{FRII}) is the product of our selection efficiency and the true fraction of quasars with double lobes.

To compute f_{FRII}, we first restrict to the quasars that are inside the FIRST footprint. We also have to account for quasars that are not contained in our sample because their radio flux falls below our radio flux limit ($S_\nu = 12$ mJy). Using the observed distribution of the optical-to-radio efficiency and the quasar redshift, we generate a hypothetical lobe luminosity for each quasar. We then remove the quasars

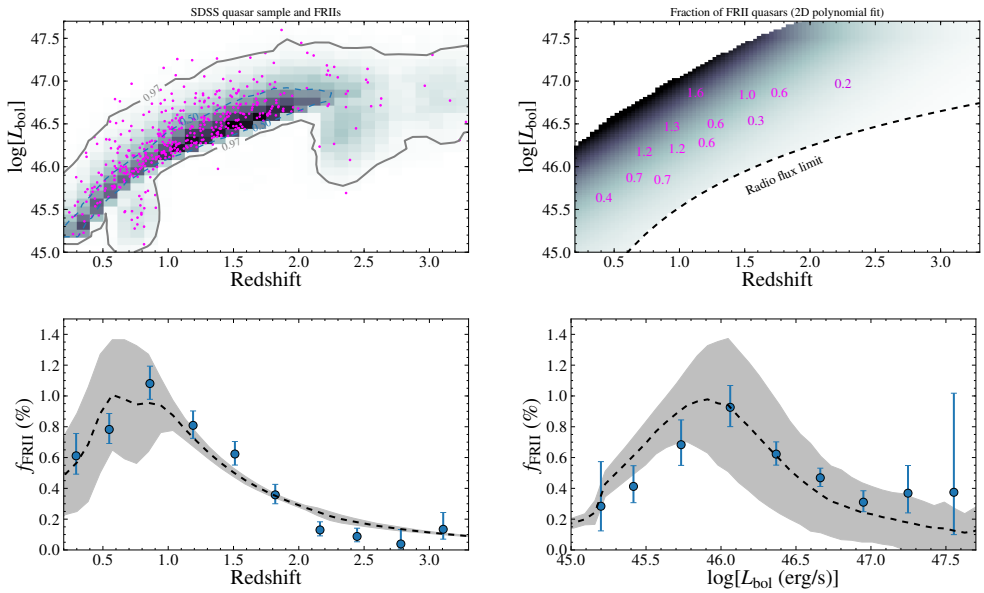

FIGURE 5.7: Different representations of the fraction of SDSS quasars that are identified as FR IIs (Sec. 5.2.2). We compute this fraction using only quasars with an estimated radio flux (from the optical-radio correlation, Fig. 5.6) that is above our radio flux limit. Top left: the distribution of the redshift and bolometric luminosity of our quasar sample (grayscale) and detected FR IIs (magenta dots). We see that the radio-loud quasars are clearly distributed differently than the parent population. Top right: we binned the detected FR II quasars in luminosity and redshift, using variable width bins that contain at least 30 sources. For each bin, we compute $f_{\rm FRII}$ (percentages are shown by the magenta numbers). The grayscale shows the result of a 2-dimensional spline fit to guide the eye. We see evolution of $f_{\rm FRII}$ with both redshift (horizontal direction) and bolometric luminosity (vertical direction). The bottom two panels show the result projected onto the redshift axis (left) and luminosity axis (right), and our analytical expression for $f_{\rm FRII}$ (Eq. 5.5); the gray area shows the rms of this prediction (due to binning over luminosity/redshift).

with a simulated lobe flux that is below our flux limit. This requirement removes 30% of the quasars in the parent sample; the majority of the quasars with an estimated radio flux below our threshold are at $z > 2$. In the parent population of quasars with a radio flux that should be high enough to be detectable, only 0.57% are detected, $\langle f_{\rm FRII} \rangle = 5.7 \times 10^{-3}$. In the upper panel of Fig. 5.7 we compare the luminosity and redshift of FR II quasars to the parent population. We see that the FR II quasars are typically found at higher luminosity and lower redshift than normal quasars.

The increase of $f_{\rm FRII}$ from low redshift to $z = 1$ is partly due to a simple geometrical effect: at low redshift the angular separation of the lobes is larger than our upper limit of 1'. The number of FR IIs that have been missed for this reason can be

computed directly from the observed distribution of physical lobe-lobe separations. At $z = 0.3$, the fraction of missing sources is 50%, while at $z = 0.6$ this is fraction is only 15%.

The fraction of quasars that are identified as doubeltjes by our algorithm can be described with the following expression:

$$\log\left[\frac{f_{\rm FRII}}{1-f_{\rm FRII}}\right] = G(z) + c_0 + c_z \log[(1+z)/2] + \log\left[1-\exp(-L/L_{\rm I/II})\right] \quad . \tag{5.5}$$

Here $G(z)$ is the geometrical factor that accounts for missing sources due to large angular separations at low redshift. The normalization of $f_{\rm FRII}$ at $z = 1$ is given by c_0, while c_z describes the redshift evolution.

We model the luminosity-dependence of $f_{\rm FRII}$ with a single break, $\exp(-L/L_{\rm I/II})$. This break is needed to account for the luminosity-dependent FR I/II transition. At $z < 0.5$ this transition is observed in the range $L_{\rm bol} = 10^{43.7-46.2}\,{\rm erg\,s^{-1}}$ (Ledlow & Owen 1996). Unfortunately, the dynamic range of the SDSS quasar catalog is not sufficient to directly determine this break from the full sample: very few quasars with $L_{\rm bol} < 10^{46}\,{\rm erg\,s^{-1}}$ are found for $z > 1$ (Fig. 5.7, top left panel). We therefore restrict to $0.6 < z < 0.9$, a small redshift window with the highest dynamical range containing 93 FR II quasars. Using an unbinned maximum likelihood method we find $L_{\rm I/II} = 45.9$. Taking into account the degeneracy with redshift evolution (c_z in Eq. 5.5), the 68% confidence interval of $L_{\rm I/II}$ is [45.7, 46.2]. We shall adopt $L_{\rm I/II} = 46$ as our fiducial choice, but we will also compute how the uncertainty on the location of the break influences our results. For the remaining two parameters that describe $f_{\rm FRII}(z, L)$ we find $\log c_0 = -1.96 \pm 0.02$, $c_z = -3.1 \pm 0.2$.

When we repeat the measurement of the FR II fraction using only sources with a triple morphology, we find $\log c_0 = -2.22 \pm 0.03$, $c_z = -3.2 \pm 0.3$ (again for $L_{\rm I/II} = 46$). For this subclass of FR IIs, the observed disk-to-lobe efficiency is $\epsilon_r = -3.72 \pm 0.42$.

5.4 Predicting the FR II density

In the previous sections we obtained a well-defined sample of 10^4 double-lobed radio sources and, using a subset of these doubeltjes, we measured a linear correlation between the rest-frame radio luminosity and the bolometric disk power. We shall now try to reproduce the areal density of the double-lobed radio sources under the assumption that all of these lobes are created by jets from quasars that follow the observed disk-lobe correlation (Fig. 5.6).

We start by converting lobe flux (S_ν) to 1.4 GHz rest-frame luminosity,

$$L_{\rm 1.4GHz}(z) = 4\pi d_L^2 S_\nu (1+z)^{-1-\alpha} \quad . \tag{5.6}$$

Here d_L is the luminosity distance. We model the radio spectral energy distribution using the observed mean spectral index between 1.4 GHz and 325 MHz ($\alpha = -0.85$) to make the K-correction. Next, we convert this radio luminosity to the bolometric luminosity of the quasar,

$$L_{\rm bol}(S_\nu, z) = \frac{4\pi d_L^2 S_\nu (1+z)^{-1-\alpha} 1.4 \text{ GHz}}{\epsilon_r} \quad , \tag{5.7}$$

using the disk-to-lobe efficiency as measured using our sample of 459 FR II quasars (Fig. 5.6).

Since the environment that is probed by the jet can vary from galaxy to galaxy, two jets with identical kinetic power may not yield lobes with equal radio luminosity (e.g., Hardcastle & Krause 2013). When the number density decreases with luminosity, this intrinsic scatter of the bolometric-to-radio efficiency (ϵ_r, Eq. 5.4) will lead to an overall increase of the predicted number of sources. The intrinsic scatter of the bolometric-to-radio conversion, $\sigma(\epsilon_r)$, is unknown, but can be constrained to a relatively narrow range. Since the fluctuations in environment as probed by the two jets from a single black hole are at least as large as the fluctuations in environment between black holes, a lower limit for $\sigma(\epsilon_r)$ follows from the observed lobe-lobe flux ratio of the FR II quasars, $\sigma(\epsilon_r) > 0.30$. An upper limit for $\sigma(\epsilon_r)$ follows from the observed rms scatter in the optical-radio correlation, minus the observational uncertainty. The latter is dominated by the dispersion of the bolometric correction, which is estimated to be 0.15 dex for our optical quasar sample (Hopkins et al. 2007). We thus obtain $\sigma(\epsilon_r) \leq (0.47^2 - 0.15^2)^{1/2} = 0.45$.

The final ingredient that is required to predict the number of FR IIs per square degree is the accretion density, i.e., the disk power per unit volume that is available to create jets. We will use the bolometric quasar luminosity function as determined by Hopkins, Richards, & Hernquist (2007). These authors combined 28 different quasar samples from optical (both broadband and emission lines), soft and hard X-ray, and near- and mid-IR bands in the redshift interval $z = [0, 6.5]$. From this wealth of data one can obtain a luminosity-dependent quasar spectral energy distribution (SED) and a distribution of column densities, which allows the datasets from different wavelengths to be fitted to a single luminosity function. The best fit is obtained for a broken power-law:

$$\phi(L) = \frac{dN}{d\log L} = \frac{\phi_*}{(L/L_*)^{\gamma_1} + (L/L_*)^{\gamma_2}} \quad , \tag{5.8}$$

All four parameters of this power-law can vary with redshift, $\phi_*(z)$, $L_*(z)$, $\gamma_1(z)$, $\gamma_2(z)$. The luminosity density peaks at $z \approx 2$, where $j_{\rm bol} \sim 10^8\, L_\odot\, {\rm Mpc}^{-3}$ (Hopkins et al. 2007).

To find the total number of FR IIs on the sky, we simply integrate the quasar

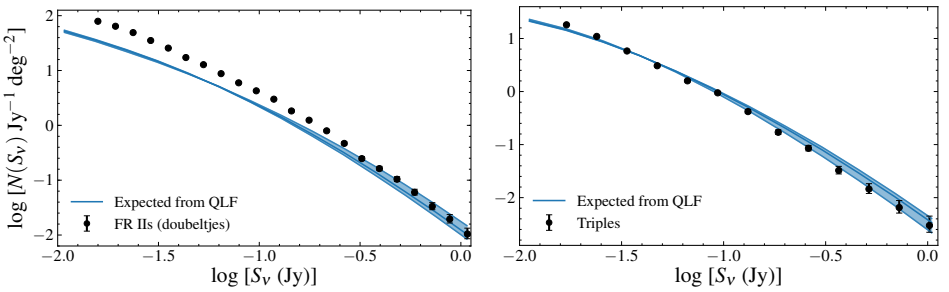

FIGURE 5.8: The observed distribution of FR II radio sources at 1.4 GHz and the predicted number using the quasar luminosity function (QLF), for our fiducial model (Sec. 5.4.1). The line thickness indicates the uncertainty due to the unknown scatter in the bolometric-to-radio efficiency. In the left panel we show all FR IIs, while in the right panel we show the result using only sources with a triple morphology (i.e., sources with radio emission from the geometrical center of the lobes).

luminosity function over the co-moving distance $d_C(z)$. We first give the analytic expression that is valid only for $\sigma(\epsilon_r) = 0$:

$$N(> S_\nu) = 4\pi D_H \int_0^6 dz \, \frac{d_C^2}{E(z)} \times \int d(\log L) \, f_{\rm FRII}(z, L) \phi(z, L) \quad , \tag{5.9}$$

with $E(z) = \sqrt{\Omega_M (1+z)^3 + \Omega_\Lambda}$ and D_H the Hubble distance (e.g., Hogg 1999). For the upper limit of the integration over quasar luminosity we use the most luminous SDSS quasar observed within that redshift (note that the steep bright-end slope of the luminosity function, $\gamma_2 \approx 2$, implies that the final predicted density is almost independent of this upper limit). To take into account the scatter of the bolometric-to-radio conversion, we replace the integration over the quasar luminosity by a Monte Carlo simulation. At each redshift, we generate a sample of quasars with a bolometric luminosity drawn from the luminosity function for that redshift. We then assign a 1.4 GHz lobe luminosity (Eq. 5.7) to each quasar using a normal distribution centered at $\log[L_{\rm bol}] - \epsilon_r$. We confirm that for $\sigma(\epsilon_r) = 0$, this Monte Carlo method yields the same result as the numerical integration (Eq. 5.9).

5.4.1 Summary

In summary, we derived a model that predicts the FR II density on the radio sky by using the luminosity function of quasars and a linear relation between the accretion disk and lobe radio luminosity. This approach requires four parameters, all of these parameters are well-constrained by observations:

- $\phi(z, L)$: the quasar bolometric luminosity function (Hopkins et al. 2007), determined for $0 < z < 6$ by combining a large number of quasars from (rest-frame) infrared (8–15μm), optical ($\approx$ 1500Å), soft X-ray (0.5–2 keV), hard X-ray (2–20 keV), and emission line observations (Hα, [O II], [O III]).

- $f_{\rm FRII}(z, L)$: the fraction of quasars that we identify as double-lobed radio sources. This parameter is a function of disk luminosity and redshift. It is the product of the true radio-loud fraction and our selection efficiency. We determined this parameter using 2×10^5 quasars from SDSS (DR7 and DR9) as test cases. For our fiducial model, we use an analytical expression for $f_{\rm FRII}$ (Eq. 5.5), but we will also present the results obtained using a non-parametric approach (see Fig. 5.9).

- $\epsilon_r \equiv \log[L_{1.4\ \rm GHz}/L_{\rm bol}] = -3.57$: the conversion from disk luminosity to the luminosity of the radio lobes at 1.4 GHz (rest-frame). This linear relation was obtained using 459 FR II SDSS quasars (Fig. 5.6) and is in good agreement with earlier work (Rawlings & Saunders 1991; Falcke et al. 1995b; Serjeant et al. 1998; Willott et al. 1999; Körding et al. 2008b; Buttiglione et al. 2009; Antognini et al. 2012).

- $\sigma(\epsilon_r)$: the intrinsic scatter in ϵ_r, i.e., the spread of lobe radio luminosity for jets launched by black holes with identical bolometric disk luminosity. We can constrain this parameter to $\sigma(\epsilon_r) = [0.30, 0.45]$, as given by the observed lobe-lobe flux ratio and the observed rms of ϵ_r. For our fiducial model we adopt $\sigma_r = 0.35$.

In Fig. 5.8 we show the result for the fiducial model. The predicted FR II density is most accurate in range of radio flux that is well-covered by the SDSS quasars: 30 mJy to 400 mJy. At the median radio luminosity of the FR II quasars, 80 mJy, we observe an excess of $N_{\rm data}/N_{\rm QLF} = 1.76$. For the radio sources with a triple morphology, the prediction is within 10% of the observed density ($N_{\rm data,triples}/N_{QLF} = 0.9$). Before discussing this result in Section 5.6, we consider sources of systematic uncertainty below.

5.4.2 Systematic uncertainty

Below we discuss sources of systematic uncertainty of our model for the FR II density. The results are summarized in Fig. 5.9. At the median radio flux of the FR II quasars (80 mJy), we find that the systematic uncertainty is 10%. For lower fluxes, however, the different models start to diverge and our prediction is less robust.

5.4.2.1 Luminosity and redshift evolution

The fraction of quasars that are identified as FR II radio sources by our method ($f_{\rm FRII}$) is observed to evolve with redshift and luminosity (Fig. 5.7). For the fiducial model this evolution is parametrized by Eq. 5.5 with $L_{\rm I/II} = 10^{46}\,{\rm erg\,s^{-1}}$. We first

investigate how the results changes for other break luminosities that are allowed by the data, $L_{\rm I/II} = 10^{46.2}\,{\rm erg\,s^{-1}}$ and $L_{\rm I/II} = 10^{45.7}\,{\rm erg\,s^{-1}}$. As shown in the left panel of Fig. 5.9, a change in $L_{\rm I/II}$ is only important at low radio flux (at higher flux, the bolometric luminosity of most of the FR IIs is well above the break). At 80 mJy, $N_{\rm data}/N_{\rm QLF} = [1.86, 1.76, 1.62]$ for $\log L_{\rm I/II} = [46.2, 46, 45.7]$, respectively.

We also considered evolution of the break luminosity with redshift: $L_{\rm I/II}(z) \propto (1+z)^{c_L}$. Our fit for $f_{\rm FRII}$ with this extra free parameter yields $c_0 = -1.82 \pm 0.02$, $c_z = -4.0 \pm 0.2$, and $c_L = 2.3 \pm 0.5$. The resulting predicted density at 80 mJy is 3% lower.

To investigate the effect of redshift evolution we first repeat the calculation using an FR II fraction that depends only on luminosity. Even though this description of the FR II fraction is clearly inaccurate (see Fig. 5.7), the resulting density at 80 mJy is only 3% higher than the fiducial model. As expected, this model diverges at lower and higher fluxes (Fig. 5.9, right panel). We also considered a different functional form to describe the fraction of FR II quasars:

$$\log f_{\rm FRII} = c_{0'} + c_{L'}(\log L_{\rm bol} - 46) + c_{z'} \log[(1+z)/2] \quad , \tag{5.10}$$

with $c_{0'} = -2.33 \pm 0.02$, $c_{L'} = 0.77 \pm 0.03$, $c_{z'} = -4.4 \pm 0.2$. For this function we find a predicted density that is 13% lower than the fiducial model. We also repeated the calculation for the predicted FR II density using an evolving spectral index as measured by Ker et al. (2012), $\alpha(z) = -0.30 \log[1+z] - 0.75$. This curved spectrum slightly reduces the detectability of high-redshift FR IIs, but yields no significant difference on the predicted density ($N_{\rm data}/N_{\rm QLF} = 1.72$).

Finally, we consider a non-parametric description for the fraction of quasars that are detected as FR IIs. We binned the 459 FR II quasars in redshift and luminosity, using 19 or 20 sources per bin, to create a "2D lookup table". Using linear interpretation we extract $f_{\rm FRII}(z, L_{\rm bol})$ from this dataset. To be able to extrapolate outside the range of the table, we set $f_{\rm FRII}$ to zero at $z = 4$ and $L_{\rm bol} = 10^{45}\,{\rm erg\,s^{-1}}$. Using this approach, we find $N_{\rm data}/N_{\rm QLF} = 1.67$, which is 5% lower than our fiducial model. Since the linear extrapolation over-estimates the number of low-luminosity FR IIs at $z \sim 1$, we should treat the density predicted by the lookup table as an upper limit.

5.4.2.2 Parametrization of the quasar luminosity function

To estimate the uncertainty due to the adopted parametrization of the quasar luminosity function, we repeat the prediction using "pure luminosity evolution" (PLE) for the quasar number density, i.e., a double power-law with evolving normalization (ϕ_*) but no change in the faint or bright end slopes. This functional form of the luminosity function is a worse description of the observed number density, $\Delta\chi^2 = 1924 - 1007 = 917$, with $511 - 508 = 3$ degrees of freedom (Hopkins et al. 2007). The resulting change to our fiducial model is an 8% increase to the predicted number of radio sources (see Fig. 5.9). When we use the luminosity function that

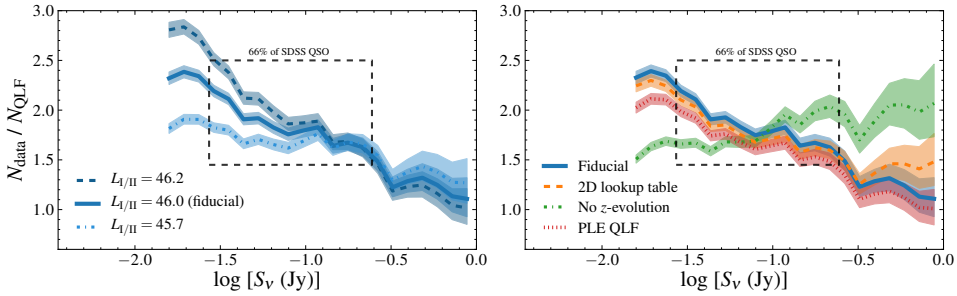

FIGURE 5.9: Left: Difference between the number of observed FR II radio sources and the predicted number from the quasar luminosity function. We show the result for the allowed range of $L_{\rm I/II}$ (see Eq. 5.5). Right: The difference between the model and the data for fiducial model and three slightly less sophisticated methods (Sec. 5.4.2). The factor two difference between the prediction and the data is robust with the range of radio fluxes covered by our 459 FR II quasars (indicated by the dashed lines). The shaded regions indicated the 1-σ confidence interval for Poisson statistics of the detected number of sources.

Hopkins et al. (2007) obtain after adding a scatter of 0.05 dex to the error estimates of each quasar sample, which reflects the variance in the sample-to-sample normalization (and thus underweights the most well-constrained samples), we obtain a predicted FR II density that is 10% higher.

5.4.2.3 Sample incompleteness

Our FR II sample is not complete: we miss small ($d < 18$") and large FR IIs ($d > 1'$), corresponding to a projected size of 150–500 kpc at $z = 1$. This incompleteness does not limit our conclusions because we measure the *fraction* of quasars that are identified by our radio-based selection method. To demonstrate the robustness of this approach, we artificially reduced our sample of doubeltjes by a factor 2 by removing a random subset. For this smaller sample we obtain $N_{\rm data}/N_{\rm QLF} = 1.88$, which is consistent with excess of sources measured using the full doubeltjes sample.

For $i < 19.1$, the areal density of a complete optically-selected quasars sample is estimated to be 10.2 deg^{-2} (Vanden Berk et al. 2005) or 12.4 deg^{-2} (by integrating the optical quasar luminosity function). The areal density of the SDSS quasar sample used in this work is about 50% lower, 6.7 deg^{-2}. Our conclusions are not affected by this incompleteness, because we only use the SDSS quasars as *examples* of unobscured AGN; completeness is obtained by using the luminosity function. For our analysis, a complete quasar sample is not required, but the sample should be large enough to accurately determine $f_{\rm FRII}$ and ϵ_r. To confirm that our quasar sample is indeed large enough, we repeated our analysis using only quasars from SDSS DR7 (i.e., we exclude the targets from DR9 which reduces the number of quasars by a factor ≈ 2),

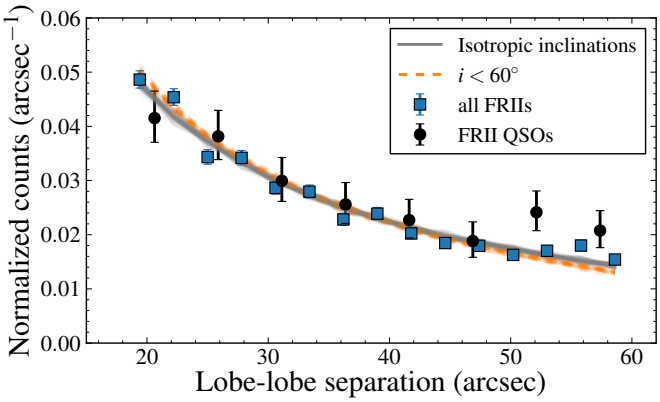

FIGURE 5.10: The distribution of angular lobe-lobe separation for all FR IIs and the FR II quasars. We also show the simulated distribution, as obtained using a Monte Carlo simulation (Sec. 5.4.2.4).

finding a change to our prediction of 3% ($N_{\rm data}/N_{\rm QLF} = 1.82$). Even if we increase the incompleteness of our quasar sample further by using only a random subsets of 50% of the SDSS DR7 quasars, the predicted density is not changed significantly (for different subsets we find $N_{\rm data}/N_{\rm QLF} = 1.8 \pm 0.1$).

We can thus conclude that our radio sample and optical quasars sample are large enough to make a robust prediction of the FR II areal density. The only remaining problem could be that our SDSS quasars are not a representative subset of the full population of quasars. This is discussed in the next section.

5.4.2.4 Potential bias due to calibration with optical AGN

We implicitly assumed that the SDSS quasars that were used to determine ϵ_r (Eq. 5.4) and $f_{\rm FRII}$ (Eq. 5.5) are a representative subsample of all quasars. Below we discuss some potential biases that this method may introduce. Again, none of these biases is found to influence our result by more than 10%.

To test whether the FR II quasars have a different disk SED compared to normal quasars, we can compare the median optical colors: $g-i = 0.27 \pm 0.01$, $g-i = 0.25 \pm 0.01$ for the FR II quasars and the full quasar sample, respectively (this comparison was made using a subsample of quasars, drawn from the probability distribution of the FR II quasar redshifts). Similar to de Vries et al. (2006, cf. their Fig. 7) we find a very small color difference in the optical SED of double-lobed quasars compared to normal quasars, implying that both populations likely have the same bolometric correction.

In the grand orientation-based unification scheme of radio-loud AGN (Urry & Padovani 1995), the number counts of type-I and type-II AGN in yield a maximum jet inclination of broad-line (type-I) AGN, $i_1 < 60°$ (e.g., Willott et al. 2000; Baldi et al.

2013; Wilkes et al. 2013). Since we used type-1 AGN to measure $f_{\rm FRII}$, this fraction could be underestimated because we sampled a restricted range of jet inclinations.

To quantify the effect of orientation bias, we ran a Monte Carlo simulation to predict the observed distribution of the lobe-lobe angular separation. We modeled the physical size (l) distribution using a power-law, $P(l) \propto l^p$ (with 100 kpc $< l <$ 1 Mpc); the redshifts were drawn from the FR II quasar redshift distribution. A power-law index of $p = -1$ was found to reproduce the observed distribution of angular distances (Fig. 5.10). Assuming the intrinsic size distribution of quasars and radio galaxies are similar (as predicted in the unified model), we find that for $i < 60°$, the number of FR IIs in our sample (i.e., with 18" $< d <$ 60") is only 4% lower compared to an isotropic distribution of jet inclinations.

The effect of orientation bias may even be smaller than 4% since at the high disk luminosity of our sample, the torus could be flattened due to dust sublimation (Simpson 2005). A decrease of the fraction of obscured AGN with luminosity (e.g., Willott et al. 2000; Ueda et al. 2003; Grimes et al. 2004; Assef et al. 2013; Lusso et al. 2013) is often taken as evidence for this receding torus model (Lawrence 1991; Falcke et al. 1995a). Orientation bias may not be relevant at all if the axis that connects the two lobes is not perpendicular a torus (Singal 1993; Lawrence & Elvis 2010).

5.5 Results

The main results of this work:

- We obtained a sample of 10^4 FR II radio sources from the FIRST survey (Fig. 5.2).
- We identified 459 photometrically selected and spectroscopically confirmed SDSS (DR7 plus DR9) quasars that match to the center of our double-lobed radio sources (Fig. 5.4).
- Using the FR II quasars, we observe a linear correlation between the bolometric disk luminosity and the lobe radio luminosity (Fig. 5.6), see also van Velzen & Falcke (2013).
- Our disk-lobe correlation is in very good agreement with the results that Körding et al. (2006b) obtained using VLSS (74 MHz) sources that match to SDSS quasars. Since the VLSS-SDSS matches are made regardless of morphology, we can conclude that sources that are (much) smaller than our FR IIs follow a similar disk-lobe correlation.
- The fraction of quasars that show 10^2 kpc-scale radio lobes decreases strongly with redshift. For $z > 1$, $f_{\rm FRII} \propto (1+z)^{-4}$. Independently of the redshift evolution, the typical bolometric disk luminosity to obtain an FR II morphology is observed at $\sim 10^{46}$ erg s^{-1} (Fig. 5.7).

- We observed no significant correlation between the project lobe-lobe separation and the radio luminosity or the disk luminosity (Fig. 5.11).
- The observed density of FR II radio sources exceeds the number predicted from the bolometric quasar luminosity function by a factor ≈ 2 (Fig. 5.8, left panel). At $S_\nu = 80$ mJy, where this result is most accurate, the systematic uncertainty is estimated to be 10% (Fig. 5.9).
- The observed density of FR II sources with a triple radio morphology agrees with the number predicted from the bolometric quasar luminosity function (Fig. 5.8, right panel).

5.6 Discussion

Below we first discuss potential explanations for the factor two difference between the observed and predicted FR II density. We consider three possibilities: radiatively inefficient accretion flows, extreme obscuration, and the lifetime of the radio lobes. The fact that the predicted and observed density agree when we restrict to radio sources with an active core provides evidence for the last explanation.

5.6.1 Explaining the excess of radio lobes

It is important to recall that our prediction for the FR II density is obtained using an empirical estimate for the fraction of quasars that are detected as double-lobed sources by our algorithm ($f_{\rm FRII}$, Eq. 5.5). In the range of radio flux that is well-sampled by the SDSS quasars ($30 < S_\nu < 400$ mJy), the predicted FR II density should therefore not exceed the observed density. The ratio of the predicted and observed FR II density measures directly what fraction of FR IIs are matched to jets from *known quasars*. Here, by known quasars we mean active black holes whose density has been accounted for in the bolometric luminosity function (Eq. 5.8). We stress once more that this luminosity function was constructed using observations at mid-IR to hard X-ray frequencies with the aim to "represent all AGNs with intrinsic (obscuration-corrected) luminosities above the observational limits at each redshift" (Hopkins et al. 2007). Below we discuss three explanations for the excess of observed double-lobed radio sources.

5.6.1.1 Radiatively inefficient accretion and FR I radio galaxies

Below an accretion rate of about 1% of the Eddington luminosity, accreting stellar mass black holes in X-ray binaries are observed (Remillard & McClintock 2006) to switch to a radiatively-inefficient accretion mode (Narayan & Yi 1995; Yuan & Narayan 2014). A consistent feature of this state is a steady (compact) jet (Fender, Belloni, & Gallo 2004). There is considerable evidence that accretion disks of AGN also have two states, depending on the (Eddington-normalized) accretion rate (Ho

1999; Ghisellini & Celotti 2001; Falcke et al. 2004a; Körding et al. 2006b; Plotkin et al. 2012; Best & Heckman 2012). Radiatively inefficient AGN are likely to be missing in the bolometric quasar luminosity function that we used. Jets from these sources, also known as low-excitation radio galaxies (Laing et al. 1994), may appear to be the solution for the observed excess of radio lobes. The strongest argument against this scenario is that it would not explain why the areal density of radio triples agrees with our prediction. Furthermore, the jet power that is needed to inflate the powerful radio lobes that we observed is likely to be too high to originate from a radiatively inefficient disk.

The jet power can be expressed as $Q_j = \eta_j \dot{m} c^2$, with $\eta_j \approx 10^{-2}$ for jets from radiatively inefficient flows (Falcke et al. 2004a; Körding et al. 2006b). The typical radio luminosity of the sources that need to be explained by radiatively inefficient flows is $L_{1.4\mathrm{GHz}} \approx 10^{42.8}\,\mathrm{erg\,s^{-1}}$ (i.e., 80 mJy at $z = 1$), which corresponds to a typical jet power of $Q_j \sim 10^{45}\,\mathrm{erg\,s^{-1}}$ (Willott et al. 1999; Godfrey & Shabala 2013). This jet power requires an accretion rate of few $M_\odot\,\mathrm{yr}^{-1}$, i.e., about 10% of the Eddington accretion rate of a black hole with a mass of $10^9\,M_\odot$. So except for black holes with a mass greater than $10^{10}\,M_\odot$, the accretion rate of the majority of our FR II sources is most likely too high to yield a radiatively inefficient flow.

In the literature, a few low-excitation FR II radio galaxies have been identified via their optical spectra. Hardcastle et al. (2009) conclude that these sources also are X-ray and mid-IR dim. A complete spectroscopic follow-up program of the 3C radio sources at $z < 0.3$ (Buttiglione et al. 2009) shows that at most 30% of low-redshift FR IIs can be marked as low-excitation radio galaxies (Buttiglione et al. 2010).

The luminosity function of Best & Heckman (2012) shows that high-excitation radio galaxies dominate over low-excitation radio galaxies for $L_{1.4\mathrm{GHz}} > 10^{42}\,\mathrm{erg\,s^{-1}}$, which corresponds to $z > 0.5$ when $S_\nu = 80$ mJy. Hence given our flux limit, low-excitation radio galaxies are only detectable at low redshift and thus make a small contribution to the areal density.

While our method is optimized for identifying relatively compact lobe emission, we will also pick up some FR I radio galaxies. The same argument used above for low-excitation radio galaxies applies to FR I radio galaxies; the typically lower luminosity of FR Is implies they contribute little to the source count at $S_\nu \sim 10^2$ mJy.

5.6.1.2 Extreme obscuration

The excess of radio-selected FR IIs could be explained by a population of powerful active black holes that have been missed in high-frequency quasar surveys due to extreme obscuration. In this scenario, one is forced to conclude that the selection of radio sources with a triple morphology completely removes the obscured population (because for the triples the predicted areal density agrees with the observed density). This could be possible within the grand unification scheme of radio-loud AGN (Urry & Padovani 1995), but only when the extreme obscuration is caused by the "torus".

Due to Doppler boosting, the selection of sources with a detected core leads to a lower jet inclination. So if the jet is oriented perpendicular to the obscuring torus, restricting to radio triples leads to a less obscured view of the accretion disk.

Type-2 quasars have been found in the SDSS spectroscopic galaxy sample (Zakamska et al. 2003) and about 10% of these are radio-loud (Lal & Ho 2010). Heavily obscured quasars can be selected by their mid- or far-infrared colors due to reprocessing of the optical/UV disk emission by warm to cool dust (for recent examples of this selection technique see Roseboom et al. 2013; Mateos et al. 2013). We note that the Hopkins et al. (2007) luminosity function includes two mid-IR selected quasar samples, namely 8 μm *Spitzer* observations of the Boötes field (Brown et al. 2006) and a 15μm sample compiled by Matute et al. (2006), but these are relatively small and contribute little to the fit for the parameters of the luminosity function.

Estimating the percentage of obscured quasars that are missing in the 2–10 keV AGN samples (e.g., Ueda et al. 2003; Barger et al. 2005; Silverman et al. 2005) that were used in the Hopkins et al. (2007) quasar luminosity function is non-trivial. Analysis of the cosmic X-ray background allows for the presence of Compton-thick AGN (with Hydrogen column densities $N_H > 10^{24}\,\mathrm{cm}^{-2}$) in roughly equal numbers as less obscured AGN (Ueda et al. 2003). However, for the high bolometric luminosities of the quasars in our sample ($L_{\mathrm{bol}} \sim 10^{46.5}\,\mathrm{erg\,s}^{-1}$), the fraction of Compton-thick AGN is estimated to be less than 10% (Hasinger 2008; Gilli 2013). If the fraction of Compton-thick AGN is indeed about 10% at the highest disk power, the luminosity function used in this work is nearly complete for our purpose, i.e., the excess of radio-selected FR IIs is not due to extreme obscuration of the accretion disk.

Observations of FR II sources selected from the 3CRR survey show that a sizable fraction (10% to 50%) of radio galaxies are underluminous at 10–70μm compared to radio-loud quasars (Shi et al. 2005; Ogle et al. 2006). Most of these sources are currently classified as low-excitation radio galaxies (e.g., Gürkan et al. 2014), but their lobes could have been created when the accretion rate was higher and the disk was radiating efficiently. So perhaps 10–50% of galaxies with luminous radio lobes no longer host powerful active engines, which supports our final hypothesis for the excess of radio lobes: the lobe lifetime.

5.6.1.3 Lobe lifetime

To appreciate our final, and preferred, explanation for the excess of radio lobes, we have to consider the nature of the lobe radio emission: synchrotron radiation. When the accretion phase ends, the jet stops supplying power to the hotspots within $\tau_{\mathrm{delay}} \sim 10^6$ yr (the light travel time), but the synchrotron cooling time of the electrons can be an order of magnitude longer. The electron cooling time can be estimated for a given synchrotron-emitting region if the properties of the magnetic field in the region are known. The typical cooling time of FR II lobes at a rest-frame frequency of 2 GHz is $\tau_{\mathrm{sync}} \sim 10^{7\pm0.5}$ yr, depending on the details of the equipartition assumption (e.g.,

Komissarov & Gubanov 1994; Blundell & Rawlings 2000).

The lobe fading time also depends on the evolution of the magnetic field energy, which is non-trivial to calculate. As the lobes expand, the particle density decreases, leading to lower synchrotron luminosity. If the magnetic fields remains in equipartition with the electrons, the field strength will rapidly decrease as the lobes expand, leading to rapid fading. On the other hand, if the plasma of the lobes behaves like a perfect conductor, the magnetic field may not decay at all. The electrons in the lobes will also cool by inverse-Compton scattering of CMB electrons, which can significantly shorten the cooling time at $z > 2$ (Mocz, Fabian, & Blundell 2011).

If the lifetime of the radio lobes is equal to the duration of the quasar phase ($\sim 10^{6-8}$ yr; Martini 2004), radio-selected lobes outnumber FR II quasars by a factor two. If the accretion disk luminosity is episodic, the density of radio lobes compared to double-lobed quasars could increase further[3]. Radio sources with a nested morphology (e.g., two young hotspots inside older lobes) are often interpreted as a sign of AGN intermittency (Stanghellini et al. 1990; Schoenmakers et al. 2000; Saikia & Jamrozy 2009; Filho et al. 2011; Nandi et al. 2014).

A few low-redshift "relic lobes" (Komissarov & Gubanov 1994) have been described in the literature (Parma et al. 2007; Murgia et al. 2011; Dwarakanath & Kale 2009). The estimates of the fading timescales are in the range 10^{6-7} yr (Parma et al. 2007); longer lifetimes are found for lobes in galaxy clusters 10^{7-8} yr (Murgia et al. 2011). One may be able to measure the importance of synchrotron cooling for the lobe fading timescale at $z \sim 1$ using observations of doubeltjes at low-frequency ($\nu < 1$ GHz). The synchrotron cooling time scales as $\nu^{-1/2}$, so the excess of radio lobes should be larger at lower frequency (as long as the fading timescale is longer than the light travel time to the lobes). Testing this idea requires a resolution of at least 20", which is currently possible with the Low-Frequency Array (LOFAR; van Haarlem et al. 2013) and the Giant Metrewave Radio Telescope (GMRT).

When only sources with a triple morphology are used, the predicted areal density from the quasar luminosity function agrees with the observed density (Fig. 5.8). For each radio triple, we know that the jet is currently active and thus their areal density cannot be significantly enhanced by the lifetime of the radio lobes. This suggests that the factor two excess of radio-selected FR IIs, most of which have a double —not a triple— morphology, can be simply explained by a delayed response of the lobes to the shutdown of the jet.

[3]Eddington-limited time variability of the accretion disk may also explain why the fraction of radio sources with an quasar counterpart is observed to increase with luminosity (Willott et al. 2000).

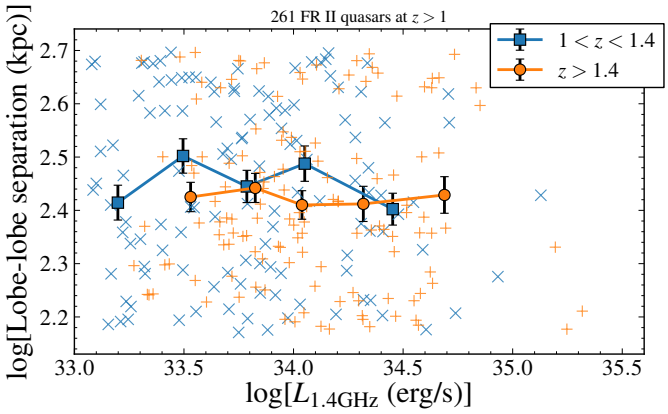

FIGURE 5.11: The mean projected physical distance between the lobes versus the lobe radio luminosity for two redshift intervals.

5.6.2 Redshift evolution of FR II properties and jet feedback efficiency

From $z = 1$ to $z = 3$, we observe a factor ≈ 10 decrease in the fraction of quasars that are identified as FR IIs (Fig. 5.7). This decrease is much stronger than the change of the angular diameter distance over this redshift interval (which only decreases the largest lobe-lobe separation that we can detect from 500 kpc to 450 kpc, Fig. 5.1). We stress that we measured f_{FRII} using only quasars with a predicted radio flux (from the radio-optical correlation) that is above our flux limit, i.e., the observed evolution is not a selection effect. We observed that the FR II fraction increases with disk luminosity, so the decrease of f_{FRII} for $z > 1$ is entirely due to redshift evolution (i.e., Malmquist bias would only lead to an increase f_{FRII} with redshift).

Two different processes could explain the observed redshift evolution: a change of external pressure which acts to disrupt the jet before reaching 10^2 kpc or electron cooling due to inverse-Compton scattering of CMB photons. Evidence for the former hypothesis follows from matching the SDSS quasars to VLSSr (74 MHz) sources. The VLSSr catalog is slightly more shallow ($F_{74\mathrm{MHz}} > 0.5$ Jy or 50 mJy at 1.4 GHz for $\alpha = -0.8$) than our sample of double-lobe sources from FIRST, yet the fraction of quasars with a VLSS match is nearly a factor 4 higher. From $z = 1$ to $z = 3$ the decrease of the fraction of quasars that match to a VLSSr source is only a factor five. This suggest that about half of the redshift evolution of the 1.4 GHz doubeltjes can be explained by size evolution: powerful radio sources are intrinsically smaller at higher redshift. We note that compact jets at very high redshift ($z \approx 10$) can be identified by their observed radio SED, which peaks at $\sim 10^2$ MHz (Falcke, Körding, & Nagar 2004b).

Earlier studies of FR II sources have also reported evolution of the physical size of

FR IIs with (photometric) redshift (Oort et al. 1987; Kapahi 1989) —see Blundell et al. (1999) for a review. Neeser et al. (1995) was the first to use (mainly) spectroscopic redshifts and complete radio samples to find $d \propto (1+z)^{-1.7\pm0.5}$ (for $\Omega_M = 1$, $\Omega_\Lambda = 0$). We note that the median size of our 459 FR II quasars is not observed to change with redshift (Fig. 5.11). This implies that size evolution at $z > 1$ only affects sources smaller than $d = 150$ kpc and thus support the idea that FR II size evolution is determined by the interaction of the jet with gas close to the host galaxy, as suggested by Neeser et al. (1995). The lack of a correlation between cluster richness and physical size for 3CR sources at $z > 0.4$ (Harvanek & Stocke 2002) is further evidence that size evolution is due to changes on scales below 10^2 kpc.

Strong evidence for evolution of the radio-loud fraction with redshift and luminosity has been observed by Jiang et al. (2007). These authors matched SDSS quasars to all FIRST sources within 30", yielding a sample that is dominated by unresolved radio quasars. Jiang et al. (2007) found that the radio-loud fraction scales as $(1 + z)^{-2}$. Using the same parametrization as Jiang et al. (2007), Eq. 5.10, we find $(1 + z)^{-4}$. This steeper slope again confirms that fewer powerful jets can grow to $d > 150$ kpc as the redshift increases. Jets at high redshift thus deposit more of the accreted energy into (or close to) their host galaxy compared to low-redshift sources; at high redshift, powerful radio jets appear to be more effective at supplying feedback to their host galaxy.

5.6.3 The quasar fraction

A traditional approach to study unification of quasars and radio galaxies is to use follow-up observations of a complete radio sample to measure what fraction of FR II radio sources have a quasar at their center. Here the meaning of 'quasar' can vary from study to study, depending on the selection method (e.g, the frequency or spectral resolution). In this work, we presented the "true" quasar fraction, i.e., as obtained from the bolometric luminosity function. For the full FR II sample we measure a true quasar fraction of about 50%, while for the triples this fraction is close to 100%.

Most relevant for a comparison to our results is the 7C redshift survey (7CRS; Willott et al. 1998). This surveys contains 130 radio sources with $S_{151} > 0.5$ Jy from the 7C survey (McGilchrist et al. 1990) with near-IR spectroscopic follow-up data that is 90% complete. At $L_{1.4\mathrm{GHz}} \sim 10^{43.5}\,\mathrm{erg\,s^{-1}}$ and $z = 1.5 \pm 0.5$, the fraction of FR IIs that are observed to have broad lines in their spectrum is $34 \pm 6\%$ At $L_{1.4\mathrm{GHz}} \sim 10^{42.5}\,\mathrm{erg\,s^{-1}}$ and $z = 0.5 \pm 0.5$, this fraction is $11 \pm 4\%$ (Willott et al. 2000). Measured over all redshifts, the 68% CL interval of the 7CRS quasar fraction is 20–37% (Grimes et al. 2004). This quasar fraction is consistent with our result if the near-IR selection of 7CRS has missed a factor ≈ 1.7 of the full quasar population (due to obscuration).

For the sake of comparing the SDSS quasars to the 7CRS quasars, we restrict our doubeltjes sample to $S_\nu > 0.5\ \mathrm{Jy} \times (1.4/0.15)^{-0.8} = 84$ mJy, leaving 3748 sources. For

the optically-selected SDSS quasars we require $m_i > 19.1$ and we use the radio-optical flux correlation to estimate that 13% of FR II quasars with $S_\nu > 84$ mJy will fall below this flux limit. We find 203 FR II quasars, with a median radio luminosity of $L_{1.4\mathrm{GHz}} \sim 10^{43.1}\,\mathrm{erg\,s^{-1}}$, giving a quasar fraction of 5%. This lower fraction compared to 7CRS is due to both the quasar selection method (optical versus near-IR) and the incompleteness of the photometrically-selected SDSS quasar sample. When we match the SDSS quasars to all radio sources from the 7C survey with $S_{151} > 0.5$ Jy, we again find a quasar fraction of 5%. (We note that the lower radio frequency and smaller size of the 7CRS sources may also influence the quasar fraction.)

Repeating the exercise for the quasars selected by their mid-IR colors in WISE (see Section 5.3.1), we find a quasar fraction of 23%. Correcting for the 78% efficiency of the photometric selection (Stern et al. 2012), the fraction is 30%. By comparing this with our true quasar fraction, we estimate that mid-IR color selection can retrieve about half of the full population of powerful radio-loud quasars. Finally, if we adopt a 50% completeness for the SDSS sample (sec. 5.4.2.3), we estimate that selection on the UV-excess (Richards et al. 2002; Bovy et al. 2011) can retrieve about one-fourth of the true quasar population. These two estimates for the obscured/missing fraction are consistent with Hopkins et al. (2007, cf. Eq. 4).

Finally, we compare our estimate of the density of radio galaxies to the luminosity function of radio-loud AGN obtained by Best & Heckman (2012) using the SDSS spectroscopic galaxy sample. At $L = 10^{25.1}\,\mathrm{W\,Hz^{-1}}$ ($L_{1.4\mathrm{GHz}} = 10^{42.2}\,\mathrm{erg\,s^{-1}}$), the density of radio-selected AGN is $\log[\phi_{\mathrm{BH12}}] = -7.2^{+0.1}_{-0.2}$ (measured per Mpc^3 per logarithmic luminosity bin) with a typical redshift of $z \approx 0.3$ (Best & Heckman 2012). Using our disk-lobe correlation, this radio luminosity yields a bolometric luminosity of $L_{\mathrm{bol}} = 10^{45.7}\,\mathrm{erg\,s^{-1}}$, corresponding to a quasar density of $\log[\phi_{\mathrm{H07}}(z = 0.3)] = 10^{-5.4}$ (Hopkins et al. 2007). Estimating f_{FRII} to be 0.8% at this luminosity (Fig. 5.7), we find an FR II density of $\log[\phi_{\mathrm{dub}}] = -7.5$. Hence our estimate of the FR II fraction combined with the quasar luminosity function agrees reasonably well with the radio-loud AGN luminosity function at low-redshift. Our density is expected to be lower than obtained from the Best & Heckman (2012) luminosity function since we are not retrieving all radio-loud AGN (due to our cut on the angular size).

5.7 Conclusion: nature and evolution of radio galaxies

We have obtained a very large sample of double-lobed radio sources and matched these to SDSS quasars, allowing for arguably the most comprehensive view of FR II evolution to date.

We found a strong redshift dependence: at $z > 1$, fewer radio-loud quasars have large radio lobes. The areal density of our radio-selected FR II sample exceeds the expected density based on the bolometric (obscuration-corrected) quasar luminosity function by a factor two. The fraction of FR II quasars that have an active radio core

(i.e., emission within 5" of the center of the lobes) was also found to be a factor two higher. Indeed when we use only sources with a triple morphology, the predicted areal density agrees with the observed areal density. We therefore argue that the excess of radio-selected FR IIs can be simply explained by the lifetime of the lobes, bringing us to the following conclusion on the nature of powerful FR II radio galaxies at $z \sim 1$: *the majority of jets that power FR II lobes originate from radiatively efficient accretion flows that obey a linear jet-disk coupling.*

Our conclusion implies an almost complete unification of radio galaxies and quasars: nearly all FR II lobes are powered (or have been powered) by jets from quasars.

5.7.1 Outlook

We presented an automated method that faithfully selects powerful AGN using only radio data. When applied to the FIRST survey, our method yields the largest sample of FR II sources to date. Surveys from the Jansky-VLA and SKA precursors (LOFAR, MeerKAT, ASKAP) will observe large parts of the radio sky to deeper flux limits, higher resolution, or lower frequencies than was technologically feasible at the time when FIRST was conducted. It will be exciting to apply our morphological selection method to these near-future surveys: we can expect to obtain a complete view of accreting black holes throughout the entire Universe.

Acknowledgments

We would like to thank G. de Bruyn, D. Cseh, A. Gruzinov, P. F. Hopkins, J. H. Krolik, H. Röttering, P. Uttley, R. L. White, and N. L. Zakamska for useful discussions. We thank the first referee and we are grateful to the second referee, M. Hardcastle, for providing constructive comments.

The FIRST and VLSS surveys were obtained with the Very Large Area, which is operated by the National Radio Astronomy Observatory. NRAO is a facility of the National Science Foundation operated under cooperative agreement by Associated Universities, Inc.

Funding for the SDSS and SDSS-II has been provided by the Alfred P. Sloan Foundation, the Participating Institutions, the National Science Foundation, the U.S. Department of Energy, the National Aeronautics and Space Administration, the Japanese Monbukagakusho, the Max Planck Society, and the Higher Education Funding Council for England.

The WENSS project was a collaboration between the Netherlands Foundation for Research in Astronomy and the Leiden Observatory. The WENSS team consisted of Ger de Bruyn, Yuan Tang, Roeland Rengelink, George Miley, Huub Röttgering, Malcolm Bremer, Martin Bremer, Wim Brouw, Ernst Raimond and David Fullagar.

This publication makes use of data products from the Wide-field Infrared Survey Explorer, which is a joint project of the University of California, Los Angeles, and the Jet Propulsion Laboratory/California Institute of Technology, funded by the National Aeronautics and Space Administration.

This work was supported by an ERC Advanced Grant (n. 227610, PI: H. Falcke).

5.A Example doubeltjes

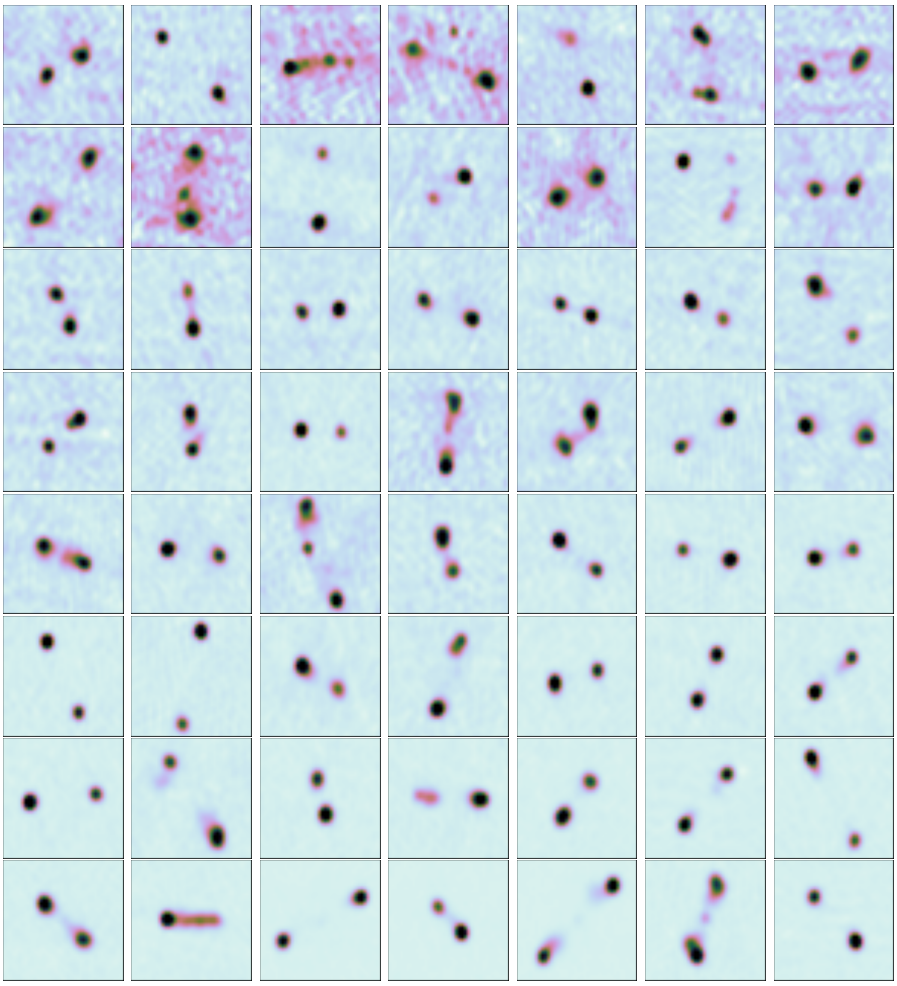

FIGURE 5.12: Random selection from the 10^4 FIRST doubeltjes that pass the quality cuts. Images are 1 arcmin wide and centered on the geometrical center of the lobes. Sources are selected using logarithmically-spaced flux-bins between 15 mJy and 222 mJy.

Part II:
Human timescales

Chapter 6

Optical discovery of probable stellar tidal disruption flares

Sjoert van Velzen, Glennys R. Farrar, Suvi Gezari, Nidia Morrell, Dennis Zaritsky, Linda Östman, Mathew Smith, Joseph Gelfand, Andrew J. Drake

2011, Astrophysical Journal, 741, 73

Abstract

Using archival SDSS multi-epoch imaging data (Stripe 82), we have searched for the tidal disruption of stars by super-massive black holes in non-active galaxies. Two candidate tidal disruption events (TDEs) are identified. The TDE flares have optical blackbody temperatures 2×10^4 K and observed peak luminosities $M_g = -18.3$ and -20.4 ($\nu L_\nu = 5 \times 10^{42}$, $4 \times 10^{43}\,\mathrm{erg\,s^{-1}}$, in the rest-frame); their cooling rates are very low, qualitatively consistent with expectations for tidal disruption flares. The properties of the TDE candidates are examined using i) SDSS imaging to compare them to other flares observed in the search, ii) UV emission measured by *GALEX* and iii) spectra of the hosts and of one of the flares. Our pipeline excludes optically identifiable AGN hosts, and our variability monitoring over 9 years provides strong evidence that these are not flares in hidden AGNs. The spectra and color evolution of the flares are unlike any SN observed to date, their strong late-time UV emission is particularly distinctive, and they are nuclear at high resolution, arguing against their being first cases of a previously-unobserved class of SNe or more extreme examples of known SN types. Taken together, the observed properties are difficult to reconcile with a SN or AGN-flare explanation, although an entirely new process specific to the inner few-hundred parsecs of non-active galaxies cannot be excluded. Based on our observed rate, we infer that hundreds or thousands of TDEs will be present in current and next-generation optical synoptic surveys. Using the approach outlined here, a

TDE candidate sample with O(1) purity can be selected using geometric resolution and host and flare color alone, demonstrating that a campaign to create a large sample of tidal disruption events, with immediate and detailed multi-wavelength follow-up, is feasible. A by-product of this work is quantification of the power-spectrum of extreme flares in AGNs.

6.1 Introduction

When a star passes too close to a super-massive black hole, the tidal shear overcomes the star's self-gravity and the star is disrupted. Much of the stellar debris is ejected from the system, but some fraction remains bound to the black hole and is accreted, resulting in a week- to year-long electromagnetic flare (Rees 1988). The fall-back rate is expected to follow a power-law of index $-5/3$ (Rees 1988; Phinney 1989), but see Lodato, King, & Pringle (2009) for predicted deviations from this canonical scaling; the light-curve does not in general show the same behavior, (e.g., Strubbe & Quataert 2009; Lodato & Rossi 2011). For $M_{\rm BH} \lesssim 10^7 M_\odot$ the initial fall-back rate is super-Eddington and the emission is usually assumed to have a blackbody spectrum. The predicted temperatures range from $\sim 10^4$ K (Loeb & Ulmer 1997) to, more commonly, $\sim 10^5$ K (e.g., Ulmer 1999). A radiatively driven wind, existing as a consequence of the super-Eddington fallback, may dominate the emission of the tidal disruption event (TDE) at early times (Strubbe & Quataert 2009). Model predictions generally depend on parameters which are quite uncertain, so observational input is needed to constrain the modeling.

Detections of tidal disruption events are of interest for a number of reasons, including: 1) The light emitted after the disruption depends sensitively on the black hole mass and spin, hence a large sample of TDEs will allow properties of black holes to be studied without relying on scaling relations with global parameters of galaxies (Gebhardt et al. 2000; Ferrarese & Merritt 2000; Graham et al. 2001; Marconi & Hunt 2003). 2) TDEs may be our only probe to obtain a large sample of dormant super-massive black holes (Frank & Rees 1976; Lidskii & Ozernoi 1979). 3) A particularly intriguing application is testing the existence of intermediate mass black holes in globular clusters and dwarf galaxies (Ramirez-Ruiz & Rosswog 2009). 4) For black holes with mass $M_{\rm BH} \gtrsim 10^8 M_\odot$, the tidal disruption radius lies inside the Schwarzschild radius (Hills 1975), hence a TDE survey that covers a sample of galaxies with a wide enough central black hole mass range is in principle sensitive to whether super-massive black holes do have an event horizon. 5) Detailed observations of the emission from a large sample of tidal disruption events will provide a new arena for testing our understanding of accretion physics and may constrain properties of the disrupted stars.

A number of candidate TDEs have been identified in X-ray surveys (Bade et al. 1996; Komossa & Bade 1999; Donley et al. 2002; Esquej et al. 2008; Cappelluti et al. 2009; Maksym et al. 2010) —for a review see Komossa (2002)— and in the UV *GALEX* Deep Imaging Survey (Gezari et al. 2006, 2008, 2009b). However establishing that a candidate tidal flare found in UV and X-ray surveys is not an exceptionally variable AGN is hampered because, although the amplitude of AGN variability at these wavelengths is much greater than in the optical (Maoz et al. 2005; Saxton et al. 2011), the range of variation has not yet been well-characterized. With the advent of optical transient surveys, such as the Palomar Transient Factory (PTF; Law et al. 2009), Pan-STARRS (Chambers 2007), Catalina Real-Time Transient Survey (CRTS) and later the Large Synoptic Survey Telescope (LSST; Ivezić et al. 2008), there should be many candidate TDEs. The challenge is to eliminate the far more common flares from variable AGNs and SNe to a) convincingly exclude these backgrounds as explanations for individual events and b) efficiently produce a high-purity sample of TDE candidates such that expending resources following up uninteresting events can be reduced to an acceptable level.

Until now, the feasibility of identifying probable tidal flares with an optical transient survey alone has not been demonstrated. Here we present two candidate stellar tidal disruption events detected in archival multi-epoch imaging data of the Sloan Digital Sky Survey (SDSS), showing that the difficulties of identifying such events in an optical survey can be resolved. There are several important advantages of using the SDSS data. First is the very large sample of galaxies, with many having spectra; this sample enables one to classify flares into well-defined categories, such that the validity of our methodology can be demonstrated. Second, the spatial resolution of SDSS is adequate to exclude a very high fraction of SNe from the nuclear-flare sample, allowing SNe to be rejected without imposing cuts based on flare properties. Third, SDSS observed the galaxies in Stripe 82 over typically 7 seasons with a mean of 70 observations in all; this allows hidden AGNs to be rejected based on variability in the non-peak seasons. Having observations in three or more filters is also useful, providing color information that is valuable in confirming that the flares are not due to AGNs or known types of SNe.

The selection pipeline we employ reduces the background from SNe and variable AGNs by two orders of magnitude or more, but positive determination that the two flares which pass the pipeline are in fact TDEs requires detailed comparison between the properties of the flares and those of AGNs and SNe. This we do with multiple tools. We have obtained spectra of both hosts and of one of the flares, found archival *GALEX* post-flare observations of both host galaxies and a pre-flare observation of one of them, and archival Catalina Real-Time Transient Survey data to extend the light curve of one of the flares to earlier and later times than observed by SDSS. Analysis of these observations and comparison between the properties of the TDE candidates and SNe and AGNs is reported.

In addition to demonstrating the feasibility of optically-initiated TDE surveys, discovery of these two flares gives needed observational insight into the tidal disruption phenomenon. An important consequence of our method of detection – which does not rely on flare properties beyond requiring them to be nuclear to reject SNe and uses host properties alone to reject AGNs – is that selection bias is minimized. With just two events we have only begun to scratch the surface, but the properties of the flares can already test and inform theory. Our candidate TDEs are both much more luminous in the optical than predicted (Strubbe & Quataert 2009), although with adjusted parameter choices the fit can be improved and some ingredients may still be missing in these early, simple models.

The outline of the remainder of this chapter is as follows. In Section 6.2 we describe our pipeline for TDE selection. In Section 6.3 we present the observed properties of the final products of the pipeline: two candidate tidal disruption flares. Follow-up observations with other instruments are reported. A detailed comparison to flares of active galaxies and supernovae is given in Section 6.4, leading to the conclusion that the two TDE candidates are indeed likely to be tidal disruption events. Section 6.5 compares our TDEs to candidates reported in other wavelengths and compares their observed properties to theory. The implications of this work for detecting TDEs and obtaining a relatively pure sample of them in future optical surveys is discussed in Section 6.6. We close with a summary (Sec. 6.7).

All magnitudes are quoted in the AB system (Oke 1974) and are corrected for Galactic extinction (Schlegel et al. 1998). We adopt a standard cosmology with $H_0 = 72\,\mathrm{km\,s^{-1}Mpc^{-1}}$, $\Omega_m = 0.3$ and $\Omega_\Lambda = 0.7$.

6.2 Identification of tidal flares

The flowchart in Fig. 6.1 summarizes our search graphically. In the following sections we discuss the steps in this chart in more detail. To achieve the goal of obtaining a large and uniformly selected sample of tidal disruption events (TDEs), it is necessary to accurately identify their flares in large volumes of optical data. Here we use SDSS observations of 2.5×10^6 galaxies in "Stripe 82", that have been observed typically 70 times over a nine year baseline. In Section 6.2.1 we explain how a sample of 342 flares was extracted from this data set. Supernovae or other stellar flares are not of interest in a search for TDEs, and in Section 6.2.2 we explain how they are removed by discarding flares offset from the center of the host. The final sample for our study consists of 42 nuclear flares having more than two observations in the flaring state.

The rejection of active galactic nuclei (AGN) is discussed in Section 6.2.3. Eliminating host galaxies with spectroscopic and photometrically identified AGNs removes all but 5 nuclear flares. The critical challenge is to identify and exclude host galaxies with active nuclei which are too weak or heavily obscured to be identified by usual spectroscopic and photometric criteria. We can identify variable unrecognized AGNs

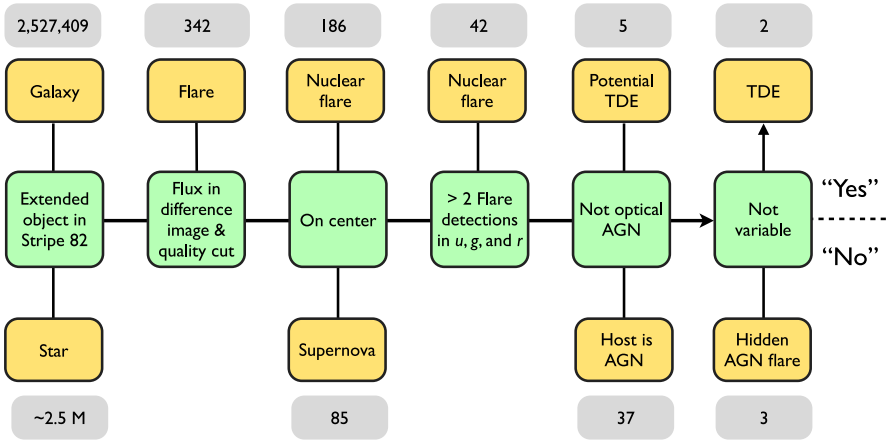

FIGURE 6.1: Flow chart summarizing the flare and TDE identification pipeline, discussed in Section 6.2. The numbers in the gray boxes indicate the number of objects in each class. The first three steps are discussed in Sections 6.2.1.1–6.2.2.2; the last three steps summarize the selection for TDE candidates discussed in Sections 6.2.2.3–6.2.3.3.

directly by their variability, thanks to SDSS's multi-year monitoring of the hosts. Three of the five candidates do display variability in other seasons, consistent with the variability we measure in our identified AGNs, while two others do not, at the $< 10^{-5}$ CL level (see Section 6.4.1). On geometric grounds alone, the probability these two flares are SNe is $< 0.5\%$ (see Section 6.4.2), assuming the distribution of SNe follows the stellar light. Thus these two flares are strong candidates to be stellar tidal disruption events and we refer to them as TDE1 and TDE2 below.

6.2.1 Selecting flares in SDSS observations

The $\sim 300\,\mathrm{deg}^2$ Sloan Digital Sky Survey (SDSS; York et al. 2000) multi-epoch imaging data Stripe 82 (Sesar et al. 2007; Bramich et al. 2008; Frieman et al. 2008; Abazajian et al. 2009) was the starting point of our search. Using the SDSS morphological star-galaxy separation (Lupton et al. 2001; Stoughton et al. 2002) and the standard checks on quality flags (Stoughton et al. 2002), we extracted $\sim 2.5\,10^6$ galaxies from this data set. The typical number of observations per galaxy is 70.

6.2.1.1 Catalog cuts

In order to focus our analysis resources and time most efficiently, we first selected candidate flares from the cataloged parameters, which reduced the number of galaxies by two orders of magnitude. Galaxies were required to have $m < 22.5$ in at least 3 of the 5 SDSS bands (u,g,r,i,z; Fukugita et al. 1996; Smith et al. 2002). A minimum

Cut	SDSS band
$m_{\rm mean} < 22.5$	≥ 3
identified as extended in co-add	all
$\chi^2/{\rm DOF} > 5$	g,r, or i
$F_{\rm peak}/F_{\rm mean} > 1.1$	≥ 2
$(F_{\rm peak} - F_{\rm baseline})/\sigma_{\rm peak} > 7$	≥ 2
$(F_{\rm peak} - F_{\rm baseline})/\sigma_{\rm rms} > 7$	≥ 2

TABLE 6.1: The first two cuts are designed to obtain a clean, flux limited sample of galaxies. The co-add runs are obtained by addition of nearly all Stripe 82 imaging data (Abazajian et al. 2009). The goal of the remaining cuts is to select flares. For all cuts we use the Petrosian flux (Stoughton et al. 2002). The subscript 'mean' is the inverse-variance-weighted mean using all observations, while the subscript 'baseline' refers to the non-flare observations only. χ^2 is calculated using mean flux as a model for the galaxy light curve. These cuts select $\sim 2 \times 10^4$ candidate flares from the $\sim 2 \times 10^6$ galaxies with $m < 22.5$ in Stripe 82.

flux increase of 10%, measured at the 7-σ level, is the most important requirement that was imposed to find flares. The cuts on the cataloged parameters were chosen to be "soft" (i.e., high efficiency, low purity) and yielded 21,383 potential flares. See Table 6.1 for a summary of the catalog cuts.

6.2.1.2 Difference imaging

Next, with this data set that is a factor of 100 smaller than the starting one, we applied a more rigorous analysis method: image subtraction. Given that there are typically 70 observations of a galaxy, we have many images of the host of the flare; from these we selected the observations with the best seeing and lowest sky level to be the reference images for subtraction. First we implemented a simple and relatively fast "direct subtraction" method, which allows quick determination that 8834 flare candidates are spurious because they show no flux in the difference image. For each of the remaining galaxies hosting a flare, nine reference images (of size $1' \times 1'$) were cross convolved using a modified version of the software by Yuan & Akerlof (2008) and subtracted to obtain nine difference images, for each filter in each night. The convolution kernels were determined using nine reference stars that were selected to lie close to the host galaxy. The mean flux of the nine difference images and its standard deviation were computed for each pixel, after applying a clipping algorithm to reject pixels that lie more than 3σ from the median. The flux, F, in the mean difference image was computed using an aperture of 2 times the full-width-half-maximum (FWHM) of the point spread function (PSF) measured in the mean image of the convolved reference stars. The minimum flux in the difference image was required to be $m < 22$. In addition, we require for each band that the flare is detected at the 7-σ level. We further require that the shape of the source in each difference image is well-fit by the PSF extracted from the mean convolved reference stars for that image.

Of the flares meeting the above conditions, 583 satisfy the requirement of detections in at least two bands. Good agreement on the flux in the difference image is obtained for the light curves produced by Holtzman et al. (2008) of supernovae from the SDSS SN Survey (Frieman et al. 2008; Sako et al. 2008) which were detected independently by our pipeline.

6.2.1.3 Rejecting moving objects

Solar system objects, when seen in front of a galaxy, can fake a flare. SDSS checks for moving objects by measuring the position of the centroid across different filters (Ivezić et al. 2001). We eliminate moving objects flagged by SDSS (Stoughton et al. 2002), and identify 32 additional solar system objects using the position of the centroid in the difference image. By requiring detections in the difference image in at least two observing nights, false flares due to solar system objects are eliminated and we are left with 419 flares.

6.2.1.4 Manual rejection

We remove galaxies with a spectroscopic redshift > 1.2, because they are mis-classified as extended. This requirement removes 7 quasars from the sample. Finally, we inspect the difference images of the remaining 412 flares to search for bad subtractions or other anomalies. The number of flares rejected after this inspection is four, which is quite low considering the large number of galaxies processed by the image subtraction pipeline ($\sim 2 \times 10^4$). In Fig. 6.2 we show examples of rejected and good subtractions. Additional quality cuts on the distance between the flare and the center of its host are discussed below.

6.2.2 Selection of nuclear flares

An accurate measurement of the distance between the center of the host galaxy and the flare is crucial for obtaining a clean nuclear flare sample (i.e., removing SNe). In Section 6.2.2.1 we discuss the details for accurately measuring this distance and in Section 6.2.2.2 we explain how the host-flare distance is used to define the nuclear flare sample.

6.2.2.1 Precise determination of host-flare distance

In this section we consider first the accuracy with which we determine the position of the flare with respect to the Sersic center of the host, and then the extent to which the Sersic center of the host is an accurate determination of the true galactic center.

The location of the flare relative to the host is found by fitting a point source corrected by the PSF to the difference image. We repeat these measurements for all reference images in all nights with detections in the g, r or i bands; this yields at least $9 \times 2 \times 2 = 36$ measurements of the distance d between the flare and the center of the host. The uncertainty on this distance in pixel coordinates, σ_x and σ_y, is

(a) Rejected: bad subtraction, one noisy filter

(b) Rejected: bad subtraction, peak displaced between filters

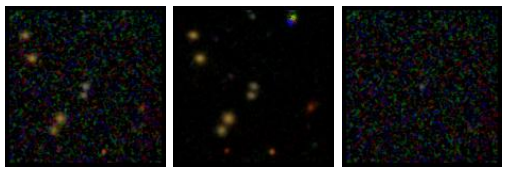

(c) Good subtraction: near the flux limit

(d) Good subtraction: off-center flare (SN)

FIGURE 6.2: Examples of bad and good image subtractions. Images size is $1' \times 1'$ (RGB=irg). Left to right: flare image, mean reference image and difference image. The bad subtractions, images (a) and (b), were rejected by manual inspection; image (c) shows the quality of a subtraction that is relatively faint, $m_r = 21.5$ in the difference image. Image (d) shows an off-center flare with $r = 0\farcs4 \pm 0\farcs02$.

obtained from the standard deviation of these measurements. As seen in Fig. 6.3, the typical measurement uncertainty on the distance between the host and the flare is 0.1 pixel. We use this as a lower limit for $\sigma_{x,y}$. To divide flares into categories of clearly nuclear, clearly non-nuclear or ambiguous, we define $\sigma_d \equiv \sqrt{(x\sigma_x)^2 + (y\sigma_y)^2}/d$, which is a measure of the uncertainty on the host-flare distance.

In the above, d is defined with respect to the coordinates of the optical center of the host obtained by fitting a Sersic profile to the convolved reference image. However a deviation from azimuthal symmetry in the galaxy (e.g., an H II region) may cause the center found by fitting a Sersic profile to be offset from the true center, thus causing

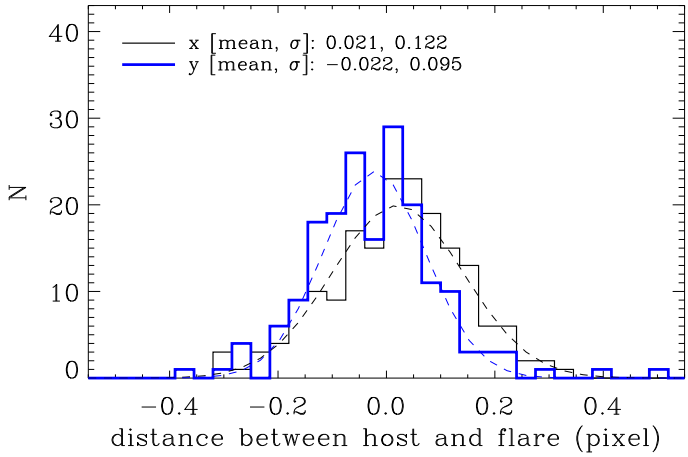

FIGURE 6.3: Histogram of the distance between the center of the host and the flare for all 186 nuclear flares (eq. 6.1). The dashed lines display the best-fit Gaussian distribution. As expected for nuclear flares, the distribution peaks at zero. The mean accuracy on the distance between the host and the flare for the nuclear sample is about 0.15 pixel or 0.″06. This is similar to the SDSS single epoch astrometric accuracy for point sources brighter than $m_r \sim 20$ (Pier et al. 2003).

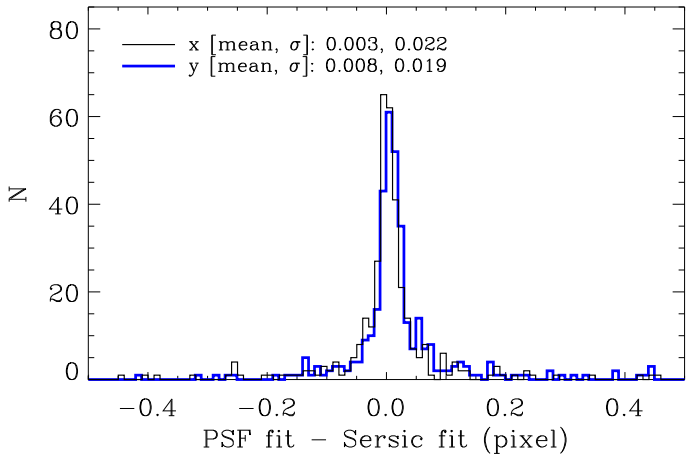

FIGURE 6.4: The distance between the center of the galaxy obtained by fitting a Sersic profile and the center obtained by fitting a PSF. Irregularities in the galaxy may push the center obtained by the Sersic fit away from the true geometrical center. To enhance this potential systematic uncertainty, we subtract 50% of the best-fit Sersic model galaxy from the original image before fitting the PSF to find the center. We find that for almost all galaxies the two methods of locating the center agree very well: the Sersic profile is not significantly affected by irregularities. (1 pixel corresponds to 0.″4)

an error in determining the separation of the flare from the galaxy center. We have investigated the impact of this on our accuracy, galaxy-by-galaxy, by comparing the center obtained from a Sersic fit to the center obtain by fitting the PSF to the galaxy. To enhance any deviation, we subtract 50% of the best-fit azimuthally symmetric model galaxy from the original image before fitting the PSF. As shown in Fig. 6.4, the two methods on average yield the same answer. Visual inspection of the few galaxies with large (> 0.1 pixel, i.e., $0\farcs04$) deviations between the two ways of measuring the center shows that they indeed have more complicated shapes or consist of close pairs of galaxies. In those rare cases that the magnitude of the difference between the PSF and Sersic centers in either coordinate is larger than the uncertainty on the separation between the flare and Sersic center, we take the flare positional uncertainty $\sigma_{x,y}$, to be the former.

Now, with the positional uncertainties understood, we proceed to define our flare sample. First, we set the maximum distance between the host and the flare to $d < 1''$ and remove all transients detected beyond this radius from our flare sample. In addition, we demand that the distance between the host and the flare is measured with a minimum accuracy of $\sigma_d < 0\farcs1$. After applying these cuts, we are left with flares in 342 galaxies.

6.2.2.2 Separating nuclear flares from non-nuclear flares

In this section we use the distance d between the center of the host galaxy and the flare to divide the sample of 342 flares into two well-separated samples of 186 nuclear flares and 85 off-center flares, plus 71 flares that are not used because their classification is ambiguous.

We begin by determining the overall fraction of SNe in the full sample of 342 flares, $P(\mathrm{SN})$. To do this we model the distribution in d as a sum of nuclear flares and stellar-distributed flares (i.e., SNe). The unsmeared probability density function (PDF) for nuclear events is a delta function at $d = 0$. We assume that stellar flares trace the stellar light, as is justified by the discussion in Section 6.4.2. The flare detection efficiency as a function of d has been modeled and tested against observations, as will be reported in detail elsewhere; for our purposes it is sufficient to note that the detection efficiency should be at most weakly dependent on d, except for a possible reduction in efficiency near the nucleus. We confirm this *a posteriori* below.

Under these assumptions, the unsmeared PDF for stellar-distributed flares at distance $d+\Delta d$ from the host center is given by the sum total galaxy flux in this interval. For each host galaxy, the surface brightness profile, $F(d)$, is taken to be that of the PSF-corrected model galaxy corresponding to the best-fit Sersic parameters in the r-band. We smear the nuclear and stellar PDFs of each galaxy according to the measured uncertainty in the flare separation for that galaxy, σ_x and σ_y.

We make an unbinned maximum likelihood fit to the sum of the resulting stellar-distributed PDF, times $P(\mathrm{SN})$, plus the nuclear PDF, times $1-P(\mathrm{SN})$, to the observed

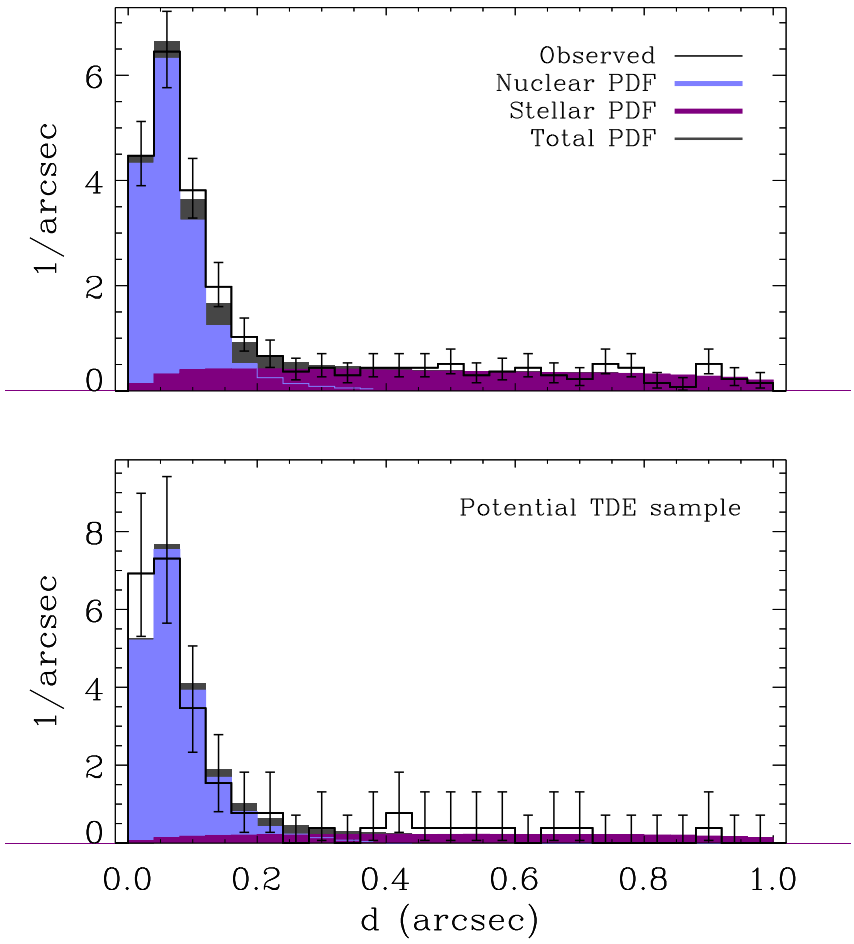

FIGURE 6.5: The observed distribution of host-flare distances (thin black histogram, with error bars given by Poisson statistics), the fit (filled black histogram) with the decomposition into nuclear flares (blue histogram) and SNe (purple histogram), all normalized to unit area. The only free parameter in the fit is the fraction of stellar-distributed flares, $P(\mathrm{SN})$. The top panel shows the d distribution for the full sample of 342 flares; the bottom panel shows the flare sample that remains after requiring at least 2 observations after the peak of the flare, imposed for TDE analysis.

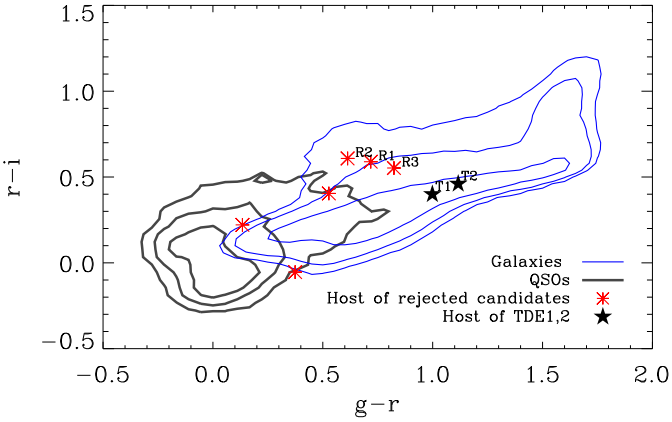

FIGURE 6.6: Color-color diagram of the PSF flux (Stoughton et al. 2002) for the 2.5×10^6 extended objects in Stripe 82 that were used in this work (thin blue line) and the SDSS QSO sample (Schneider et al. 2007) with $z < 1$. For both samples, contours encompass 50, 80 and 90%. The TDE candidates that fall outside the QSO locus but are rejected based on additional variability are labeled R1–R3; TDE1 and TDE2 are labeled T1 and T2, respectively.

d distribution, with the result $P(\mathrm{SN}) = 0.34 \pm 0.04$ (90% CL). The observed and predicted distributions are shown in Fig. 6.5 (top panel). The quality of this fit, in which the SN fraction $P(\mathrm{SN})$ is the only free parameter, validates the assumption that the detection efficiency is independent of d for $d > 0\farcs2$ and shows that we understand the distribution of host-flare separations.

Based on Fig. 6.5, we formulate the cut for nuclear flares:

$$\mathrm{cut} \equiv (d/\sigma_d < 2) \text{ and } (d < 0\farcs2) \quad . \tag{6.1}$$

This gives 186 on-center flares, with a loss of 15% of the true nuclear flares. The probability of a background event (i.e., a stellar-distributed flare within this cut), can be computed directly from the d-histogram and is $P(\mathrm{SN}|\mathrm{cut}) = 0.052$, giving an expected number of background events in the total nuclear flare sample of 10. This result is independent of whether the g, r or i-filter is used to obtain the surface brightness profile of the galaxies. This procedure gives an upper bound on the contamination of the SNe in the nuclear sample, since a possible reduction in detection efficiency for $d < 0\farcs2$ would result in a lower predicted number of SNe in the nuclear sample (and larger rate of nuclear flares relative to SNe, generating the observed flare sample).

A high-purity sample of flares which are clearly off-center from their host is obtained by requiring

$$(d/\sigma_d > 3) \text{ and } (d > 0\farcs2) \quad . \tag{6.2}$$

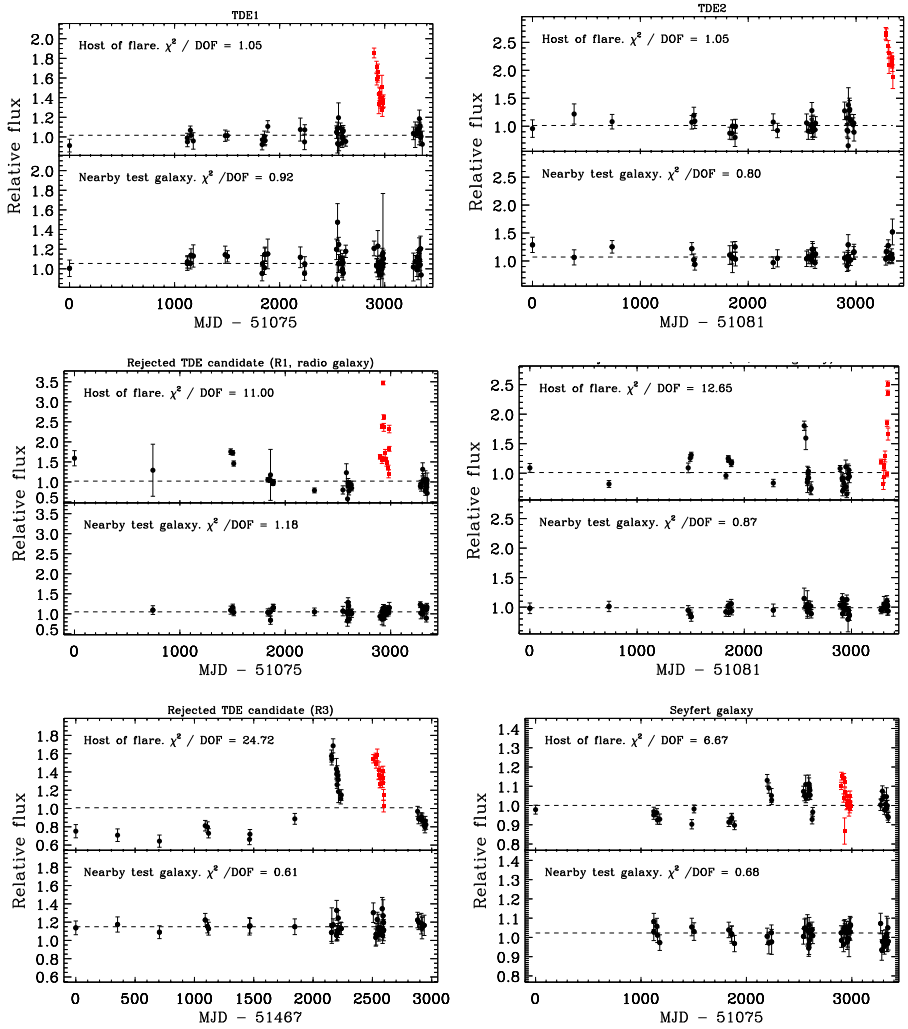

FIGURE 6.7: Relative photometry light curves, using the Petrosian g-band flux, of the hosts of potential TDEs and one Seyfert (see Section 6.4.1). Each observation is scaled using the flux of nearby (distance $< 20'$) galaxies that are of similar magnitude ($\Delta m < 1$). The lower portion of each panel displays the light curve of one of the ten test galaxies. The observations in the season that contained the flare (indicated with red boxes) are excluded in the calculation of χ^2. Variability in the non-flare season is evident for all galaxies except the host of TDE1,2.

This selects 85 flares, of which 27% have been spectroscopically identified as SNe by the Sloan Digital Sky Survey-II Supernova Survey (Frieman et al. 2008). We assume that the remaining off-center flares are SNe as well and take these 85 flares as our SN sample below. It is important to note that – because this sample is obtained by a cut on the host-flare distance only – the properties of the SNe in this sample are not subject to the selection biases that exist for spectroscopic SNe surveys, and are representative of the properties of SNe that appear in the nuclear sample (to the extent that SNe properties are independent of their location in the host galaxy).

6.2.2.3 Potential TDE sample

To be able to obtain a well-measured decay rate – a valuable diagnostic in separating SNe, AGN flares, and TDE flares – we require at least two detections after the peak of the flare in the u, g and r bands. (At this step, the nuclear – potential TDE – sample is reduced to 42 flares and SNe sample to 12 flares.) Repeating the d-distribution analysis of Section 6.2.2.2, the expected number of residual SNe in the nuclear flare sample is 0.9. The corresponding histogram is shown in Fig. 6.5 (bottom panel).

6.2.3 AGN rejection

AGNs are well-known to be variable and we expect that the majority of the 42 nuclear flares that remain at this stage of the analysis originate from active black holes. Fortunately, AGN hosts are readily identified using SDSS spectra of the host galaxy and, with a small loss in efficiency, can be identified photometrically too. After applying these methods to identify AGNs in sections 6.2.3.1 and 6.2.3.2, five potential TDE remain. Motivated by previous work on Stripe 82 showing that at least 90% of unresolved, spectroscopically confirmed quasars are variable at the 0.03 mag level (rms) (Sesar et al. 2007), in Section 6.2.3.3 we use variability beyond the flare season to reject three more AGNs, leaving only two flares, we label these TDE1 and TDE2.

6.2.3.1 Spectroscopic AGN Identification

SDSS spectra with a median S/N greater than 3 are available for about 2/3 of the hosts of the 186 nuclear flares. The Princeton Reductions[1] classify galaxies with spectra into three classes using a Principal Component Analysis: STAR, GALAXY or QSO. Here, QSO does not refer to the classical $M_B < -21$ luminosity cut, but implies that the spectral energy distribution (SED) is dominated by an AGN-like spectrum inside the fiber ($3''$) that was used to obtained the spectrum. Of the 42 nuclear flares suitable for our TDE analysis, 32 are in hosts that are classified as QSOs; we eliminate these from our candidate sample. We also reject hosts in the class GALAXY which we can identify as Seyfert galaxies based on either of the following criteria:

[1] http://spectro.princeton.edu

- Galaxies that show broad (> 200 km/s line-width, at the 7-σ level) Hα, Hβ, [OIII]λ5007, [OII]λ3727, or MgIIλ2799 emission lines. We only consider lines detected at the 3-σ level with rest-frame equivalent width > 5Å.

- Galaxies that can be classified as Seyferts using the Baldwin, Phillips, & Terlevich (1981) diagram:

$$\log\left(\frac{[\mathrm{OIII}]\lambda 5007}{\mathrm{H}\beta}\right) > \frac{0.61}{\log(\mathrm{NII}\lambda 6583/\mathrm{H}\alpha) - 0.05} + 1.3 \tag{6.3}$$

  (Kauffmann et al. 2003). We apply this formula only if all four emission lines are measured at the 3-σ level.

This eliminates two more objects from the TDE analysis, reducing the sample of potential TDEs to 8 flares.

6.2.3.2 Photometric AGN Identification

We use the photometric properties of the hosts of the 8 flares that remain at this point to test if they are QSOs. We define a locus that contains 90% of the 20,710 spectroscopic QSOs identified by SDSS (Schneider et al. 2007) with $z < 1$ and reject all hosts that fall inside; 23% of the $\sim 2.5 \times 10^6$ galaxies that were in the original sample and processed in the flare search fall inside this locus. This cut on QSO locus removes 3 flares from the potential TDE sample, see Fig. 6.6.

6.2.3.3 Additional AGN variability

Fig. 6.6 shows that the hosts of five flares in the potential TDE sample fall outside the QSO locus. We investigated the light curves of these hosts to look for additional variability beyond the season that contains the flare. Having an efficient but accurate means to quantify the flux variability is applicable to a number of studies, so in this subsection we give details of the method we use to produce relative flux light curves.

As explained in Section 6.2.1.1, we use the SDSS Petrosian flux to search for flares in a galaxy light curve. The Petrosian flux is designed to yield a robust estimate of the total flux of a galaxy (Blanton et al. 2001; Stoughton et al. 2002), yet night to night differences in seeing or other observational conditions introduce a small amount of jitter to our light curves. In most cases, nearby and similar galaxies suffer the same attenuation (e.g., worse seeing causes a lower Petrosian flux for all faint galaxies in the field), hence this jitter can be reduced by normalizing the observations of each night using a set of reference galaxies. For each host of a flare, we select this set by looking for nearby (within $20'$) galaxies, whose apparent magnitude difference (in a given filter) with respect to the target host is less than one, and for which the rms variance in the magnitude in all observations is smaller than 30%; this typically yields 70–100 galaxies for each host. For each point in the light curve of the host, we determine an overall flux correction by averaging the rescalings required to bring the

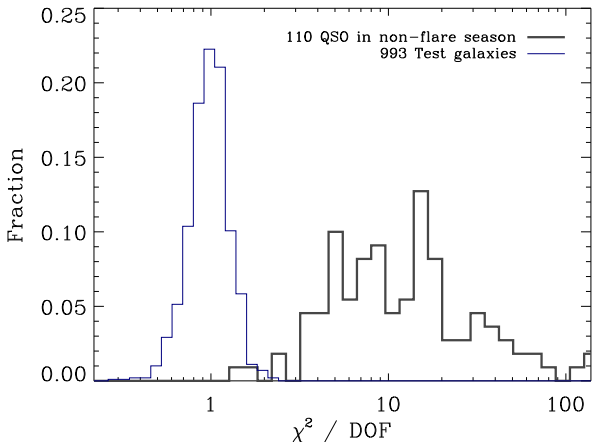

FIGURE 6.8: Histogram of χ^2/ DOF obtained for the relative photometry light curves fit to a constant flux, showing the difference between QSOs and ordinary galaxies. We use the non-flaring seasons for the QSO, and all seasons for the nearby test galaxies (see Section 6.2.3.3). For three spectroscopically identified Seyfert galaxies with flares we find: χ^2/DOF = {5.14, 2.51, 1.54}. The lowest value in this list is larger than 99% of the test galaxies. We may thus conclude that flares from Seyfert galaxies can also be identified based on additional variability of their host.

flux of each reference galaxy to equality with its mean flux. The above procedure can be applied to any filter; for our variability studies we use the Petrosian g-band flux.

To test the quality of the resulting light curves, we select ten test galaxies from among the reference galaxies, chosen to be even more similar to the host of the flare by requiring $|\Delta m| < 0.3$. Sometimes, fewer than ten test galaxies are found; if none are found, no relative flux light curve is produced for this host. SDSS provides errors – let us call them $\sigma_{\mathrm{SDSS}\,i,t}$ – for each observation i of each test galaxy t. We test empirically whether these error bars are a good representation of the flux uncertainty after rescaling, by computing χ^2_t, the reduced chi-squared assuming a constant flux of the light curve of the each test galaxy. If all of the uncertainty in the flux measurement were captured in the $\sigma_{\mathrm{SDSS}\,i,t}$, the χ^2_t values would obey a χ^2 distribution but they do not. We find that the errors reported by SDSS sometimes underpredict the true uncertainty of the flux. We therefore use the fact that the expectation value of χ^2 per degree of freedom should equal 1 for the test galaxies, to obtain a better estimate of the measurement uncertainty on the relative flux the host or any of its test galaxies, e.g., $\sigma_i = \sigma_{\mathrm{SDSS}\,i}\sqrt{<\chi^2_t>}$.

The relative flux light curves produced by this method using the Petrosian flux in the g-band for the five potential TDEs are displayed in Fig. 6.7. Three of the hosts clearly show additional flaring activity: χ^2 per degree of freedom of the flux calculated from their relative flux light curves excluding the season with the primary flare is > 10; for reference, we label these R1–R3. However two hosts show no additional

Name	z	M_g	L_g (10^{43} erg s^{-1})	$d\ln L_g/dt$ (10^{-2} day^{-1})
TDE1	0.136 ± 0.001	-18.3 ± 0.04	0.54 ± 0.02	-1.7 ± 0.1
TDE2	0.251 ± 0.002	-20.4 ± 0.05	4.1 ± 0.2	-0.8 ± 0.1
	T (10^4 K)	$d\ln T/dt$ ($\times 10^{-3}$ day^{-1})	d (")	d_{68} (")
TDE1	$2.4^{+0.3}_{-0.2}$	-2 ± 4	0.058	0.124
TDE2	$1.82^{+0.07}_{-0.06}$	-3 ± 2	0.068	0.075

TABLE 6.2: Properties of the TDEs. The rest-frame g-band peak observed absolute magnitudes, luminosities and blackbody temperatures of the flares, measured in their SDSS difference images. We exploited the absence of significant color evolution to improve the accuracy of the blackbody temperature determination by using the mean flux in each band over the SDSS light curve. In the eighth column, d denotes the distance between the center of the host and the flare (see Section 6.2) and d_{68} the 68% confidence radius. The host properties (including coordinates) are given in Table 6.3.

variability, with each having $\chi^2/\mathrm{DOF} = 1.05$. We show in Fig. 6.8 that this is significantly smaller than measured for any QSO or Seyfert galaxy in our sample. These are the hosts of the flares we designate as TDE1 and TDE2. In Section 6.4.1 we use the observations of QSOs and Seyferts to quantify the probability that TDE1 or TDE2 are flares from AGN which had quiet years in the other observing seasons.

6.3 Properties of the identified tidal flares

In this section we report on the properties of the two stellar tidal disruption flare candidates, based on SDSS imaging data and observations using other instruments. Although we did not rely on properties of the flaring state to *select* TDEs, to avoid unnecessarily biasing the selection and because theoretical predictions are uncertain, the TDEs identified by our pipeline prove to be quite distinct from SNe and flaring AGNs. This increases confidence that TDE1,2 are not examples of familiar phenomena occurring in improbable circumstances, such as SNe accidentally close to the nucleus or AGNs which flare dramatically in the midst of a multi-year quiet phase.

We begin with an overview of the two events by giving their light curves, cooling rate and flare colors based mainly on the SDSS Stripe 82 observations. The SDSS images of the TDEs and their host galaxies are given in Fig. 6.9. Tables 6.2 & 6.3 summarize the properties of the TDEs and their hosts, respectively. Then we describe the observations of TDE1 and TDE2 obtained with other telescopes. Finally, we combine the observations to quantify attributes of the host and flare relevant to the possibility they may be produced by a supernova or variable AGN. In Section 6.4, we attempt to account for the totality of these observations with supernovae and variable AGN hypotheses, but find that no known phenomenon other than tidal disruption is compatible with all of the observations.

(a) TDE1

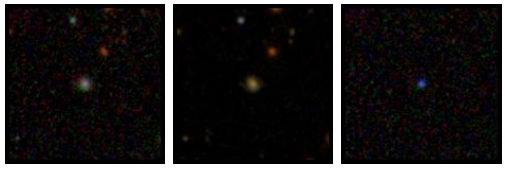

(b) TDE2

FIGURE 6.9: False-color (RGB=*irg*) images ($1' \times 1'$) of the TDE flares and their host galaxies. Left to right: flare image, mean reference image and difference image for TDE1 and TDE2. We see that the hosts can be classified as E/S0. The difference image of TDE1 shows a subtraction artifact at the location of the bright point source, which is not subtracted perfectly because our difference imaging method is optimized for the center of the field.

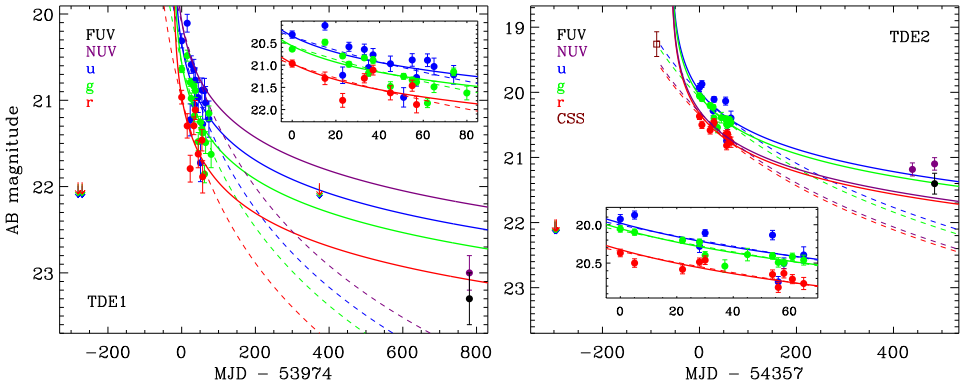

FIGURE 6.10: UV and optical light curves for TDE1 and TDE2 as a function of days since observed peak. The SDSS difference image flux (i.e., host subtracted) in the r, g, and u bands is shown with red, green, and blue solid circles. The orange open square indicates the mean of the 3 CSS observations 3 months before the first SDSS flare observation (see Section 6.3.3.3). The dashed (solid) lines display the result of fitting a $(t - t_D)^p$ power law decay with $p = -5/3\,(-5/9)$ to the SDSS observations only. The corresponding NUV curves (purple) are obtained from the blackbody fit to the mean optical colors of the flare, assuming no cooling. Because the UV baseline of the host of TDE1 is unknown, we show the *GALEX* aperture flux for TDE1, while for TDE2 we show the *GALEX* difference flux.

Flare	RA (J2000)	Decl. (J2000)	M_r	$u-g$	$g-r$	$M_{\rm BH}$ ($M_\odot$)
TDE1	350.95257	−1.1361928	−19.85	1.95 ± 0.3	0.73 ± 0.02	$(6\text{–}20)\times10^{6\pm0.3}$
TDE2	355.50586	1.1081316	−21.30	0.99 ± 0.2	0.73 ± 0.05	$(2\text{–}10)\times10^{7\pm0.3}$

TABLE 6.3: Properties of the hosts of the TDEs. The host magnitude and colors are obtained from the K-corrected (Blanton & Roweis 2007), inverse-variance-weighted mean Petrosian magnitude of the non-flare seasons. The black hole mass is estimated using the correlation between M_r and $M_{\rm BH}$ (Häring & Rix 2004; Tundo et al. 2007), using two different estimates for the bulge magnitude (see Section 6.3.1).

6.3.1 SDSS observations

Figure 6.10 shows the u, g, and r-band light curves for the flares (i.e., the difference images). Also plotted are the FUV and NUV fluxes from *GALEX* (see Sections 6.3.2 & 6.3.3 for details on these *GALEX* observations), and the flux estimated from the CRTS optical observation of TDE2 3 months prior to the first SDSS observation in the flaring state (see Section 6.3.3.3). Both flares were detected by SDSS in the first observation of a Stripe 82 season, so were most likely past their peaks when first detected; this is confirmed by the CRTS detection in the case of TDE2 (see Section 6.3.3.3). For comparison, we show fits of the SDSS data to $f_\nu(t) \propto (t-t_D)^p$, where t_D is the time of disruption. The SDSS optical observations do not cover a long enough period to break the degeneracy between t_D and p. For $p=-5/3$ (the fallback rate of the debris (Rees 1988)), the inferred time delay between when the disruption occurred and when it was first observed by SDSS is 107 and 220 days for TDE1,2 respectively, while for $p=-5/9$, as predicted by Strubbe & Quataert (2009) for the initial super-Eddington outflow phase, these become 24 and 55 days. In Fig. 6.10 we show the $p=-5/3$ and $-5/9$ extrapolations assuming constant temperature to obtain the NUV magnitude, for orientation.

The photometric observations are well-fit by a rest-frame blackbody spectrum with temperatures given in Table 6.2, as can be seen in Fig. 6.11. An estimate of the cooling rate was obtained by least-squares fitting for the slope of color as a function of time, using only SDSS observations starting with the peak of the flare. We also computed the mean colors by averaging all observations of the flare. Comparing the mean color to the cooling (Fig. 6.12a), gives strong evidence that the TDE flares are not (ordinary) supernovae: they are very much bluer than any observed off-center flare in our sample and show negligible cooling, whereas SNe are either blue and rapidly cooling or red with little cooling because they start hot and cool very rapidly. Furthermore, Fig. 6.12b shows that the colors of the TDE1,2 flares are strikingly different from those of QSOs; if these were AGN flares, the spectrum of the flare itself (with the galaxy subtracted) should more closely resemble the spectrum of a QSO flare.

To estimate the black hole mass ($M_{\rm BH}$) of the host of TDE1,2 we use the Häring & Rix (2004) black hole mass-bulge mass relation, calibrated for the SDSS r-band by

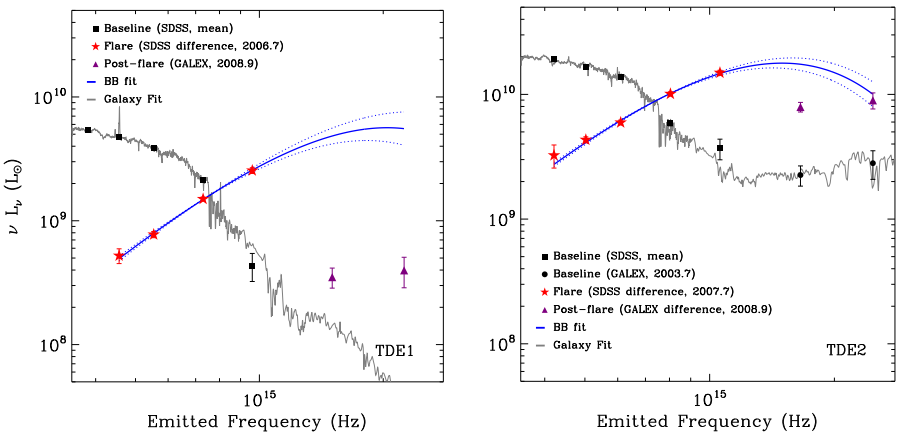

FIGURE 6.11: The SED for TDE1 (top) and TDE2 (bottom). The optical baseline flux of the host is shown (black squares) with the best-fit combination of eigen spectra (Blanton & Roweis 2007) (gray line). For TDE2, the *GALEX* observations before the flare (black circles) are also used in this fit. The flux of the flare in the optical difference images is shown with red stars. It is well-fit by a blackbody shown as a blue line, with dotted lines indicating the 1-σ uncertainty. The post-flare UV flux is shown with purple triangles; for TDE1 it is the total flux (no baseline being available) while for TDE2 the difference flux is shown. The detailed interpretation of the post-flare UV detections are unclear; the dynamics of the tidal debris and associated accretion are complex – a single blackbody need not be valid and the cooling behavior is uncertain.

Tundo et al. (2007). Unfortunately, the S/N in the co-added images of the host of the flare is too low to measure the bulge magnitude by decomposing the images into a bulge and disk component. We therefore estimate the bulge magnitude using two different assumptions for the bulge-to-total ratio (B/T). *(i)* The typical ratio for S0 galaxies, $B/T = 0.55$ (Aller & Richstone 2002). *(ii)* The ratio that follows from the correlation between B/T and the concentration index (i.e., R90/R50, where R90 and R50 are the radii enclosing 90 and 50 percent of the galaxy flux) (Gadotti 2009), which yields $B/T = 0.16, 0.13$ for TDE1,2. Using these estimates to obtain a range for the bulge luminosity of the host we obtain $M_{\rm BH} = (6-20) \times 10^{6\pm0.3}\,M_\odot$ for TDE1 and $M_{\rm BH} = (2-10) \times 10^{7\pm0.3}\,M_\odot$ for TDE2, where the error in the exponent reflects the scatter in the $M_{\rm BH}$-bulge luminosity relation and the range in the prefactor reflects the uncertainty in the bulge luminosity.

6.3.2 Additional observations of TDE1

For TDE1 we have a single *GALEX* NUV and FUV detection on 2008 October 25, $\sim$ 800 days after the optical flare. The *GALEX* UV flux values, corrected for the energy lost due to the 6″ radius aperture, and using the pipeline-generated sky background

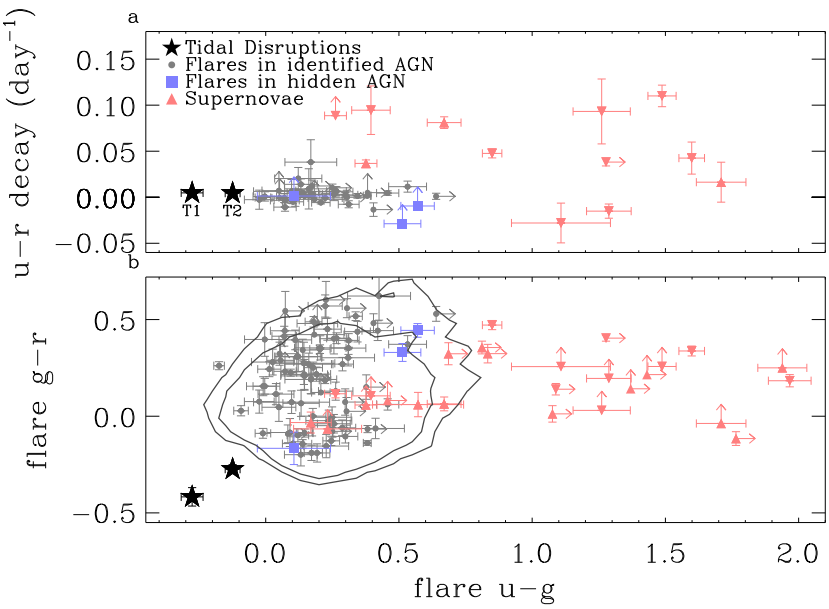

FIGURE 6.12: *a:* The cooling time measured by fitting $u-r$ as a function of time. The two TDE candidates are incompatible with being ordinary SNe because they show no signs of cooling and have very blue colors. *b:* Color-color diagram using the mean colors of the decaying part of the light curve. Contours containing 90 and 95% of 14,776 nearby ($z < 0.8$) spectroscopic QSOs (Richards et al. 2004) are also shown. Fewer objects appear in the upper panel because two simultaneous detections in both bands are required to measure the cooling time. For SNe and potential TDEs, the flux shown is that of the difference image; AGN are shown in their high state. Colors are obtained from the error-weighted mean of all observations of the flare. Blue boxes mark flares from hosts that are not identified as AGNs based on their spectra or color, but whose variability in other seasons shows they are, in fact, AGN. The supernovae in this work are selected purely geometrically by being off-center (Eq. 6.2) and thus their properties are unbiased. The SNe that survive the TDE quality cuts (Sec. 6.2.2.3) are indicated with a downward pointing triangles.

value in counts per pixel and assuming Poisson errors aperture (Morrissey et al. 2007), are: FUV $= 23.3 \pm 0.3$, NUV $= 23.0 \pm 0.2$. These UV magnitudes are plotted in Figs. 6.10 and 6.11 without host subtraction since we have no pre-flare observation to establish the baseline.

We observed the host galaxy of TDE1 on 2009 November 7 with the MagE spectrograph on the Magellan II Clay telescope with a spectral resolution of $R = 4100$ or 1.6 Å. The spectrum, shown in Fig. 6.13, shows Balmer absorption features, as well as Mg Ib and NaI absorption, which yields $z = 0.136 \pm 0.001$. No emission lines are detected: $L_{\mathrm{H}\alpha} < 4.4 \times 10^{37}\,\mathrm{erg\,s^{-1}}$ and $L_{[\mathrm{OIII}]} < 1.3 \times 10^{38}\,\mathrm{erg\,s^{-1}}$.

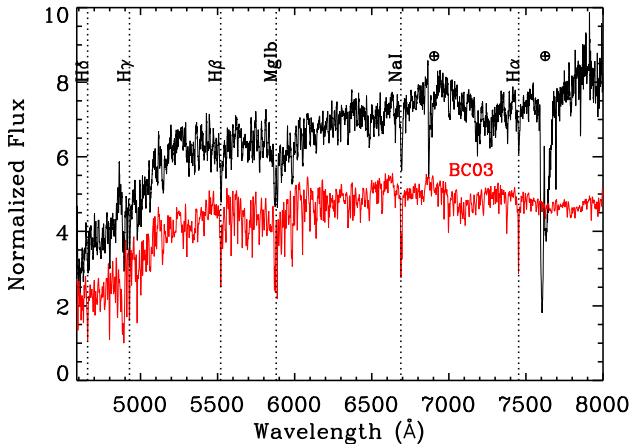

FIGURE 6.13: Host spectrum of TDE1. A template Bruzual & Charlot (2003) spectrum is also shown. Note lack of [OIII] emission lines and the Hα absorption. Hatch marks indicate the locations of the strong O_2 telluric B- and A-band absorption features that were not removed in the data reduction.

6.3.2.1 Origin of UV emission of TDE1

Star formation contributes little to the observed UV in TDE1. This follows from the $L_{\mathrm{H}\alpha}$–L_{FUV} relation (Kennicutt 1998) which predicts that if the FUV luminosity observed by *GALEX* ∼800 days after the optical flare were due to star formation, the Hα luminosity should be 2.4×10^{40} erg s^{-1} – two orders of magnitude above the observed upper limit. The contribution of stellar sources that evade the correlation between FUV and Hα (e.g., blue horizontal branch stars) is constrained by using the color-magnitude relation observed by Haines et al. (2008) for galaxies that have been spectroscopically identified as passively evolving. At the luminosity of the host of TDE1 ($M_r = -19.85$), these galaxies are observed at NUV $- r = 5.4$. The scatter in this relation, $\sigma_{\mathrm{NUV}-r} = 0.37$, can be attributed to different amounts of residual star formation. Thus the UV detection of the host of TDE1, with NUV$-r = 3.6$, is a 4.6-σ blue outlier to these galaxies. Moreover, with FUV$-r = 3.7 \pm 0.3$, it is distinctly bluer than passive galaxies of similar luminosity, which cluster at FUV $- r = 7$. The UV color, FUV$-$NUV $= 0.0 \pm 0.36$, is also bluer than any of the early type galaxies which have been targeted by the SAURON project (Jeong et al. 2009) to study residual star formation. These galaxies are observed to cluster at FUV $-$ NUV $= 1.5$, with the bluest object at FUV$-$NUV $= 0.6$. Recent or residual star formation is thus excluded as a significant contributor to the observed UV emission detected 800 days after the first observation of TDE1.

Nor can an active nucleus account for the observed UV flux 800 days after the TDE1 flare. The upper limit on the [OIII] luminosity from the Magellan spectrum places a limit on the optical baseline luminosity of a possible active nucleus. Using

the conversion between [OIII] and optical luminosity for type 1 AGNs obtained by Heckman et al. (2004), yields an upper limit on the luminosity of an active nucleus in the TDE1 host: $L_{5000} < 4.2 \times 10^{40\pm0.34}\,\mathrm{erg\,s^{-1}}$, where L_{5000} is the monochromatic continuum luminosity at 5000 Å in the rest frame. Although the Heckman et al. (2004) relation is not valid for [OIII] emission from LINERs (Heckman 1980), we can still use it to obtain an upper limit on the baseline luminosity of a potential AGN in such galaxies, because at similar [OIII] luminosity, the active nuclei of LINER galaxies have an order of magnitude lower bolometric luminosity compared to normal AGNs, as well as an lower optical luminosity for a given bolometric luminosity (Ho 1999). We convert L_{5000} to a g-band magnitude (centered at $\lambda = 4670\,\text{Å}$), by assuming that the luminosity per unit wavelength at the g-band is equal to L_{5000}. This is the conservative approach since $F_\nu \propto \nu^{-0.44}$ is typical for an AGN (Vanden Berk et al. 2001). This yields NUV $- g < -2.9 \pm 0.9$, a NUV to g-band ratio greater than the maximal value that can be reached with photons that are in thermal equilibrium; such an extreme color has never been observed for any of the sources detected in both SDSS and *GALEX* (Bianchi et al. 2007). Because we obtained our upper limit on the g-band luminosity of the accretion disk from the [OIII] line, this limit applies to the baseline luminosity of the AGN, i.e., time-averaged over the light crossing time of the narrow line region, $> 10^2$ yr (Murayama & Taniguchi 1998). Thus we conclude that the UV flux present 800 days after the optical flare does not originate from the baseline of an AGN.

6.3.3 Additional observations of TDE2

We have *GALEX* NUV and FUV detections of the TDE2 host in both the pre-flare (2003 24 August) and post-flare (2008 14 October) state. The TDE2 host was also observed by *GALEX* on 2008 30 August, but the image was at the edge of the field and the sky was noisy, so we display the NUV value in Fig. 6.10b) but do not use it further. Figure 6.14 shows the *GALEX* images. The pre-flare *GALEX* UV flux values, corrected for the energy lost due to the 6″ radius (Morrissey et al. 2007), are FUV $= 23.0 \pm 0.3$, NUV $= 22.8 \pm 0.2$. The *GALEX* post-flare *difference* magnitudes are: FUV $= 21.4 \pm 0.2$, NUV $= 21.1 \pm 0.1$. Figure 6.11b shows the optical-UV SED.

In addition to the UV data, we have two serendipitous and two follow-up optical observations of TDE2 and its host as discussed in greater detail below. The spectrum of the host galaxy was obtained in a follow-up observation with the William Herschel Telescope (WHT) in November 2010. Serendipitously, the first points on the SDSS light-curve of TDE2 suggested it might prove to be a supernova and an alert was issued (Pojmanski 2007). As a result, an optical spectrum was obtained with ESO's New Technology Telescope (NTT) on 2007 September 18, 4 days after the first detection of the flare, and radio observations were obtained with the VLA 7 and 92 days after the first SDSS detection; these observations are discussed in Section 6.3.3.1 below. Furthermore, a review of Catalina Real-time Transient Survey observations

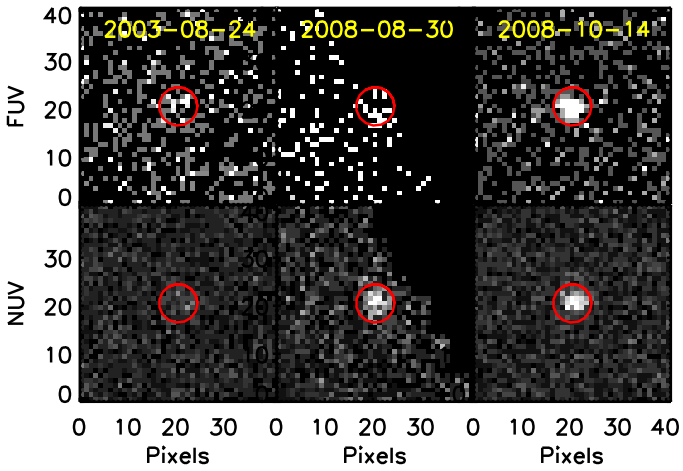

FIGURE 6.14: *GALEX* FUV and NUV images before and during the flare in TDE2. Red circles show the 6 arcsec radius aperture used to measure the photometry. The plate-scale of the image is 1.5 arcsec/pixel. Note that in the second epoch (2008-08-30), the source is at the edge of the field where the photometry is more susceptible to systematic errors due to distortions in the PSF.

after discovery of TDE2 reveals a detection of the flare 95 days before the beginning of the Stripe 82 observing season. A preliminary report on this data is given in Section 6.3.3.3.

6.3.3.1 TDE2 Host and Flare Spectra

In November 2010, 850 days after the first SDSS detection of the flare, the host galaxy of TDE2 was observed with the WHT for two nights. On 01 November two ACAM exposures of 900s were taken using a V400 grating and a slit width of 1". On 05 November, the host was observed again using the same specifications and exposure times, except that a slit width of 1.″5 was used. The data of both nights (1h total integration time) was reduced separately, using standard IRAF[2] routines, to yield four 1D spectra which were then combined. The overall flux normalization was obtained using a standard reference star; the wavelength dependent flux normalization was fixed using the SDSS PSF flux of the host.

The NTT spectrum – taken 5 days after the first SDSS detection of the flare – was taken using the ESO Multi-Mode Instrument (EMMI) (Dekker et al. 1986) in the RILD mode (Red Imaging and Low-Dispersion spectroscopy). The grism that was used, Gr 2, has a wavelength coverage of 3800-9200 Å, 300 grooves/mm, a wavelength dispersion of 1.74 Å/pixel, and a spatial resolution of 0.″166 /pixel (before binning).

[2]IRAF is distributed by NOAO, which is operated by AURA, under cooperative agreement with NSF

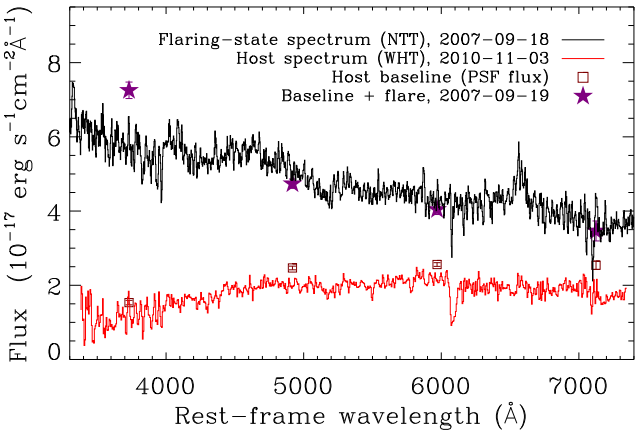

FIGURE 6.15: Host and flaring-state spectra for TDE2: NTT spectrum in the flaring state and WHT spectrum of the host. We also show the SDSS PSF (Stoughton et al. 2002) flux of the host in the quiescent state (open squares) and the SDSS flux during the flare (purple stars). We see that the photometric and spectroscopic flux calibration agree reasonably well. The narrow Hα emission is consistent with the level expected from star-formation as implied by the pre-flare FUV luminosity (Kennicutt 1998). A zoom on Hα is shown in Fig. 6.16.

During the observation a binning of 2x2 was used. The slit width was 1.″5 and the exposure time was 1200 s. The flux calibration was performed using spectra of spectrophotometric standard stars observed with a 5″ slit. The standard star spectra were also used to construct a telluric spectrum by isolating the telluric absorption in them. The spectrum of TDE2 was then corrected by subtracting a scaled version of the telluric spectrum. Finally the spectrum was corrected for dust extinction in the Milky Way (Schlegel et al. 1998) using the Cardelli et al. (1989) CCM extinction law with $R_V = 3.1$. For a more detailed description of the data reduction we refer to Östman et al. (2011). Because the spectrum of TDE2 was not obtained in parallactic angle, it is affected by differential atmospheric refraction. The wavelength dependent flux loss was estimated and corrected for, taking into account the seeing, slit width, airmass, the angle from parallactic angle and the wavelength at which the object was centered on the slit (Owens 1967).

Figure 6.15 shows the host and flaring-state spectra together with the SDSS photometry; a zoom on Hα is shown in Fig. 6.16. The H_α line luminosity in the host spectrum, measured by fitting the observed flux to a Gaussian whose width is given by the PSF, is $L_{\mathrm{H}\alpha} = 1.2 \pm 0.2 \times 10^{40}\,\mathrm{erg\,s^{-1}}$; we simultaneously fit for the [NII] emission lines which yields $\log([\mathrm{NII}]\lambda6583/\mathrm{H}\alpha) = -0.4 \pm 0.2$. Using the redshift obtained from this simultaneous fit as an initial guess, we measure the flux of other well-known emission and absorption lines in the spectrum; only lines measured above the 3-σ level,

Name	EW host (Å)	EW flare (Å)	Flux host (10^{-16} erg s^{-1}cm^{-2})	Flux flare (10^{-16} erg s^{-1}cm^{-2})
H_α	4.2 ± 0.8	4.1 ± 0.7	0.8 ± 0.1	1.8 ± 0.3
[NII] 6585	1.4 ± 0.7	2.8 ± 0.7	0.2 ± 0.1	1.3 ± 0.3
Ca H	-5.7 ± 1.8	-2.8 ± 0.7	-0.8 ± 0.3	-1.5 ± 0.4
Ca K	-7.6 ± 1.3	-3.3 ± 0.7	-1.1 ± 0.2	-1.9 ± 0.4
H_δ	-3.4 ± 1.1	–	-0.6 ± 0.2	–

TABLE 6.4: Unresolved lines detected in the host (WHT) and flaring-state (NTT) spectrum of TDE2. Only lines detected above 3σ are shown.

that are displaced by no more than 2% from the initial redshift, are considered real detections. The results of running this procedure for the host and flare spectrum are shown in Table 6.4. Using all detected lines in the NTT and WHT spectrum we obtain $z = 0.2515 \pm 0.0036$. From the WHT spectrum we obtain $L_{[\mathrm{OIII}]} < 3.6 \times 10^{39}\,\mathrm{erg\,s^{-1}}$.

Because TDE2 occurred at the center of its host, the NTT spectrum contains a large galaxy component that has to be subtracted to obtain the "pure" flare spectrum. After subtraction, no narrow (i.e., unresolved) lines remain (Fig. 6.16, bottom panel). However at the rest-frame wavelength of H_α we identify a broad feature which can be fitted by a single Gaussian of $\sigma = 75 \pm 5$ Å or FWHM $= 8 \times 10^3\,\mathrm{km\,s^{-1}}$ and has an equivalent width of 87 ± 5 Å.

Besides the NTT spectrum, the initial identification of TDE2 as a possible SN also triggered radio observations. We reduced the data from two 8.5 GHz VLA observations, obtained as part of project AS 887 – the only VLA observations of this field after this event. The first VLA observation was 7 days after the first SDSS detection of TDE2 and the second was 85 days later. For both observations, we calibrated the recorded visibilities to flux density using data from short observations of 3C48, and used visibility data of PMN J2323-0317 for phase calibration (Baars et al. 1977). Imaging the two observations separately yielded no detection of TDE2 at either epoch. Combining the visibility data of TDE2, we obtained an image with an rms noise of $\sim 35\,\mu$Jy per beam using natural weighting. No source was detected at the location of TDE2, allowing us to place a 3-σ upper limit of ~ 0.1 mJy on its 8.5 GHz flux density.

6.3.3.2 Interpretation of Host and Flare Spectra

The WHT host spectrum is consistent with the conclusion based on photometry in Section 6.2.3.3, that the flare is not due to extreme variability of a hidden AGN. Such an AGN would reveal itself by a higher [NII]λ6583 to Hα ratio than observed. Using the BPT diagram (Eq. 6.3), we see that the observed ratio is consistent with the narrow Hα originating entirely from star formation. Moreover, using the Kennicutt (1998) relation, we conclude that the star formation rate inferred from the narrow Hα luminosity ($0.5\,M_\odot\,\mathrm{yr^{-1}}$) is consistent with the rate expected from the pre-flare FUV luminosity ($0.7\,M_\odot\,\mathrm{yr^{-1}}$).

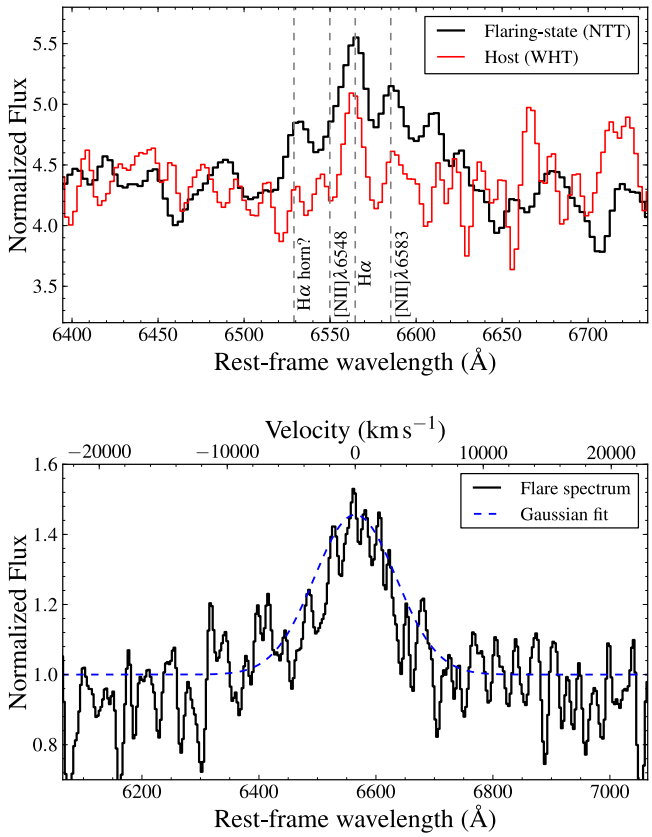

FIGURE 6.16: Zoom on the Hα emission of TDE2 for the flaring-state and host spectrum (top) and the host-subtracted spectrum (bottom). The host spectrum is arbitrarily rescaled for comparison to the shape of the flare spectrum. For display purposes, all spectra are smoothed using a Gaussian filter with $\sigma = 1.5$ Å. The intermediate width Hα line in the host-subtracted spectra can be fit with a single Gaussian to find a FWHM of 8×10^3 km s^{-1}. The feature at 6529.7 Å is marginally detected (EW $= 1.5 \pm 0.7$ Å); it may be interpreted as weak, blueshifted Hα emission (with a velocity of 1.5×10^3 km s^{-1}), but is more likely to be due to noise. The full range of the host-subtracted spectrum is shown in Fig. 6.21.

Employing the widely-used cross correlation method (Tonry & Davis 1979) for identifying SNe, using SNID (Blondin & Tonry 2007) on the host-subtracted spectrum, gives the best match to be an early SN type IIn spectrum, but this match is not very convincing: the degree of cross-correlation of the best-matching SN spectrum is similar to the value obtained for a template galaxy or AGN spectrum and is close to the cutoff value of the SNID software. A further comparison of TDE2 to type IIn SN is presented in Section 6.4.2.

The interpretation of the intermediate width line in the host-subtracted flare spectrum (Fig. 6.16, bottom panel) is not straightforward. Strubbe & Quataert (2011) calculate that the line-broadening due to the line-of-sight velocities of the super-Eddington outflows is probably too broad to be detectable. However the stellar debris orbiting the black hole at eccentric orbits could also produce a broad component (Komossa et al. 2009). Since intermediate width H_α lines are a well-known property of many AGN and some type II SNe, their detection in the host-subtracted spectrum of TDE2 is not particularly constraining to the nature of this flare.

6.3.3.3 CRTS observations

The Catalina Real-Time Transient Survey (CRTS) analyzes data from the Catalina Sky Survey which repeatedly covers >30,000 deg^2 on the sky, in order to search for optical transients with timescales of minutes to years (Drake et al. 2009). The Catalina Sky Survey (CSS) Schmidt Telescope and Mount Lemmon (MLS) telescopes are located north of Tucson, Arizona and survey the northern sky using unfiltered 4k $\times$ 4k CCD cameras. Images from the MLS telescope cover 1.1 deg^2 and reach V =21.5, while images from the CSS cover 8 deg^2 and reach V = 19.5. On a clear night, these two telescopes cover $\sim$ 1500 deg^2 of sky in sequences of four 30 s exposures. Although CRTS began in 2007 November archival CSS and MLS data dates back to 2004.

CRTS observations of TDE2 are available both in between and beyond the SDSS observational seasons. Here we only show the mean "unfiltered" CSS difference magnitude (within $\sim$ 20% of the SDSS r-band) of the three CSS detections of the TDE2, obtained 95 to 80 days prior to the first SDSS detection. These data are shown in Fig. 6.10 to:

- date the first SDSS observation and NTT spectrum as being at least 95 and 100 days respectively after the peak of the flare, and
- show that (Fig. 6.10) the peak luminosity of the flare is considerably higher than observed by SDSS, by approximately one magnitude.

6.4 Comparison of tidal flares to AGN and supernovae

In this section we quantify the likelihood that TDE1 and TDE2 are examples of some already-observed phenomenon.

6.4.1 Comparison to AGN flares

Our pipeline was designed to exclude AGN flares based on the host properties (Secs. 6.2.3, 6.3.2 and 6.3.3). Here we examine the properties of the flare observations themselves to understand how often the behavior displayed by TDE1,2 may occur by chance in the AGN population. We use two attributes of variable AGNs that we measure in our data – the range of variability per season and the spectrum of the

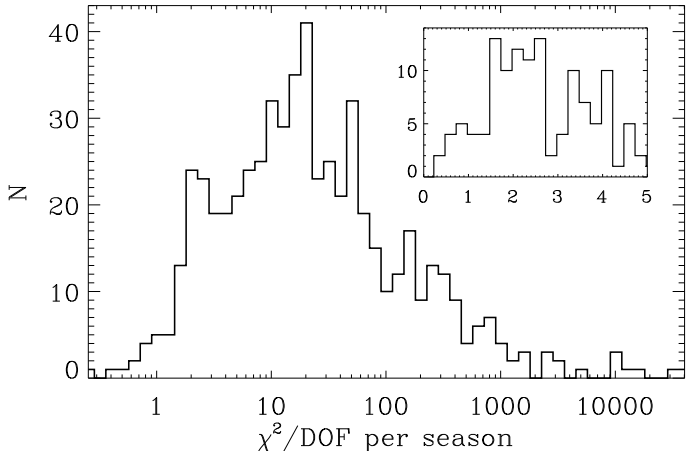

FIGURE 6.17: The χ^2/DOF distribution of all non-flare seasons with three or more observations (χ^2_s), for the spectroscopic QSOs and Seyfert galaxies. The values of χ^2_s in the non-flare seasons of TDE1,2 are respectively {1.4, 2.6, 0.6, 1.7, 1.9} and {1.0, 1.6, 1.0, 2.0}. The inset zooms in on the first few bins of the histogram, using a linear bin size.

most extreme flares over the entire Stripe 82 observing period – to quantitatively compare TDE1,2 to AGNs. First, we consider the likelihood for an AGN to have a flare meeting our selection requirements in one season, yet be as quiet as TDE1,2 in the other observed seasons. Next, we consider the spectrum of flare amplitudes in the AGN population and compare to those of TDE1,2. Finally we compare the spectral properties of the TDE1,2 flares to AGN flares.

As discussed Section 6.2.3.3, we rejected three candidates which pass all cuts except that their flux in other seasons is not consistent with being constant. We can use the measure of variability developed there to determine the likelihood that an AGN is as quiet as TDE1,2 in all but one observing season. We have a sample of variable AGNs with the same selection criteria as TDE1,2 – our sample of flares that are in QSOs and identified Seyfert galaxies – with which we can quantify the flux excursions in "off" seasons. To do this, we introduce χ^2_s: the χ^2/DOF per season, s. The median flux excluding the season that contains the main flare is used as a model for the light curve in other seasons. We calculate χ^2_s for all seasons (other than the one with the primary flare) having three or more detections, since that is the minimum number of detections for the TDE candidate sample. Fig. 6.17 shows the distribution of these χ^2_s values. Let $f_j^{(1,2)}$ be the fraction of AGNs with as low or lower value of χ^2_s as TDE1,2 in season j. Our estimate for the likelihood for an AGN

to have as little activity in the off seasons as displayed by TDE1,2 is then

$$P_{\rm AGN}^{(1,2)} \leq \prod_{j}^{N_s} 2\, f_j^{(1,2)} \quad . \tag{6.4}$$

Here the product runs over the non-flare seasons with three or more detections; $N_s = 5, 4$ for TDE1,2. The factor 2 is inserted in Eq. 6.4 because the mean value of f_j for AGNs is 0.5. Using the relative photometry light curves introduced in Section 6.2.3, we find $P_{\rm AGN} \leq 2 \times 10^{-6}$, 2×10^{-5} for TDE1,2 respectively.

This estimate of the chance probability for a variable AGN to have several quiet years surrounding a major flare, and thus to be able to mimic TDE1,2's variability properties, assumes the flux variability in the years surrounding the major flare is uncorrelated. This is a reasonable first approximation and can be improved by studying the statistics of the AGN fluctuations in the years near a major flare. It is important to emphasize that we are *not* making the assumption that the natural flux variability of AGNs in seasons near a major flare is the same as in randomly chosen seasons long before or after a major flare: if there is an enhancement or suppression of flux excursions before or after major AGN flares, it is captured in our measured χ_s^2 distribution, which is measured in AGNs in years surrounding a flare selected by the same criteria as for TDE1,2.

We can use another property of the flaring QSO sample to obtain a second, independent probability measure that TDE1 or TDE2 are AGN flares. For this, we quantify the spectrum of flux increase at the peak of QSO flares relative to their baseline flux. An upper limit on the [OIII] line luminosity of a galaxy can be converted to an upper limit on the baseline luminosity of its active nucleus at 5000 Å in the rest-frame (Heckman et al. 2004). The observed luminosities of TDE1,2 at this wavelength imply a minimum flux increase with respect to the baseline state of the accretion disk of a factor 87, 21 respectively. A flux increase of this magnitude is extremely unlikely for an AGN: out of the 1304 extended QSOs in Stripe 82 that we monitored for flares, the largest flux increase measured in the g, r or i bands, is a factor of 5. The spectrum of $\Delta F/F$ for the QSO flares meeting our selection criteria is shown in Fig. 6.18; it is a power-law with slope $\alpha = -3.9 \pm 0.2$. Using this power-law fit to calculate the probability of as large a flux excursion as seen in TDE1,2, if they were variable QSOs, gives $P(\Delta F/F > 87) = 3 \times 10^{-7}$, $P(\Delta F/F > 21) = 2 \times 10^{-5}$, respectively.

The probability estimates above are valid if there is only one type of AGN variability. Evidence that a single phenomenon is responsible for the variability observed in most accreting super-massive black holes can be found in the literature. Using ~ 9000 spectroscopically confirmed QSOs of Stripe 82, MacLeod et al. (2010) showed that a damped random walk model can explain quasar light curves at an impressive fidelity level ($0.01 - 0.02$ mag), indicating that one single physical process, e.g., turbulent

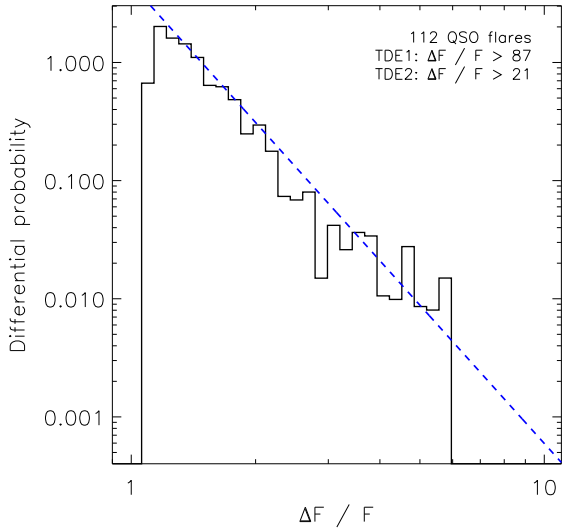

FIGURE 6.18: The flux increase of QSO flares with respect to the baseline of the flare for the g, r and i-bands. We fit the histogram with $P(\Delta F/F) \propto (\Delta F/F)^{\alpha}$ for all bins with a flux increase larger than 10% and obtain $\alpha = -3.9 \pm 0.2$. The probability of finding a flare as large or larger than a given $\Delta F/F$ is obtained by integrating this fit and multiplying by 112/1304, the ratio of flaring QSO to all QSO that have been searched for flares. For reference, we also give the lower limits on the flux increase of TDE1,2 with respect to a hypothetical AGN baseline flux as derived from the (upper limit on) the [OIII] luminosity.

magnetic fields within the accretion disk (Kelly et al. 2009), is the dominat source of the variability. This analysis does not apply to BL Lacs, which show larger amplitude fluctuations (up to $\Delta m \sim 1$) than QSOs on all timescales (Bauer et al. 2009), but as we shall see, the properties of TDE1,2 do not place them in this class.

The violent fluctuations in BL Lac type AGNs are very likely due to a fluctuating contribution from a relativistic jet. A good example is the flare found by Vanden Berk et al. (2002). The first SDSS photometrical observations showed a red source ($g - r = 0.3$); the SDSS spectrum obtained about a year later, showed this sources had faded by ≈ 2.5 mag and revealed a galaxy spectrum. Follow-up observations by Gal-Yam et al. (2002) showed broad H_{α} in the host spectrum, and a second flare with a blue continuum. The radically different SED for the second flare, combined with a detection at 1.4 GHz in FIRST (Becker et al. 1995) and other radio catalogs that revealed radio flux variability, lead Gal-Yam et al. (2002) to conclude the flare originated from a radio-loud AGN, probably in the BL Lac class. We note that the Vanden Berk et al. (2002) flare is somewhat similar to R1 and R2, the flares we rejected based on additional variability of the host (section 6.2.3.3), which are also detected in FIRST at $F_{1.4\,\mathrm{GHz}} > 90$ mJy and have similar red colors. TDE1,2 are

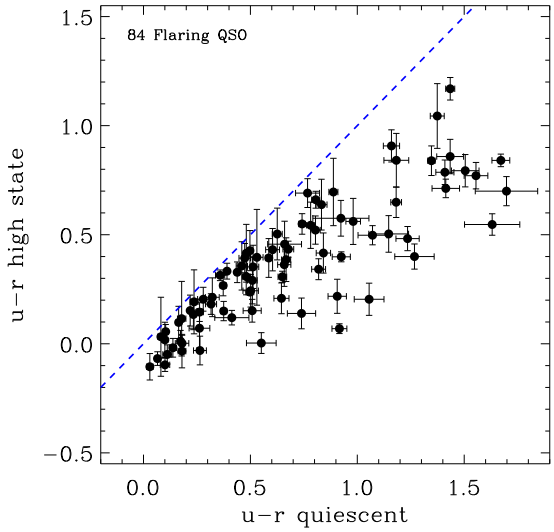

FIGURE 6.19: Colors of spectroscopic QSO. The quiescent state is calculated from the mean PSF flux of the non-flare nights. The high state is obtained by adding the flux of the quiescent state to the difference image and taking the mean colors. No color change during a flare is indicated by the striped line. We see that QSOs in their high state are slightly bluer; this effect is most pronounced for flares from relatively red QSO (quiescent $u-r > 0.5$) which can be explained by stellar contamination. For reference, the $u-r$ colors of TDE1,2 measured in the difference image are -0.62 ± 0.06, -0.36 ± 0.03.

nothing like the Vanden Berk et al. (2002) flare: their post-flare spectra show no broad lines, the flare SED is nearly constant, additional seasons of observations in Stripe 82 show no additional variability, and they are not detected in FIRST (or targeted VLA observations for TDE2).

To quantify the difference between the host of the Vanden Berk et al. (2002) flare and TDE1,2, we use the 3-σ upper limit on the radio luminosities ($L_\nu < 1 \times 10^{29}\,\mathrm{erg\,s^{-1}Hz^{-1}}$ at 1.4 GHz for TDE1 from FIRST and $L_\nu < 2 \times 10^{29}\,\mathrm{erg\,s^{-1}Hz^{-1}}$ at 8.5 GHz for TDE2) to compute the optical-to-radio spectral indices,

$$\alpha_{\rm ro} = -\log(F_{\rm r}/F_{\rm o})/\log(\nu_{\rm r}/\nu_{\rm o}) < 0.08, 0.04 \tag{6.5}$$

for TDE1,2 using the g-band peak flux for $F_{\rm o}$. From SDSS observations, optically selected radio-loud BL Lacs have a Gaussian distribution with $\langle\alpha_{\rm ro}\rangle = 0.42 \pm 0.08$ (Plotkin et al. 2010b), hence the low radio-to-optical ratio of the hosts of TDE1 or TDE2 is not consistent with a blazar-origin of these flares; they would have to members of a new class of radio-quiet BL Lacs with violent flares.

About 80 radio-quiet objects ($\alpha_{\rm ro} < 0.2$) with spectra that resemble BL Lacs

at optical wavelengths (i.e., no or very weak emission lines, blue continuum), are known at $z < 2.2$ (Plotkin et al. 2010a,b). Using Stripe 82 data, Plotkin et al. (2010a) conclude that the level of optical variability of these AGNs is consistent with other radio-quiet quasars: $\chi^2/\mathrm{DOF} > 10$ for all Stripe 82 observations in the g-band (which can be compared to Fig. 6.8) and no excursions from the mean flux greater than $\Delta m = 0.5$. Hence all of these peculiar AGNs would be identified by our pipeline and excluded based on their additional variability, and none show flares that are large enough to hide the underlying AGN. We conclude that on the radio-quiet branch of AGN, there is no evidence for a different, more violent mode of variability as seen in radio-loud BL Lacs, but more data is needed to fully exclude the existence of such a mode.

6.4.1.1 QSO flares

Figure 6.12b shows that the colors of the TDE flares, as measured in the difference image, fall outside the locus that contains 97% of all spectroscopically confirmed low-redshift ($z < 0.8$) QSOs in SDSS (Schneider et al. 2007). Here we investigate whether, when they flare, QSOs may change color radically enough that our TDEs' SEDs could be consistent with that of a flaring QSO. To explore this question, we compare in Fig. 6.19 the $u-r$ colors of QSOs in the flaring and baseline states. QSOs are bluer in their high state than in the quiescent state, but the change is not nearly enough to push a QSO out of the QSO-locus sufficiently to match the colors of TDE1 or TDE2. A large color change is observed only for flares from QSOs with a relatively red baseline, i.e., where the galaxy contribution is relatively large and is not subtracted, whereas for the TDE flares the galactic contribution has been subtracted.

6.4.1.2 Seyfert flares

Comparing the properties of the TDE1,2 flares to the flares of QSOs is powerful because the large number of QSOs allows the dispersion in the QSO flare properties to be measured. However the TDE hosts are clearly not QSOs so we also compare specifically to the three examples in our flare sample in which the host galaxy is a Seyfert as defined in Section 6.2.3.1 (galaxies having broad lines or satisfying the BPT criteria, not labeled QSO by SDSS). In Seyfert galaxies, the AGN contributes only a moderate fraction of the total flux, unlike in QSOs for which the AGN dominates by definition. Hence for Seyferts the difference image flux gives a better measure of the flux of the AGN, and we therefore compare the properties of the difference images of the TDEs with those of the three flares with identified Seyfert hosts which pass our selection criteria. The magnitude and color decay rates of the three Seyfert flares cluster around zero; the bluest Seyfert flare has $u - g = g - r = -0.2$ which is roughly as blue as TDE2. To obtain more thorough comparison of the broadband properties, we fit each of the five mean SEDs (i.e., the average color) of the difference image to blackbody spectra. The Seyfert flares all have poor fits to a blackbody ($\chi^2/\mathrm{DOF} = 5.9$, 7.6. 22.7)

while TDE1,2 are both well-fit by blackbody spectra (χ^2/DOF = 1.9, 0.4), at optical wavelengths.

The light curves of the Seyfert flares are also different from those of TDE1,2. They are more symmetric (i.e., rising and falling at similar rates) or show more substructure, and they also show variability in the non-flare season. To illustrate this, the light curve of a Seyfert galaxy that hosted at nuclear flare is shown in the bottom right panel of Fig. 6.7.

6.4.2 Comparison to supernovae

In this section we show that TDE1 and TDE2 are unlike any off-center SN recovered by our pipeline, based on the properties of the flares. We examine the possibility that TDE1,2 could be exotic SNe, but find no examples of SNe which resemble the TDEs in all significant respects. We calculate the likelihood that TDE1,2 are the most similar type of known SNe – SNIIn – and are by chance as close as observed to the centers of their galaxies to be $\lesssim 0.08$ %. Finally, we consider the possibility that TDE1,2 are examples of a new type of extreme SN which occur only near the centers of galaxies, but this requires a thousand-fold or greater enhancement in the rate of such explosions in stars in the nuclear region compared to elsewhere.

6.4.2.1 Constraints from late-time UV emission

The residual UV radiation detected 781, 485 days after the first optical detection of TDE1,2 is incompatible with observed UV properties of SNe. To estimate their maximum possible NUV flux at these times, if TDE1,2 were SNe, we assume that when first detected in the optical, they had the bluest NUV to g-band ratio ever observed in any SN: NUV $- g = -1$ (Bianchi et al. 2007). We further assume that the UV flux falls off with the slowest linear decay rate of UV magnitude that has been measured for a large sample of Ia, Ib/c and type II SN (Brown et al. 2009): $dm_{\rm NUV}/dt = 0.05\,{\rm mag\,day}^{-1}$, which is similar to the UV decay rate of SN 2008es (Gezari et al. 2009a; Miller et al. 2009). This yields upper limits on the NUV fluxes for TDE1,2 under the SN hypothesis which are far below those observed: apparent magnitude of $m_{\rm NUV,\,SN} > 59, 42$ compared to $m_{\rm NUV,\,TDE} = 23.0, 21.1$. We see that a linear decay, as commonly observed for normal SNe, vastly under predicts the UV flux, while a power law decay, which is predicted for stellar tidal disruption events (Rees 1988), can explain the large residual UV flux, years after the flare event.

The sample of Brown et al. (2009) does not include type IIn SNe. To obtain an estimate of the limit of the NUV magnitude for this type of stellar explosion we use the slowest B-band decay measured for the Kiewe et al. (2012) sample of type IIn SNe ($dm_B/dt = 0.016\,{\rm mag\,day}^{-1}$), to find $m_{\rm NUV,\,IIn} > 32, 26$. This upper limit on the NUV flux for type IIn SN is orders of magnitude below the observed late-time UV flux for both TDE1 and TDE2.

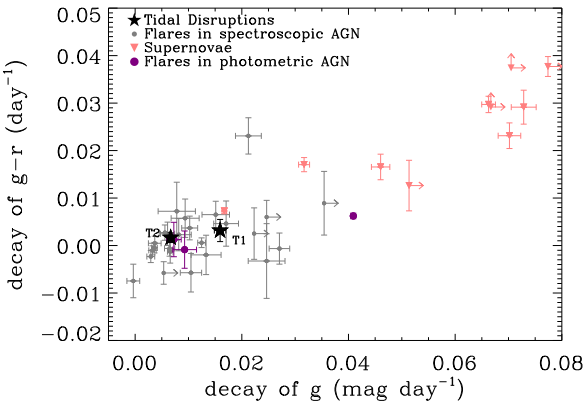

FIGURE 6.20: The change in magnitude and color measured after the peak of the flare. In this plot we only show the flares that passed the quality cut for the final TDE study (see Section 6.2.2.3). The decay rate (color evolution) is obtained from the slope of the best-fit line to the flare magnitude (color) after the peak as function of time. All identified SNe show significant cooling, as expected, and their light curves decay faster than TDE1 and TDE2, except for one: a type II-P SN whose mean color, $u-g=1.3$, is far redder than the TDEs. One flare from the photometric AGN sample is more like a SN than an AGN flare; this is consistent with the 0.9 SNe expected in the sample for the TDE analysis.

6.4.2.2 Comparison of TDE1,2 to flares in our SN sample

In Section 6.2.2.2 we defined a sample of 85 flares which are clearly off-center from their host (Eq. 6.2). This sample allows up to compare the properties of TDE1,2 to normal SNe (exotic SNe are discussed below). Because this sample is obtained by a cut on the host-flare distance only, their properties are representative of the properties of SNe that appear in the nuclear sample, which would not be the case if we compared to SNe identified in spectroscopic follow-up campaigns. We note that requiring at least three u-band detections, as is imposed for the potential TDE sample, biases the selection toward bluer-than-average flares, likely increasing the fraction of type IIn SNe. Even so, the TDE1 and TDE2 flares are significantly different from all SNe flares we observed with respect to the mean colors and cooling rate measured using the mean $u-g$, $g-r$ colors and the slope of $u-r$, respectively (Figs. 6.12). Also the decay rate measured using the slope of g is lower for TDE1,2 compared what is observed for the SN in the sample that meet the TDE quality cuts (Fig. 6.20), except for one: a II-P SN (2006fg, D'Andrea et al. 2010). However, as expected, this SN decays much faster in the u-band and is also red, $u-g=1.3$.

6.4.2.3 Comparison of TDEs to type IIn and Exotic SNe

We saw above that the colors and cooling rates of the flares in our SN sample do not resemble those of TDE1,2, but this does not apply to all type IIn SNe and some

exotic SNe. Here we review such SNe and compare them to TDE1,2.

Recently, Kiewe et al. (2012) presented four type IIn from the Caltech Core-Collapse Project (Gal-Yam et al. 2007) which aims at producing an unbiased sample (i.e., essentially every young core-collapse SN that is observable was followed-up). At their peak, all four SNe presented by Kiewe et al. (2012) have similar or even bluer $B-V$ colors and a similar decay rate as TDE1,2. Two of them, 2005bx and 2005cp, show this decay rate over the full extent of their light curves (observed for 50 and 119 days after their peak, respectively), while for the other two the flux drops rapidly after about 2 months. SN 2005bx shows rapid cooling ($d(B-V)/dt = 0.04\,\mathrm{day}^{-1}$), while SN 2005cp has nearly constant color, $d(B-V)/dt = 0.002\,\mathrm{day}^{-1}$, compared to $d(B-V)/dt = 0.003, 0.004\,\mathrm{day}^{-1}$ for TDE1,2. The presence of one among four type IIn SNe in the small but unbiased sample of Kiewe et al. (2012), which has similar colors and cooling with respect to the TDEs, thus shows that flare colors and cooling alone (Fig. 6.12) is insufficient to reject *all* SNe.

We now compare the luminosity and spectral features observed for TDE2 to the Kiewe et al. (2012) type IIn SNe which most resemble them. With $M_B = -18.9, -18.0$, SN 2005bx, cp are significantly less luminous at the peak than TDE2, whose equivalent M_B value is -20.3 when first observed, an unknown time after the peak. In Fig. 6.21 we compare the host-subtracted flare spectrum of TDE2 to the spectra of SN 2005bx and 2005cp. The emission lines and P-Cygni absorption profiles, a classic feature of SNe spectra, are absent in the TDE2 spectrum. While there is substantial dispersion within the sample of spectra of SN IIn, at all times in their evolution, the SNe spectra show stronger Hα emission than in TDE2. Furthermore, the spectrum of TDE2 was taken at least ~ 40 days after the peak – if the peak occurs between the CSS and CRTS observations – and otherwise the spectrum is at least 100 days post-peak, yet the blue continuum shape seen in spectrum of TDE2 is observed for only tens of days after the peak for the type IIn SN in sample of Kiewe et al. (2012).

We examined above the SNe IIn in the small but unbiased Kiewe et al. (2012) sample. Here we consider specific SNe reported in the literature; due to selection biases these tend to be particularly luminous and unusual. Only exceptionally blue and slowly decaying, relatively luminous SNe could mimic our TDEs. An example of a slowly decaying and luminous SN is 2006gy (Quimby 2006), which was a rather bright explosion ($M_R = -21.3 \pm 0.1$) that is considered to be an interaction-dominated type II SN (Agnoletto et al. 2009). Immediately after its peak, the decay of 2006gy, at $0.2\,\mathrm{mag\,day}^{-1}$, is much faster than in either of our TDEs (see Fig. 6.20). At 270 days after its peak, the decay rate of 2006gy slows down to $0.004\,\mathrm{mag\,day}^{-1}$, which is similar to known SNe of type II such as 1995G (IIn) (Pastorello et al. 2002) and 1999E (IIa, hybrid class) (Rigon et al. 2003). This might lead one to speculate that our TDEs can be explained as emission from the late-time tail of the light curve of type II SNe. However, by the time their decay of flux becomes similar to our

TDEs', the colors of SN 1995G, 1999E and 2006gy are red: $B - V > 0.8$. This is very different from TDE1,2 whose colors can be converted (Jester et al. 2005) to find $B - V = -0.12, -0.02$. Furthermore, the spectrum of 2006gy at $t > 270$ days is characterized by large and broad emission lines, which is inconsistent with the flare spectrum of TDE2 (Fig. 6.15).

An example of a blue and UV bright SN is 2008es (Gezari et al. 2009a; Miller et al. 2009). However the fast cooling of this SN implies a mean color of $B - V = 0.6$ over the 60 day period after the peak, which is far more red than our TDEs averaged over a similar period. By day 91 the UV had faded 5 magnitudes fainter than the optical peak, in contrast to the ~ 2 magnitude decrement seen in the TDEs after $\sim$ 800, 400 days. We can also compare the TDEs to the transient SCP 06F6 (Barbary et al. 2009). This has been suggested by Quimby et al. (2011) to be a high-redshift example of a new class of blue transients that mark the deaths of the most massive stars. Using $z = 1.19$ for the redshift of SCP 06F6 (Quimby et al. 2011), we extract a rest-frame u-band decay rate of $0.08\,\mathrm{mag\,day^{-1}}$. This is an order of magnitude faster than the decay rate of TDE1 and TDE2 in their rest-frame. Furthermore, the proposed new class of SNe should originate from faint, metal-poor galaxies (Quimby et al. 2011), which are very different from the hosts of TDE1 and TDE2.

Finally, we consider SN 2003ma (Rest et al. 2011), an extreme type IIn SN. The peak magnitude of the SN, $M_R = -21.5$, is similar to that observed in TDE2, and its decay rate during the first 300 days after the peak ($\sim 0.008\,\mathrm{mag\,day^{-1}}$ in the VR_{SM} band, centered at 6250Å) is also similar to TDE1,2. The SN was detected at $d \approx 460 \pm 85$ pc projected distance from its host. Like the TDE2 spectrum, the spectrum of 2003ma shows no emission and no P-Cygni absorption up to the last detection at 1423 days after the peak of the SNe. However the intermediate width Hα emission is much stronger than what is observed for TDE2. Another difference is that SN 2003ma is redder than TDE1,2: its color averaged over the first 50-100 days after the peak is $B-R \approx 0.35$ compared to $B-R = -0.35, -0.18$ for TDE1,2. The SN also shows strong evolution of the foreground-extinction-corrected colors: $V - I \approx 0$ at peak to $V - I > 1$ one year after the peak. There were no UV observations of SN 2003ma but already by day 213 the B magnitude was 3.5 magnitudes below the peak in the I band, suggesting that by days 400-800 no UV would be seen. We note that the host galaxy of 2003ma is a starburst galaxy (Rest et al. 2011), as expected for the presumably rather massive ($M > 10M_{\odot}$) progenitor of the SN; the star formation rate, derived from the narrow line Hα emission of the host of SN 2003ma is one (five) orders of magnitude greater than the (upper limit on) the star formation rate from the TDE2 (TDE1) host spectrum.

We conclude that TDE1,2 are not members of a *known* type of exotic SNe. However new types of SNe are discovered on a yearly basis so we have to consider the possibility that we discovered a new exotic class of stellar explosion. In the following

section we will use the distance between the host and the flare to evaluate this possibility.

6.4.2.4 Rejection of known SNe

Although we rule out that TDE1,2 are ordinary SNe on the basis of the properties of the flares, it is of interest to know the chance probability for two flares whose progenitors follow the stellar distribution to be found as close to the nucleus as observed. We assume that the rate of ordinary SNe is proportional to the stellar light. This is justified by the good quality of the fit to the host-flare distance distribution (Fig. 6.5) and the existing literature on SN distributions. Fruchter et al. (2006) conclude that, while gamma-ray bursts are more concentrated on the brightest regions, the probability of a SN type Ia exploding in a particular pixel is roughly proportional to the surface brightness of the galaxy at that pixel. This result was confirmed by Kelly et al. (2008) using also type II SNe; they conclude that both type Ia and type II SNe follow the galaxy light measured in the g-band, with a clear exception being the rarer SNe Ic associated with long-duration gamma-ray bursts. (The observation by Anderson & James (2008) that SN type II do not trace star formation estimated from H_α + [NII] emission is not relevant for this work, because our model relies on stellar light, not star formation. Indeed Anderson & James (2009) conclude that, except for a central deficit, type II SNe seem to follow the R-band light, while SNIb/c appear more centrally concentrated with respect to the stellar light.)

Taking the SN distribution to be given by the fit to the d distribution shown in Fig. 6.5, the expected contamination in the TDE sample is 0.9 SNe, in the mean. The probability that TDE1 and TDE2 are ordinary SNe found by chance as close as observed to their hosts is the product of two factors. First, the Poisson probability of finding two or more SNe, in the TDE candidate (nuclear) sample, when 0.9 are expected; this probability is 23%. Furthermore and independently, if TDE1,2 were ordinary SNe in the nuclear flare sample, the separations from the centers of their hosts would follow the distribution of stellar light within $d < 0\farcs2$. The chance that two objects, drawn randomly from this distribution, have d values less than those of the TDEs, is $\approx 7\%$. Thus the probability that the TDEs are actually ordinary SNe in the sample of flares passing our selection criteria, yet are so perfectly centered on their hosts as they are, is ≈ 1.6 %. This is the purely geometric suppression factor that must be applied to any hypothesized exotic type of flare whose progenitor follows the stellar light distribution.

We have seen above in Section 6.4.2.3, that individual cases can be found of SNe IIn which come close to matching particular properties of TDE1,2, but that when the ensemble of observations – luminosity, late time UV emission, spectrum, color evolution – are considered, TDE1,2 bear no resemblance to any SN observed to date. Nevertheless, the properties of extreme SNe depend strongly upon their environment, so one might think that the TDEs could simply be the latest exotic SNe, whose

properties differ from any SN seen earlier. In such a scenario, TDE1,2 would be on the tail of the distribution of SNe IIn, which are themselves a small fraction of all SNe. Only 17% of SNe in a flux limited search such as ours are type II (Li et al. 2010), of which about 29% are type IIn and extreme examples are still more rare. The radial distribution of type II SNe is approximately the same as for all SNe, c.f., Fig. 8 in (Leaman et al. 2011), so the 1.6% geometrical penalty for the SNe occurring so close to their galaxy centers applies. Thus the probability of finding two type IIn SNe hosts and such central locations as TDE1,2 is < 0.08 %, and is still lower for more exotic types of SNe for which TDE1,2 might be first examples.

We note that SN 2006gy is a type IIn SN which would have passed our pipeline selection criteria had it been at the redshift of TDE1,2: its proximity to the center of its galaxy would have placed it in the nuclear sample, being resolved only due to its low redshift and high-resolution imaging as at ≈ 350 pc (Smith et al. 2007), and its host would not have been excluded by the QSO locus. SN 2006gy is readily recognized as a SN and distinguished from TDE1,2 based on the color-evolution of the flare, as discussed above, but it is a concrete reminder that geometrical background rejection alone is not sufficient to eliminate SNe in a sufficiently large sample of TDE candidates, and in practice flare properties need to be considered.

6.4.2.5 New SN type, only found near the centers of galaxies

Since the properties of TDE1,2 are unlike any known SN, one could entertain the idea that there may be some special type of previously-undetected SNe which occur exclusively as close or closer to the center of galaxies than TDE1,2. In that case the above statistical arguments would not apply. To assess the viability of such an option, in this section we make the ansatz that TDE1,2 are examples of a new class of centrally concentrated SNe and see if the properties of the required class are reasonable. The distance between TDE1,2 and the center of its host is $d = 0\farcs058$, $0\farcs068$ with a mean accuracy of $\approx 0\farcs06$; this corresponds to 0.14, 0.26 kpc in projection (but consistent with zero), respectively.

Nuclear star clusters are a rather mysterious phenomenon, observed in all Hubble-types and studied in considerable detail in the Milky Way (Genzel et al. 2010). The nuclear star clusters reported by Walcher et al. (2005) in nine late-type spirals range from $8 \times 10^5 - 6 \times 10^7\, M_\odot$ with a median $\approx 10^{6.5}\, M_\odot$; the mean age of the last star formation burst is 34 Myr with the youngest stellar population having a mean mass of $10^{5.5}\, M_\odot$(Walcher et al. 2006). Having a radius of ≈ 5 pc, star clusters provide a concrete example of a possible scenario with concentrated sources.

If every galaxy contains a nuclear star cluster, we can infer the minimum required rate of TDE-like explosions as follows. The average stellar mass of the galaxies monitored in our search is $\approx 10^{10}\, M_\odot$, so $\approx 3 \times 10^{-4}$ of all stars could be in nuclear star clusters. The total number of SNe that would have been detected in the TDE search if we had not imposed a cut on the host-flare distance or additional quality cuts is

≈ 150.[3] Thus if a new class of "nuclear" SNe is to explain the existence of two SNe we require the average rate per star of TDE-like SNe in a nuclear star cluster to be a factor κ larger than the rate of normal SNe per star, where

$$\kappa \, 3 \times 10^{-4} \approx 2 \, / \, 150 \quad , \tag{6.6}$$

giving $\kappa \approx 45$.

This factor, $\kappa = 45$, is the enhancement factor by which stars in the nuclear star cluster must explode as a SN of the new type, compared to having a normal SN explosion, if the TDE candidates are to be explained as first cases of a new class of nuclear SNe. Much more challenging theoretically, is to explain the *absence* of TDE-like SNe at larger radii, where none are observed. With ≈ 3000 times as many stars in an average galaxy as in its nuclear star cluster, we would expect to have seen ≈ 6000 TDE-like events at larger radii if the rate per star were the same, requiring a suppression in the rate-per-star by a factor of at least 2.3/6000 compared to the rate in the nuclear star cluster (2.3 being the 90% CL upper limit on the number if 0 are seen).

Although star clusters contain on average younger, more massive stars than in the ensemble of monitored galaxies, a mechanism which produces a factor $\sim 60,000$ contrast between the rates of this new type of SNe in stars in a nuclear star cluster, compared to their rate elsewhere in the galaxy, may be difficult to devise. We note that the unusual SN 2006gy, which occurred at about 350 pc from the center of its host (Smith et al. 2007), could be an example of a "galactic nucleus SN", but a larger sample of similar SNe is needed to assess this possibility.

6.4.2.6 Summary of comparison of TDE1,2 to SNe

We have compared TDE1 and TDE2 to "ordinary" SNe, to an unbiased sample of type IIn SNe, and to particular exotic SNe. Ordinary SNe have entirely different properties than the TDEs in their color, color evolution and decay rates. Although some SNe IIn and exotic SNe resemble the TDEs in some respects, e.g., rate of change in magnitude and color, there are no examples of SNe whose properties are not significantly different than the TDEs in at least some important respects. Flares from known SNe types including IIn's follow the stellar distribution to a good approximation, with the result that the probability of two SNe IIn flares occurring so close to the nucleus as TDE1 and TDE2, is $\lesssim 0.08$ %.

Thus if TDE1,2 are SNe, they must be the first examples of a new exotic type of flare which occurs only very near the center of galaxies, to evade the 2×10^{-2} geometrical penalty and explain the failure to detect many more events at larger

[3]The total number of SNe that would be detected if the $d < 1$" requirement were not imposed can be estimated by integrating the fit to the d-distribution (Fig. 6.5) to $d \to \infty$ and taking into account the number of SN lost by requiring two detections after peak of the flare (in the g and r band only, to avoid a color bias) and restricting to host outside the QSO locus.

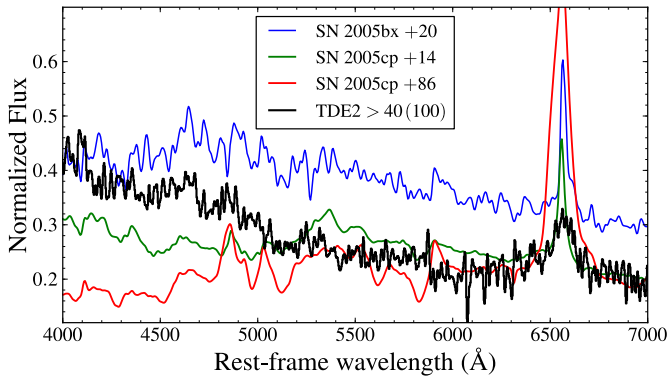

FIGURE 6.21: Comparison of the TDE2 flare spectrum (host subtracted) to the two type IIn SNe from Kiewe et al. (2012) which are most similar to TDE1,2 in terms of cooling rate and color. The spectra are normalized to be equal at long wavelengths. The legend lists the time difference with respect to the peak of the light curve. For TDE2, the location of the peak in the light curve is unknown but we have a lower limit based on the first CSS detection of the flare (see Fig. 6.10 and discussion in Section 6.3.3.3). The blue continuum of the pre-peak spectrum of SN 2005cp is similar to that of TDE2, but this SN spectrum shows more narrow and much stronger Hα emission. The P-Cygni absorption profiles, a classic feature of SNe spectra, are clearly inconsistent with the TDE2 spectrum.

radii. Since known SNe are essentially local phenomenon – depending only on the progenitor star and its immediate environment – and there are so many more stars in the bulk of the galaxy than in any physical system near the galactic center, a model along these lines requires that either the progenitors of TDE-like SNe are concentrated by a large factor near the nucleus of the galaxy or some process in the nucleus stimulates TDE-like explosions at a much higher rate than in ordinary SNe. We considered nuclear star clusters as a possible example, and found a minimum required enhancement factor of ≈ 45. Equally or more challenging, the rate of these new SNe must be at least a factor ≈ 3000 *lower* for stars outside the nuclear star cluster than for stars in it.

Given the evidence above, we conclude that TDE1 and TDE2 – the two events which survived our pipeline cuts – are unlikely to be supernovae.

6.5 Discussion

In this section we first compare the observed properties of TDE1,2 with properties of TDE candidates in the literature, and then compare with theoretical predictions.

6.5.1 Comparison to TDE candidates in the literature

Gezari et al. (2009b) presented two candidate TDEs discovered with *GALEX* that had simultaneous weekly optical difference imaging. The optical colors and light curve shape of TDE1,2 are similar to the g, r, and i and NUV light curves of those two *GALEX* TDE candidates. The blackbody temperatures of these *GALEX* candidates, measured by fitting to both UV and optical data, are $\sim 5 \times 10^4$ K. This is to be compared to $\sim 2 \times 10^4$ K for TDE1,2, obtained by fitting to optical data only. Thus the observed optical properties of our two TDEs are similar to each other and to the *GALEX* TDE candidates. Given the small number of examples, the differences can be attributed either to variations within the TDE population or to the differences in the selection biases of the observations.

Unfortunately, simultaneous optical imaging is not available for the X-ray selected TDE candidates, hence a comparison is possible only for derived properties. As discussed in Gezari et al. (2009b), the blackbody temperatures derived from the X-ray spectra are higher than those obtained for the UV and optical-selected TDE candidates, which can be explained by the geometry of the emitting region (i.e., the high energy photons are produced closer to the black hole).

6.5.2 Comparison of flare properties to theory

Predicting the properties of optical TDE flares is nontrivial, and the range of variation in observed flare properties for a given black hole mass is expected to be large due to the variety of possible pericentric distances, masses and radii of the disrupted star, black hole spin, and viewing angles. Therefore, a much larger sample of TDEs will be needed – selected as done here based on host and geometrical criteria rather than flare properties, with spectra and much more finely sampled light curves and simultaneous observations outside the optical band – before the full complexity of the tidal disruption phenomenon can be even superficially explored.

Here we give a preliminary comparison of the most basic properties of the flares – summarized in Table 6.2 – to the predictions of two theoretical models, Loeb & Ulmer (1997, LU97) and Strubbe & Quataert (2009, SQ09). LU97 is a simple model based on thermal emission at the Eddington luminosity, while SQ09 follows the evolution of the tidal debris and makes detailed numerical predictions for emission during and after the super-Eddington period, in three illustrative examples.

The most massive black hole in the SQ09 examples has $M_{\rm BH} = 10^7\,M_\odot$ – in the middle of the estimated black hole mass range for the TDE1 host galaxy, but at the very low end of the range for TDE2. For this example, SQ09 predict a peak value of $\nu L_\nu \approx$ few $\times\, 10^{41}$erg/s in the g-band. This is 1 (2) orders of magnitude below the *observed, i.e., post-peak* maxima of TDE1 and TDE2, respectively. Furthermore, SQ09 predicts a temperature which is considerably larger than found with a blackbody fit to the optical SED.

The discrepancy in the SQ09 modeling is particularly severe for TDE2 because

i) according to SQ09 Fig. 4, the peak luminosity decreases for larger $M_{\rm BH}$ and the central mass estimate for the TDE2 black hole is higher than in the SQ09 example, ii) we know from the CSS pre-SDSS observation that the flare is at least ≈ 40 and possibly greater than 90 days old when seen by SDSS, depending on whether the peak occurs after or before the CSS observation, and iii) the observed g-band luminosity is a factor ≈ 100 higher than predicted at the peak for this example. (Interestingly, the peak optical luminosities and blackbody temperatures of the TDE candidates discovered by *GALEX* (Gezari et al. 2009b, Table 2) are also inconsistent with SQ09 predictions.)

Table 6.2 reveals that the color and time evolution of TDE1 and TDE2 are quite similar to each other. The pipeline selection process did not place constraints on the color and, although too-short flares would not be accepted, the lifetimes of TDE1,2 are far longer than required to pass the selection criteria. Thus it is reasonable to think that these properties are typical for optically discovered TDE flares. Luminosities on the other hand are naturally biased toward the high end of the distribution. Since the volume of detectability of a flare increases as $L^{3/2}$, we cannot exclude the existence of a population of dimmer flares.

This raises the question of how to account for the observed flare properties. The earlier and simpler model of LU97, based on thermal emission at the Eddington luminosity, correctly predicts the observed temperature (within uncertainties) and its slow evolution, but predicts a much *higher* luminosity than observed. LU97 also predicts that the luminosity decays much more slowly than observed. The LU97 model can be reconciled with observation if their hypothesized optically thick envelope subtends only a fraction of the 4π solid angle, and this fraction decreases with time. Or perhaps SQ09 are on the right track but they adopted parameter choices which need modification, or better modeling of the radiatively driven wind is needed (Lodato & Rossi 2011). Or some important aspect of the process may be missed completely; for instance the presence of a weak, pre-existing accretion disk might significantly enhance the power of the flare, as proposed by Farrar & Gruzinov (2009) as an explanation for the correlation reported between ultra-high energy cosmic rays and AGNs (The Pierre Auger Collaboration 2007, 2008) whose luminosities are too low to accelerate protons to the observed energies (Farrar & Gruzinov 2009; Zaw et al. 2009).

After the properties of TDE1,2 were presented in the preliminary archive version of this work (van Velzen et al. 2011), Strubbe & Quataert (2011) explored a larger parameter space in their model and found that TDE1 can be readily explained adopting adjusted parameter assumptions. They report that the luminosity of TDE2 can be explained in their framework as well, but agree with our observation that its color and slow decay are more suggestive of the state considered by LU97.

The luminosity and temperature of a tidal disruption flare, and their time evolution, depend on the (unknown) time between disruption and first observation, and on unknown or poorly-known parameters of the black hole ($M_{\rm BH}$ and spin) and the

initial star and the orbit and viewing angle. This means that the range of flare types is enormous and one might despair of being able to test theoretical models. Remarkably, however, the *ratio* of the cooling rate to the bolometric luminosity decay, $(d\ln \mathrm{T}/dt)/(d\ln L/dt)$, is independent of all these unknown parameters and also independent of the time since disruption, in the SQ09 model during the super-Eddington phase. Combining equations 2, 11, and 13 of SQ09 we derive that

$$(d\ln \mathrm{T}/dt)/(d\ln L/dt) = -5/4 \tag{6.7}$$

for any TDE, at any time during the super-Eddington phase. This is certainly not the evolution observed for TDE1,2 in the g-band, for which we measure $(d\ln \mathrm{T}/dt)/(d\ln L_g/dt) = 0 \pm 0.2$ and $0.2 - 0.7$ respectively. Whether this is further evidence of a problem with the SQ09 model requires detailed modeling since the evolution of the g-band luminosity may not follow that of the bolometric luminosity, and a single blackbody may not correctly describe the SED. We present the relation Eq. 6.7 here because of its power to test the picture of the wind-driven super-Eddington phase independently of the initial conditions of the disruption event. Simultaneous measurement of a larger portion of the SED, to allow Eq. 6.7 to be tested, would therefore be highly beneficial in future observational campaigns to explore the TDE phenomenon.

6.6 Future surveys

We estimate below the *detection* rate of TDEs which can be expected in current and future optical transient surveys, for the pipeline used here and similar observational conditions and cadence as SDSS Stripe 82. This estimate differs from earlier estimates such as (Gezari et al. 2009b; Strubbe & Quataert 2009) because those ignore the cost in event-rate implied by cuts needed to insure clean and unambiguous detections, and our estimate here incorporates the observed properties of TDEs rather than relying on models.

The total effective time spanned by the SDSS Stripe 82 data, $\tau_{\rm obs}$, is just the total time between observations within a season; the > 9 month gap between seasons is not included in $\tau_{\rm obs}$. To account for the difference in sampling across Stripe 82 we calculate $\tau_{\rm obs}$ in bins of width 3.6 degree along right ascension. The mean $\tau_{\rm obs}$ is 1.03 yr with a mean cadence of 7.5 days. Thus two detected TDEs correspond to a TDE detection rate of $\dot{N}_{\rm obs} = 1.9\,{\rm yr}^{-1}$. We can scale this detection rate to current and future optical surveys of similar cadence and selection criteria using the flux limit, $F_{\rm lim}$, and faction of the sky observed, $f_{\rm sky}$:

$$\dot{N}_{\rm obs} \propto f_{\rm sky}\, F_{\rm lim}^{-3/2} \quad . \tag{6.8}$$

This yields $\dot{N}_{\rm obs} = 13, 14, 4180$ yr^{-1} for the PTF, Pan-STARRS Medium Deep Survey

and LSST, respectively. In Table 6.5 we list the adopted values of $F_{\rm lim}$, $f_{\rm sky}$. These detection rates are lower bounds on the actual number of TDEs which can be observed (if the observational quality is equal to that of SDSS and these TDEs have typical luminosities), because the cadence can be optimized and the pipeline made more efficient, to maximize detections for any targeted light-curve type in a dedicated survey.

Future optical surveys will be predominantly photometric and will generally not have a large fraction of hosts for which spectra have been obtained, as we have for SDSS Stripe 82. In fact, this need not prevent obtaining a TDE candidate sample for follow-up with O(1) false positives, if the angular resolution allows adequate rejection of non-nuclear flares. The first line of defense against SNe contamination is good resolution. The purity of the nuclear sample is determined by the accuracy with which the flare-host separation can be measured, because SN background increases very rapidly as the resolution is compromised.

When the goal is rapid, intensive spectral and multi-wavelength follow-up rather than discovery in archival data, the appropriate selection strategy changes from the one used for here for TDE1,2. The first priority is to be confident that a flare passing the selection criteria has a very high chance of being a TDE and low chance of being uninteresting. Elements of such a strategy are:

• QSOs can be suppressed in the target sample by excluding galaxies within the QSO locus in Fig. 6.6; galaxies showing continuing irregular variability during monitoring can be excluded as presumptive AGNs without spectroscopic follow-up, if spectroscopic resources are limited.

• TDE1,2 both fall in a"TDE-locus" based on photometric properties of the flares alone (Fig. 6.12), allowing powerful rejection of AGN flares and SNe without spectroscopic follow-up. Fig. 6.20 shows that flares from the hosts which are identified as QSOs based on their photometric properties only, have properties similar to the flares from spectroscopically confirmed QSOs. Moreover requiring a flare to fall in a "TDE-locus" of very blue flares – $u - g \leq -0.1$ and $g - r \leq -0.2$ (Fig. 6.12) – reduces the contamination of SNe in a TDE search by a factor of $\gtrsim 50$. Thus photometry alone, without prior spectroscopy, is sufficient to reduce the variable-AGN contamination of the TDE candidate sample, and rejects almost all SNe.

• The only SNe which are observed in the TDE-locus in flare color are of type IIn, but these occur only very rarely in E/S0 galaxies (Li et al. 2010). Thus without introducing a bias in the selection of TDEs, targeting can be restricted to early-type galaxies. This reduces the contamination of SNe IIn, the most troublesome SN contaminant in a TDE search, based on color alone. The appropriate trade-off between stringency of rejection of SNIIn and loss of real TDEs will be determined by the specifics of the survey and follow-up resources.

Survey Name	Cadence	$F_{\rm lim}$ (mag)	$f_{\rm sky}$	$\dot{N}_{\rm obs}$ ($\rm yr^{-1}$)
CSS [1]	14 days	19.5	0.6	5
MLS [1]	14 days	21.5	0.09	12
QUEST [2]	hours to years	20.5	0.36	12
PTF [3]	5 days	21.0	0.2	13
Pan-STARRS MD [4]	4 days	24.8	0.0012	15
Pan-STARRS 3π [4]	6 months	23.5	0.75	1557
LSST [5]	3 days	24.5	0.5	4131

TABLE 6.5: Detection rates of other optional surveys. The survey plus reference used to obtain or estimate the cadence, flux limit ($F_{\rm lim}$) and fraction of the sky covered ($f_{\rm sky}$) are listed. We scale the detection rate using, Eq. 6.8 and $\dot{N}_{\rm obs} = 1.9\,\rm yr^{-1}$ for the analysis presented here. We have used 300 $\rm deg^2$ as the angular area for Stripe 82. Since the cadence of the observations of Stripe 82 decreases towards the edges, Sesar et al. (2007) have used 290 $\rm deg^2$ for this area. However the total area of Stripe 82 that is imaged is 312 $\rm deg^2$; we thus adopted 300 $\rm deg^2$ as a reasonable value to obtain $f_{\rm sky}$. References: [1] Drake et al. (2009), [2] Hadjiyska et al. (2011), [3] Law et al. (2009), [4] Gezari et al. (2008), [5] Ivezić et al. (2008)

.

6.7 Summary

We have presented here the first two compelling, optically-discovered, stellar tidal disruption candidates. This work demonstrates the feasibility of discovering TDEs in optical synoptic surveys without imposing selection criteria depending on the properties of the flare.

Our pipeline rejection of non-TDEs is based on geometrical criteria to eliminate supernovae and on host properties to eliminate variable AGN flares, rather than being based on properties of the flares themselves, in order to minimize selection bias. The pipeline rejection gives an *a priori* probability of the flares being SNe or variable AGNs of less than 3%. Thanks to the very large sample of galaxies in SDSS Stripe 82, with a large number of them having spectra, we have excellent data on the properties of host galaxies and their variability. This allows us to remove 90% of the QSO hosts by a color-color cut on the host galaxy. The most serious remaining background comes from variable emission from hidden active nuclei. These cases are excluded by the variability of their hosts in the non-peak seasons, eliminating 3 of the 5 TDE candidates which survived the SNe geometrical and QSO color-locus cuts. Based on the variability observed in QSOs and identified Seyferts, we estimate the probability that a QSO or Seyfert which satisfies our flare selection criteria in some season, shows as little variability in the other seasons as TDE1,2, to be $< 2 \times 10^{-5}$.

Further SDSS observations, follow-up spectra and *GALEX* observations provide powerful *a posteriori* evidence that TDE1,2 are neither SNe nor variable AGNs. The host spectra are consistent with the hosts not having active nuclei. Although no requirement was placed on the flare properties in the selection process, the TDE flares are very distinctive in comparison to SNe and flares in variable QSOs and AGNs. The

lower limit on their increase in flux compared to a possible AGN contribution to the baseline flux is far greater in the TDEs than any QSO flare in the Stripe 82 data (Fig. 6.18). The mean color and cooling rate, as well as the decay rate, of the TDE flares are significantly different from any SN in our sample, as shown in Figs. 6.12 and 6.19. The TDE flares are significantly bluer than QSOs and QSO flares, although like QSO flares their color evolves very slowly compared to SNe. In particular, *GALEX* recorded a level of UV emission from TDE2 $\approx$ 800 days after the flare that is orders of magnitude greater than in any known SN. *GALEX* observations of TDE2 combined with color information, show that TDE2's flare is unlike every known SN flare in at least one respect. The closest resemblance is to type IIn SNe and a few exotic SNe.

Serendipitously, a spectrum of TDE2 was taken during the flare, a few days after the first SDSS detection of the flaring state. We have recently taken a spectrum of the host galaxy, giving us by subtraction a spectrum of the flare itself. We compared of this spectrum to spectra from an unbiased sample of type IIn SNe, finding that these SNe spectra show stronger Hα emission.

The properties of the flares argue against the possibility that TDE1,2 are an unusual but known type of SN. The most TDE1,2-like SNe are type IIn's, but the probability of finding two of those, and in such central locations as TDE1,2, is $\lesssim$ 0.08 %, and is still lower for more exotic types of SNe. A final option, that these are the first examples of a new class of SNe occurring only at the centers of galaxies is shown to require a thousand-fold or greater enhancement in the rate of such events in stars near the nucleus compared to the rate in stars located elsewhere.

With only two examples of probable TDEs to study, it is still very much early-days for testing models in the literature. Nevertheless, the events have already enabled refinement of the recent detailed modeling of the process by Strubbe & Quataert (2009, SQ09): the observed luminosities of TDE1,2 are at least 1-2 orders of magnitude higher than predicted there, and the temperatures determined by a blackbody fit to the optical SED are considerably lower than in the simulations, for the assumed parameter choices. However with adjusted parameter choices the features of TDE1 can be explained and the luminosity of TDE2 as well (Strubbe & Quataert 2011). The earlier and simpler model of Loeb & Ulmer (1997), based on thermal emission at the Eddington luminosity, can be reconciled with observation if their hypothesized optically thick envelope subtends only a fraction of the 4π solid angle, and this fraction decreases with time.

Our work demonstrates that candidate tidal disruption events can be efficiently identified using photometric imaging alone. We conclude based on our observed TDE rate and pipeline efficiency, that current and next-generation optical synoptic surveys should contain hundreds or thousands of TDEs. We have shown that a TDE candidate sample with $O(1)$ purity can be identified using host selection, geometric resolution and color alone. With such a sample, the cost of excluding imposters with a follow-up observation the next night or later that night on another instrument is

sufficiently low, that a campaign to create a large sample of tidal disruption events with high-frequency, multi-wavelength observations is feasible. This will allow the tidal disruption phenomenon to be explored in full detail, opening an exciting new chapter in black hole astrophysics.

Acknowledgments

GRF and SvV acknowledge valuable conversations with M. Blanton, A. Filippenko, J. Frieman, J. Greene, A. Gruzinov, D. Hogg, S. Komossa, M. Modjaz, J. Moustakas, N. Smith, L. Strubbe, N. Zakamska and G. Zhu; in addition we thank P. Massey for assistance with obtaining the TDE1 spectrum, A. Goobar and R. Nichol for cooperation in use of the TDE2 spectrum, A. Gal-Yam and O. Yaron for cooperation in use of CCCP data, P. Groot and K. Verbeek for help with the WHT spectrum, and G. Djorgovski and E. Beshore for cooperation in use of CRTS and CSS data. We are grateful to the anonymous referee for the comments that improved the manuscript and made the presentation more balanced The research of SvV was supported in part by the Huygens Scholarship Programme. The research of GRF was supported in part by NSF-PHY-0701451.

Funding for the SDSS and SDSS-II has been provided by the Alfred P. Sloan Foundation, the Participating Institutions, the National Science Foundation, the U.S. Department of Energy, the National Aeronautics and Space Administration, the Japanese Monbukagakusho, the Max Planck Society, and the Higher Education Funding Council for England. The SDSS Web Site is http://www.sdss.org/. The SDSS is managed by the Astrophysical Research Consortium for the Participating Institutions. The Participating Institutions are the American Museum of Natural History, Astrophysical Institute Potsdam, University of Basel, University of Cambridge, Case Western Reserve University, University of Chicago, Drexel University, Fermilab, the Institute for Advanced Study, the Japan Participation Group, Johns Hopkins University, the Joint Institute for Nuclear Astrophysics, the Kavli Institute for Particle Astrophysics and Cosmology, the Korean Scientist Group, the Chinese Academy of Sciences (LAMOST), Los Alamos National Laboratory, the Max-Planck-Institute for Astronomy (MPIA), the Max-Planck-Institute for Astrophysics (MPA), New Mexico State University, Ohio State University, University of Pittsburgh, University of Portsmouth, Princeton University, the United States Naval Observatory, and the University of Washington.

This work includes data gathered with the 6.5 meter Magellan Telescopes located at Las Campanas Observatory, Chile, with the ESO New Technology Telescope at the La Silla observatory, and with the William Herschel Telescope, operated on the island of La Palma by the Isaac Newton Group in the Spanish Observatorio del Roque de los Muchachos of the Instítuto de Astrofísica de Canarias. The CSS survey is funded by the National Aeronautics and Space Administration under Grant No. NNG05GF22G issued through the Science Mission Directorate Near-Earth Objects Observations Program. J.L.P. is supported by NSF grant AST-0707982. The CRTS survey is supported by the U.S. National Science Foundation under grants AST-0909182. We acknowledge NASA's support for construction, operation, and science analysis for the *GALEX* mission, developed in cooperation with Centre National d'Etudes Spatiales of France and the Korean Ministry of Science and Technology.

Chapter 7

Measurement of the rate of stellar tidal disruption flares

Sjoert van Velzen & Glennys R. Farrar
2014, Astrophysical Journal, in press

Abstract

We report an observational estimate of the rate of stellar tidal disruption flares (TDFs) in inactive galaxies, based on a successful search for these events among transients in galaxies using archival SDSS multi-epoch imaging data (Stripe 82). This search yielded 186 nuclear flares in galaxies, of which two are excellent TDF candidates. Because of the systematic nature of the search, the very large number of galaxies, the long time of observation, and the fact that non-TDFs were excluded without resorting to assumptions about TDF characteristics, this study provides an unparalleled opportunity to measure the TDF rate. To compute the rate of optical stellar tidal disruption events, we simulate our entire pipeline to obtain the efficiency of detection. The rate depends on the light curves of TDFs, which are presently still poorly constrained. Using only the observed part of the SDSS light curves gives a model-independent upper limit to the optical TDF rate, $\dot{N} < 2 \times 10^{-4}\,\mathrm{yr}^{-1}\mathrm{galaxy}^{-1}$ (90% CL), under the assumption that the SDSS TDFs are representative examples. We develop three empirical models of the light curves, based on the two SDSS light curves and two more recent and better-sampled Pan-STARRS TDF light curves, leading to our best estimate of the rate: $\dot{N}_{\mathrm{TDF}} = (1.5 - 2.0)^{+2.7}_{-1.3} \times 10^{-5}\ \mathrm{yr}^{-1}\mathrm{galaxy}^{-1}$. We explore the modeling uncertainties by considering two theoretically motivated light curve models, as well as two different relationships between black hole mass and galaxy luminosity, and two different treatments of the cutoff in the visibility of TDFs at large M_{BH}. From this we conclude that these sources

of uncertainty are not significantly larger than the statistical ones. Our results are applicable for galaxies hosting black holes with mass in the range of a few 10^6 to $10^8\,M_\odot$, and translates to a volumetric TDF rate of $(4-8)\times10^{-8\pm0.4}\,\mathrm{yr}^{-1}\mathrm{Mpc}^{-3}$, with the statistical uncertainty in the exponent.

7.1 Introduction

Perturbations to the orbit of a star can bring it within a few gravitational radii of the supermassive black hole at the center of its galaxy, where the star will be torn apart in the strong tidal gravity field of the black hole. The resulting electromagnetic burst can outshine the host galaxy for months to years (Rees 1990). The stellar debris is ejected into high-eccentricity orbits, and after a time

$$t_{\rm fb} \approx 0.11(M_{\rm BH}/10^6 M_\odot)^{1/2}\ \mathrm{yr} \quad , \tag{7.1}$$

roughly half of this gas is expected to return to the pericenter at a rate $\dot{m}_{\rm fb} \propto t^{-5/3}$ (Evans & Kochanek 1989; Rees 1988; Phinney 1989). Deviations from this single power law description of the fallback rate are expected at early times, with the exact shape depending on the distribution of internal energy in the star (Lodato, King, & Pringle 2009; Guillochon & Ramirez-Ruiz 2013). For non-spinning black holes with a mass of $\lesssim 10^8\ M_\odot$ the disruption of a solar-type star typically occurs outside the Schwarzschild radius and thus is visible to observers outside the horizon (Hills 1975). For rapidly spinning black holes, the maximum mass for a visible disruption is a factor of five or higher (Kesden 2012).

Only a small number of (candidate) TDFs are known. They were primarily found by searching for short-lived flares in soft X-ray (e.g., Komossa & Bade 1999; Grupe et al. 1999; Saxton et al. 2012), UV (Gezari et al. 2009b, 2012), or optical surveys (van Velzen et al. 2011; Cenko et al. 2012a; Chornock et al. 2014; Arcavi et al. 2014), or by looking for the signal that such a flare could leave in the optical spectrum of a galaxy (Komossa et al. 2008; Wang et al. 2012). The properties of the optical/UV TDFs are roughly consistent with the predicted signature of thermal emission from the stellar debris as it falls back onto the black hole (Loeb & Ulmer 1997; Ulmer 1999; Strubbe & Quataert 2009; Lodato & Rossi 2011). Recently, two candidate TDFs with a transient radio counterpart were discovered in γ-rays by *Swift* (Bloom et al. 2011; Burrows et al. 2011; Levan et al. 2011; Zauderer et al. 2011; Cenko et al. 2012b); these non-thermal flares are best explained by a relativistic outflow that was launched as a result of the disruption, seen in "blazar mode" (Bloom et al. 2011).

The frequency of stellar capture by supermassive black holes depends on how the orbits of stars evolve. The rate of flares due to the tidal disruption of stars can thus be used to probe the gravitational potential and phase space disruption of stellar orbits in

their host galaxies, which are essentially unconstrained by observations for $z > 0.01$. Furthermore, it will be interesting to compare the rate of tidal disruptions to the production rate of hypervelocity stars. These unbound stars have been observed in the outer Milky Way halo (Brown et al. 2005). Their ages (Brown et al. 2012) imply that most of them are likely the result of a three-body interaction of a binary star system and the central supermassive black hole (Hills 1988), which ejects one binary partner at high speed. It has been suggested (Gould & Quillen 2003; Ginsburg & Loeb 2006; Perets et al. 2009) that the members of the binary that remain bound to Sgr A* could explain the origin of the S stars (Eckart & Genzel 1996; Ghez et al. 2005) at the Galactic center. Since orbital diffusion of these stars on tight orbits leads to capture by the supermassive black hole, the disruption of stellar binaries could provide a single framework to explain three different phenomena: hypervelocity stars, the S star cluster, and TDFs (Bromley et al. 2012).

The rate of tidal disruptions is also important for understanding the origin of the relativistic TDFs discovered by *Swift*. If a large fraction of tidal flares are accompanied by a relativistic jet these events will dominate the transient radio sky, and upcoming radio variability surveys should detect tens to hundreds per year (Frail et al. 2012; van Velzen et al. 2013). By comparing the radio and optical TDF rates, we can thus determine the fraction of stellar tidal disruptions that launch jets. Measuring this fraction should provide new insight to tidal disruption jet models (Metzger et al. 2012; van Velzen et al. 2011), such as testing the prediction that a pre-existing accretion disk is required for the production of tidal disruption jets (Tchekhovskoy et al. 2014). A measurement of the rate is also required to test the suggestion that jets from stellar tidal disruptions are the primary source of ultra-high energy cosmic rays (Farrar & Gruzinov 2009).

The rate of TDFs not been well constrained by observations until now. Donley et al. (2002) conducted a systematic search for large amplitude X-ray outbursts using archival data of the *ROSAT* All Sky Survey (Voges et al. 1999) and recovered the three known X-ray flares from inactive galaxies. From this, they deduced a rate of $9^{+9}_{-5} \times 10^{-6}$ yr^{-1} galaxy^{-1} (1σ uncertainty from Poisson statistics). Although Donley et al. (2002) presented a detailed analysis of the complicated selection effects to estimate the effective survey area, they assumed that all galaxies host equally luminous flares, which is not expected theoretically. Gezari et al. (2008) did not have a systematic procedure for finding the UV flare candidates they identified and therefore they could not determine a flare rate, but those authors concluded that a disruption rate of $\sim 1 \times 10^{-4}\,\mathrm{yr}^{-1}$ can reproduce the number of UV flares they found, although a rate of an order of magnitude lower is not ruled out due to the uncertainty on their adopted TDF light curve model.

In this work, we derive the rate of tidal disruptions from a survey of nuclear flares in galaxies using the Sloan Digital Sky Survey (SDSS). The straightforward selection function of this search allows, for the first time, a study of how the inferred disruption

rate depends on the assumed flare light curve. In Section 7.2, we give a summary of the SDSS search for nuclear flares and explain how we compute the efficiency of this search. Theoretical background on the interpretation of the TDF rate and the existing models of optical emission from TDFs is given in Section 7.3. In Section 7.4, we discuss in detail the light curve models that we adopted for our analysis. The results are presented in Section 7.5 and discussed in Section 7.6.

We adopt the following cosmological parameters: $h = 0.72$, $\Omega_{\rm m} = 0.3$, and $\Omega_\Lambda = 0.7$.

7.2 TDF search & rate methodology

7.2.1 Summary of SDSS nuclear flare search

Our search for optical TDFs (van Velzen et al. 2011) was conducted in SDSS Stripe 82 (Sesar et al. 2007; Bramich et al. 2008; Frieman et al. 2008), which is part of the seventh data release (Abazajian et al. 2009). The stripe consists of about 300 deg^2 along the celestial equator; it contains three seasons of about three months long with high cadence observations (~ 5 days), plus six more years with (much) sparser sampling.

The first step of our TDF search was to select galaxies with a flux increase of 10% or more, detected at the 7σ level using the Petrosian flux of the galaxy as cataloged by SDSS (Blanton et al. 2001; Strauss et al. 2002; Stoughton et al. 2002). The Petrosian flux essentially measures the total galaxy flux using a circular aperture with a radius that is independent of redshift and robust against changes in seeing. The catalog-based selection yields $\sim 10^4$ galaxies with flare candidates that were processed by a difference imaging algorithm. Nuclear flares were selected based on the distance between the center of the host and the flare in the difference image ($d < 0\farcs2$), yielding 186 transients.

To obtain a high-quality parent sample of potential TDFs, we applied the following criteria to the flux in the difference image: $m < 22$ for at least three nights in the u, g, and r filters. After removing galaxies that fall inside the photometric QSO locus and removing galaxies with additional variability, two flares remained; we shall refer to these as TDE1 and TDE2. Using the Häring & Rix (2004) scaling relation yields an estimate of the black hole mass of $M_{\rm BH} \approx 0.6$ and $3\times10^7\,M_\odot$, respectively. Additional analysis and follow-up observations showed that these flares are best explained as stellar tidal disruption events (van Velzen et al. 2011).

7.2.2 Analysis

The number of detected flares in a variability survey that targets $N_{\rm gal}$ galaxies is given by

$$N_{\rm TDF} = \tau \sum_i^{N_{\rm gal}} \epsilon_i \dot{N}_i \quad , \tag{7.2}$$

where $\dot{N}_i$ and ϵ_i are the flare rate and detection efficiency for the ith monitored galaxy, and τ is the survey time. For the TDF search in Stripe 82, two TDFs were found so $N_{\rm TDF} = 2$. SDSS monitored Stripe 82 with an adequate cadence for a potential TDF to pass our cuts starting in 2000, so $\tau = 7.6$ yr. Finally, the number of galaxies monitored in our search, $N_{\rm gal} = 1.5 \times 10^6$, is the number of galaxies that have a photometric redshift and are outside the QSO locus.

The rate of TDFs is expected to depend only weakly on black hole mass as long as $M_{\rm BH} < 10^8\,M_\odot$. Above this mass, the rate of visible disruptions is suppressed due to the horizon of the black hole (Hills 1975), with a cutoff depending on the black hole spin (Kesden 2012). We use two different ways to parameterize the decrease of visible TDFs due to these so-called direct captures: a simple step function at the "classical" maximum mass,

$$\dot{N}_i = \begin{cases} \dot{N} & M_{\rm BH} < 10^8\,M_\odot \\ 0 & M_{\rm BH} > 10^8\,M_\odot \end{cases} \quad , \tag{7.3}$$

and an exponential suppression for $M_{\rm BH} > 2 \times 10^7\,M_\odot$,

$$\dot{N}_i = \dot{N} \times \exp[-(M_{\rm BH}/3 \times 10^7)^{0.9}], \tag{7.4}$$

which fits the analytical results for a black hole spin of $a \approx 0.5$ (Kesden 2012). Now Eq. 7.2 can be rewritten to obtain a galaxy-independent rate:

$$\dot{N} = \frac{N_{\rm TDF}}{N_{\rm gal}\tau\,\epsilon} \tag{7.5}$$

Here we have defined the mean efficiency

$$\epsilon \equiv N^{-1} \sum_i^N \epsilon_i \quad . \tag{7.6}$$

with the sum running over galaxies according to Eq. 7.3 or Eq. 7.4.

Computing the rate of TDFs thus boils down to determining the efficiency. The result will obviously depend on the flare's luminosity and duration, e.g., a long, bright flare will be above the detection threshold long after the peak and thus is more readily detected with a given set of observations. In the next section, we discuss our approach to measure the detection probability.

7.2.3 Pipeline model: detection probabilities

As discussed in Section 7.2.1, our detection pipeline consists of two stages: a series of catalog cuts followed by difference imaging. Here we discuss how we measure the efficiency for each stage.

The catalog cuts are applied to the Petrosian flux of the galaxy, so computing the probability that a simulated light curve passes these cuts is easy. By construction, a nuclear flare always falls inside the original Petrosian radius of the galaxy and this radius is not changed significantly by the presence of this flare. This implies that the new Petrosian flux should, to good approximation, be given by the original Petrosian flux plus the flare flux. We confirmed this empirically by inserting point sources into the images of 100 different galaxies and measuring the new Petrosian flux. The mean magnitude difference between this newly measured Petrosian flux and the original Petrosian flux plus the inserted flux is -0.02 ± 0.05. This difference is negligible, so trivial arithmetic can be used to determine whether a simulated flare in a given galaxy will pass our catalog cuts (i.e., re-running the entire SDSS pipeline to derive new catalog fluxes from a simulated image is not required).

Due to variations in seeing on different nights, determining the detection probability in the difference imaging stage of the pipeline is more challenging. To do so, we selected 1400 galaxies at random and inserted flares at the center of their images. We then selected three nights per galaxy, drawn uniformly from the set of all observations, and used the point-spread function of each night to create the nuclear flare. Both the host and flare magnitudes were distributed equally in bins between $m = 19$ and $m = 23$. From the number of detected point sources in each magnitude bin, we obtain the detection probability as a function of both flare and host magnitude. The resulting detection probability as a function of flare magnitude is shown for illustration in Fig. 7.1.

To compute the overall efficiency, ϵ, appearing in Eq. 7.6, we first draw a time for the start of the flare from a uniform distribution. We then add the flare flux to the Petrosian flux and check if this galaxy would pass our catalog cuts. In the final step, we use the probability of detection for the given flare and host magnitude to compute whether this flare would be detected at the required level for at least three nights in the u, g, and r bands. After repeating this process for a large sample of galaxies, the overall efficiency follows from the fraction of flares that are detected by the model pipeline.

Because the flares are inserted into observed galaxy light curves, our method fully takes into account the inhomogeneous cadence and varying data quality of Stripe 82. Our simulation converges after inserting flares into $\sim 10^4$ galaxies; the results presented in Section 7.5 are derived using 2×10^5 galaxies chosen at random from the total of 1.2×10^6 galaxies in our analysis. The numbers of galaxies used for the different stages were large enough to achieve convergence of the result while being computationally efficient.

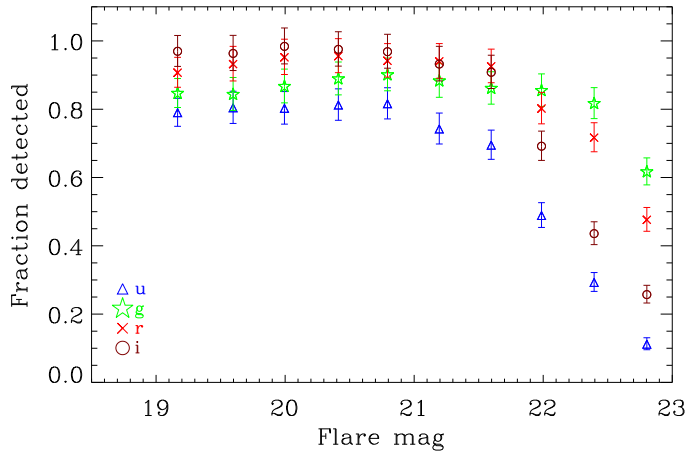

FIGURE 7.1: Probability of detecting a nuclear flare in the difference image as a function of flare magnitude (each bin contains a range of host galaxy magnitudes). For the TDF search, the flux limit applied to the difference image was $m < 22$.

7.3 Theoretical Background

We gather in this section discussions of several theoretical matters pertinent to this study.

7.3.1 Tidal disruption rate: theory

For each location in the galaxy, the set of orbits (in momentum space) that lead to the disruption or capture of a star defines the so-called loss cone. Since this cone empties quickly, theoretical estimates of the TDF rate often boil down to computing the refill rate of the loss cone. The most efficient refill mechanism is the gravitational encounter of stars, which perturbs the orbital angular momentum (Frank & Rees 1976; Lightman & Shapiro 1977; Young 1977). To quantify the rate of these encounters, the phase space distribution of the stars is needed. Two different approaches have been used.

Early estimates using nearby galaxies with well-measured surface brightness profiles, (Magorrian & Tremaine 1999; Syer & Ulmer 1999) have a scatter of one order of magnitude for black holes of similar mass. More recently, the rate for M32 ($M_{\rm BH} \approx 2 \times 10^6$) was estimated to be $\dot{N} = 1.7 \times 10^{-4}$ yr^{-1} (Wang & Merritt 2004). N-body simulations of the diffusion of stars into the loss cone by Brockamp et al. (2011) yield a lower rate, and suggest a black hole mass dependence

$$\dot{N} = 3.5 \times 10^{-5} \left(\frac{M_{\rm BH}}{10^6 M_\odot} \right)^{+0.31} \quad \text{yr}^{-1} \quad . \tag{7.7}$$

(This equation is normalized using the same $M_{\rm BH}$-σ relation, Eq. 7.9, that we used to derive Eq. 7.10.)

Another approach has been to adopt the stellar density profile of a nuclear star cluster, which can be described by an singular isothermal sphere: $\rho(r) \propto \sigma^2/r^2$, with σ the velocity dispersion. For this model, the flux of stars into the loss cone yields the following disruption/feeding rate (Wang & Merritt 2004):

$$\dot{N} = 7.1 \times 10^{-4} \left(\frac{\sigma}{70\,{\rm km\,s^{-1}}}\right)^{7/2} \left(\frac{M_{\rm BH}}{10^6\,M_\odot}\right)^{-1} \ {\rm yr}^{-1}. \tag{7.8}$$

Using the empirical relation between black hole mass and velocity dispersion (Ferrarese & Merritt 2000; Gebhardt et al. 2000) as updated in Graham et al. (2011),

$$\frac{M_{\rm BH}}{10^8 M_\odot} = 1.35 \left(\frac{\sigma}{200\,{\rm km\,s^{-1}}}\right)^{5.13} \quad , \tag{7.9}$$

Eq. 7.9 leads to

$$\dot{N} = 9.9 \times 10^{-4} \left(\frac{M_{\rm BH}}{10^6\,M_\odot}\right)^{-0.32} \ {\rm yr}^{-1} \quad . \tag{7.10}$$

However, while nuclear star clusters are expected to occur in all low-luminosity stellar spheroids, they can only be resolved for very nearby or large galaxies (e.g, Filippenko & Ho 2003; Ferrarese et al. 2006) and such galaxies typically host black holes that are too massive to yield visible disruptions. Thus the general applicability of this estimate is not clear.

A further uncertainty arises from various mechanisms that can lead to deviations from the canonical loss cone framework described above. First of all, the galactic potential may be triaxial such that the chaotic orbits of stars bring them close enough to the central black hole to be disrupted even without two-body gravitational encounters (Merritt & Poon 2004). Also, the presence of a "massive perturber", such as a giant molecular cloud, can significantly shorten the relaxation timescale (Perets, Hopman, & Alexander 2007); see Alexander (2012) for a review. Finally, the merger of two supermassive black holes is also likely to increase the disruption rate, either simply because the two nuclear star clusters of the two galaxies merge (Wegg & Nate-Bode 2011), or as a result of the loss cone sweeping through the galaxy due to the recoil of the merged black hole (Komossa & Merritt 2008; Stone & Loeb 2011). Clearly, a good measurement of the TDF rate can give valuable insight on numerous interesting issues.

7.3.2 Optical emission from TDFs

If an accretion disk forms after the stellar disruption, the luminosity at late time, at a fixed frequency in the Rayleigh–Jeans part of the spectral energy distribution (SED),

has the black hole mass dependence and time evolution

$$L_{\rm TDF} \propto (t - t_D)^{-5/12} M_{\rm BH}^{3/4} \tag{7.11}$$

(Lodato & Rossi 2011). The time of disruption (t_D) that follows from fitting this power-law decay to the observed light curve is 15, 37 days for TDE1,2. This time is shorter than the typical fallback time (Eq. 7.1), suggesting that this simple disk model does not provide a good description of the early part of the observed light curve. Therefore, we must explore more advanced models.

Besides an accretion disk, an important component of optical emission from TDF could be an outflow driven by photon pressure. This wind is expected, since for $M_{\rm BH} \lesssim 5 \times 10^7\, M_\odot$ the fallback rate exceeds the Eddington limit (e.g., Ulmer 1999). Because the temperature of the photosphere of the wind is a function of black hole mass and may increase with time (Strubbe & Quataert 2011), a single power law is not sufficient to describe the optical light curve. One of the light curve models we develop below is based on the disk plus wind emission computed by Lodato & Rossi (2011, LR11 hereafter) for the disruption of a star of one solar mass (see their Fig. 3).

A different kind of light curve model is presented in Guillochon, Manukian, & Ramirez-Ruiz (2014, GMR14 hereafter), see also J. Vinko et al. (in preparation). In this scenario, the luminosity in the UV/optical regime is reprocessed disk emission. Contrary to Strubbe & Quataert (2011) and LR11, the origin of the reprocessing layer is not assumed to be a photon-pressure wind, but is suggested to be due to the ejection of stellar debris. When the accretion rate is super-Eddington, a faction $f_{\rm out}$ of the accretion energy is assumed to be reprocessed by the same layer. The radius of the photosphere of the reprocessing layer as well as $f_{\rm out}$ are *a priori* unconstrained and need to be obtained by fitting the light curve. Other parameters in the GMR14 model include the mass and polytropic index of the star and the impact parameter. These three parameters yield the fallback rate of stellar debris, as described by the hydrodynamical simulations of Guillochon & Ramirez-Ruiz (2013). As shown in GMR14, this approach yields an excellent fit to the light curve of the well-sampled TDF PS1-10jh (Gezari et al. 2012).

7.3.3 Estimating the black hole mass

In the black hole mass regime that is relevant for optical TDFs ($M_{\rm BH} = 10^{5-7.5} M_\odot$), few accurate measurements of black hole mass are available (for a review, see Kormendy & Ho 2013). Most authors assume that the (near) linear scaling of black hole mass with the stellar mass in the bulge (Magorrian et al. 1998) remains valid in this mass range and we also adopted this approach, using the Häring & Rix (2004) scaling relation. We also consider the conjecture by Graham (2012) that the $M_{\rm BH}$-σ relation combined with the L-σ relation yields a broken power law. (This happens because the relation between bulge luminosity and velocity dispersion bends at $M_g \approx -20.5$

(Davies et al. 1983), so one should use $M_{\rm BH} \propto L^{2.5}$ for bulge luminosities $M_g > -20.5$, and $M_{\rm BH} \propto L^{1.0}$ otherwise).

To estimate the bulge magnitude of the galaxies in our sample, we use a method similar to Marconi et al. (2004). The Petrosian flux of the host is multiplied by the bulge-to-total ratio (B/T) determined by Aller & Richstone (2002) for different Hubble types. Because we are summing over a very large sample, in our simulation it is sufficient to assign the Hubble type of individual galaxies at random, based on the abundance of each type in a flux-limited sample (Fukugita et al. 1998). The bulge magnitudes of TDE1,2 are found using the mean B/T for S0 galaxies (Aller & Richstone 2002). We use the galaxy photometric redshifts of Oyaizu et al. (2008) to convert between apparent and absolute magnitudes. (Although photometric redshifts are individually subject to error, they are systematically reliable for the large number of galaxies in this study.)

7.4 Light Curve Models

Even with the inherent statistical uncertainty that stems from having only two observed TDFs in our SDSS Stripe 82 search, a major uncertainty of the rate estimate at present is our limited understanding of the optical emission of TDFs. The SDSS data for the two TDFs (TDE1 and TDE2, see Section 7.2.1) does not completely cover the time they are detectable (i.e., above the flux limit). Their light curves are thus only partially determined so we have to extrapolate the observed light curve forward and backward in time. Furthermore, we also need to know the average light curves of flares from galaxies that host black holes with a mass that is different from the black holes that produced the two SDSS TDFs. We shall approach this problem by using multiple light curve models. Below we present these models, in order of increasing reliance on theory.

7.4.1 Empirical TDF models

Our simplest, "empirical" TDF models use no scaling of the luminosity with black hole mass. To keep the results obtained for these models independent of the adopted $M_{\rm BH}$ scaling (see Section 7.3.3), we do not use a suppression of the rate based on black hole mass (e.g., Eq. 7.3), but simply compute the per-galaxy rate using only galaxies with a luminosity that is within one magnitude of TDE1 and TDE2.

7.4.1.1 SDSS-only

We start with a light curve that is identical to the observed light curve: no extrapolation is used. This completely model-independent approach yields an upper limit to the true rate of optical TDF, under the assumption that TDE1 and 2 are reasonably representative. For the computation of the efficiency (ϵ, Eq. 7.6) we restrict to galax-

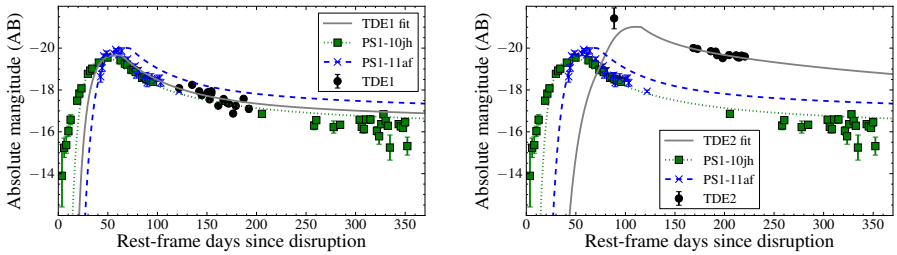

(a) Phenomenological model.

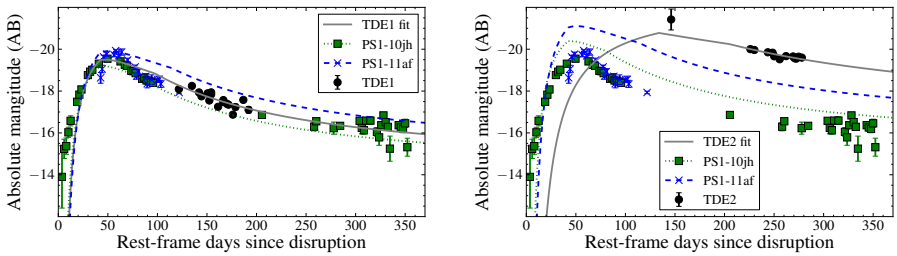

(b) Disk + Wind model (based on Lodato & Rossi 2011).

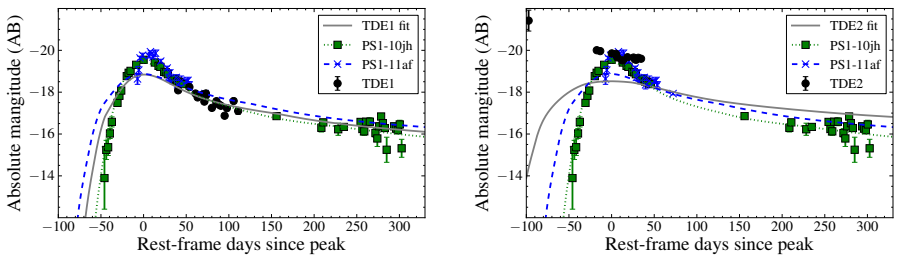

(c) GMR14 model.

FIGURE 7.2: Observed g-band light curves of TDE1 and 2 (left and right columns, respectively) and PS1-10jh and -11af, compared to our three different models. The top and bottom rows show the predictions for the phenomenological and GMR14 models, respectively, in which we fit only for the time of disruption. In the Disk+Wind model shown in the center row, we allow a different overall normalization for TDE1 and TDE2 as discussed in the text.

ies with a host luminosity that is within ± 0.25 mag of the luminosity of the host of TDE1 ($M_r = -19.9$) or TDE2 ($M_r = -21.3$).

7.4.1.2 Pan-STARRS events

The two TDFs discovered in Pan-STARRS data, PS1-10jh (Gezari et al. 2012) and PS1-11af (Chornock et al. 2014), have well-sampled light curves, allowing us to use them as example light curves in the computation of the efficiency, under the assump-

tion that all TDFs are similar to the PS1 events. As shown in Fig. 7.2, the light curve of TDE1 is consistent with the post-peak decay rate and luminosity of PS1-10jh, but that of TDE2 is substantially more luminous. We further note that three TDF candidates that were recently discovered in data from the Palomar Transient Factory (PTF; Law et al. 2009) by Arcavi et al. (2014) have a similar peak luminosity and decay rate as PS1-10jh. This suggests that the two PS1 flares are reasonable examples of true TDFs, for black hole masses similar to those of their host galaxies. In our simulation of the efficiency using the PS1 light curves, we select either the PS1-10jh or 11af light curve with a probability that is linear with the mass of the host galaxy (e.g., the probability to select the 11af light curve increases from zero at the mass of the host galaxy of 10jh to unity at the mass of its host). The black-hole masses of the 4 TDEs, TDE1,2, PS1-10jh and -11af, computed as discussed in Section 7.3.3, are respectively $10^{6.8}$, $10^{7.4}$, $10^{6.6}$, and $10^{6.9}\,M_{\odot}$ with about 0.3 dex uncertainty from the scatter in the relation between black hole mass and galaxy luminosity.

7.4.1.3 Phenomenological Model

We also used TDE1 and TDE2 plus the two PS1 TDFs to construct a function that returns a light curve as a function of the mass of the stellar bulge. This 'phenomenological model' is simply a collection of power laws that are chosen to roughly reproduce the observed light curves of these four TDFs. Figure 7.2(a) shows the success of this fitting function.

7.4.2 Theory-based models

The phenomenological model discussed in the previous section provides only a crude way to extrapolate the luminosity of flare with black hole mass. Ideally one would use a framework that yields a set of light curves for a given black hole mass, corresponding to the range of possible disruption parameters (impact parameter, stellar mass, etc.). This is however beyond the scope of this work because such a framework is not yet available, i.e., it is not yet understood how/where the optical emission of TDFs is produced.

To further quantify to what extent the uncertainty in TDF light curves impacts our estimate of the TDF rate, we use two different light curve models, which are based on the two models introduced in Section 7.3.2. For both models, we restrict the estimate of the efficiency to galaxies with a bulge luminosity that is with 1 mag of TDE1 or 2. This restriction is imposed to avoid extrapolating the models deep into parameter space that has not been covered by observations.

7.4.2.1 Disk+Wind model

For the fiducial parameters of LR11, the predicted disk and wind emission is about an order of magnitude lower than the observed luminosity of known TDFs. We therefore renormalized this model such that the total emission (disk plus wind) matches the

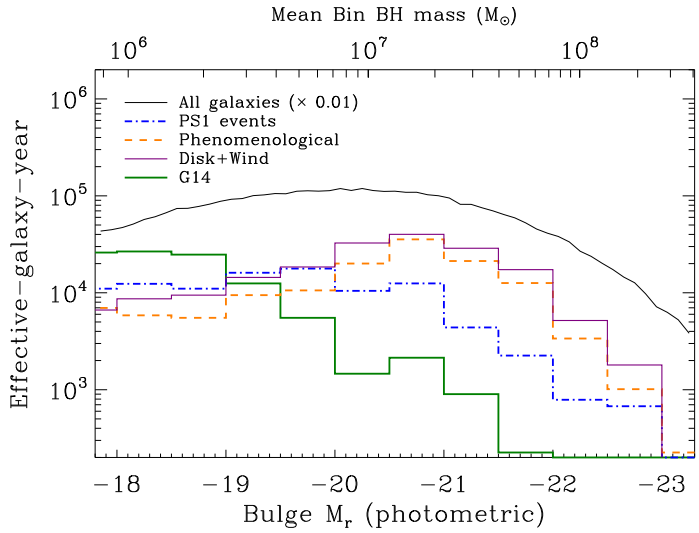

FIGURE 7.3: Effective-galaxy-years ($N_{\rm gal} \times \tau \times \epsilon$) for different light curve models in bins of absolute bulge magnitude of the host. We also show the parent galaxy sample by setting $\epsilon = 1$ (thin black line). The mean black hole mass in each bin, as obtained using the Häring & Rix (2004) scaling, is indicated on the upper axis. The bulge luminosities of the hosts of TDE1,2 are $M_r = -19.2, -20.7$.

observed luminosity of TDE1 or TDE2, i.e., we allow a separate normalization of each TDF. As we remarked above, the decay rate of TDE2 is too steep to fit with only disk emission, but at $M_{\rm BH} > 10^7\ M_\odot$, the LR11 model predicts that the disk emission dominates over the emission from the wind. We therefore applied one more modification to the LR11 model, namely multiplying the luminosity of the wind emission with $M_{\rm BH}/5 \times 10^6 M_\odot$.

7.4.2.2 GMR14 model

We can use the model presented in GMR14 to extrapolate the observed light curve of PS1 10jh to galaxies with a lower or higher black hole mass. The `TDEfit` software (Guillochon et al. 2014) was used to obtain the free parameters of that model (the stellar mass, impact parameter, etc), when the black hole mass of PS1 10jh is fixed at the value expected from the Häring & Rix (2004) scaling relation (i.e., the black hole mass was not used as a free parameter in the fit for the parameters of the GMR14 model). Then, taking those parameters as typical, light curves for other black hole masses are calculated. As expected, due to its similarity to PS1-10jh ,the GMR14 model provides a good fit for TDE1, whereas the observed light curve of TDE2 exceeds the GMR14 model prediction; see Fig. 7.2(c). We note TDE2 can be fit within the Guillochon et al. (2014) framework, but its best-fit parameters are different from those of PS1-10jh (J. Vinko et al., in preparation).

In contrast to the Disk+Wind model, in the GMR14 model, the peak luminosity increases with decreasing black hole mass. We capped the luminosity at the Eddington limit (i.e., $\nu L_\nu < 1.3 \times 10^{38} M_{\rm BH}/M_\odot \,{\rm erg\,s^{-1}}$), which only influences light curves for $M_{\rm BH} < 10^6\, M_\odot$. If the flare luminosity does increase to super-Eddington levels at low $M_{\rm BH}$, our rate estimate would not apply to low-mass black holes, and TDFs should be a powerful probe of the low mass black hole population.

7.5 Results

The rate obtained using the suite of light curve models discussed in the previous section is reported below and summarized in Table 7.1. In Fig. 7.3 we show the effective-galaxy-years of our pipeline as a function of the bulge luminosity of the host galaxy. The effective-galaxy-years is given by $N_{\rm gal} \times \tau \times \epsilon$ (i.e., the denominator of Eq. 7.5).

7.5.1 TDF rate per galaxy

Using only the observed SDSS light curve (Sec. 7.4.1.1), we find a model-independent upper limit to the rate of optical TDFs:

$$\dot{N} < 2 \times 10^{-4}\,{\rm yr^{-1}galaxy^{-1}}. \tag{7.12}$$

Here we used $N_{\rm TDF} < 5.3$, the 90% CL upper limit when two events are detected.

Using the two TDFs discovered in Pan-STARRS to yield example light curves (Sec. 7.4.1.2) we find

$$\dot{N} = 2.0^{+2.7}_{-1.3} \times 10^{-5}\ {\rm yr^{-1}galaxy^{-1}} \tag{7.13}$$

(1σ uncertainty for Poisson statistics). Needless to say, this rate is only valid for TDFs that are similar to the two PS1 events. However given the similarity between these PS1 events and three new TDFs discovered in PTF, it appears to be a reasonable assumption that these light curves are representative of those for black holes with a mass of $\sim 10^{6.5}$.

For the phenomenological model (Sec. 7.4.1.3), we obtain a rate of

$$\dot{N} = 1.5^{+2.0}_{-1.0} \times 10^{-5}\ {\rm yr^{-1}galaxy^{-1}} \quad . \tag{7.14}$$

This rate is slightly lower than the result based on the PS1 events. This happens because the phenomenological model includes TDE2, which increases our estimate of the efficiency for flares from galaxies with $M_{\rm BH} > 10^7\ M_\odot$, see Fig. 7.3.

For the theory-based Disk+Wind and GMR14 models (Sec. 7.4.2), we used two different ways to estimate the suppression of visible TDFs due to the event horizon (shown in the last two columns of Table 7.1), plus two different scaling relations for

the black hole mass (shown as a second entry for these models in Table 7.1). For our Disk+Wind model, the rate increases about 80% when the Graham (2012) scaling is used instead of our default (Häring & Rix 2004) scaling relation, while for the GMR14 model the rate decreases by 50%. Our two methods of correcting for the event horizon of the black holes yields a 40%-50% difference in the derived rate. Taking the full range of results gives

$$\dot{N}_{\rm D+W} = (1.2 - 3.2) \times 10^{-5}\ {\rm yr}^{-1}{\rm galaxy}^{-1} \tag{7.15}$$

and

$$\dot{N}_{\rm GMR14} = (1.2 - 1.9) \times 10^{-5}\ {\rm yr}^{-1}{\rm galaxy}^{-1} \quad . \tag{7.16}$$

The difference between the rate derived for the Disk+Wind and the GMR14 model is relatively small. This agreement is encouraging since we forced the Disk+Wind model to fit our TDE1 and TDE2, while the GMR14 model was normalized using independent data. However, we caution that this agreement could be deceptive, since the models predict virtually opposite sensitivity as a function of $M_{\rm BH}$ as evident in Fig. 3. In the event that GMR14 gives the best description of the flares in the low mass range and the Disk+Wind model is best in the high mass range, the rate estimate would decrease by about a factor of 1.5 with respect to the result based on the phenomenological model. (The GMR14 model, with parameters tuned to PS1-10jh as used here, does not fit the high mass range (i.e., TDE2) so we do not consider the opposite combination.)

7.5.2 Volumetric TDF rate

To estimate the volumetric rate of TDFs , we compute the efficiency of a given model in bins of galaxy luminosity and integrate this against the galaxy luminosity function (ϕ). This yields an effective galaxy density:

$$\rho_{\rm eff} = \frac{\int dM\, \phi(M)\epsilon(M)}{\int dM \epsilon(M)} \quad . \tag{7.17}$$

We use the SDSS r-band galaxy luminosity function (Blanton et al. 2001). For integration limits, we adopt $M_r = [-19, -23]$, which covers 90% of the galaxies in our sample. For a given model, the volumetric rate follows by multiplying the effective galaxy density with the rate per galaxy.

For the PS1 and the phenomenological models the effective galaxy densities are $4 \times 10^{-3}\,{\rm Mpc}^{-3}$ and $3 \times 10^{-3}\,{\rm Mpc}^{-3}$, respectively. This corresponds to a volumetric rate of $(4-8) \times 10^{-8\pm0.4}\,{\rm yr}^{-1}{\rm Mpc}^{-3}$ for these two empirical light curve models; here we have put the statistical uncertainty in the exponent. For the Disk+Wind model we obtain $\rho_{\rm eff} = 3 \times 10^{-3}\,{\rm Mpc}^{-3}$ (a factor of five lower than the unweighted galaxy density), which implies a volumetric TDF rate in the range $(4-10)\times10^{-8\pm0.4}\,{\rm yr}^{-1}{\rm Mpc}^{-3}$;

for the GMR14 model, $\rho_{\rm eff} = 5 \times 10^{-3}\,{\rm Mpc}^{-3}$.

7.5.3 Comments, Uncertainties and Caveats

We note that the low value of the mean efficiency of our pipeline, $\epsilon \sim 1\%$, seen in Table 7.1) is a result of defining ϵ with respect to the full duration of the survey ($\tau = 7.6$ yr). Many of the simulated flares are simply not detected because they fall into the gap between two observing seasons or occur in a season with few observations. If we only consider the 3 yr with high cadence observations, the efficiency is a factor of ~ 10 higher.

Our search is most sensitive to galaxies hosting black holes with masses in the range $M_{\rm BH} = (0.5 - 5) \times 10^7\,M_\odot$, as expected for a flux-limited galaxy sample. The requirement that $M_{\rm BH} < 10^8\,M_\odot$, reduces the galaxy sample by 5% (or 1% for the Graham scaling relation), while the correction of direct captures (Eq. 7.4) reduces the sample by 33% (21%). Hence the TDF rate for a flux-limited galaxy sample with no restriction on black hole mass can be obtained from Table 7.1 using these percentages. As explained in Section 7.2.1, our rate is valid only for galaxies outside the photometric locus of QSO (i.e., our search is not sensitive to TDF inside active galactic nuclei). This cut on the galaxy colors reduced the parent sample by 80%.

Finally, we note that obscuration due to circumnuclear dust is a systematic uncertainty in using optical measurements to determine the rate of TDFs. Some flares will not be detectable at optical frequencies due to extinction, e.g., the (model-dependent) estimate of the extinction for one of the *Swift*-discovered TDF (Swift 1644+57) is high, $A_V \sim 3$–5 mag (Bloom et al. 2011). The result of extinction by dust is that the optical TDF rate is lower than the intrinsic tidal disruption rate by some factor. Estimating this factor is non-trivial because the region that obscures the TDF light may occupy only a tiny volume of the full galaxy. The optical spectrum of the host galaxy may therefore not reveal (e.g., via the Balmer decrement) the presence of this dust. With a larger sample of TDFs, in the future it may be possible to measure the influence of dust via reddening of the TDF SED, depending on the intrinsic variance in the SEDs.

7.6 Discussion

The optical TDF rate based on our search of SDSS Stripe 82 galaxies is consistent with the rate of large-amplitude, soft X-ray flares from inactive galaxies detected in the *ROSAT* All-Sky Survey deduced by Donley et al. (2002), and for most light curve models our rate is within the (very broad) range $0.1 - 2 \times 10^{-4}\,{\rm yr}^{-1}{\rm galaxy}^{-1}$ of values deemed compatible with the UV observations (Gezari et al. 2008). As noted in the Introduction, the earlier studies were based on more naive treatments of the light curves and dependence on $M_{\rm BH}$ than we have used here and those studies did not attach a systematic uncertainty due to their sensitivity to light curve model. Donley et al. (2002) simply used the median peak luminosity of the X-ray outburst to find the

Name	Mean efficiency (%)	TDF Rate ($\mathrm{yr}^{-1}\mathrm{galaxy}^{-1}$)	
SDSS-only	0.13, 0.62	$< 1.5 \times 10^{-4}$	
PS1 events	1.0	2.0×10^{-5}	
Phenomenological	1.4	1.5×10^{-5}	
M_{BH} scaling: Häring & Rix (2004)		Correction for captures: step-function	exponential
Disk+Wind	0.83, 3.3	1.2×10^{-5}	1.7×10^{-5}
GMR14	1.2	1.8×10^{-5}	1.9×10^{-5}
M_{BH} scaling: Graham (2012)		Correction for captures: step-function	exponential
Disk+Wind	0.22, 1.5	2.1×10^{-5}	3.2×10^{-5}
GMR14	1.6	1.2×10^{-5}	1.3×10^{-5}

TABLE 7.1: Light curve model efficiencies & resulting optical TDF rates. In the first column we list the different light curve models. The second column shows the mean efficiency computed using Eq. 7.6; where the light curve model is based directly on TDE1 and 2, we give the efficiency as obtained for each of them separately. The tidal disruption rate is shown in the last column(s). The results shown in the first three rows of this table are independent of black holes mass (Sec. 7.4.1). For the two light curve models that depend on black hole mass (Sec. 7.4.2), we compute the rate per galaxy using only those galaxies that can yield visible disruptions. The fraction of visible disruptions is computed in two ways: a step function at $M_{\mathrm{BH}} = 10^8\,M_\odot$ (Eq. 7.3), and the more realistic exponential suppression due to direct captures (Eq. 7.4).

effective volume, ignoring the shape of the light curve and dependence on black hole mass, but did a detailed analysis of their complicated selection effects. Gezari et al. (2008) used a peak luminosity that scaled with black hole mass using the Eddington luminosity fraction function from Ulmer (1999), but used an oversimplified light curve model to estimate their selection function, namely a single blackbody temperature characterized by Eddington luminosity radiation at the tidal disruption radius and a $t^{-5/3}$ power-law decay.

All three studies are hampered by low statistics. Thus to get a statistically better estimate and to make a proper comparison of the optical TDF rate with the results from *ROSAT* and *GALEX*, the rates of the latter surveys need to be estimated using the more realistic light curve modeling that we have developed and used here. With a TDF model covering the entire frequency range of optical, UV, and soft X-rays, the effective-galaxy-years could be determined for *ROSAT*, GALEX, and SDSS, and thus derive a rate using the $3 + 3 + 2 = 8$ events discovered by these three surveys. If this process reveals a significant lack of consistency between the number of events detected in each study individually, it would give useful insight into the validity of the light curve modeling and the importance of systematic effects which will differ from one frequency to another.

Turning now to the comparison with predictions, the analytical disruption rate computed by Wang & Merritt (2004) for a singular isothermal sphere (see Eq. 7.10), $\approx 4 \times 10^{-4}\,\mathrm{yr}^{-1}$ for our black hole population (see Fig. 7.3), exceeds our upper limit by a factor of two and our highest estimate of the rate by a factor 10. In order for

the optical TDF rate to be compatible with the Wang & Merritt (2004) prediction, either the light curve model must be seriously in error, or if it is accurate, $\approx 90\%$ of the flares are obscured in the optical. (A larger sample of optical TDFs will readily resolve this question because intermediate examples with severe reddening not seen in TDE1 and 2 should show up if most optical TDFs are too obscured to be detected by the pipeline.) However, not all galaxies may host a nuclear star cluster that can be modeled as an isothermal sphere, and the discrepancy between prediction and our observation may just be a reflection of the breakdown of this hypothesis. Indeed, the optical flare rate we have determined here is well inside the estimated range of tidal disruption rates for $M_{\rm BH} \sim 10^7\,M_\odot$ based the measured surface brightness profiles of nearby elliptical galaxies, $(1-20)\times 10^{-5}\,{\rm yr}^{-1}$ (Syer & Ulmer 1999; Wang & Merritt 2004).

7.7 Conclusion

We have estimated the rate of TDFs in inactive galaxies implied by the detection of two TDFs in a systematic search for nuclear transients in SDSS Stripe 82 galaxies outside the QSO locus (van Velzen et al. 2011) by applying our detection pipeline to simulated light curves. For a given model light curve, the detection efficiency is the fraction of simulated flares that pass all of our selection criteria for the actual cadence and quality of the observations. The minimal flare model for each event is simply the observed light curve; this yields a model-independent upper limit on the optical TDF rate of $\dot{N} < 2\times 10^{-4}\,{\rm yr}^{-1}{\rm galaxy}^{-1}$ (90% CL).

To obtain a more realistic estimate of the TDF rate, we used a phenomenological model that fits both the TDE1 and TDE2 light curves and light curves from two more recently discovered events in the Pan-STARRS survey, whose sampling covered both the rise and decay of the flares. This gives a rate of

$$\dot{N}_{\rm TDF} = (1.5-2.0)^{+2.7}_{-1.3}\times 10^{-5}\ {\rm yr}^{-1}{\rm galaxy}^{-1} \quad , \tag{7.18}$$

with 1σ uncertainty for Poisson statistics. The corresponding volumetric TDF rate is $(4-8)\times 10^{-8\pm 0.4}\,{\rm yr}^{-1}{\rm Mpc}^{-3}$, with the statistical error given as an uncertainty in the exponent. We also considered two different theoretically motivated light curve models, two different models for how the TDF light curve cuts off at high $M_{\rm BH}$, and two alternatives for the relationship between galaxy luminosity and black hole mass. From the range of the resultant rates, one can conservatively estimate that the theoretical (i.e., not statistical) uncertainty in $\dot{N}_{\rm TDF}$ is not significantly greater than the statistical one indicated in Eq. 7.18.

Acknowledgments

We are grateful to E. M. Rossi, G. Lodato, and J. Guillochon for supplying their model light curves in tabulated form, and to J. Guillochon for extensive discussions. We also like to

thank S. Gezari and D. Zaritsky for providing feedback to an early draft, and W. R. Brown, A. Gal-Yam, M. Kesden, D. Merritt, E. O. Ofek and E. Ramirez-Ruiz for useful discussions. The research of GRF was supported in part by NSF-PHY-1212538

Chapter 8

Radio jets from stellar tidal disruption events

Sjoert van Velzen, Elmar Körding, and Heino Falcke

2011, Monthly Notices of the Royal Astronomical Society Letters, 417, L51

Abstract

A star that passes too close to a massive black hole will be torn apart by tidal forces. The flare of photons emitted during the accretion of the stellar debris is predicted to be observable and candidates of such events have been observed at optical to X-ray frequencies. If a fraction of the accreted material is fed into a jet, tidal flares should be detectable at radio frequencies too, thus comprising a new class of rare radio transients. Using the well-established scaling between accretion power and jet luminosity and basic synchrotron theory, we construct an empirically-rooted model to predict the jet luminosity for a time-dependent accretion rate. We apply this model to stellar tidal disruptions and predict the snapshot rate of these events. For a small angle between the observer and the jet, our model reproduces the observed radio flux of the tidal flare candidate GRB 110328A (also known as Swift 1644+57). We find that future radio surveys will be able to test whether the majority of tidal disruptions are accompanied by a jet.

8.1 Introduction

When a star wanders too close to the massive black hole at the center of its galaxy, it will be tidally disrupted by the gravity of the hole (Hills 1975). After the disruption, about half of stellar mass remains bound (e.g., Rees 1988; Evans & Kochanek 1989) and an electromagnetic flare is produced as the debris falls back onto the black hole. Theoretical efforts to predict this emission have focused predominately on the accretion of the bound stellar debris (e.g., Rees 1988; Loeb & Ulmer 1997; Ulmer 1999; Bogdanović et al. 2004) and the contribution from a super-Eddington outflow (Strubbe & Quataert 2009, 2011; Lodato & Rossi 2011).

The electromagnetic flare from a stellar tidal disruption event (TDE) may be our only tool to probe dormant black holes, e.g., like the Galactic center black hole (Melia & Falcke 2001), beyond the Local Universe and could allow a much-anticipated study of black hole demographics as a function of galaxy type and cosmic time. Individual TDE are also interesting since the sudden increase of accretion rate after the disruption, from zero to super-Eddington in a few months or even hours, is much more rapid than the timescale of normal accretion onto super-massive black holes.

A number of (candidate) TDE have been identified in X-ray (Bade et al. 1996; Komossa & Bade 1999; Komossa & Greiner 1999; Esquej et al. 2008) —for a review see Komossa (2002), UV (Gezari et al. 2006, 2008, 2009b) and optical surveys (van Velzen et al. 2011; Drake et al. 2011; Cenko et al. 2012a). Based on the optical luminosity of observed TDE one can predict that near-future synoptic surveys, such as LSST (Ivezić et al. 2008), should detect thousands of such events per year (Gezari et al. 2009b; van Velzen et al. 2011).

Follow-up observations of candidate TDE at radio frequencies is important to identify these events, as was realized when the first X-ray candidates were detected (Komossa 2002). However, blind radio variability surveys also have the potential to *discover* TDE. The rapid increase of sky coverage and sensitivity of variability surveys at both high and low frequencies promises an exciting future for this field.

Recently, Giannios & Metzger (2011) proposed a model for the radio emission from TDE, based on the interaction of the jet with the interstellar medium (ISM); Bower (2011) compared their predictions to upper limits of existing radio surveys for transients. The present work is an extension of the approach outlined in van Velzen, Falcke, & Farrar (2010), where we use the well-established jet-disk symbiosis model to calculate a time-dependent jet model for TDEs. We will only consider the emission from the compact core of the jet; interactions with the surrounding medium may enhance the jet luminosity in some cases, but here we aim to obtain a conservative model and we therefore consider solely the internal jet emission.

In Section 8.2, we present our time-dependent jet model. In Section 8.3, we discus the light curves produced by our model and compare them to radio observations of candidate TDE. We predict the snapshot rate of jets from TDE in Section 8.4 and compare this rate to the sensitivity of current and future radio transient surveys.

8.2 Time-dependent jet model

There is already quite a range of time-dependent models for radio jets in super-massive black holes in the literature (e.g., Chiaberge & Ghisellini 1999; Gupta et al. 2006), but they typically only address relatively small changes or focus on a subclass of AGN. A major question remains how jets evolve, as a function of time when accretion suddenly sets in and increases by many orders of magnitude. There is increasing consensus that accretion discs and jets are intrinsically coupled and are best understood as a symbiotic system. Evidence that jets are ubiquitous to accretion comes from the 'fundamental plane of black holes', which provides a universal scaling law for the non-thermal emission of black holes over all mass scales (Merloni, Heinz, & di Matteo 2003; Falcke, Körding, & Markoff 2004a). We thus proceed under the hypothesis that all accreting massive objects, including TDEs, launch a jet, but, as discussed later, take potential radio-loud/radio-quiet switches at high accretion rates into account.

In this section, we will first generalize the jet-disk symbiosis model of Falcke & Biermann (1995, FB95, hereafter) to a time-dependent accretion rate and we then apply this model to TDE.

8.2.1 Basic jet model

The essence of jet-disk symbiosis is power unification: $Q_j = q_j L_d \propto q_j \dot{m}$, the jet power ($Q_j$) is some fraction ($q_j$) of the disk luminosity (L_d), which is a linear function of the accretion rate ($\dot{m}$). If we assume equipartition between the energy in relativistic particles and the magnetic field, the synchrotron emissivity follows from the accretion rate: $\epsilon_{\rm syn} \propto B^{3.5} \propto (q_j \dot{m})^{1.75} z^{-3.5}$, with z the distance to the origin of the jet (FB95, Eq. 19). We obtain the synchrotron luminosity of the jet (L_ν) by integrating the emissivity over the jet volume, a cylindrical-symmetric cone,

$$L_\nu = C_{\rm eq} \int_{z_{\rm ssa}}^{\infty} {\rm d}z \, z^2 \epsilon_{\rm syn}(z, \nu/\delta) \propto (q_j L_d)^{17/12} \tag{8.1}$$

(FB95, Eqs. 52 & 56). Here δ is the Doppler factor of the jet and ν is the observed frequency. The lower limit of integration, $z_{\rm ssa}(\nu/\delta)$, is the distance where the jet becomes optically thin to synchrotron self-absorption. The normalization ($C_{\rm eq}$) is the conversion factor between jet power and jet luminosity, which can be estimated using equipartition arguments or obtained by observations.

The great success of jet-disk symbiosis is that the observed properties of all accreting black holes with radio-loud jets can be fit with $q_j = 0.2 \equiv q_{\rm loud}$ and a single value of the normalization ($C_{\rm eq}$) of Eq. 8.1 (Falcke et al. 1995b; Körding et al. 2008b). In his work, we will fix $C_{\rm eq}$ using the empirical normalization found by Körding et al. (2008b) for efficient accretion, $L_d = 0.1 c^2 \dot{m}$, and we will use a jet Lorentz factor $\gamma_j = 5$ (Falcke et al. 1995b) throughout.

The "classic" jet model (Eq. 8.1) is derived for a constant accretion rate; to use this

model for a time-dependent accretion rate, $\dot{m}(t)$, we have to consider three things: (i) the non-zero time delay of photons emitted at different locations in jet, (ii) $z_{\rm ssa}(t)$ will set the time scale of the emission, and (iii) the emissivity becomes a function of time. The latter of these changes is trivial to apply because at the base of the jet, the relation between the synchrotron emissivity and accretion rate is given by the standard jet-disk model and all one has to do is to propagate $\epsilon_{\rm syn}$ forward in time using $z(t) = t\beta_j c$. To account for (ii) we use $\tau \propto z\kappa_{\rm syn}/\sin(i) = 1$, where $\kappa_{\rm syn}$ is the synchrotron absorption coefficient, to find

$$z_{\rm ssa} = 1\,{\rm pc}\, f \frac{\rm GHz}{\nu/\delta} \left(\frac{q_j(t)}{0.2} \frac{L_d(t)}{10^{45}\,{\rm erg\,s^{-1}}} \right)^{\frac{2}{3}} \left(\frac{\beta_j}{\sin(\frac{i}{30^\circ})} \frac{5}{\gamma_j} \right)^{\frac{1}{3}} \tag{8.2}$$

(FB95, Eq. 52), here $f \sim 1$, is a factor that depends on the details of equipartition. We perform a check on the latter using observations of NGC 4258 at 22 GHz showing the base of the jet at a minimum distance of 0.012 pc from the dynamical center of the accretion disk (Herrnstein et al. 1997); using $i_{\rm obs} = 83^\circ$ and $\gamma_j = 3$ (Yuan et al. 2002) at the base of the jet and $\dot{m} = 0.01 M_\odot\,{\rm yr}^{-1}$ (Gammie et al. 1999), we obtain $f \approx 0.5$.

We can now modify the integral of Eq. 8.1 to obtain our time-dependent jet model,

$$L_\nu(t) = C_{\rm eq}\delta^2 \int_0^{z_{\rm dec}} {\rm d}z\, z^2 \epsilon_{\rm syn}(t_r, z, \nu/\delta)\Theta_{\rm ssa}(t_r, z, \nu/\delta) \quad . \tag{8.3}$$

Here $\Theta_{\rm ssa}(t, z, \nu)$ is a step function that enforces a crude radiative transfer: it is zero for $z < z_{\rm ssa}(t)$ and unity for $z > z_{\rm ssa}(t)$. The retarded time, t_r, is introduced to ensure that we integrate using only the photons that will arrive simultaneously at the observer, $t_r(t, z) = t - z\cos(i)\, c^{-1}$with i the angle between the jet and observer, in the rest-frame of the jet. Note that for observed angles $\cos(i_{\rm obs}) < \beta_j$, we have $t_r > t$; the photons from the middle of the jet arrive simultaneous with photons emitted further ahead, i.e., the jet appears to be seen from behind in the observer frame (e.g., Jester 2008). The upper limit of integration, $z_{\rm dec}$, is the radius where the jet will slow down significantly because the initial jet energy equals the energy of the shocked matter swept up by the jet (e.g., Piran 2004): $z_{\rm dec} \propto (E_j/n\gamma_j^2)^{1/3}$, with $E_j \propto \int q_j \dot{m}\, {\rm d}t$ and n the ISM number density. In the following section we discus $q_j(t)$ and $\dot{m}(t)$ for tidal disruption events and give the physical scale of $z_{\rm dec}$.

8.2.2 Accretion states of TDE

To apply the time-dependent jet-disk symbiosis model (Eq. 8.3) to TDE we need the accretion rate as a function of time and black hole mass. We first consider the time it takes for most of the stellar debris to return to the pericenter (R_p) after the disruption, $t_{\rm fallback} \sim 0.1(M_{\rm BH}/10^6 M_\odot)^{1/2}(R_p/R_t)^3\,{\rm yr}$ for a solar-type star (e.g., Ulmer 1999,

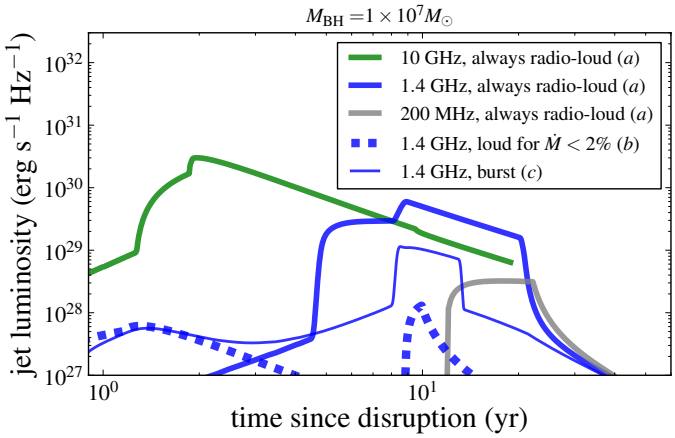

FIGURE 8.1: Light curves for synchrotron emission for jets from TDE for $i_{\rm obs} = 30°$, $M_{\rm BH} = 10^7\,M_\odot$ and three different scenarios of coupling between accretion and jet power (*a*, *b* and *c* in the legend refer to Eq. 8.4). For the "always radio-loud" scenario, we show three different frequencies (thick solid lines). The highest frequencies are visible at the earliest times and at highest luminosity because $z_{\rm ssa} \propto \nu^{-1}$ (Eq. 8.2). For the "burst" scenario (thin line) we see a strong luminosity increase corresponding to the radio-loud part of the jet during the start of the accretion, as expected, this peak coincides with the peak of scenario *a*.

Eq. 3), R_t is the tidal disruption radius. After this time, the material falls back onto the black hole at a rate, $\dot{m}_{\rm fallback} \approx 1/3\,M_*/t_{\rm fallback}(t/t_{\rm fallback})^{-5/3}$ (Rees 1988), here M_* is the mass of the star. We will use $\dot{m}_{\rm fallback}$ with $R_p = R_t$ for the accretion rate onto the black hole that can be fed into the jet. For $M_{\rm BH} <$ few $10^7 M_\odot$, the fallback rate will (greatly) exceed the Eddington rate for some time, but we will conservatively asume that $\dot{m}(t) = \dot{m}_{\rm Edd}$ during this time; we use an exponential rise to the peak accretion rate for $t < t_{\rm fallback}$. Our results are not sensitive to potential deviations from the canonical $t^{-5/3}$ scaling of the fallback rate (e.g., Lodato, King, & Pringle 2009), because most of the energy is injected into the jet during the super-Eddington phase, where $\dot{m}$ is capped at $\dot{m}_{\rm Edd}$.

With the accretion rate given by the theory of tidal disruptions, we only have to provide one more ingredient to produce radio light curves for these events: the fraction of accretion power that is fed into the jet. Jets from active super-massive black holes can be radio-loud or radio-quiet (Kellermann et al. 1989), which appears to be at odds with jet-disk symbiosis. However, detailed observations have shown that nearly all radio-quiet AGN do show some radio emission which can be interpreted as originating from the core of a relativistic jet (Brunthaler et al. 2000; Falcke 2001). Indeed radio-quiet jets can also be accommodated by Eq. 8.1 by reducing $C_{\rm eq}$ or q_j with a factor $\sim 10^2$ with respect to radio-loud systems.

If we assume that the physics behind launching the jet and producing the synchrotron emission is no different for TDE and "normal" active black holes, we are left to answer the following question: *is a TDE jet radio-loud or radio-quiet?* Observations of accreting stellar mass black holes (i.e., X-ray binaries) can help to answer this question since they are variable on timescales down to minutes (Belloni et al. 2005) and they can serve as examples for AGN (McHardy et al. 2006; Chatterjee et al. 2011).

When X-ray binaries experience a burst of accretion, they follow a predefined track in the hardness-intensity diagram (Belloni et al. 2005) corresponding to distinct accretion states with associated jet properties (Fender et al. 2004). In the quiescent mode (the hard-state) and during the onset of the burst, jets in X-ray binaries are radio-loud, while in the high-accretion mode (the soft-state) they are radio-quiet.

The sudden enhancement of the accretion rate during a TDE, may move it through the different modes of accretion in two ways: directly into the radio-quiet soft-state, or into the soft-state via the radio-loud burst-state. Alternatively, the jet from a TDE may behave like a radio-loud quasar at all times. We therefore consider three different scenarios for the fraction of accretion energy that is fed into the jet:

$$q_j = \begin{cases} q_{\rm loud} & \text{all times} & (a) \\ q_{\rm loud}/10^2 & \dot{m}(t) > 2\%\dot{m}_{\rm Edd} & (b) \\ q_{\rm loud} & t < t_{\rm fallback} & (c) \end{cases} . \tag{8.4}$$

where each scenario reverts to the preceding one if the condition on t or $\dot{m}$ is not true (e.g., $q_j = q_{\rm loud} = 0.2$ if $\dot{m} < 2\%\dot{m}_{\rm Edd}$ in all three scenarios). In scenario b the jet becomes radio-loud only when the accretion drops below $< 2\%\dot{m}_{\rm Edd}$ (Maccarone 2003), while in scenario c the systems makes a full loop trough all accretion modes, starting with a radio-loud burst during the onset of the accretion. We consider a most optimistic, b most pessimistic, and c the most likely scenario. The two orders of magnitude difference in q_j between scenarios a and b can also be taken to reflect our uncertainty on the coupling between jet power and accretion during the super-Eddington phase of the disruption.

With q_j and $\dot{m}$ at hand, we can now calculate, $z_{\rm dec}$, the radius where the jet will slow down significantly, which is the upper limit of the integral over jet volume (Eq. 8.3). For $M_{\rm BH} = 10^7\,M_\odot$ and scenario a (Eq. 8.4), using a jet opening angle of 7° (FB95) and an ISM density of 1 proton per cm^{-3}, we obtain $z_{\rm dec} = 3.5\,$pc. Comparing this to $z_{\rm ssa}$ (Eq. 8.2) this implies a significant suppression of the luminosity for observers looking at $\nu < 500\,$MHz because $z_{\rm dec} < z_{\rm ssa}(\nu)$. However, this suppression is less relevant at lower $M_{\rm BH}$ or q_j, since $z_{\rm dec} \propto (q_j L_d)^{1/3}$ while $z_{\rm ssa} \propto (q_j L_d)^{2/3}$. Clearly, the density distribution within a few parsec from the black hole varies between galaxies: each TDE jet will face a different deceleration radius. In elliptical galaxies, $z_{\rm dec}$ is likely to be larger by at least a factor 10 with respect to the value adopted in this work, due to the low gas density in these galaxies (e.g., Biermann &

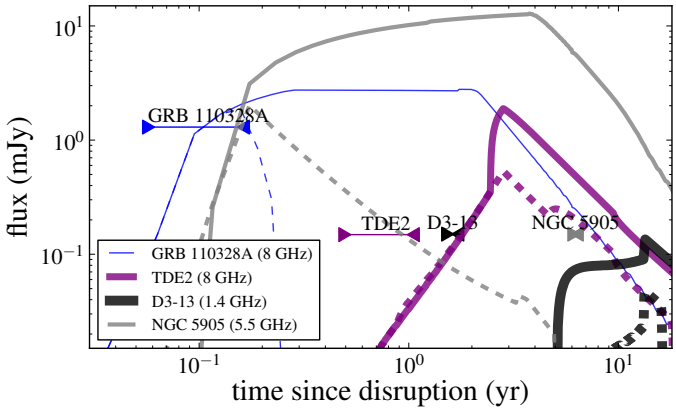

FIGURE 8.2: The predicted flux for TDE2, $M_{\rm BH} \approx 5 \times 10^7\,M_\odot$ (van Velzen et al. 2011), D3-13, $M_{\rm BH} \approx 2 \times 10^7\,M_\odot$ (Gezari et al. 2008), the X-ray flare from NGC 5905, $M_{\rm BH} \approx 2 \times 10^5\,M_\odot$ (Komossa & Bade 1999) and GRB 110328, assuming $M_{\rm BH} \approx 1 \times 10^6\,M_\odot$. We show our most optimistic model *a* (solid line) and the more realistic "burst model" *c* (dashed line). We use $i_{\rm obs} = 30^\circ$ for the first three candidates and show the 3-σ upper limits at $\nu = 8$ GHz (van Velzen et al. 2011), $\nu = 1.4$ GHz (Bower 2011) and $\nu = 8$ GHz (Komossa 2002) from the last radio observations. For GRB 110328, we use $i_{\rm obs} = 1^\circ$ and we show the VLBA detection at 8.4 GHz (Levan et al. 2011). The triangles pointing right and left correspond to the lower and upper limit on the time of disruption, respectively.

Kronberg 1983). On the other hand, $z_{\rm dec}$ can decrease if the jet runs into a high-density clump of matter, which will enhance the luminosity, as seen in an exemplary way in the radio-intermediate quasar III Zw 2 (Brunthaler et al. 2000). For galaxies where $z_{\rm dec} < 0.1\,{\rm pc}$, the external emission as modeled by Giannios & Metzger (2011) dominates over emission from the core of the jet at all relevant frequencies. Discriminating between core and external emission for individual TDE jets may be possible using the time delay between the radio emission and the time of disruption.

8.3 Radio light curves

In Fig. 8.1 we show the radio light curves that result from applying the jet-disk symbiosis to TDEs. For the scenario in which the jet is always radio-loud (Eq. 8.4*a*), one can see most clearly how the opacity sets the timescale of the emission. Since $z_{\rm ssa} \propto \nu^{-1}$ (Eq. 8.2), the jet is visible at earlier times and at higher luminosity for higher frequencies. The sudden drop in luminosity after about 20 yr is caused by our fixed upper limit of Eq. 8.3 ($z_{\rm dec}$): we stop following the jet beyond this point because the aim of this work is to predict the internal jet emission. Connecting the internal and external emission in a single model will be the subject of future work. At $\nu = 200$ MHz, we see a plateau of constant luminosity which is caused by the photons produced

after the super-Eddington phase. For a given black hole mass, the duration of the radio flare is maximal if viewed along the critical angle, $i_{\rm obs} = \arccos(\beta_j)$; within this angle, the timescale is shorter because most photons arrive nearly simultaneously at the detector, while at larger viewing angles, the frequency in the rest-frame of the jet (ν/δ) increases, making the jet visible at earlier times.

In Fig. 8.2 we show follow-up radio observations that have been obtained for some candidate TDE. The upper limits on the radio luminosity are consistent with our most optimistic prediction for the jet luminosity, except for the candidate in NGC 5905 which is only consistent with scenarios *b* and *c*. We note that observations of similar depth obtained today, ~ 5 years after the flare, should yield a detection. Finally we consider the recently discovered GRB 110328A / Swift J164449.3+573451, which may be an example of a strongly beamed TDE (e.g., Bloom et al. 2011; Levan et al. 2011; Zauderer et al. 2011); indeed for $i_{\rm obs} < 10^\circ$ and $M_{\rm BH} = 10^6 M_\odot$ our model with scenarios *a* yields the observed VLBA radio flux (Levan et al. 2011) of this transient. If we conservatively assume that the first *Swift* detection marks the start of the disruption, our model requires $i_{\rm obs} < 1^\circ$ to explain the $\sim$ days delay between gamma-ray and radio photons; this angle constraint becomes less stringent if the high-energy photons originate from the jet.

8.4 Snapshot rate

Using the model presented in Section 8.2, we can predict how many jets are visible above a certain flux limit ($F_{\rm lim}$) at any moment in time,

$$N(F_{\rm lim},\nu) = (4\pi)^{-1}\dot{N}_{\rm tde}\int {\rm d}\Omega_{\rm obs}\int {\rm d}z\, 4\pi d_C^2(z)\times \int {\rm d}M_{\rm BH}\ \phi_{\rm BH}\,\tau_{\rm eff}(L_\nu, d_L(z), F_{\rm lim})\ . \quad (8.5)$$

Here $d_C(z)$ and $d_L(z)$ are the co-moving and luminosity distance[1], respectively and $\phi_{\rm BH}$ is the black hole mass function. The integration over viewing angles, ${\rm d}\Omega_{\rm obs}$, accounts for the effects of Doppler boosting. Finally, our jet model enters via $\tau_{\rm eff}$ or the "effective time" given by the part of the light curve that obeys $L_\nu(t)/(4\pi d_L^2) > F_{\rm lim}$. We also consider the model by Giannios & Metzger (2011) using their Eq. 8, with fiducial parameters.

We use the local black hole mass function of Marconi et al. (2004) for $\phi_{\rm BH}$ and a TDE rate per black hole of $\dot{N}_{\rm tde} = 10^{-5}\,{\rm yr}^{-1}$ which is based on the observed rate per galaxy from SDSS observations ($3\times10^{-5}\,{\rm yr}^{-1}$, van Velzen et al. 2011) and ROSAT observations ($9\times10^{-6}\,{\rm yr}^{-1}$, Donley et al. 2002). At the lowest flux limit we consider, $F_{\rm lim} = 0.05\,{\rm mJy}$, $\tau_{\rm eff}(z)\times d_c^2$ peaks at $z = 0.5$ so we are not sensitive to cosmological evolution of $\phi_{\rm BH}$ or $\dot{N}_{\rm TDE}$. Since L_ν peaks at $M_{\rm BH}\sim 5\times10^7\,M_\odot$ and $\phi(M_{\rm BH})$ flattens

[1]We adopt a standard cosmology with $H_0 = 72\,{\rm km\,s^{-1}Mpc^{-1}}$, $\Omega_m = 0.3$ and $\Omega_\Lambda = 0.7$.

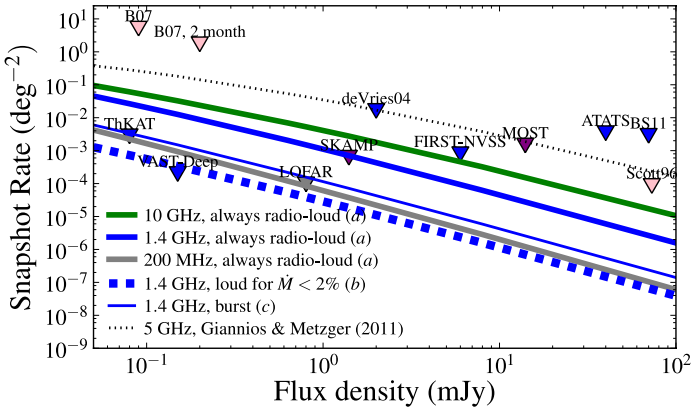

FIGURE 8.3: The snapshot rate of TDE jets. We show 2-σ upper-limits from: Scott (1996) and Bower et al. (2007, B07) at 5 GHz, Levinson et al. (2002); Gal-Yam et al. (2006, FIRST-NVSS), de Vries et al. (2004), ATAS (Croft et al. 2010) and Bower & Saul (2011, BS11) at 1.4 GHz, MOST (Bannister et al. 2011) at 843 MHz. We also show the limits that can be obtained if no candidates are detected in (near) future variability surveys. We refer to Ofek et al. (2011) for an overview of radio variability surveys.

towards low black hole mass, Eq. 8.5 is not sensitive to the upper or lower boundaries of the integration over black hole mass.

In Fig. 8.3 we show the snapshot rate for the three different scenarios we consider (Eq. 8.4) and three different frequencies. At higher frequencies the jets are brighter and thus visible out to a larger volume, while at lower frequencies the duration is longer. These competing effects also imply that any uncertainty on $z_{\rm ssa}$ (Eq. 8.2) has limited influence on the predicted snapshot rate. We also compare our predicted snapshot rate to observed upper limits on the rate of extra-galactic radio transients. For surveys with detected transients, we use the classification by Bower (2011) to limit these radio transients to potential TDE jets only.

The current radio transient surveys are not sensitive or large enough to test our prediction of the snapshot rate. This changes, however, when we consider the potential of near-future projects. For LOFAR (van Haarlem et al. 2013), we use 0.25 mJy for the thermal rms obtained at 180 MHz in a survey that will cover 2π steradian in about 3 months. We also consider SKAMP[2], ThunderKAT, which is part of MeerKAT (Booth et al. 2009), and VAST (Murphy et al. 2013), which is part of ASKAP[3]. Using 3 times the rms for the detection threshold, we find that for the optimistic scenario (Eq. 8.4*a*), the SKAMP, LOFAR, surveys should contain about 2 jets from TDE. The VAST project is sensitive enough to test even our most conservative scenario.

[2] `www.physics.usyd.edu.au/sifa/Main/SKAMP`
[3] `www.atnf.csiro.au/projects/askap`

8.5 Conclusion

We have presented a time-dependent jet-disk symbiosis model that yields a conservative and robust estimate of the radio luminosity of the compact jet that likely accompanies stellar tidal disruption events. This model is consistent with current constraints of the radio properties of TDE candidates and naturally predicts the observed radio flux of the newly discovered GRB 110328A. Based on our predicted snapshot rate we conclude that future radio surveys will be able to test whether the majority of tidal disruptions are indeed accompanied by a relativistic jet.

Acknowledgments

We thank the anonymous referee for comments that improved the manuscript, A. Marconi for sharing data of $\phi_{\rm BH}$ and D. A. Frail, D. Giannios, S. Komossa, B. D. Metzger, and R. Wijnands for useful discussions.

Chapter 9

Constraints on off-axis jets from stellar tidal disruption flares

Sjoert van Velzen, Dale A. Frail, Elmar Körding, and Heino Falcke

2013, Astronomy & Astrophysics 552, A5

Abstract

Many decades of observations of active galactic nuclei and X-ray binaries have shown that relativistic jets are ubiquitous when compact objects accrete. One could therefore anticipate the launch of a jet after a star is disrupted and accreted by a massive black hole. This birth of a relativistic jet may have been observed recently in two stellar tidal disruption flares (TDFs), which were discovered in gamma-rays by *Swift*. Yet no transient radio emission has been detected from the tens of TDF candidates that were discovered at optical to soft X-ray frequencies. Because the sample that was followed-up at radio frequencies is small, the non-detections can be explained by Doppler boosting, which reduces the jet flux for off-axis observers. And since the existing follow-up observation are mostly within 10 months of the discovery, the non-detections can also be due to a delay of the radio emission with respect to the time of disruption. To test the conjecture that all TDFs launch jets, we obtained 5 GHz follow-up observations with the Jansky VLA of seven known TDFs. To avoid missing delayed jet emission, our observations probe 1-8 years since the estimated time of disruption. None of the sources are detected, with very deep upper limits at the 10 micro Jansky level. These observations rule out the hypothesis that these TDFs launched jets similar to radio-loud quasars. We also constrain the possibility that the flares hosted a jet identical to Swift 1644+57, the first and best-sampled relativistic TDF. We thus obtain evidence for a dichotomy in the stellar tidal disruption population, implying that the jet launching mechanism is sensitive to the parameters of the disruption.

9.1 Introduction

The disruption of a star by a massive black hole leads to arguably the most spectacular form of accretion onto these compact objects. The stellar debris that remains bound after the disruption returns to the black hole at a rate that initially can exceed the Eddington limit ($\dot{m}_{\rm Edd}$) by many orders of magnitude. This fallback rate declines with a power law index of $-5/3$ (Rees 1988; Phinney 1989), reaching 1% of $\dot{m}_{\rm Edd}$ within a few to ten years. A tidal disruption flare (TDF) may thus be used to sample different modes of accretion (e.g., Abramowicz & Fragile 2013) for a single supermassive black hole. Considerable effort is needed to simulate the dynamics of the disruption (e.g., Nolthenius & Katz 1982; Evans & Kochanek 1989; Rosswog et al. 2009; Guillochon & Ramirez-Ruiz 2013) and to estimate the resulting optical to X-ray light curve of the flare (e.g., Loeb & Ulmer 1997; Bogdanović et al. 2004; Strubbe & Quataert 2009; Lodato & Rossi 2011). Efficient detection to obtain a large sample of TDFs is much anticipated, as this will allow, for example, a study of the demographics of dormant black holes beyond the Local Universe (Frank & Rees 1976; Lidskii & Ozernoi 1979).

Tens of (candidate) stellar tidal disruption events have been found by searching for flares in soft X-ray (Komossa & Bade 1999; Grupe et al. 1999; Komossa & Greiner 1999; Greiner et al. 2000; Esquej et al. 2008; Maksym et al. 2010; Lin et al. 2011; Saxton et al. 2012), UV (Gezari et al. 2006, 2008, 2009b, 2012), or optical surveys (van Velzen et al. 2011; Drake et al. 2011; Cenko et al. 2012a), or based on spectra with extreme coronal lines (Komossa et al. 2008; Wang et al. 2012). None of these thermal flares are associated with a radio transient, but only a handful have been followed-up at this frequency. The only tidal disruption candidates with a *detected* transient radio counterpart are those discovered in γ-rays by *Swift*: Swift 1644+57 (Bloom et al. 2011; Burrows et al. 2011; Levan et al. 2011; Zauderer et al. 2011) and Swift 2058+05 (Cenko et al. 2012b). Since the radio and X-ray emission of these two events most likely originates from a relativistic jetted outflow, they are often referred to as relativistic TDFs. In this chapter we shall refer to the other class of TDFs as 'thermal', since they are all discovered at optical to soft X-ray frequencies.

One is left to wonder why the two TDFs discovered with *Swift* are the only events with evidence for a newly-born jet. Interpreting this as a radio-loud/radio-quiet dichotomy, similar to the devision of radio-loudness in quasars (Kellermann et al. 1989; Falcke et al. 1996; Sikora et al. 2007), would require that the tidal disruption jet launching mechanism is sensitive to the properties of the disruption (e.g., mass ratio, impact parameter, orientation of the orbit of the star with respect to the black hole spin, or circumnuclear environment). The explanation that quasars spend only a fraction of their time as radio-loud objects, similar to the jets in the 'hard intermediate state' of X-ray binaries (e.g., Körding et al. 2006b), does not apply to tidal disruptions because their accretion rate is not constant. On the other hand, based on the observed fundamental plane of black hole accretion (Merloni, Heinz, & di Matteo 2003; Falcke, Körding, & Markoff 2004a), and the abundance of jets in low luminosity AGN (Nagar

et al. 2000) and X-ray binaries or microquasars (Mirabel & Rodríguez 1999; Fender 2001), one may postulate that *all* stellar tidal disruptions launch jets. Likewise, Mïller & Gültekin (2011) argue that the fundamental plane can be used to estimate the black hole mass of a TDF (if X-ray and radio observations of the flare are available).

If all stellar disruptions are indeed accompanied by a relativistic outflow, the current upper limits on the radio flux of the thermal TDFs can be explained by the orientation of this jet which can dramatically reduce the flux due to relativistic Doppler boosting. The current non-detections may also be explained by a delay of the radio emission of the jet with respect to the time of disruption. However, the number of TDFs that have been followed-up at radio frequencies is currently not sufficient to test this unification based on viewing angle.

Recent advances in the hardware of the Very Large Array (VLA) have made it possible to obtain very deep radio observations of stellar tidal disruptions in a relatively short amount of time. To use this opportunity, we selected all thermal stellar tidal disruptions that occurred after 2004 for follow-up observations. These observations significantly increase the number of TDFs with deep radio observations. And because our radio observations span a wide range of times since the disruption, we can, for the first time, test the hypothesis that all stellar tidal disruptions launch jets.

The remainder of chapter is organized as follows. In Section 9.2 we present two different tidal disruption (TD) jet models and compute off-axis light curves. In Section 9.3 we discuss the radio observations and sample selection. We use these observations to constrain the jet models in Section 9.4 and we close with a discussion in Section 9.5.

9.2 Tidal disruption jet models

To be able to interpret our radio observations, we need a model that describes the radio emission of jets in accreting objects. In this section we therefore review two models of tidal disruption jets and we present off-axis light curves for these models. We have divided the models into two classes[1] based on the origin of the emitting particles: external or internal. In both models, some fraction of the accretion power ends up in the jet and the emission mechanism is synchrotron radiation.

9.2.1 External model: off-axis light curves for Swift 1644+57

The external model of radio emission from TD jets was first presented by Giannios & Metzger (2011) and further developed by Metzger, Giannios, & Mimica (2012).

[1] Other models of TD jets (Lei & Zhang 2011; Krolik & Piran 2012; De Colle et al. 2012), are not discussed here since these make no predictions for off-axis light curves at a given observer frequency.

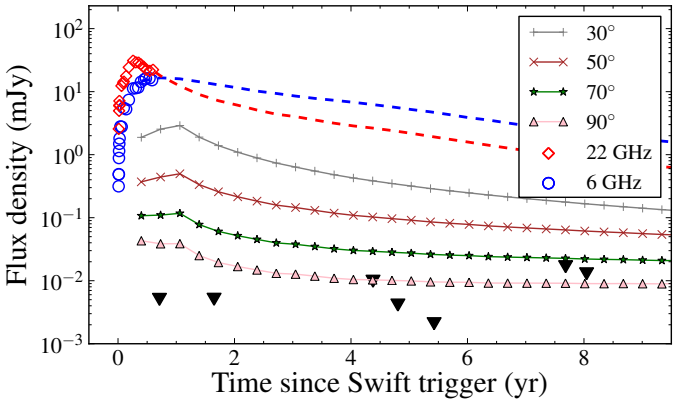

FIGURE 9.1: The observed light curve of Swift 1644+57 (open symbols), with the predicted late-time light curve (dashed lines) for a total jet energy of $E_j = 10^{52}$ erg (Berger et al. 2012). We show the estimated 5 GHz light curve of different off-axis observers, Eq. 9.2, assuming that the Lorentz factor of the jet decreases with $\Gamma_j \propto t^{-0.2}$, as inferred by Berger et al. (2012). We modified the extrapolated light curve to match a Sedov-Taylor solution, $L_j \propto t^{-1.9}$, when $\Gamma_j < 2$. The 2-σ upper limits on the radio flux of seven other TDF candidates (Table 9.2) are shown with black triangles (we scaled these limits to the redshift of Swift 1644+57, see Section 9.4.1).

Shock interaction between the jet and the gaseous circumnuclear medium powers the emission, similar to afterglow models of gamma-ray bursts (e.g., Sari & Piran 1995).

The external model has been applied to the radio light curve of the relativistic TDF Swift 1644+57 (Metzger et al. 2012; Berger et al. 2012). We show the fit and predicted late-time light curve in Fig. 9.1. We note that this fit requires a continuous increase of the isotropic jet power during the first year of observations.

The scaling of the synchrotron peak and self absorption frequency in the Metzger et al. (2012) model of Swift 1644+57 are based on spherical expansion of an ultra-relativistic shell and thus require $\theta_j \Gamma_j < 1$ (with θ_j, Γ_j the jet opening angle and Lorentz factor, respectively), plus an on-axis observer $i_1 < 1/\Gamma_j(t = 0)$; both requirements are supported by the observed radio light curve (Metzger et al. 2012).

To compute the light curve for an off-axis observer, we first boost the observed on-axis flux $F_1(\nu)$ into the jet rest-frame

$$L_j(\nu) = d_L^2 \delta_1^{3-\alpha} F_1(\nu) \tag{9.1}$$

(e.g., Lind & Blandford 1985; Jester 2008). Here we introduced the Doppler factor for the on-axis observer $\delta_1 = [\Gamma_j(1 - \beta_j \cos i_1)]^{-1}$ with $\beta_j = v_j/c$, α is the spectral index defined as $F(\nu) \propto \nu^\alpha$, and d_L is the luminosity distance. Next, we transform the jet luminosity to the off-axis observer using a different Doppler factor, δ_2. If the

size of the emitting region is small compared to the distance to the black hole, the time delay due to the geometrical separation of the synchrotron peak with frequency can be ignored, and we can estimate the flux for an observer sitting at i_2:

$$F_2(t,\nu) = \left(\frac{\delta_2}{\delta_1}\right)^{3-\alpha(t)} F_1(t,\nu)$$
$$\approx \left(\frac{1-\beta_j(t)}{1-\beta_j(t)\cos i_2}\right)^{3-\alpha(t)} F_1(t,\nu). \quad (9.2)$$

Here t is measured in the observer-frame, $\alpha(t)$ is obtained from the light curve, and we used $\cos i_1 \approx 1-\Gamma_j^{-2}/2 \sim 1$ to simplify the equation. If Swift 1644+57 was indeed a relativistic outflow that we observed on-axis, the light curve for off-axis observers depends only $\Gamma_j(t)$ and i_2. The latter is a free-parameter, which we shall constrain by our follow-up observations in Section 9.4.

To obtain $\Gamma_j(t)$ and the light curve beyond the last published radio observation of Swift 1644+57 (about one year after the *Swift* trigger), we used the external model of TD jets (Metzger et al. 2012) applied to the Sw 1644+57 radio data by Berger et al. (2012). The off-axis light curve that is derived here may thus be viewed as a test for this model. We consider two scenarios. First, we set $\Gamma(t > 1\ \mathrm{yr}) = 2$, and use the extrapolated light curve presented in Berger et al. (2012). This constant Lorentz factor is required because the extrapolated light curve is no longer valid when the jet slows down to mildly relativistic speed and lateral expansion becomes important. This happens at $\Gamma_j \lesssim 2$ (Zhang & MacFadyen 2009). We also consider a decreasing jet velocity $\Gamma_j \propto t^{-0.2}$ (as inferred for Swift 1644+57), but modify the extrapolated light curve to match the non-relativistic Sedov-Taylor evolution when $\Gamma_j < 2$. To estimate the light curve decay in the Sedov-Taylor phase, we assume an electron power-law index $p = 2.5$ and describe the density of circumnuclear gas with a power-law of index $k = 3/2$ (Berger et al. 2012) to find $L_j \propto t^{-1.9}$ (Granot et al. 1999; Leventis et al. 2012). We show the light curves in Fig. 9.1.

9.2.2 Internal model: off-axis light curves for known TDFs

The internal model of radio emission from TD jets was first presented in van Velzen, Falcke, & Farrar (2010) and further developed by van Velzen, Körding, & Falcke (2011). The model is based on the simple idea of jet-disk coupling (Rawlings & Saunders 1991; Falcke & Biermann 1995): a constant fraction of the accretion luminosity (L_d) is fed into the jet, $Q_j = q_j L_d$. The conversion from jet power (Q_j) to radio luminosity (L_j) follows by assuming equipartition between the energy in relativistic particles and magnetic fields, and has been calibrated using observations of AGN (Falcke et al. 1995b; Willott et al. 1999; Körding et al. 2008b).

Stellar mass black holes show rapid switches from radio-loud ($q_j = 0.2$) to radio-quiet ($q_j < 0.002$) coupling as the accretion rate increases from sub-Eddington to

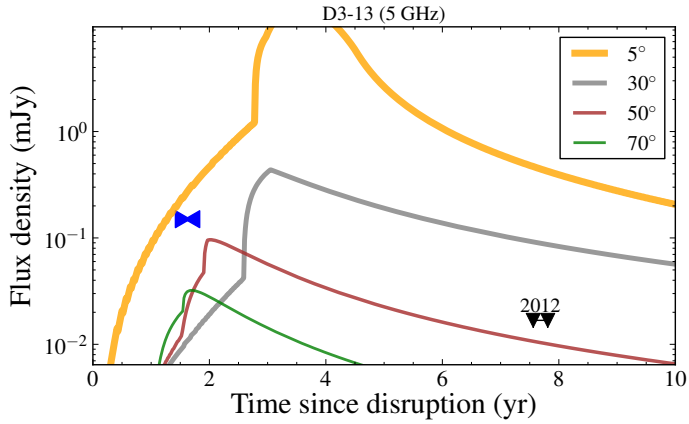

FIGURE 9.2: Predicted 5 GHz curves for the tidal disruption candidate D3-13 (Gezari et al. 2009b) for the internal jet model in the optimistic scenario (Eq. 9.3*a*). The existing upper limits on the 1.4 GHz flux density (Bower 2011) are shown with triangles, pointing left and right to indicate the uncertainty on the time of disruption. The downward pointing triangles labeled "2012" show our upper limits to the 5 GHz flux. For $\cos i < \beta_j$, the peak of the light curve decreases in time and magnitude as i increases, because a fixed observed frequency corresponds to a smaller radius where the jet becomes optically thin to synchrotron self-absorption (i.e., $z_{\rm ssa} \propto \delta/\nu$). For $\cos i > \beta_j$ the light curve is compressed due to time retardation.

(near) the Eddington limit (Fender, Belloni, & Gallo 2004). Motivated by the growing evidence that accretion onto super-massive black holes can also be divided into these two modes (e.g., Ho 1999; Ghisellini & Celotti 2001; Falcke et al. 2004a; Körding et al. 2006b; Best & Heckman 2012; Plotkin et al. 2012), we considered the following three scenarios for the jet-disk coupling in tidal disruptions:

$$q_j = \begin{cases} 0.2 & \text{all times} & (a) \\ 0.002 & \dot{m}(t) > 2\%\dot{m}_{\rm Edd} & (b) \\ 0.2 & t < t_{\rm fallback} & (c) \end{cases} \tag{9.3}$$

where each scenario reverts to the preceding one if the condition on t or $\dot{m}$ is not true (e.g., $q_j = 0.2$ when $\dot{m} < 2\%\dot{m}_{\rm Edd}$ in all three scenarios). In the optimistic scenario (a), the TD jet behaves like a radio-loud quasar at all times. In the most conservative scenario (b), the jet becomes radio-loud only when the accretion drops below $< 2\%\dot{m}_{\rm Edd}$ (Maccarone 2003). In scenario c, the system starts with a radio-loud burst during the onset of the accretion. We consider c the most realistic scenario, since it most closely resembles the observed behavior of X-ray binaries.

Besides q_j (Eq. 9.3) the internal model requires a jet Lorentz factor and the disk luminosity as a function of time. The latter is obtained from the fallback rate of the stellar debris for a pericenter passage at the disruption radius, capped at the

name	t_D (yr)	F_ν (mJy)	ν (GHz)	Δt (yr)
NGC 5905[1]	1990.5	< 0.15	8.5	6.0
D3−13[2]	2004.5	< 0.15	1.4	1.8
TDE2[3]	2007.8	< 0.10	8.4	1.1
CSS100217[4]	2010.2	0.50 ± 0.03	7.9	0.3
SDSS J1201+30[5]	2010.4	< 0.22	4.8	1.4
RX J1624+7554[6]	1990.8	< 0.085	3.0	21.8
IC 3599[7]	1990.9	0.19 ± 0.03	3.0	21.6
RX J1420+5334[8]	1990.9	0.11 ± 0.02	3.0	21.6
RX J1242−1119[9]	1992.5	< 0.090	3.0	20.0
SDSS J1323+48[10]	2003.9	< 0.170	3.0	8.6
SDSS J1311−01[11]	2004.1	< 0.095	3.0	8.4

TABLE 9.1: Existing radio follow-up observations of TDF candidates that were discovered at optical to soft X-ray frequencies (our new observations are shown in Table 9.2). In the third column we show 5-σ upper limits on the radio flux or the detected flux and 1-σ uncertainty. Δt denotes the time of the radio observation with respect to the estimated time of disruption (t_D). The radio observation of the first five candidates were published before mid-2012, the last six are taken from Bower et al. (2013). We note that most of the TDF candidates that were discovered in the nineties also have post disruption radio upper limits from large radio surveys (e.g., NVSS, Condon et al. 1998), these are listed in Komossa (2002). References: (1: Bade et al. 1996; Komossa 2002), (2: Gezari et al. 2008; Bower 2011), (3: van Velzen et al. 2011), (4: Drake et al. 2011), (5: Saxton et al. 2012), (6: Grupe et al. 1999) (7: Komossa & Bade 1999) (8: Greiner et al. 2000), (9: Komossa & Greiner 1999), (10: Esquej et al. 2007), (11: Maksym et al. 2010).

Eddington limit. We vary Γ_j between 5, the default value in van Velzen et al. (2011), and $\Gamma_j = 2$. In Fig. 9.2 we show an example light curve of the TDF candidate D3-13 (Gezari et al. 2009b) for $\Gamma_j = 5$, using the black hole mass as estimated from the luminosity of the host.

In the internal TD jet model, the typical time scale of the light curve is set by the radius where the jet becomes optically thin to synchrotron self-absorption, $z_{\rm ssa} \propto \delta\nu^{-1}L_d^{2/3}$. This is different from our off-axis version of the external model, where we assumed that the emission is dominated by the head of the jet, which explains the dissimilar scaling of the peak of the light curve with the Doppler factor for the internal and external model.

9.3 Observations

In Table 9.1 we summarize the published radio follow-up observations of TDF candidates that were discovered at optical to soft X-ray wavelengths. To increase this sample, we selected all TDF candidates with an estimated time of disruption after

name	redshift	$M_{\rm BH}$ $M_\odot \times 10^7$	$t_{\rm int}$ (min)	$\sigma(F_\nu)$ (μJy)	Δt (yr)
D1-9[1]	0.326	5	30	9	8.0
D3-13[1]	0.370	2	18	8	7.6
TDE1[2]	0.136	1	28	10	5.4
D23H-1[3]	0.186	5	28	8	4.8
TDE2[2]	0.252	5	25	12	4.3
PTF10iya[4]	0.224	1	18	8	1.6
PS1-10jh[5]	0.170	0.4	39	15	0.71

TABLE 9.2: Jansky VLA observations at 5 GHz of TDF candidates discovered at UV or optical frequencies. We list the redshift and estimated black hole mass of these candidates in the second and third column, respectively. No significant emission was detected at the phase center of the images. We list integration time after removal of interference, the rms of the images, and the time of the observations with respect to the estimated time of disruption. References: (1: Gezari et al. 2008), (2: van Velzen et al. 2011), (3: Gezari et al. 2009b), (4: Cenko et al. 2012a), (5: Gezari et al. 2012).

2004 for follow-up observations. This limit is used since the internal model of TD jets is no longer valid when the jet slows down significantly. Our sample also includes TDFs with existing radio upper limits, since the radio emission can be delayed with respect to the time of disruption. We removed CSS100217 from the sample because it is detected at 1 GHz *before* the time of disruption with a flat spectral index, indicating an AGN origin for the radio emission (Drake et al. 2011). SDSS J1201+30 was not selected for follow-up observations because this TDF was published after our observations were scheduled. Details of the data reduction of the remaining six candidates are summarized below.

The radio observations were carried out on the Karl G. Jansky Very Large Array on 29 January 2012 under program 12A-005. We observed at a central frequency of 5.0 GHz with 16 subbands each with 64 2 MHz channels, spanning 2 GHz of total bandwidth. The VLA was in the C configuration yielding typical angular resolution of 4 arcsec. The total observing time was 2.5 hrs, with integration times for individual TDF sources varied from 18-30 min. Phase calibration was carried out by making short observations of nearby point source calibrators every 10 minutes, while amplitude and bandpass calibration was achieved using an observation of 3C 286 or 3C 48 at the beginning or end of each observing run. The data were reduced following standard practice in the Astronomical Image Processing System (AIPS) software package.

In addition to these data, we identified one public data set from the VLA archive (project AS 1020) for the TDF candidate PS1-10jh (Gezari et al. 2012). These observation were made with the VLA on 29 March 2011 in the B configuration with two subbands (each with 64 2 MHz channels) centered at 4.83 and 4.96 GHz, for a total bandwidth of 256 MHz. The calibration and imaging of these data was similar to the

method described above.

Our final sample that we shall use to constrain TD jet models thus consists of seven TDF candidates that were observed with the Jansky VLA. We summarize the results of these observations in Table 9.2.

9.4 Analysis

In this section we first compute the constraints that can be placed on TD jet models using our Jansky VLA follow-up observation and then consider the potential of radio transient surveys.

9.4.1 Constraints from follow-up observation

If we assume that the angle between the observer and the jet is drawn from a uniform distribution (on a sphere), we can calculate the probability of non-detections for a given flux density limit. One simply has to find the largest angle for which the predicted flux is above the flux limit and then calculate the probability to observe a jet within this angle. The flux limit is set at twice the rms of the radio image of each TDF. (This is lower than the limit for a blind-detection experiment since we use the threshold to find the probability of a non-detection, not to claim a discovery.) In Table 9.3 we list the results of this exercise.

The probability that all seven TDFs in our sample hosted jets, but were not detected due to Doppler boosting is $P_7 = \Pi_i P_i$, with P_i the probability of the observations of each TDF candidate, as listed in Table 9.3. We also consider the possibility that, given our observations, *at least one* of the seven TDFs hosted a jet, $P_{\geq 1}$. This is obtained by taking the mean value of the product of all combinations of the seven P_i's (e.g., the probability that only one jet was launched is $P_1 = \sum_i P_i/7$). For the optimistic scenario of the internal model (Sec. 9.2.2) with $\Gamma_j = 5$, four of the seven TDF candidates (D23H-1, TDE2, PTF10iya, PS1-10jh) should have yielded a detection above the 2-σ level, hence $P_7 = 0$, while $P_{\geq 1}$=2%. The probability that all of the other three TDF candidates hosted a jet is 1.7%. For the most conservative scenario (Eq. 9.3*b*), $P_7 = 48\%$, while for the realistic scenario (Eq. 9.3*c*) this is lower at 21%. In Fig. 9.3 we show P_7 and $P_{\geq 1}$ for lower Lorentz factors; at $\Gamma_j < 3$, the hypothesis that all seven TDFs hosted a jet is ruled out at 95% confidence for all three scenarios of the internal jet model.

Our upper limits also constrain the possibility that a jet similar to Swift 1644+57 was launched after the disruption. To place the Jansky VLA observations on the estimated off-axis light curve (Eq. 9.2), we equate the time of disruption to the time of the *Swift* trigger and we scale the flux using $(d_{L,\rm Sw}/d_L)^2$, with $d_{L,\rm Sw}$ being the luminosity distance of Swift 1644+57. From Fig. 9.1 we see that our upper limits on the radio flux of five TDFs (TDE1, D23H-1, PTF10iya, and PS1-10jh) are inconsistent

name	Internal jet model			Swift 1644+57, off-axis	
	a	c	b	$\Gamma_j = 2$	$\Gamma_j \propto t^{-0.2}$
D1-9	39	78	83	49	17
D3-13	62	89	91	52	26
TDE1	7	92	100	0	0
D23H-1	0	52	70	0	0
TDE2	0	75	98	20	1
PTF10iya	0	86	95	0	0
PS1-10jh	0	95	97	0	0

TABLE 9.3: Probability (%) that the jet orientation is such that the predicted flux is below the 2σ-level of our 5 GHz observation. Zero probability implies that the predicted flux is above the threshold even for $i_2 = \pi/2$, while $P_i = 100\%$ implies the data cannot constrain the model. In the second to fourth column we list the results for the internal jet model, for the optimistic to the conservative scenario (Eq. 9.3), for $\Gamma_j = 5$. In Fig. 9.3 we show the results for lower Lorentz factors. In the fifth and sixth column we give the probably of detecting a jet that is identical to Swift 1644+57, but observed off-axis, using two different estimates of the light curve past the last available observation (see Section 9.2.1).

with the estimated off-axis light curve of Swift 1644+57 for all viewing angles and both versions of the late-time evolution we considered in Section 9.2.1.

9.4.2 Constraints from (future) radio transients surveys

A different method to test whether jets like Swift 1644+57 are common to stellar tidal disruptions is to compute the rate of these transients. The snapshot rate (or areal density) at a given flux density limit $F_{\nu,\rm lim}$ can be estimated directly from the Swift 1644+57 light curve:

$$R(F_{\nu,\rm lim}) \sim 8 \times 10^{-3}\,\Gamma_j^{-2} \left(\frac{F_{\nu,\rm Sw}}{F_{\nu,\rm lim}}\right)^{3/2} \frac{\Delta T \dot{N}_{\rm TDJ}}{10^{-5}} \frac{\rho_{\rm BH}}{5 \times 10^{-3}\ {\rm Mpc}^{-3}}\ {\rm deg}^{-2} \quad . \tag{9.4}$$

Here ΔT is the time in years that the flux of Swift 1644+57 is above $F_{\nu,\rm Sw}$, $\rho_{\rm BH}$ is the black hole density, and $\dot{N}_{TDJ}$ is the rate of stellar tidal disruptions with jets. If Swift 1644+57 was a typical stellar tidal disruption, this rate should be of the same order as the TDF rate inferred from soft X-ray (Donley et al. 2002) or optical (van Velzen & Farrar 2012) surveys, i.e., $\dot{N}_{\rm TDJ} \sim 10^{-5}\,{\rm yr}^{-1}$.

The 5 GHz light curve of Swift 1644+57 implies $\Delta T \approx 1$ yr for $F_{\nu,\rm Sw} = 20$ mJy. For $\Gamma_j = 2$, we can thus obtain the snapshot rate for a radio variability survey with a threshold at 10 mJy: $R(10\,{\rm mJy}) = 5 \times 10^{-3}\,{\rm deg}^{-2}$. This rate is close to the existing upper limits on the snapshot rate at 5 GHz (e.g., Scott 1996; Bower et al. 2007, 2011)

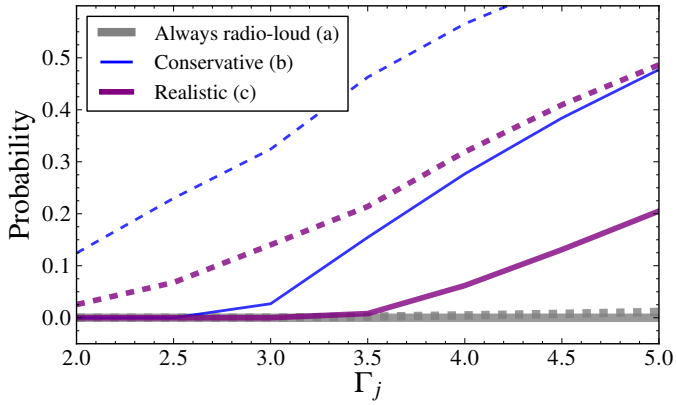

FIGURE 9.3: The probability of our data (i.e., no flux above two times the image rms) for the three scenarios of the internal model (Eq. 9.3). The solid lines show P_7 the probability that all seven TDFs we observed indeed hosted a jet; the dashed lines show $P_{\geq 1}$ the probability that at least one flare hosted a jet. For $\Gamma_j < 3$ the former hypothesis is ruled out at 95% confidence for all scenarios.

—see Frail et al. (2012) for a review. Hence the observed light curve of Swift 1644+57 implies that near-future radio variability survey will either measure or constrain $\dot{N}_{\rm TDJ}$.

9.5 Discussion

We obtained upper limits at the ~ 10 μJy level of the 5 GHz flux of seven stellar tidal disruptions events that were discovered with optical/UV imaging surveys. This is three orders of magnitude lower than the recently discovered TDFs with radio emission, suggesting that stellar tidal disruptions come in different flavors, ranging from radio-loud to radio-quiet (or radio-silent). To explore how this conclusion would be biased by the large possible parameter range inherent to TDFs, we compared our upper limits to currently available jet models, taking into account Doppler boosting and temporal evolution of the radio emission.

We used our observations to constrain the jet model of van Velzen et al. (2011). For a jet Lorentz factor of $\Gamma_j = 5$, we can rule out the optimistic ("alway radio-loud") scenario for four of the seven flares. The probability that the other three TDF candidates did launch such jets, but are not detected because Doppler boosting reduced the flux below two times the image rms is only 4%. The hypothesis that all events hosted jets that only becomes radio-loud when the fallback rate drops below 2% of the Eddington accretion rate (i.e., as observed in stellar mass black holes) is less constrained. Only for jets with $\Gamma_j < 3$ this hypothesis is ruled out at 95% CL. Our results are consistent with the recent radio observations of X-ray detected TDFs

by Bower et al. (2013), which yielded two detections (Table 9.1), implying that 0–10% of these flares launched relativistic jets (the radio-loud fraction in this sample could be zero because an AGN-origin for the radio emission of the two detected events is currently not ruled out).

We have also investigated the possibility that our sample of TDFs hosted a jet which is identical to Swift 1644+57, but oriented at a larger angle between the observer and the jet. Under the conservative assumption that jet Lorentz factor is constant ($\Gamma_j = 2$), the estimated off-axis light curves of this relativistic TDF are inconsistent with the non-detection for four of the seven flares, for all possible observer angles. The hypothesis that all of the other TDFs hosted jets identical to Swift 1644+57 is ruled out at the 95% confidence level.

Our results are not sensitive to our assumption that the time of disruption equals the time of the *Swift* trigger. If the hard X-rays of the jet are emitted only after ten times the fallback time (~ 1 yr), the predicted off-axis flux is increased by just 50%. A more serious caveat is that the off-axis light curves we used in this work are only valid for circumnuclear environments that are identical to the host of Swift 1644+57. This is not likely to be the case: the blue colors of optical/UV flares imply little optical extinction (i.e., reddening), while for Swift 1644+57 this extinction is much higher, $A_V = 3 - 5$ mag (Bloom et al. 2011). Finally, we note that the black hole mass of Swift 1644+57 may be a factor 5–10 smaller than the median black hole mass of thermal TDFs that we followed-up. The duration of the super-Eddington fallback rate of the flares in our sample may therefore be a year shorter, while the total jet energy could be factor 3 higher (for an accretion rate that is capped at the Eddington limit). A more sophisticated treatment of the off-axis light curves in the external model should take these differences into account, e.g., using radiative transfer onto the output of 2D hydrodynamical simulations (van Eerten & MacFadyen 2011) for a range of black hole masses and environments.

Definite proof that relativistic TDFs with evidence for jetted emission are an intrinsically different class can be obtained by radio transient surveys. For a disruption rate that is of the same of order as the rate of thermal TDFs, the areal density of radio transients like Swift 1644+57 (Eq. 9.4) almost exceeds the current upper limits. Near-future radio variability surveys, such as VAST (Murphy et al. 2013), ThunderKAT, which is part of or MeerKAT (Booth et al. 2009), or the LOFAR Transients Key Science Project (Fender 2012), will either detect tens to hundreds of TD jets per year, or conclude that the rate of stellar tidal disruptions with jets is lower than the rate of thermal TDFs.

If a division between tidal disruptions with and without jets indeed exists, it presents a challenge to the idea that radio-loudness can be explained by state changes of accretion disk. Some authors have argued that the spin of the black hole is an important parameter in the production of stellar tidal disruption jets (e.g., Lei & Zhang 2011; Krolik & Piran 2012; Stone & Loeb 2012): TD jets may require rapidly spin-

ning black holes or an alignment of the disk angular momentum vector and the black hole spin vector. Testing these ideas will require observations of the disk emission of relativistic tidal disruptions to see if this component is similar to TDFs without jets.

Acknowledgments

We would like to thank the anonymous referee for the quick reply and useful comments. The VLA is operated by the National Radio Astronomy Observatory, a facility of the National Science Foundation operated under cooperative agreement by Associated Universities, Inc.

Summary and conclusion

While jets from accreting black holes have been studied for many decades, it is still unclear how they are launched. Both black hole spin and the inner part of the accretion disk could provide the energy to power jets. For supermassive black holes, we are also stuck with the question what triggers the creation of jets and how long a single jet episode lasts.

In this thesis, I studied jets from supermassive black holes using two distinct astrophysical phenomena: radio lobes of galaxies (Chapters 2–5) and stellar tidal disruption flares (Chapters 6–9). Below I provide a brief overview of the results and conclusions from each chapter and highlight how they are related to the two main themes of this thesis, namely jet launching and jet triggering. An overview of how the main results are linked together is given in Table 1.

Part I: Radio galaxies

In Chapter 2 we presented a new all-sky catalog of radio-emitting galaxies. We confirmed that the fraction of galaxies that host a large-scale jet increases with galaxy mass, but we showed that this trend saturates at about 20%. If we assume that all of the high mass galaxies could potentially support steady jets (since they accrete sufficient fuel for the central black hole and $\dot{m} \ll \dot{m}_{\rm Edd}$), then this 20% duty cycle can be interpreted as evidence for jet-induced feedback (i.e., without feedback, the fraction of galaxies that have jets should rise to 100% for the highest masses).

We also studied the clustering of local radio galaxies ($L_{\rm 1GHz} \sim 10^{40}\,{\rm erg\,s^{-1}}$). The galaxy density around these radio galaxies is enhanced by a factor 3. This enhanced clustering remained significant after correcting for the galaxy mass and morphology of the radio galaxies. Hence in low-power radio galaxies, jet production is causally related to galaxy environment. One explanation is that in an environment with higher galaxy density, the black hole receives a more steady supply of fuel, allowing the jet to grow to large scales. Alternatively, the hot gas that is supplied to galaxies in a

group/cluster could be a *necessary* requirement for the production of steady jets in AGN (Kauffmann et al. 2008).

In Chapter 3, we used the all-sky catalog of Chapter 2 for a different purpose. We investigated whether radio galaxies could be the source of ultra-high energy cosmic rays (UHECRs). At an angular separation of 15° to 20° from the radio galaxies, we find an overdensity of UHECRs which exceeds the signal expected from the local matter distribution by 3-σ. After subtracting the UHECRs that arrive from the region around Cen A, the significance of the overdensity is reduced to 2-σ. Due to the unknown composition of UHECRs, this lack of a strong cross-correlation does not yet rule out the hypothesis that radio galaxies are the source of these particles. However, if the magnetic deflection of UHECRs is less than 20° (as expected for protons), radio galaxies cannot be the source of UHECRs because the number density of radio galaxies is too low.

In Chapters 4 & 5, we move from the Local Universe ($z < 0.03$) to higher redshifts. We exploited the fact that at $z \gtrsim 1$ FR II radio galaxies can be readily identified since their hotspots are separated by an angular distance of 10 to 60 arcsec. We used this property to obtain a homogeneous sample of 10^4 FR IIs from the FIRST survey. For about 500 of these we found a quasar at the geometrical center of the lobes. We found a linear correlation between optical disk luminosity and lobe radio luminosity with a scatter of 0.5 dex.

In Chapter 4, we singled out an important application of the disk-lobe correlation. The scatter to this correlation was found to be dominated by environmental effects. The intrinsic scatter to jet-disk coupling is at most 0.24 dex, which presents a challenge for the Blandford–Znajek mechanism. If this mechanism operates in AGN, the dispersion of magnetic flux times spin has to be smaller than 0.12 dex. Within the spin-paradigm, this would imply the following distribution of the spin parameter of SMBHs: a sharp peak for the radio-loud population (e.g., $0.3 < a < 0.5$), with a large gap to explain the radio-quiet quasars. This is an unlikely outcome of black hole evolution (e.g., Volonteri et al. 2013): spin-up and spin-down should both occur and from the central limit theorem we expect a single (broad) distribution.

The linear optical-radio correlation implies that a fixed fraction of the disk luminosity is converted to radio luminosity of the lobes. Since the luminosity density ($\mathrm{erg\,s^{-1}Mpc^{-3}}$) of quasars has been measured (i.e., in the bolometric luminosity function), one can use the optical-radio correlation to predict the areal density of radio lobes that are powered by jets from quasars. This was the main aim of Chapter 5. We found that the observed number of radio-selected FR IIs exceeds the predicted density by a factor two. If we selected only sources with a triple morphology, the predicted density is consistent with the observed density. We therefore argued that the excess of radio-selected FR IIs is due to a delayed response of the lobes to jet intermittency.

The fraction of quasars that have powerful radio lobes is rather low ($\approx 1\%$), which

provides further evidence that quasar jets are episodic. The argument is simple[2]. If all radio-loud quasars are continuously powered and grow to become FR IIs, the number of jets that are unresolved at the resolution of FIRST ($d < 30$ kpc) should be smaller than the number of double-lobed sources in our sample (with $d > 150$ kpc). Instead, we observe the opposite: the number of unresolved radio sources that match to quasars is an order of magnitude larger than the number of FR IIs in our sample. In Chapter 5 we showed that 40% of FR II quasars in FIRST have a triple morphology, so the apparent overabundance of unresolved radio sources is not likely to be explained by Doppler boosting of the compact jet core. A slow hotspot advance speed inside the host galaxy is also an unlikely explanation since the speed for $d < 10$ kpc would have to be $\sim 10^2$ times lower (in fact, the hotspots of young jets are observed to drill faster than outer-galaxy hotspots, see Taylor et al. 2000). Instead, we argue that the low fraction of FR II quasars is due to jet intermittency. If single jet episodes are short, breaking out of the galaxy requires multiple cycles and some quasars may never grow large enough to become FR IIs. Via the same logic, one can argue that disk intermittency (e.g., due to chaotic accretion) could also explain the overabundance of small jets. However, such strong disk variability is not consistent with our observations since it would quickly wash out the correlation between disk power and lobe luminosity.

In Chapter 5 we also found that the fraction of quasars that have radio lobes decreases more rapidly with redshift than the fraction of quasars that are point sources (at the resolution of FIRST). We concluded that the fraction of jets that are smaller than $d \approx 150$ kpc increases with redshift; breaking out of the galaxy appears to be more difficult at higher redshift. This also implies that high-redshift jets deposit a larger faction of their energy into their host galaxy.

Jet intermittency of quasars supports the scale-invariant view of accretion, which dictates that radio-loud quasars are similar to X-ray binaries (XRBs) in the intermediate state. In this regime, XRBs show transient ($\sim$month timescales) jet production. If the timescale is linear with mass, the duration of a single transient jet episode would be 10^{6-7} yr for quasars. Our observations point to one important difference between XRBs and radio-loud quasars. To explain the excess FR IIs by a delay of the radio lobes, the last radio-loud phase must coincide with the end of the quasar phase (otherwise the delayed radio emission of the lobes would not yield FR IIs without optical counterparts). This is different from XRBs, which often spend the final part of the outburst in the soft state (in the soft state, XRBs show no sign of jet activity). Finally, we stress that quasar jet intermittency can be tested by measuring the spectral index of quasars at sufficient resolution to separate the core from the lobes (e.g., using LOFAR or JVLA surveys).

[2]Reynolds & Begelman (1997) arrived at a similar conclusion, but they had to combine multiple radio samples, namely 3CR and the O'Dea & Baum (1997) catalog of compact jets.

	Jets are powered by black hole spin	**Jets are powered by the accretion disk**	**Scale-invariant accretion versus environment**
Clustering of local FR I radio galaxies (Ch. 2).	–	–	Galaxy environment is causally linked to jet production.
Radio-optical correlation of FR IIs (Ch. 4).	Challenged: low scatter implies limited range of black hole spin.	Strong support: the disk-lobe correlation is linear.	Environment contributes to the scatter in the correlation.
Excess of radio lobes; explained by quasar jet intermittency (Ch. 5).	Challenged: tight jet-disk coupling applies for all radio-selected FR IIs.	Supported: linear jet-disk coupling applies for all radio-selected FR IIs.	Intermittency of quasar jets is expected in the scale-invariant model.
Radio and optical observations of stellar disruptions (Ch. 7–9).	Weak support: spin could explain why not all TDFs have jets.	Weak support: the X-ray luminosity of Swift 1644+57 appears to track the fallback rate.	Scale-invariant view is challenged: extra parameter needed to explain TDF jets?

Table 1: Matrix of conclusions.

Main conclusions of Part I

Our observation of radio galaxies support the hypothesis that jets are powered by the accretion disk. We reject the simplest version of the spin-paradigm, in which both radio-loud and radio-quiet quasars are explained by the distribution of black hole spin. Instead, our results show that radio-quiet quasars can be explained by intermittent jet production at a fixed accretion rate. This behavior resembles XRBs that show transient jet production when the source switches between accretion states and thus supports the scale-invariant model of black hole accretion. An important difference between XRBs and low-power radio galaxies is that for the latter the environment can enhance nuclear activity.

Below we present the results from the second part of this thesis, allowing us to confront the scale-invariant model from a different angle.

Part II: Stellar tidal disruption flares

In Chapter 6 we presented the first stellar tidal disruption flares (TDFs) discovered using an optical survey. We showed that TDFs occupy a separate location in the color-cooling diagram: they are very blue and have a nearly constant temperature. These properties can be used to find many more TDFs with current and future synoptic surveys. Indeed, two recent TDFs discovered in Pan-STARRS data (Gezari et al. 2012; Chornock et al. 2014) fall into our "TDF locus" (Fig. 6.12).

The systematic nature of our search allowed for a relatively straightforward computation of the TDF rate. As presented in Chapter 7, we found $\dot{N}_{\rm TDF} \approx 2 \times 10^{-5}$ per galaxy per year, with a factor ≈ 2.5 statistical uncertainty and a factor ≈ 1.5 systematic uncertainty due to the poor constraints on the scaling of the light curve with black hole mass.

A new theoretical model for the radio emission of jets from tidal disruptions was presented in Chapter 8. We based our calculations on the conical jet model, which is well calibrated by many decades of observations. Radio light curves were computed for an optimistic scenario (TDFs are always radio-loud), and for a more conservative scenario (efficient jet-disk coupling only occurs when the fallback rate is below 2% of the Eddington rate). We also predicted the rate of TDFs for (near-future) radio transient surveys, concluding that they are sensitive enough to test our conservative scenario.

In the final chapter of this thesis, we confronted our tidal disruption jet model with new radio observations. Six known TDFs (including TDE1 and TDE2 of Chapter 6) were observed with the JVLA at 5 GHz. None of the sources were detected, we obtained deep ($\sim 10\mu$Jy) upper limits. This allowed us to rule out the optimistic scenario: not all TDFs behave like radio-loud AGN. The more conservative scenarios remain possible, but only if the jet Lorentz factor is large ($\Gamma > 3$).

In Chapter 8 we also showed that the observed light curve of Swift 1644+57 (the best-sampled relativistic TDF) can be used to make a rough, but model-independent estimate for the number of TDFs detected by radio transient surveys. Input to this estimate is the tidal disruption rate; based on Chapter 7, we used a conservative value limit of $10^{-5}\,{\rm yr}^{-1}\,{\rm galaxy}^{-1}$. For this disruption rate, the predicted snapshot rate of jetted TDF exceeds the recent upper limits from radio transient surveys (Mooley et al. 2014) by an order of magnitude. We thus have to conclude that Swift 1644+57 was special and that at most 10% of tidal disruptions are accompanied by this type of jet.

The low fraction of TDFs with jets clearly presents a challenge for the scale-invariant model of accretion: if one tidal disruption launched a jet, the rest should behave similarly. A solution could be a strong bias due to environment, implying that powerful jets require dense circumnuclear gas. Since flares at optical/UV wavelengths can only be detected if obscuration by dust is low, they may not produce strong radio transients. However we note that the emission mechanism of the jet model presented in Chapter 8 is *internal* to the jet, no interaction with the environment is required.

A strong selection bias on black hole mass could also explain the lack of flares from known TDFs. The relativistic TDFs may prefer low mass ($M_{\rm BH} \sim 10^{5-6}\,M_\odot$) black holes (because for lower mass the duration of the super-Eddington phase is longer), while the median mass of the optical/UV TDF discovered so far is higher ($\sim 10^7\,M_\odot$). Alternatively, black hole spin could explain why Swift 1644+57 was special, or perhaps a pre-existing magnetic field (Tchekhovskoy et al. 2014) or the disruption of a white dwarf (Krolik & Piran 2011) is required for jet production in tidal disruption events.

Looking forward

The discussion at the end of the previous section makes two things clear: (i) not all TDFs launch jets; (ii) with just a handful of events that is about all we can safely conclude. This situation will soon change, since based on the results of Chapters 6 & 7 we predict that current optical transient surveys (Gaia, Pan-STARRS, PTF) should detect tens to hundreds of new TDFs per year.

We end this summary by recalling that the X-ray luminosity of the best-sampled tidal disruption jet (Swift 1644+57) follows the theoretically predicted fallback rate of the stellar debris (i.e., $t^{-5/3}$). This presents a new and intriguing piece of evidence in favor of linear jet-disk coupling. At this point, the evidence remains indirect because the fallback rate may not translate directly into an accretion rate. To solve this problem we have to discover TDFs with detected emission from *both* the jet and the disk. I predict that these events will be discovered within the next four years and will open up a new avenue of research, leading to a better understanding of jet formation in supermassive black holes.

Bibliography

Abazajian, K. N., Adelman-McCarthy, J. K., Agüeros, M. A., et al. 2009, ApJS, 182, 543
Abbasi, R., Abdou, Y., Abu-Zayyad, T., et al. 2012, Nature, 484, 351
Abbasi, R. U., Abu-Zayyad, T., Allen, M., et al. 2008, Physical Review Letters, 100, 101101
Abraham, J., Abreu, P., Aglietta, M., et al. 2008, Physical Review Letters, 101, 061101
Abramowicz, M. A., Chen, X., Kato, S., Lasota, J.-P., & Regev, O. 1995, ApJ, 438, L37
Abramowicz, M. A., Czerny, B., Lasota, J. P., & Szuszkiewicz, E. 1988, ApJ, 332, 646
Abramowicz, M. A., & Fragile, P. C. 2013, Living Reviews in Relativity, 16, 1
Abramowicz, M. A., Kluźniak, W., & Lasota, J.-P. 2002, A&A, 396, L31
Agnoletto, I., Benetti, S., Cappellaro, E., et al. 2009, ApJ, 691, 1348
Ahn, C. P., Alexandroff, R., Allende Prieto, C., et al. 2014, ApJS, 211, 17
Alexander, D. M., & Hickox, R. C. 2012, New A Rev., 56, 93
Alexander, T. 2012, in EPJ Web of Conferences, Vol. 39, 5001
Allen, S. W., Dunn, R. J. H., Fabian, A. C., Taylor, G. B., & Reynolds, C. S. 2006, MNRAS, 372, 21
Aller, M. C., & Richstone, D. 2002, AJ, 124, 3035
Almheiri, A., Marolf, D., Polchinski, J., & Sully, J. 2013, J. High Energ. Phys., 2, 62
Anderson, J. P., & James, P. A. 2008, MNRAS, 390, 1527
Anderson, J. P., & James, P. A. 2009, MNRAS, 399, 559
Antognini, J., Bird, J., & Martini, P. 2012, ApJ, 756, 116
Antoniadis, J., Freire, P. C. C., Wex, N., et al. 2013, Science, 340, 448
Antonucci, R. R. J., & Miller, J. S. 1985, ApJ, 297, 621
Arcavi, I., Gal-Yam, A., Sullivan, M., et al. 2014, ArXiv e-prints, 1405.1415
Assef, R. J., Stern, D., Kochanek, C. S., et al. 2013, ApJ, 772, 26
Baars, J. W. M., Genzel, R., Pauliny-Toth, I. I. K., & Witzel, A. 1977, A&A, 61, 99
Bade, N., Komossa, S., & Dahlem, M. 1996, A&A, 309, L35
Baldi, R. D., Capetti, A., Buttiglione, S., Chiaberge, M., & Celotti, A. 2013, A&A, 560, A81
Baldwin, J. A., Phillips, M. M., & Terlevich, R. 1981, PASP, 93, 5
Baloković, M., Smolčić, V., Ivezić, Ž., et al. 2012, ApJ, 759, 30
Bamford, S. P., Nichol, R. C., Baldry, I. K., et al. 2009, MNRAS, 393, 1324
Bannister, K. W., Murphy, T., Gaensler, B. M., Hunstead, R. W., & Chatterjee, S. 2011, MNRAS, 412, 634
Barbary, K., Dawson, K. S., Tokita, K., et al. 2009, ApJ, 690, 1358
Bardeen, J. M., & Petterson, J. A. 1975, ApJ, 195, L65
Barger, A. J., Cowie, L. L., Mushotzky, R. F., et al. 2005, AJ, 129, 578

Bauer, A., Baltay, C., Coppi, P., et al. 2009, ApJ, 696, 1241
Bauer, F. E., Condon, J. J., Thuan, T. X., & Broderick, J. J. 2000, ApJS, 129, 547
Becker, R. H., White, R. L., & Helfand, D. J. 1995, ApJ, 450, 559
Beckwith, K., Hawley, J. F., & Krolik, J. H. 2008, ApJ, 678, 1180
Bell, A. R. 1978, MNRAS, 182, 147
Bell, E. F., McIntosh, D. H., Katz, N., & Weinberg, M. D. 2003, ApJS, 149, 289
Belloni, T., Homan, J., Casella, P., et al. 2005, A&A, 440, 207
Berezinsky, V. 2008, Advances in Space Research, 41, 2071
Berger, E., Zauderer, A., Pooley, G. G., et al. 2012, ApJ, 748, 36
Best, P. N., & Heckman, T. M. 2012, MNRAS, 421, 1569
Best, P. N., Kauffmann, G., Heckman, T. M., et al. 2005a, MNRAS, 362, 25
Best, P. N., Kauffmann, G., Heckman, T. M., & Ivezić, Ž. 2005b, MNRAS, 362, 9
Best, P. N., von der Linden, A., Kauffmann, G., Heckman, T. M., & Kaiser, C. R. 2007, MNRAS, 379, 894
Bianchi, L., Rodriguez-Merino, L., Viton, M., et al. 2007, ApJS, 173, 659
Biermann, P., & Kronberg, P. P. 1983, ApJ, 268, L69
Biermann, P. L., & de Souza, V. 2012, ApJ, 746, 72
Blandford, R. D., & Königl, A. 1979, ApJ, 232, 34
Blandford, R. D., & Payne, D. G. 1982, MNRAS, 199, 883
Blandford, R. D., & Znajek, R. L. 1977, MNRAS, 179, 433
Blanton, M. R., & Roweis, S. 2007, AJ, 133, 734
Blanton, M. R., Dalcanton, J., Eisenstein, D., et al. 2001, AJ, 121, 2358
Blanton, M. R., Schlegel, D. J., Strauss, M. A., et al. 2005, AJ, 129, 2562
Blondin, S., & Tonry, J. L. 2007, ApJ, 666, 1024
Bloom, J. S., Giannios, D., Metzger, B. D., et al. 2011, Science, 333, 203
Blundell, K. M., & Rawlings, S. 2000, AJ, 119, 1111
Blundell, K. M., Rawlings, S., & Willott, C. J. 1999, AJ, 117, 677
Bock, D. C.-J., Large, M. I., & Sadler, E. M. 1999, AJ, 117, 1578
Bogdanović, T., Eracleous, M., Mahadevan, S., Sigurdsson, S., & Laguna, P. 2004, ApJ, 610, 707
Booth, R. S., de Blok, W. J. G., Jonas, J. L., & Fanaroff, B. 2009, ArXiv e-prints, 0910.2935
Bovy, J., Hennawi, J. F., Hogg, D. W., et al. 2011, ApJ, 729, 141
Bower, G. C. 2011, ApJ, 732, L12
Bower, G. C., Metzger, B. D., Cenko, S. B., Silverman, J. M., & Bloom, J. S. 2013, ApJ, 763, 84
Bower, G. C., & Saul, D. 2011, ApJ, 728, L14
Bower, G. C., Saul, D., Bloom, J. S., et al. 2007, ApJ, 666, 346
Bower, G. C., Whysong, D., Blair, S., et al. 2011, ApJ, 739, 76
Bower, R. G., Benson, A. J., Malbon, R., et al. 2006, MNRAS, 370, 645
Bramich, D. M., Vidrih, S., Wyrzykowski, L., et al. 2008, MNRAS, 386, 887
Brockamp, M., Baumgardt, H., & Kroupa, P. 2011, MNRAS, 418, 1308
Bromberg, O., Nakar, E., Piran, T., & Sari, R. 2011, ApJ, 740, 100
Bromley, B. C., Kenyon, S. J., Geller, M. J., & Brown, W. R. 2012, ApJ, 749, L42
Brown, M. J. I., Jannuzi, B. T., Floyd, D. J. E., & Mould, J. R. 2011, ApJ, 731, L41
Brown, M. J. I., Brand, K., Dey, A., et al. 2006, ApJ, 638, 88
Brown, P. J., Holland, S. T., Immler, S., et al. 2009, AJ, 137, 4517
Brown, W. R., Cohen, J. G., Geller, M. J., & Kenyon, S. J. 2012, ApJ, 754, L2
Brown, W. R., Geller, M. J., Kenyon, S. J., & Kurtz, M. J. 2005, ApJ, 622, L33
Brunthaler, A., Falcke, H., Bower, G. C., et al. 2000, A&A, 357, L45

Bruzual, G., & Charlot, S. 2003, MNRAS, 344, 1000
Burns, J. O. 1990, AJ, 99, 14
Burrows, D. N., Kennea, J. A., Ghisellini, G., et al. 2011, Nature, 476, 421
Buttiglione, S., Capetti, A., Celotti, A., et al. 2009, A&A, 495, 1033
Buttiglione, S., Capetti, A., Celotti, A., et al. 2010, A&A, 509, A6
Cappelluti, N., Ajello, M., Rebusco, P., et al. 2009, A&A, 495, L9
Caramete, L. I., & Biermann, P. L. 2011, ArXiv e-prints, 1107.2244
Cardelli, J. A., Clayton, G. C., & Mathis, J. S. 1989, ApJ, 345, 245
Carilli, C. L., Perley, R. A., Dreher, J. W., & Leahy, J. P. 1991, ApJ, 383, 554
Cattaneo, A., Faber, S. M., Binney, J., et al. 2009, Nature, 460, 213
Cavagnolo, K. W., McNamara, B. R., Nulsen, P. E. J., et al. 2010, ApJ, 720, 1066
Cenko, S. B., Bloom, J. S., Kulkarni, S. R., et al. 2012a, MNRAS, 420, 2684
Cenko, S. B., Krimm, H. A., Horesh, A., et al. 2012b, ApJ, 753, 77
Chambers, K. C. 2007, in Bulletin of the AAS, Vol. 38, 995
Chandrasekhar, S. 1931, ApJ, 74, 81
Chatterjee, R., Marscher, A. P., Jorstad, S. G., et al. 2011, ApJ, 734, 43
Chen, X., Abramowicz, M. A., Lasota, J.-P., Narayan, R., & Yi, I. 1995, ApJ, 443, L61
Chiaberge, M., & Ghisellini, G. 1999, MNRAS, 306, 551
Chornock, R., Berger, E., Gezari, S., et al. 2014, ApJ, 780, 44
Churazov, E., Sazonov, S., Sunyaev, R., et al. 2005, MNRAS, 363, L91
Cohen, A. S., Lane, W. M., Cotton, W. D., et al. 2007, AJ, 134, 1245
Condon, J., Darling, J., Kovalev, Y. Y., & Petrov, L. 2011, in 11th Asian-Pacific Regional IAU Meeting (NARIT Conference Series)
Condon, J. J. 1984, ApJ, 287, 461
Condon, J. J., Cotton, W. D., & Broderick, J. J. 2002, AJ, 124, 675
Condon, J. J., Cotton, W. D., Greisen, E. W., et al. 1998, AJ, 115, 1693
Condon, J. J., Kellermann, K. I., Kimball, A. E., Ivezić, Ž., & Perley, R. A. 2013, ApJ, 768, 37
Condon, J. J., Odell, S. L., Puschell, J. J., & Stein, W. A. 1981, ApJ, 246, 624
Cooper, B. F. C., Price, R. M., & Cole, D. J. 1965, Australian Journal of Physics, 18, 589
Corbel, S., Nowak, M. A., Fender, R. P., Tzioumis, A. K., & Markoff, S. 2003, A&A, 400, 1007
Croft, S., de Vries, W., & Becker, R. H. 2007, ApJ, 667, L13
Croft, S., Bower, G. C., Ackermann, R., et al. 2010, ApJ, 719, 45
Croston, J. H., Hardcastle, M. J., Harris, D. E., et al. 2005, ApJ, 626, 733
Croton, D. J., Springel, V., White, S. D. M., et al. 2006, MNRAS, 365, 11
Curtis, H. D. 1918, Publications of Lick Observatory, 13, 9
Daly, R. A. 2009, ApJ, 691, L72
D'Andrea, C. B., Sako, M., Dilday, B., et al. 2010, ApJ, 708, 661
Davies, R. L., Efstathiou, G., Fall, S. M., Illingworth, G., & Schechter, P. L. 1983, ApJ, 266, 41
Dawson, K. S., Schlegel, D. J., Ahn, C. P., et al. 2013, AJ, 145, 10
De Colle, F., Guillochon, J., Naiman, J., & Ramirez-Ruiz, E. 2012, ApJ, 760, 103
de Vries, W. H., Becker, R. H., & White, R. L. 2006, AJ, 131, 666
de Vries, W. H., Becker, R. H., White, R. L., & Helfand, D. J. 2004, AJ, 127, 2565
Dekker, H., Delabre, B., & D'Odorico, S. 1986, in SPIE Conference Series, ed. D. L. Crawford, Vol. 627, 339
Donley, J. L., Brandt, W. N., Eracleous, M., & Boller, T. 2002, AJ, 124, 1308
Donoso, E., Best, P. N., & Kauffmann, G. 2009, MNRAS, 392, 617

Donoso, E., Li, C., Kauffmann, G., Best, P. N., & Heckman, T. M. 2010, MNRAS, 407, 1078
Drake, A. J., Djorgovski, S. G., Mahabal, A., et al. 2009, ApJ, 696, 870
Drake, A. J., Djorgovski, S. G., Mahabal, A., et al. 2011, ApJ, 735, 106
Dressler, A. 1980, ApJ, 236, 351
Dunlop, J. S., & Peacock, J. A. 1990, MNRAS, 247, 19
Dunn, J. P., Bautista, M., Arav, N., et al. 2010, ApJ, 709, 611
Dunn, R. J. H., Fender, R. P., Körding, E. G., Cabanac, C., & Belloni, T. 2008, MNRAS, 387, 545
Dwarakanath, K. S., & Kale, R. 2009, ApJ, 698, L163
Eckart, A., & Genzel, R. 1996, Nature, 383, 415
Eisenstein, D. J., Weinberg, D. H., Agol, E., et al. 2011, AJ, 142, 72
Esquej, P., Saxton, R. D., Freyberg, M. J., et al. 2007, A&A, 462, L49
Esquej, P., Saxton, R. D., Komossa, S., et al. 2008, A&A, 489, 543
Evans, C. R., & Kochanek, C. S. 1989, ApJ, 346, L13
Evans, I. N., Primini, F. A., Glotfelty, K. J., et al. 2010, ApJS, 189, 37
Fabian, A. C. 1994, ARA&A, 32, 277
Fabian, A. C. 2012, ARA&A, 50, 455
Fabian, A. C., Sanders, J. S., Allen, S. W., et al. 2003, MNRAS, 344, L43
Falcke, H. 2001, in Reviews in Modern Astronomy, ed. R. E. Schielicke, Vol. 14, 15
Falcke, H., & Biermann, P. L. 1995, A&A, 293, 665
Falcke, H., Gopal-Krishna, & Biermann, P. L. 1995a, A&A, 298, 395
Falcke, H., Körding, E., & Markoff, S. 2004a, A&A, 414, 895
Falcke, H., Körding, E., & Nagar, N. M. 2004b, New A Rev., 48, 1157
Falcke, H., Malkan, M. A., & Biermann, P. L. 1995b, A&A, 298, 375
Falcke, H., Sherwood, W., & Patnaik, A. R. 1996, ApJ, 471, 106
Falcke, H., Bower, G. C., Lobanov, A. P., et al. 1999, ApJ, 514, L17
Falle, S. A. E. G. 1991, MNRAS, 250, 581
Fanaroff, B. L., & Riley, J. M. 1974, MNRAS, 167, 31P
Farrar, G. R., & Gruzinov, A. 2009, ApJ, 693, 329
Fender, R. P. 2001, MNRAS, 322, 31
Fender, R. P. 2012, in IAU Symposium, ed. R. E. M. Griffin, R. J. Hanisch, & R. Seaman, Vol. 285, 11
Fender, R. P., Belloni, T. M., & Gallo, E. 2004, MNRAS, 355, 1105
Fender, R. P., Gallo, E., & Russell, D. 2010, MNRAS, 406, 1425
Ferrarese, L., & Merritt, D. 2000, ApJ, 539, L9
Ferrarese, L., Côté, P., Jordán, A., et al. 2006, ApJS, 164, 334
Filho, M. E., Brinchmann, J., Lobo, C., & Antón, S. 2011, A&A, 536, A35
Filippenko, A. V., & Ho, L. C. 2003, ApJ, 588, L13
Fisher, K. B., Huchra, J. P., Strauss, M. A., et al. 1995, ApJS, 100, 69
Frail, D. A., Kulkarni, S. R., Ofek, E. O., Bower, G. C., & Nakar, E. 2012, ApJ, 747, 70
Frank, J., & Rees, M. J. 1976, MNRAS, 176, 633
Frieman, J. A., Bassett, B., Becker, A., et al. 2008, AJ, 135, 338
Fruchter, A. S., Levan, A. J., Strolger, L., et al. 2006, Nature, 441, 463
Fukugita, M., Hogan, C. J., & Peebles, P. J. E. 1998, ApJ, 503, 518
Fukugita, M., Ichikawa, T., Gunn, J. E., et al. 1996, AJ, 111, 1748
Gadotti, D. A. 2009, MNRAS, 393, 1531
Gal-Yam, A., Cenko, S. B., Fox, D. B., et al. 2007, in American Institute of Physics Conference Series, Vol. 924, The Multicolored Landscape of Compact Objects and Their Explosive Origins, ed. L. A. Antonelli, G. L. Israel, L. Piersant, A. Tornambe, 297

Gal-Yam, A., Ofek, E. O., Filippenko, A. V., Chornock, R., & Li, W. 2002, PASP, 114, 587
Gal-Yam, A., Ofek, E. O., Poznanski, D., et al. 2006, ApJ, 639, 331
Gammie, C. F., Narayan, R., & Blandford, R. 1999, ApJ, 516, 177
Gammie, C. F., Shapiro, S. L., & McKinney, J. C. 2004, ApJ, 602, 312
Gebhardt, K., Bender, R., Bower, G., et al. 2000, ApJ, 539, L13
Gendre, M. A., Best, P. N., & Wall, J. V. 2010, MNRAS, 404, 1719
Gendre, M. A., & Wall, J. V. 2008, MNRAS, 390, 819
Genzel, R., Eisenhauer, F., & Gillessen, S. 2010, Reviews of Modern Physics, 82, 3121
Gezari, S., Martin, D. C., Milliard, B., et al. 2006, ApJ, 653, L25
Gezari, S., Basa, S., Martin, D. C., et al. 2008, ApJ, 676, 944
Gezari, S., Halpern, J. P., Grupe, D., et al. 2009a, ApJ, 690, 1313
Gezari, S., Heckman, T., Cenko, S. B., et al. 2009b, ApJ, 698, 1367
Gezari, S., Chornock, R., Rest, A., et al. 2012, Nature, 485, 217
Ghez, A. M., Salim, S., Hornstein, S. D., et al. 2005, ApJ, 620, 744
Ghisellini, G., & Celotti, A. 2001, A&A, 379, L1
Ghisellini, G., Tavecchio, F., & Chiaberge, M. 2005, A&A, 432, 401
Ghisellini, G., Tavecchio, F., Foschini, L., & Ghirlanda, G. 2011, MNRAS, 414, 2674
Ghosh, P., & Abramowicz, M. A. 1997, MNRAS, 292, 887
Giannios, D., & Metzger, B. D. 2011, MNRAS, 416, 2102
Gillessen, S., Eisenhauer, F., Fritz, T. K., et al. 2009, ApJ, 707, L114
Gilli, R. 2013, ArXiv e-prints, 1304.3665
Ginsburg, I., & Loeb, A. 2006, MNRAS, 368, 221
Ginzburg, V. L., & Syrovatskii, S. I. 1963, Astronomicheskii Zhurnal, 40, 466
Globus, N., & Levinson, A. 2013, Phys. Rev. D, 88, 084046
Godfrey, L. E. H., & Shabala, S. S. 2013, ApJ, 767, 12
Gould, A., & Quillen, A. C. 2003, ApJ, 592, 935
Graham, A. W. 2012, ApJ, 746, 113
Graham, A. W., Erwin, P., Caon, N., & Trujillo, I. 2001, ApJ, 563, L11
Graham, A. W., Onken, C. A., Athanassoula, E., & Combes, F. 2011, MNRAS, 412, 2211
Granot, J., Piran, T., & Sari, R. 1999, ApJ, 527, 236
Greiner, J., Schwarz, R., Zharikov, S., & Orio, M. 2000, A&A, 362, L25
Greisen, K. 1966, Phys. Rev. Lett., 16, 748
Grimes, J. A., Rawlings, S., & Willott, C. J. 2004, MNRAS, 349, 503
Grupe, D., Thomas, H.-C., & Leighly, K. M. 1999, A&A, 350, L31
Guillochon, J., Manukian, H., & Ramirez-Ruiz, E. 2014, ApJ, 783, 23
Guillochon, J., & Ramirez-Ruiz, E. 2013, ApJ, 767, 25
Gupta, S., Böttcher, M., & Dermer, C. D. 2006, ApJ, 644, 409
Gürkan, G., Hardcastle, M. J., & Jarvis, M. J. 2014, MNRAS, 438, 1149
Hada, K., Doi, A., Kino, M., et al. 2011, Nature, 477, 185
Hadjiyska, E. I., Rabinowitz, D., Baltay, C., et al. 2011, in AAS Meeting Abstracts #217, Vol. 43, 433.18
Haines, C. P., Gargiulo, A., & Merluzzi, P. 2008, MNRAS, 385, 1201
Hardcastle, M. J. 2010, MNRAS, 405, 2810
Hardcastle, M. J., Evans, D. A., & Croston, J. H. 2009, MNRAS, 396, 1929
Hardcastle, M. J., & Krause, M. G. H. 2013, MNRAS, 430, 174
Häring, N., & Rix, H. 2004, ApJ, 604, L89
Harvanek, M., & Stocke, J. T. 2002, AJ, 124, 1239
Hasegawa, T., Wakamatsu, K.-i., Malkan, M., et al. 2000, MNRAS, 316, 326
Hasinger, G. 2008, A&A, 490, 905

Hawley, J. F., & Krolik, J. H. 2006, ApJ, 641, 103
Healey, S. E., Romani, R. W., Taylor, G. B., et al. 2007, ApJS, 171, 61
Heckman, T. M. 1980, A&A, 87, 152
Heckman, T. M., Kauffmann, G., Brinchmann, J., et al. 2004, ApJ, 613, 109
Herrnstein, J. R., Moran, J. M., Greenhill, L. J., et al. 1997, ApJ, 475, L17
Hillas, A. M. 1984, ARA&A, 22, 425
Hills, J. G. 1975, Nature, 254, 295
Hills, J. G. 1988, Nature, 331, 687
Ho, L. C. 1999, ApJ, 516, 672
Hodge, J. A., Zeimann, G. R., Becker, R. H., & White, R. L. 2009, AJ, 138, 900
Hogg, D. W. 1999, ArXiv e-prints, astro-ph/9905116
Holtzman, J. A., Marriner, J., Kessler, R., et al. 2008, AJ, 136, 2306
Hopkins, P. F., Hernquist, L., Cox, T. J., et al. 2006, ApJS, 163, 1
Hopkins, P. F., Richards, G. T., & Hernquist, L. 2007, ApJ, 654, 731
Huchra, J. P., Macri, L. M., Masters, K. L., et al. 2012, ApJS, 199, 26
Hughes, S. A., & Blandford, R. D. 2003, ApJ, 585, L101
Igumenshchev, I. V. 2008, ApJ, 677, 317
Ivezić, Z., Tyson, J. A., Allsman, R., Andrew, J., & Angel, R. 2008, ArXiv e-prints, 0805.2366
Ivezić, Ž., Tabachnik, S., Rafikov, R., et al. 2001, AJ, 122, 2749
Ivezić, Ž., Menou, K., Knapp, G. R., et al. 2002, AJ, 124, 2364
Jansson, R., & Farrar, G. R. 2012, ApJ, 757, 14
Jarrett, T. 2004, PASA, 21, 396
Jarrett, T. H., Chester, T., Cutri, R., et al. 2000, AJ, 119, 2498
Jeong, H., Yi, S. K., Bureau, M., et al. 2009, MNRAS, 398, 2028
Jester, S. 2008, MNRAS, 389, 1507
Jester, S., Schneider, D. P., Richards, G. T., et al. 2005, AJ, 130, 873
Jiang, L., Fan, X., Ivezić, Ž., et al. 2007, ApJ, 656, 680
Jones, D. H., Peterson, B. A., Colless, M., & Saunders, W. 2006, MNRAS, 369, 25
Jones, P. A., & McAdam, W. B. 1992, ApJS, 80, 137
Kaiser, C. R., & Alexander, P. 1997, MNRAS, 286, 215
Kaiser, C. R., & Best, P. N. 2007, MNRAS, 381, 1548
Kapahi, V. K. 1989, AJ, 97, 1
Kapińska, A. D., Uttley, P., & Kaiser, C. R. 2012, MNRAS, 424, 2028
Katz, B., Budnik, R., & Waxman, E. 2009, J. Cosmol. Astropart. Phys., 3, 0811.3759
Kauffmann, G., & Haehnelt, M. 2000, MNRAS, 311, 576
Kauffmann, G., Heckman, T. M., & Best, P. N. 2008, MNRAS, 384, 953
Kauffmann, G., Heckman, T. M., Tremonti, C., et al. 2003, MNRAS, 346, 1055
Kellermann, K. I., Sramek, R., Schmidt, M., Shaffer, D. B., & Green, R. 1989, AJ, 98, 1195
Kelly, B. C., Bechtold, J., & Siemiginowska, A. 2009, ApJ, 698, 895
Kelly, P. L., Kirshner, R. P., & Pahre, M. 2008, ApJ, 687, 1201
Kennicutt, Jr., R. C. 1998, ARA&A, 36, 189
Ker, L. M., Best, P. N., Rigby, E. E., Röttgering, H. J. A., & Gendre, M. A. 2012, MNRAS, 420, 2644
Kesden, M. 2012, Phys. Rev. D, 86, 064026
Kharb, P., O'Dea, C. P., Baum, S. A., Colbert, E. J. M., & Xu, C. 2006, ApJ, 652, 177
Kiewe, M., Gal-Yam, A., Arcavi, I., et al. 2012, ApJ, 744, 10
Kimball, A. E., & Ivezić, Ž. 2008, AJ, 136, 684
Kimball, A. E., Ivezić, Ž., Wiita, P. J., & Schneider, D. P. 2011, AJ, 141, 182
Klein-Wolt, M., Fender, R. P., Pooley, G. G., et al. 2002, MNRAS, 331, 745

Komissarov, S. S., & Gubanov, A. G. 1994, A&A, 285, 27
Komossa, S. 2002, in Lighthouses of the Universe, ed. M. Gilfanov, R. Sunyeav, & E. Churazov, 436
Komossa, S., & Bade, N. 1999, A&A, 343, 775
Komossa, S., & Greiner, J. 1999, A&A, 349, L45
Komossa, S., & Merritt, D. 2008, ApJ, 683, L21
Komossa, S., Zhou, H., Wang, T., et al. 2008, ApJ, 678, L13
Komossa, S., Zhou, H., Rau, A., et al. 2009, ApJ, 701, 105
Körding, E., Rupen, M., Knigge, C., et al. 2008a, Science, 320, 1318
Körding, E. G., Fender, R. P., & Migliari, S. 2006a, MNRAS, 369, 1451
Körding, E. G., Jester, S., & Fender, R. 2006b, MNRAS, 372, 1366
Körding, E. G., Jester, S., & Fender, R. 2008b, MNRAS, 383, 277
Kormendy, J., & Ho, L. C. 2013, ARA&A, 51, 511
Kratzer, R. M., & Richards, G. T. 2014, ArXiv e-prints, 1405.2344
Krolik, J. H., & Piran, T. 2011, ApJ, 743, 134
Krolik, J. H., & Piran, T. 2012, ApJ, 749, 92
Kuehr, H., Witzel, A., Pauliny-Toth, I. I. K., & Nauber, U. 1981, A&AS, 45, 367
Laing, R. A., Jenkins, C. R., Wall, J. V., & Unger, S. W. 1994, in Astronomical Society of the Pacific Conference Series, Vol. 54, The Physics of Active Galaxies, ed. G. V. Bicknell, M. A. Dopita, & P. J. Quinn, 201
Laing, R. A., Riley, J. M., & Longair, M. S. 1983, MNRAS, 204, 151
Lal, D. V., & Ho, L. C. 2010, AJ, 139, 1089
Lane, W. M., Cotton, W. D., & van Velzen, S. e. a. 2014, MNRAS in press
Laplace, S. 1799, Geographische Ephemeriden, 4, 1
Lattimer, J. M. 2012, Annual Review of Nuclear and Particle Science, 62, 485
Law, N. M., Kulkarni, S. R., Dekany, R. G., et al. 2009, PASP, 121, 1395
Lawrence, A. 1991, MNRAS, 252, 586
Lawrence, A., & Elvis, M. 2010, ApJ, 714, 561
Leaman, J., Li, W., Chornock, R., & Filippenko, A. V. 2011, MNRAS, 412, 1419
Ledlow, M. J., & Owen, F. N. 1995, AJ, 109, 853
Ledlow, M. J., & Owen, F. N. 1996, AJ, 112, 9
Lei, W.-H., & Zhang, B. 2011, ApJ, 740, L27
Lense, J., & Thirring, H. 1918, Physikalische Zeitschrift, 19, 156
Levan, A. J., Tanvir, N. R., Cenko, S. B., et al. 2011, Science, 333, 199
Leventis, K., van Eerten, H. J., Meliani, Z., & Wijers, R. A. M. J. 2012, MNRAS, 427, 1329
Levinson, A., Ofek, E. O., Waxman, E., & Gal-Yam, A. 2002, ApJ, 576, 923
Li, W., Leaman, J., Chornock, R., et al. 2010, MNRAS, 412, 1006.4612
Lidskii, V. V., & Ozernoi, L. M. 1979, Soviet Astronomy Letters, 5, 16
Lightman, A. P., & Shapiro, S. L. 1977, ApJ, 211, 244
Lin, D., Carrasco, E. R., Grupe, D., et al. 2011, ApJ, 738, 52
Linares, M., Watts, A., Altamirano, D., et al. 2010, ApJ, 719, L84
Lind, K. R., & Blandford, R. D. 1985, ApJ, 295, 358
Liu, R., Pooley, G., & Riley, J. M. 1992, MNRAS, 257, 545
Livio, M., Ogilvie, G. I., & Pringle, J. E. 1999, ApJ, 512, 100
Lodato, G., King, A. R., & Pringle, J. E. 2009, MNRAS, 392, 332
Lodato, G., & Rossi, E. M. 2011, MNRAS, 410, 359
Loeb, A., & Ulmer, A. 1997, ApJ, 489, 573
Lupton, R., Gunn, J. E., Ivezić, Z., Knapp, G. R., & Kent, S. 2001, Astronomical Data Analysis Software and Systems X, 238, 269

Lusso, E., Hennawi, J. F., Comastri, A., et al. 2013, ApJ, 777, 86
Lynden-Bell, D. 1969, Nature, 223, 690
Maccarone, T. J. 2003, A&A, 409, 697
MacDonald, G. H., Kenderdine, S., & Neville, A. C. 1968, MNRAS, 138, 259
Mackay, C. D. 1971, MNRAS, 154, 209
Macklin, J. T. 1982, MNRAS, 199, 1119
MacLeod, C. L., Ivezić, Ž., Kochanek, C. S., et al. 2010, ApJ, 721, 1014
MacLeod, C. L., Ivezić, Ž., Sesar, B., et al. 2012, ApJ, 753, 106
Magorrian, J., & Tremaine, S. 1999, MNRAS, 309, 447
Magorrian, J., Tremaine, S., Richstone, D., et al. 1998, AJ, 115, 2285
Maksym, W. P., Ulmer, M. P., & Eracleous, M. 2010, ApJ, 722, 1035
Maoz, D., Nagar, N. M., Falcke, H., & Wilson, A. S. 2005, ApJ, 625, 699
Maoz, E. 1998, ApJ, 494, L181
Marconi, A., & Hunt, L. K. 2003, ApJ, 589, L21
Marconi, A., Risaliti, G., Gilli, R., et al. 2004, MNRAS, 351, 169
Markoff, S., Falcke, H., & Fender, R. 2001, A&A, 372, L25
Martí-Vidal, I., Marcaide, J. M., Alberdi, A., et al. 2011, A&A, 533, A111
Martini, P. 2004, Coevolution of Black Holes and Galaxies, 169
Massardi, M., Bonaldi, A., Negrello, M., et al. 2010, MNRAS, 404, 532
Mateos, S., Alonso-Herrero, A., Carrera, F. J., et al. 2013, MNRAS, 434, 941
Mathews, W. G., & Brighenti, F. 2003, ARA&A, 41, 191
Matthews, T. A., Morgan, W. W., & Schmidt, M. 1964, ApJ, 140, 35
Matthews, T. A., & Sandage, A. R. 1963, ApJ, 138, 30
Matute, I., La Franca, F., Pozzi, F., et al. 2006, A&A, 451, 443
Mauch, T., Murphy, T., Buttery, H. J., et al. 2003, MNRAS, 342, 1117
Mauch, T., & Sadler, E. M. 2007, MNRAS, 375, 931
Mazur, P. O., & Mottola, E. 2001, ArXiv e-prints, gr-qc/0109035
McClintock, J. E., Narayan, R., & Steiner, J. F. 2013, Space Sci. Rev., 1303.1583
McGilchrist, M. M., Baldwin, J. E., Riley, J. M., et al. 1990, MNRAS, 246, 110
McHardy, I. M., Koerding, E., Knigge, C., Uttley, P., & Fender, R. P. 2006, Nature, 444, 730
McKinney, J. C. 2005, ApJ, 630, L5
McKinney, J. C., & Blandford, R. D. 2009, MNRAS, 394, L126
McNamara, B. R., & Nulsen, P. E. J. 2012, New Journal of Physics, 14, 055023
Meier, D. L. 2001, ApJ, 548, L9
Melia, F., & Falcke, H. 2001, ARA&A, 39, 309
Merloni, A., Heinz, S., & di Matteo, T. 2003, MNRAS, 345, 1057
Merritt, D., & Poon, M. Y. 2004, ApJ, 606, 788
Metzger, B. D., Giannios, D., & Mimica, P. 2012, MNRAS, 420, 3528
Meyer, F., & Meyer-Hofmeister, E. 1981, A&A, 104, L10
Meyer-Hofmeister, E., Liu, B. F., & Meyer, F. 2009, A&A, 508, 329
Michell, J. 1784, Philosophical Transactions of the Royal Society, 74, 35
Migliari, S., & Fender, R. P. 2006, MNRAS, 366, 79
Miller, A. A., Chornock, R., Perley, D. A., et al. 2009, ApJ, 690, 1303
Mïller, J. M., & Gültekin, K. 2011, ApJ, 738, L13
Mills, B. Y. 1981, Proceedings of the Astronomical Society of Australia, 4, 156
Mirabel, I. F., & Rodríguez, L. F. 1994, Nature, 371, 46
Mirabel, I. F., & Rodríguez, L. F. 1999, ARA&A, 37, 409
Mocz, P., Fabian, A. C., & Blundell, K. M. 2011, MNRAS, 413, 1107

Mocz, P., Fabian, A. C., & Blundell, K. M. 2013, MNRAS, 432, 3381
Moderski, R., Sikora, M., & Lasota, J.-P. 1998, MNRAS, 301, 142
Mooley, K. P., Myers, S. T., Hallinan, G., et al. 2014, in AAS Meeting Abstracts, Vol. 223
Morganti, R., Fogasy, J., Paragi, Z., Oosterloo, T., & Orienti, M. 2013, Science, 341, 1082
Morrissey, P., Conrow, T., Barlow, T. A., et al. 2007, ApJS, 173, 682
Mullin, L. M., Riley, J. M., & Hardcastle, M. J. 2008, MNRAS, 390, 595
Murayama, T., & Taniguchi, Y. 1998, ApJ, 497, L9
Murgia, M., Parma, P., Mack, K.-H., et al. 2011, A&A, 526, A148
Murphy, T., Mauch, T., Green, A., et al. 2007, MNRAS, 382, 382
Murphy, T., Sadler, E. M., Ekers, R. D., et al. 2010, MNRAS, 402, 2403
Murphy, T., Chatterjee, S., Kaplan, D. L., et al. 2013, PASA, 30, 6
Nagar, N. M., Falcke, H., Wilson, A. S., & Ho, L. C. 2000, ApJ, 542, 186
Nandi, S., Roy, R., Saikia, D. J., et al. 2014, ApJ, 789, 16
Narayan, R., Igumenshchev, I. V., & Abramowicz, M. A. 2003, PASJ, 55, L69
Narayan, R., & McClintock, J. E. 2008, New A Rev., 51, 733
Narayan, R., & McClintock, J. E. 2012, MNRAS, 419, L69
Narayan, R., & Yi, I. 1994, ApJ, 428, L13
Narayan, R., & Yi, I. 1995, ApJ, 452, 710
Neeser, M. J., Eales, S. A., Law-Green, J. D., Leahy, J. P., & Rawlings, S. 1995, ApJ, 451, 76
Nemmen, R. S., Bower, R. G., Babul, A., & Storchi-Bergmann, T. 2007, MNRAS, 377, 1652
Nesvadba, N. P. H., Lehnert, M. D., De Breuck, C., Gilbert, A. M., & van Breugel, W. 2008, A&A, 491, 407
Nipoti, C., Blundell, K. M., & Binney, J. 2005, MNRAS, 361, 633
Nixon, C., & King, A. 2013, ApJ, 765, L7
Nixon, C., King, A., Price, D., & Frank, J. 2012, ApJ, 757, L24
Nolthenius, R. A., & Katz, J. I. 1982, ApJ, 263, 377
O'Dea, C. P., & Baum, S. A. 1997, AJ, 113, 148
Ofek, E. O., Frail, D. A., Breslauer, B., et al. 2011, ApJ, 740, 65
Ogle, P., Whysong, D., & Antonucci, R. 2006, ApJ, 647, 161
Oke, J. B. 1974, ApJS, 27, 21
Oort, M. J. A., Katgert, P., & Windhorst, R. A. 1987, Nature, 328, 500
Oppenheimer, J. R., & Volkoff, G. M. 1939, Physical Review, 55, 374
Östman, L., Nordin, J., Goobar, A., et al. 2011, A&A, 526, A28
Owen, F. N., White, R. A., & Ge, J. 1993, ApJS, 87, 135
Owens, J. C. 1967, Appl. Opt., 6, 51
Oyaizu, H., Lima, M., Cunha, C. E., et al. 2008, ApJ, 674, 768
Pacholczyk, A. G. 1970, Radio astrophysics. Nonthermal processes in galactic and extragalactic sources (Freeman and Co., San Francisco)
Pâris, I., Petitjean, P., Aubourg, É., et al. 2012, A&A, 548, A66
Parma, P., Murgia, M., de Ruiter, H. R., et al. 2007, A&A, 470, 875
Pastorello, A., Turatto, M., Benetti, S., et al. 2002, MNRAS, 333, 27
Penrose, R. 1969, Nuovo Cimento Rivista Serie, 1, 252
Perets, H. B., Gualandris, A., Kupi, G., Merritt, D., & Alexander, T. 2009, ApJ, 702, 884
Perets, H. B., Hopman, C., & Alexander, T. 2007, ApJ, 656, 709
Petrov, L., Hirota, T., Honma, M., et al. 2007, AJ, 133, 2487
Phinney, E. S. 1989, in IAU Symposium, Vol. 136, The Center of the Galaxy, ed. M. Morris (Dordrecht: Kluwer), 543
Pier, J. R., Munn, J. A., Hindsley, R. B., et al. 2003, AJ, 125, 1559

Piran, T. 2004, Reviews of Modern Physics, 76, 1143
Plotkin, R. M., Anderson, S. F., Brandt, W. N., et al. 2010a, ApJ, 721, 562
Plotkin, R. M., Anderson, S. F., Brandt, W. N., et al. 2012, ApJ, 745, L27
Plotkin, R. M., Anderson, S. F., Brandt, W. N., et al. 2010b, AJ, 139, 390
Pojmanski, G. 2007, IAUCirc., 8875, 1
Proctor, D. D. 2011, ApJS, 194, 31
Punsly, B., & Coroniti, F. V. 1990, ApJ, 354, 583
Quimby, R. 2006, Central Bureau Electronic Telegrams, 644, 1
Quimby, R. M., Kulkarni, S. R., Kasliwal, M. M., et al. 2011, Nature, 474, 487
Radburn-Smith, D. J., Lucey, J. R., Woudt, P. A., Kraan-Korteweg, R. C., & Watson, F. G. 2006, MNRAS, 369, 1131
Ramirez-Ruiz, E., & Rosswog, S. 2009, ApJ, 697, L77
Rawlings, S., & Saunders, R. 1991, Nature, 349, 138
Rees, M. J. 1988, Nature, 333, 523
Rees, M. J. 1990, Science, 247, 817
Rees, M. J., Begelman, M. C., Blandford, R. D., & Phinney, E. S. 1982, Nature, 295, 17
Reipurth, B., & Bally, J. 2001, ARA&A, 39, 403
Remillard, R. A., & McClintock, J. E. 2006, ARA&A, 44, 49
Rengelink, R. B., Tang, Y., de Bruyn, A. G., et al. 1997, A&AS, 124, 259
Rest, A., Foley, R. J., Gezari, S., et al. 2011, ApJ, 729, 88
Reynolds, C. S., & Begelman, M. C. 1997, ApJ, 487, L135
Richards, G. T., Fan, X., Newberg, H. J., et al. 2002, AJ, 123, 2945
Richards, G. T., Nichol, R. C., Gray, A. G., et al. 2004, ApJS, 155, 257
Rigon, L., Turatto, M., Benetti, S., et al. 2003, MNRAS, 340, 191
Risaliti, G., Harrison, F. A., Madsen, K. K., et al. 2013, Nature, 494, 449
Robertson, J. G. 1991, Australian Journal of Physics, 44, 729
Roseboom, I. G., Lawrence, A., Elvis, M., et al. 2013, MNRAS, 429, 1494
Ross, N. P., Myers, A. D., Sheldon, E. S., et al. 2012, ApJS, 199, 3
Rosswog, S., Ramirez-Ruiz, E., & Hix, W. R. 2009, ApJ, 695, 404
Rovelli, C., & Vidotto, F. 2014, e-prints, 1401.6562
Russell, D. M., Gallo, E., & Fender, R. P. 2013a, MNRAS, 431, 405
Russell, D. M., Miller-Jones, J. C. A., Maccarone, T. J., et al. 2011, ApJ, 739, L19
Russell, H. R., McNamara, B. R., Edge, A. C., et al. 2013b, MNRAS, 432, 530
Sadler, E. M., Cannon, R. D., Mauch, T., et al. 2007, MNRAS, 381, 211
Saikia, D. J., & Jamrozy, M. 2009, Bulletin of the Astronomical Society of India, 37, 63
Sako, M., Bassett, B., Becker, A., et al. 2008, AJ, 135, 348
Sari, R., & Piran, T. 1995, ApJ, 455, L143
Saxton, R., Read, A., Esquej, P., Miniutti, G., & Alvarez, E. 2011, in Narrow-Line Seyfert 1 Galaxies and their place in the Universe, ed. L. Foschini (PoS)
Saxton, R. D., Read, A. M., Esquej, P., et al. 2012, A&A, 541, A106
Scaringi, S., Körding, E., Uttley, P., et al. 2012, MNRAS, 421, 2854
Schawinski, K., Lintott, C. J., Thomas, D., et al. 2009, ApJ, 690, 1672
Schellart, P. 2013, K3Match: Point matching in 3D space, 1307.003, astrophysics Source Code Library
Scheuer, P. A. G. 1974, MNRAS, 166, 513
Schlegel, D. J., Finkbeiner, D. P., & Davis, M. 1998, ApJ, 500, 525
Schmidt, M. 1963, Nature, 197, 1040
Schmidt, M. 1968, ApJ, 151, 393
Schneider, D. P., Hall, P. B., Richards, G. T., et al. 2007, AJ, 134, 102

Schneider, D. P., Richards, G. T., Hall, P. B., et al. 2010, AJ, 139, 2360
Schödel, R., Ott, T., Genzel, R., et al. 2002, Nature, 419, 694
Schoenmakers, A. P., de Bruyn, A. G., Röttgering, H. J. A., & van der Laan, H. 2001, A&A, 374, 861
Schoenmakers, A. P., de Bruyn, A. G., Röttgering, H. J. A., van der Laan, H., & Kaiser, C. R. 2000, MNRAS, 315, 371
Schwarzschild, K. 1916, Sitzungsberichte der Königlich Preussischen Akademie der Wissenschaften, 7, 189
Scott, W. K. 1996, PhD thesis, University Of British Columbia
Serjeant, S., Rawlings, S., Lacy, M., et al. 1998, MNRAS, 294, 494
Sesar, B., Ivezić, Ž., Lupton, R. H., et al. 2007, AJ, 134, 2236
Shabala, S. S., & Godfrey, L. E. H. 2013, ApJ, 769, 129
Shakura, N. I., & Sunyaev, R. A. 1973, A&A, 24, 337
Shapiro, S. L., & Teukolsky, S. A. 1983, Black holes, white dwarfs, and neutron stars: The physics of compact objects (Wiley)
Shen, Y., Richards, G. T., Strauss, M. A., et al. 2011, ApJS, 194, 45
Shi, Y., Rieke, G. H., Hines, D. C., et al. 2005, ApJ, 629, 88
Sikora, M., & Begelman, M. C. 2013, ApJ, 764, L24
Sikora, M., Stawarz, Ł., & Lasota, J.-P. 2007, ApJ, 658, 815
Silk, J., & Rees, M. J. 1998, A&A, 331, L1
Silverman, J. D., Green, P. J., Barkhouse, W. A., et al. 2005, ApJ, 624, 630
Simpson, C. 2005, MNRAS, 360, 565
Singal, A. K. 1993, MNRAS, 263, 139
Singal, A. K., & Rajpurohit, K. 2012, ArXiv e-prints, 1212.0667
Singal, J., Petrosian, V., Stawarz, Ł., & Lawrence, A. 2013, ApJ, 764, 43
Skrutskie, M. F., Cutri, R. M., Stiening, R., et al. 2006, AJ, 131, 1163
Slee, O. B., Siegman, B. C., & Mulhall, P. S. 1982, Proceedings of the Astronomical Society of Australia, 4, 278
Smith, A. J., Loveday, J., & Cross, N. J. G. 2009, MNRAS, 397, 868
Smith, J. A., Tucker, D. L., Kent, S., et al. 2002, AJ, 123, 2121
Smith, N., Li, W., Foley, R. J., et al. 2007, ApJ, 666, 1116
Sol, H., Pelletier, G., & Asseo, E. 1989, MNRAS, 237, 411
Soltan, A. 1982, MNRAS, 200, 115
Sommers, P. 2001, Astroparticle Physics, 14, 271
Spruit, H. C., Foglizzo, T., & Stehle, R. 1997, MNRAS, 288, 333
Stanghellini, C., Baum, S. A., O'Dea, C. P., & Morris, G. B. 1990, A&A, 233, 379
Steiner, J. F., McClintock, J. E., & Narayan, R. 2013, ApJ, 762, 104
Stern, D., Assef, R. J., Benford, D. J., et al. 2012, ApJ, 753, 30
Stocke, J. T., Morris, S. L., Weymann, R. J., & Foltz, C. B. 1992, ApJ, 396, 487
Stone, N., & Loeb, A. 2011, MNRAS, 412, 75
Stone, N., & Loeb, A. 2012, Physical Review Letters, 108, 061302
Stoughton, C., Lupton, R. H., Bernardi, M., et al. 2002, AJ, 123, 485
Strauss, M. A., Weinberg, D. H., Lupton, R. H., et al. 2002, AJ, 124, 1810
Strittmatter, P. A., Hill, P., Pauliny-Toth, I. I. K., Steppe, H., & Witzel, A. 1980, A&A, 88, L12
Strubbe, L. E., & Quataert, E. 2009, MNRAS, 400, 2070
Strubbe, L. E., & Quataert, E. 2011, MNRAS, 415, 168
Syer, D., & Ulmer, A. 1999, MNRAS, 306, 35
Tananbaum, H., Gursky, H., Kellogg, E., Giacconi, R., & Jones, C. 1972, ApJ, 177, L5

Tasse, C., Best, P. N., Röttgering, H., & Le Borgne, D. 2008a, A&A, 490, 893
Tasse, C., Le Borgne, D., Röttgering, H., et al. 2008b, A&A, 490, 879
Taylor, G. B., Marr, J. M., Pearson, T. J., & Readhead, A. C. S. 2000, ApJ, 541, 112
Tchekhovskoy, A., Metzger, B. D., Giannios, D., & Kelley, L. Z. 2014, MNRAS, 437, 2744
Tchekhovskoy, A., Narayan, R., & McKinney, J. C. 2010, ApJ, 711, 50
Tchekhovskoy, A., Narayan, R., & McKinney, J. C. 2011, MNRAS, 418, L79
The Pierre Auger Collaboration. 2007, Science, 318, 938
The Pierre Auger Collaboration. 2008, Astroparticle Physics, 29, 188
The Pierre Auger Collaboration. 2010a, Phys. Rev. Lett., 104, 091101
The Pierre Auger Collaboration. 2010b, Astroparticle Physics, 34, 314
The Pierre Auger Collaboration. 2013, J. Cosmol. Astropart. Phys., 009
Tonry, J., & Davis, M. 1979, AJ, 84, 1511
Tundo, E., Bernardi, M., Hyde, J. B., Sheth, R. K., & Pizzella, A. 2007, ApJ, 663, 53
Ueda, Y., Akiyama, M., Ohta, K., & Miyaji, T. 2003, ApJ, 598, 886
Ulmer, A. 1999, ApJ, 514, 180
Urry, C. M., & Padovani, P. 1995, PASP, 107, 803
Uttley, P., & McHardy, I. M. 2001, MNRAS, 323, L26
van Eerten, H. J., & MacFadyen, A. I. 2011, ApJ, 733, L37
van Haarlem, M. P., Wise, M. W., Gunst, A. W., et al. 2013, A&A, 556, A2
van Velzen, S., & Falcke, H. 2013, A&A, 557, L7
van Velzen, S., Falcke, H., & Farrar, G. R. 2010, in ISKAF2010 Science Meeting
van Velzen, S., Falcke, H., Schellart, P., Nierstenhöfer, N., & Kampert, K.-H. 2012, A&A, 544, A18
van Velzen, S., & Farrar, G. R. 2012, in EPJ Web of Conferences, Vol. 39, 8002
van Velzen, S., Frail, D. A., Körding, E., & Falcke, H. 2013, A&A, 552, A5
van Velzen, S., Körding, E., & Falcke, H. 2011, MNRAS, 417, L51
van Velzen, S., Farrar, G. R., Gezari, S., et al. 2011, ApJ, 741, 73
van Weeren, R. J., Hoeft, M., Röttgering, H. J. A., et al. 2011, A&A, 528, A38
Vanden Berk, D. E., Richards, G. T., Bauer, A., et al. 2001, AJ, 122, 549
Vanden Berk, D. E., Lee, B. C., Wilhite, B. C., et al. 2002, ApJ, 576, 673
Vanden Berk, D. E., Schneider, D. P., Richards, G. T., et al. 2005, AJ, 129, 2047
Véron, M. P., & Véron, P. 1974, A&AS, 18, 309
Véron-Cetty, M., & Véron, P. 2006, A&A, 455, 773
Voges, W., Aschenbach, B., Boller, T., et al. 1999, A&A, 349, 389
Volonteri, M., Sikora, M., & Lasota, J.-P. 2007, ApJ, 667, 704
Volonteri, M., Sikora, M., Lasota, J.-P., & Merloni, A. 2013, ApJ, 775, 94
Walcher, C. J., Böker, T., Charlot, S., et al. 2006, ApJ, 649, 692
Walcher, C. J., van der Marel, R. P., McLaughlin, D., et al. 2005, ApJ, 618, 237
Wang, J., & Merritt, D. 2004, ApJ, 600, 149
Wang, T.-G., Zhou, H.-Y., Komossa, S., et al. 2012, ApJ, 749, 115
Waxman, E. 1995a, Phys. Rev. Lett., 75, 386
Waxman, E. 1995b, ApJ, 452, L1
Wegg, C., & Nate-Bode, J. 2011, ApJ, 738, L8
White, R. L., Becker, R. H., Helfand, D. J., & Gregg, M. D. 1997, ApJ, 475, 479
White, R. L., Helfand, D. J., Becker, R. H., Glikman, E., & de Vries, W. 2007, ApJ, 654, 99
White, R. L., Becker, R. H., Gregg, M. D., et al. 2000, ApJS, 126, 133
Wilkes, B. J., Kuraszkiewicz, J., Haas, M., et al. 2013, ApJ, 773, 15
Willick, J. A., Strauss, M. A., Dekel, A., & Kolatt, T. 1997, ApJ, 486, 629
Willott, C. J., Rawlings, S., Blundell, K. M., & Lacy, M. 1998, MNRAS, 300, 625

Willott, C. J., Rawlings, S., Blundell, K. M., & Lacy, M. 1999, MNRAS, 309, 1017
Willott, C. J., Rawlings, S., Blundell, K. M., & Lacy, M. 2000, MNRAS, 316, 449
Willott, C. J., Rawlings, S., Blundell, K. M., Lacy, M., & Eales, S. A. 2001, MNRAS, 322, 536
Wilson, A. S., & Colbert, E. J. M. 1995, ApJ, 438, 62
Wright, E. L., Eisenhardt, P. R. M., Mainzer, A. K., et al. 2010, AJ, 140, 1868
Wu, Q., Xu, Y.-D., & Cao, X. 2011, Journal of Astrophysics and Astronomy, 32, 223
Xu, C., Livio, M., & Baum, S. 1999, AJ, 118, 1169
Yahil, A., Tammann, G. A., & Sandage, A. 1977, ApJ, 217, 903
York, D. G., Adelman, J., Anderson, Jr., J. E., et al. 2000, AJ, 120, 1579
Young, P. J. 1977, ApJ, 215, 36
Yuan, F., & Akerlof, C. W. 2008, ApJ, 677, 808
Yuan, F., Markoff, S., Falcke, H., & Biermann, P. L. 2002, A&A, 391, 139
Yuan, F., & Narayan, R. 2004, ApJ, 612, 724
Yuan, F., & Narayan, R. 2014, ArXiv e-prints, 1401.0586
Zakamska, N. L., & Greene, J. E. 2014, MNRAS, 442, 784
Zakamska, N. L., Strauss, M. A., Krolik, J. H., et al. 2003, AJ, 126, 2125
Zatsepin, G. T., & Kuz'min, V. A. 1966, Soviet Journal of Experimental and Theoretical Physics Letters, 4, 78
Zauderer, B. A., Berger, E., Margutti, R., et al. 2013, ApJ, 767, 152
Zauderer, B. A., Berger, E., Soderberg, A. M., et al. 2011, Nature, 476, 425
Zaw, I., Farrar, G. R., & Greene, J. E. 2009, ApJ, 696, 1218
Zhang, W., & MacFadyen, A. 2009, ApJ, 698, 1261

Nederlandse samenvatting

Stel je voor dat je op een gaswolkje zit dat richting een zwart gat valt. Je weet dat zodra je de horizon van het zwarte gat passeert, er geen weg terug meer is. Toch is er nog hoop: vlakbij de horizon bevindt zich een *jet*, een nauwe straalstroom waarin deeltjes met zeer hoge snelheid wegvliegen van het zwarte gat. Een klein aantal gasdeeltjes uit de wolk kan meeliften met deze jet en zo aan het zwarte gat ontsnappen.

Jets ontstaan niet alleen rond zwarte gaten, maar zijn bijvoorbeeld ook zichtbaar tijdens de vorming van sterren (zie Figuur 1.1 op pagina 2). Ondanks een grote hoeveelheid waarnemingen en gedetailleerde computersimulaties is er nog geen consensus over de vraag hoe jets ontstaan. Het is belangrijk om deze vraag te beantwoorden aangezien jets van zwarte gaten de evolutie van een heel melkwegstelsel kunnen beïnvloeden. Als we willen weten hoe onze Melkweg zijn huidige vorm en inhoud heeft gekregen, moeten we de invloed van jets begrijpen.

Zwarte gaten en accretie

Een zwart gat is een object waarvan de zwaartekracht zo groot is dat zelfs licht niet kan ontsnappen. Onze planeet aarde is dus duidelijk geen zwart gat – het is relatief eenvoudig om een raket voldoende energie mee te geven om aan de aantrekkingskracht van de aarde te ontsnappen. Als we de aarde echter laten krimpen tot een bol met een straal van 0,9 centimeter, dan is de ontsnappingssnelheid gelijk aan de lichtsnelheid. Bij deze verschrikkelijk kleine straal zou de aarde een zwart gat zijn.

De massa van de aarde is laag genoeg om te voorkomen dat ze ineenstort tot een zwart gat: de electromagnetische kracht, die atomen uit elkaar houdt, is sterker dan de zwaartekracht. Voor zware sterren die aan het einde van hun leven zijn gekomen is dit niet het geval. Voor de zon en andere normale sterren, zorgt kernfusie in het centrum voor de tegendruk tegen de zwaartekracht. Zware sterren verbruiken de brandstof voor kernfusie echter in slechts een paar miljoen jaar (ter vergelijking, de aarde is ruim vier miljard jaar oud). Zodra de druk die kernfusie levert wegvalt, zit

er voor deze sterren niets anders op dan ineenstorten tot een zwart gat.

Zwarte gaten worden groter als hun massa toeneemt. Accretie[1] op zwarte gaten is echter niet zo makkelijk als het klinkt. Stel dat we de zon veranderen in een zwart gat dan zou dit voor de baan van de aarde geen effect hebben – we blijven nog steeds onze jaarlijkse rondjes draaien, de aarde wordt niet *geaccreteerd*. Hetzelfde principe geldt voor gas dat rond een zwart gat draait. Om het gas te accreteren moet door wrijving de baan van de gasdeeltjes kleiner worden gemaakt (of in natuurkundige termen: viscositeit is nodig om het impulsmoment te doen afnemen).

Net als dat je handen warm worden door ze tegen elkaar aan te wrijven, komt er bij accretie ook energie vrij. Deze energie wordt uitgestraald, dus een accretieschijf geeft licht (je verwarmde handen geven ook licht, maar dit is niet zichtbaar voor het menselijk oog omdat het wordt uitgestraald in het infrarode deel van het elektromagnetische spectrum). Accretie op zwarte gaten is de meest efficiënte manier om energie te genereren uit massa. Wanneer een gaswolk de horizon van het zwarte gat bereikt, is ongeveer 10% van mc^2 aan energie vrijgekomen (met m de massa van de gaswolk en c de lichtsnelheid). Ter vergelijking, de energie die vrijkomt bij een atoombom is "slechts" 0,001% van mc^2.

Hoe vind je iets wat je niet kan zien?

Dankzij de enorme hoeveelheid licht die vrijkomt bij accretie zijn zwarte gaten die groeien in massa redelijk makkelijk te vinden. We zien dus nooit het zwarte gat zelf[2], maar enkel het licht dat wordt geproduceerd in de accretieschijf. Twee soorten zwarte gaten zijn tot nu toe gevonden: de "stellaire" zwarte gaten, met een massa van een paar maal de massa van de zon en de "superzware" zwarte gaten, met een massa van minstens een miljoen maal de zon.

De stellaire zwarte gaten onttrekken gas uit een ster die in een nauwe baan rond het zwarte gat draait. Het resultaat is een accretieschijf die zeer veel röntgenlicht uitstraalt. We noemen deze bronnen daarom röntgendubbelsterren (of *X-ray binaries*); enkele tientallen zijn tot nu toe gevonden.

De superzware zwarte gaten worden gevonden in het centrum van melkwegstelsels. Bijvoorbeeld in het centrum van onze Melkweg, waar een zwart gat huist met een massa van vier miljoen maal de massa van de zon. Als het signaal van de accretieschijf zichtbaar is in het licht van een sterrenstelsel spreken we van een *active galactic nuclei* (AGN). *Quasars* zijn de allerhelderste AGN en zijn zichtbaar tot diep in het heelal. Door systematisch de hemel af te zoeken (bijvoorbeeld met de Sloan Digital Sky Survey) zijn tot nu meer dan honderdduizend AGN gevonden.

[1] *Accretie* is het verzamelen van massa (uit het Latijn: accretio, toename).

[2] Met een telescoop met extreem hoge resolutie zou je de schaduw van een zwart gat waar kunnen nemen, maar dit is momenteel nog niet mogelijk.

Radiomelkwegstelsels

Op een tijdschaal van miljoenen jaren boren jets van AGN zich een weg door het melkwegstelsel. Hierbij produceren de jets *synchrotronstraling*, waardoor ze goed zichtbaar zijn met radiotelescopen. Vandaar dat AGN met jets ook wel radiomelkwegstelsels worden genoemd (zie Fig. 1.3 op pagina 13 voor een beroemd voorbeeld). Uiteindelijk kunnen jets van superzware zwarte gaten tot wel honderd keer groter worden dan het melkwegstelsel waaruit ze zijn ontsprongen.

Jets van superzware zwarte gaten vormen het hoofdonderwerp van dit proefschrift. Door bestaande waarnemingen van verschillende golflengte te combineren heb ik twee nieuwe catalogi van radiomelkwegstelsels gemaakt. In Hoofdstuk 2 & 3 ligt de focus op melkwegstelsels in het lokale universum (met een typische afstand van honderd miljoen lichtjaar). Onze catalogus is de eerste in zijn soort die de hele hemel bestrijkt; 30% van de radiomelkwegstelsels waren nog niet eerder beschreven (mooie plaatjes zijn te vinden op pagina 51). Tevens ging ik opzoek naar radiomelkwegstelsels dieper in het universum (Hoofdstuk 4 & 5); met behulp van een nieuw algoritme vonden we ruim tienduizend stuks, op een gemiddelde afstand van tien miljard lichtjaar (zie pagina 104 voor een paar voorbeelden). Met deze twee nieuwe catalogi kunnen we proberen te begrijpen hoe jets ontstaan.

Hoe (en wanneer) maak je een jet?

Er zijn grofweg twee verschillende theorieën over de vorming van jets. Ten eerste is er de "universele theorie" die stelt dat de energie van alle soorten jets – zowel jets van zwarte gaten als jets in jonge sterren – wordt geleverd door de accretieschijf. De "spintheorie" daarentegen stelt dat jets van zwarte gaten een uitzondering zijn. De energie die is opgeslagen in de draaiing van het zwarte gat (de *spin*) kan worden gebruikt om extra krachtige jets te maken.

Aan het eind van de jaren tachtig van de vorige eeuw werd het duidelijk dat slechts 10% van alle quasars jets laten zien. Tot op de dag van vandaag is hier nog geen sluitende verklaring voor. Volgens de spintheorie komt dit doordat maar 10% van de superzware zwarte gaten een voldoende hoge spin heeft om krachtige jets te maken. Een even goede verklaring is dat quasars slechts gedurende 10% van hun levensduur krachtige jets kunnen maken, namelijk waneer de accretieschijf een faseovergang[3] maakt.

Gerelateerd aan de vraag *hoe* een jet wordt gemaakt is de vraag *wanneer* dit gebeurt. Voor röntgendubbelsterren kunnen we deze vraag simpelweg beantwoorden door deze bronnen een paar jaar in de gaten te houden. Deze stellaire zwarte gaten vertonen namelijk een cyclus van een ongeveer een jaar. Als het accretieniveau laag is, zien we zwakke, maar stabiele jets. Kortlevende krachtige jets worden waargenomen als het accretieniveau toeneemt en de schijf een faseovergang maakt.

[3]Een voorbeeld van een meer alledaagse faseovergang is vloeibaar water naar waterdamp

De evolutie van AGN (i.e., de superzware zwarte gaten) is te langzaam om waar te kunnen nemen op een menselijke tijdschaal, wat het moeilijk maakt te meten wanneer AGN-jets ontstaan. Als we aannemen dat accretie *schaalinvariant* is kunnen deze vraag wel proberen te beantwoorden met behulp van de waarnemingen van röntgendubbelsterren. Het – zeer elegante – idee van schaalinvariantie is dat de eigenschappen van de accretie schijf enkel en alleen afhangen van de massa van het centrale object (dus als we de massa "wegdelen" zijn alle accretieschijven gelijk). Dit betekent dat we röntgendubbelsterren kunnen beschouwen als miniatuur versies van AGN en dus de evolutie van superzware zwarte gaten versneld afgespeeld zien.

De belangrijkste conclusie van de radiowaarnemingen van AGN (Hoofdstuk 2 t/m 5) is dat we de (simpelste versie van) de spintheorie voor de productie van jets kunnen verwerpen. In Hoofdstuk 4 wordt duidelijk dat de lineaire relatie tussen het vermogen van de jet en lichtkracht van accretieschijf niet compatibel is met de spintheorie. In Hoofdstuk 5 laten we bovendien zien dat deze relatie voldoende is om bijna alle krachtige radiomelkwegstelsels te verklaren. We vinden ook bewijs voor het idee dat jets van quasars korter bestaan dan de totale levensduur van de quasar, zoals voorspeld door de schaalinvariante theorie van accretie.

In de laatste vier hoofdstukken (6 t/m 9) van dit proefschrift gebruik ik de zeldzame "spaghettificatie" van sterren om het idee dat accretie schaalinvariant is op een geheel nieuwe manier te testen.

Stellar tidal disruption flares (spaghettisterren)

De getijdenwerking van de maan is een gevolg van de zwaartekracht; de maan trekt harder aan de kant van de aarde die dichterbij staat, met eb en vloed tot gevolg. Het is waarschijnlijk geen verassing dat de getijdenwerking van een zwart gat een vernietigend effect kan hebben. Als een ster te dicht in de buurt komt van een superzwaar zwart gat wordt de getijdenwerking zo sterk dat ster uit elkaar wordt getrokken tot een soort spaghettisliert. Het gas van de ster wordt geaccreteerd door het zwarte gat wat zorgt voor een korte uitbarsting van licht, daarom noemen we deze gebeurtenissen *stellar tidal disruption flares* (TDFs). Een TDF duurt een paar maanden en kan helderder zijn dan het licht van alle sterren van een melkwegstelsel bij elkaar.

De spaghettificatie van sterren vormt een unieke mogelijkheid om accretie op superzware zwarte gaten te bestuderen op een menselijke tijdschaal. Helaas zijn TDFs behoorlijk zeldzaam; de frequentie is slechts eens per tienduizend tot honderdduizend jaar per melkwegstelsel. We moeten dus miljoenen melkwegstelsels tegelijk in de gaten houden om een handjevol spaghettisterren te kunnen vinden, een ontwikkeling die pas recent mogelijk is geworden. In Hoofdstuk 6 presenteer ik twee TDFs die zijn gevonden met optische waarnemingen (dit was de eerste keer dat iemand hierin geslaagd is).

Op basis van de resultaten in Hoofdstuk 7 t/m 9 kunnen we concluderen dat er twee populaties van TDFs zijn: mét en zonder jets. Dit betekent dat een extra parameter

een rol zou kunnen spelen in de productie van een TDF-jet en dat schaalinvariantie "gebroken" is. Mogelijke extra parameters zijn: de spin van het zwarte gat, een magnetisch veld (dat al aanwezig was voor de ster langskwam), of een speciaal type ster dat vernietigd wordt. Het is ook mogelijk dat schaalinvariantie niet gebroken is omdat enkel voor een hoge dichtheid van het gas rond het zwarte gat de detectie van een TDF-jet mogelijk is.

Kortom, het onderzoek naar TDFs staat nog in de kinderschoenen, maar de resultaten uit Hoofdstuk 6 kunnen worden gebruikt om de komende jaren veel meer nieuwe spaghettisterren te verzamelen. We staan aan het begin van een nieuwe weg, een nieuwe manier van kijken naar superzware zwarte gaten. Deze weg resulteert zeer waarschijnlijk in meer duidelijkheid over jets, maar zal met zekerheid ook leiden tot nieuwe, uitdagende vragen.

List of publications

Refereed journals

1. van Velzen, S., Falcke, H., & Körding, E. *Nature and evolution of powerful radio galaxies and their link with the quasar luminosity function*, 2014, MNRAS submitted
2. van Velzen, S., & Farrar, G. R., *Measurement of the rate of stellar tidal disruption flares*, 2014, ApJ in press
3. Lane, W. M., Cotton, W. D., van Velzen, S., et al. *The Very Large Array Low-frequency Sky Survey Redux (VLSSr)*, 2014, MNRAS, 400, 327
4. van Velzen, S., & Falcke, H. *The contribution of spin to jet-disk coupling in black holes*, 2013, A&A letters, 557, L7
5. van Velzen, S., Frail, D. A., Körding, E., & Falcke, H. *Constraints on off-axis jets from stellar tidal disruption flares*, 2013, A&A 552, A5
6. van Velzen, S., Falcke, H., Schellart P., et al. *Radio galaxies of the Local Universe: all-sky catalog, luminosity functions, and clustering*, 2012 A&A, 544, A18
7. van Velzen, S., Körding, E., & Falcke, H. *Radio jets from stellar tidal disruptions*, 2011, MNRAS letters, 417, L51
8. van Velzen, S., Farrar, G. R., Gezari, S., et al. *Optical Discovery of Probable Stellar Tidal Disruption Flares*, 2011, ApJ, 741, 73
9. van Weeren, R. J., Hoeft, M., Röttgering, H. J. A., Brüggen, M., Intema, H. T., & van Velzen, S. *A double radio relic in the merging galaxy cluster ZwCl 0008.8+5215*, 2011, A&A, 528, A38

Conference proceedings

1. van Velzen, S. & Falcke, H. *All-sky catalog of local radio galaxies*, 2013, The Intriguing Life of Massive Galaxies, in Proceedings of the IAU, 295, 271-271
2. van Velzen, S., Frail, D. A., Körding, E. & Falcke, H. 2013, *Radio follow-up observations of stellar tidal disruption flares: Constraints on off-axis jets*, 2012, in EPJ Web of Conferences, Vol. 39, 4002

3. van Velzen, S. & Farrar, G. R. 2013, *Measurement of the rate of stellar tidal disruption flares*, 2012, in EPJ Web of Conferences, Vol. 39, 8002
4. van Velzen, S., Falcke, H., & Farrar, G. R. 2010, *Prospects for detecting stellar tidal disruptions with LOFAR*, 2010 in ISKAF2010 Science Meeting, p.86

Internal research notes of the Auger Collaboration

1. van Velzen, S., Falcke, H. & Hörandel, J. 2012, *Radio galaxies as the source of ultra-high energy cosmic rays: Hillas diagram, energy injection, and cross-correlation*, 2012, GAP-2012-081

Acknowledgments

Looking back at the last 4.5 years of being a PhD student at the Radboud University, I can only conclude that I have had a fantastic time. Here, I would like to thank the people that made this possible.

First of all I want to thank my supervisor, Heino. Regardless of your ultra-busy travel schedule, you almost always replied to my messages promptly and we could always find time to sit down and chat. I have learned many things from you; not only about astrophysics but also how to make the presentation of a paper more clear, more convincing, and a bit bold (e.g., a very instructive comment on an earlier version of Chapter 4 was: "you sound too much like a politician, trying to keep everyone happy"). I am grateful that you gave me plenty of freedom to play around and work on topics outside our original idea of the PhD project. I am also happy that you encouraged me to go abroad to meet people and present my work (and had the generous travel budget to make all these trips possible).

I also want to thank Elmar for always allowing me to drop into his office to discuss anything from statistics to new research ideas. I appreciate how you approached the latter as a potential referee, which was very stimulating.

I am very grateful to Glennys, my former Master's supervisor, for the many times she invited me back to New York to continue our collaboration. I felt privileged to be staying in the guest apartments near Washington Square. Also, I will never forget the Thanksgiving dinner at your house (my first Turducken!).

I would also like to thank all the other co-authors for their valuable input to the chapters of this thesis —especially Dale, Dennis, Pim S., and Suvi.

I thank the members of the reading committee for their time and effort, in particular Glennys, Frank, and Paul for their comments/suggestions. Thanks also to: Sera, for inviting me to attend her group meetings at the University of Amsterdam and giving useful career advice; Paul, for sending me to the William Herschel Telescope in La Palma to hunt for spectra of optical transients; Manu, for introducing me to radio astronomy.

A shout-out to Jochem at Studio BAR for designing the cover and special thanks to Mark and Bob for their help with proof reading. I look forward to defending this thesis because I know that a strong team of paranymphs will have my back: Joost (my brother) and Sander (my bandmate).

Many thanks to all my colleagues for keeping our department a fun place to work, especially to all my office mates (Kars, Sarka, Silvia, Manu, Mikkel, Serena, Pim O., David, Christiaan, Emilio, Payaswini) for the good times at our alluring jungle office.

Peter en Henny zijn absoluut de liefste ouders die ik me wensen kan; altijd klaar om te helpen en altijd geïnteresseerd in waar ik mee bezig ben, daarvoor heel veel dank.

Finally, Iris, my love. You must know that your support has been indispensable. I look forward to continuing with the expansion of our own little universe.

Sjoert van Velzen
Augustus 2014

About the author

Sjoert van Velzen was born in Amsterdam in 1984. He obtained his Bachelor's degree from the Institute of Interdisciplinary Studies at the University of Amsterdam, with a major in Physics & Astrophysics (*cum laude*). Continuing his education at the University of Amsterdam, he obtained a dual Master's in Particle Physics and Astrophysics (*cum laude*) in 2010. The research for his Master's thesis was carried out at New York University under the supervision of Glennys Farrar. Between 2010 and 2014 he was a PhD student in an ERC-funded project at the Radboud University Nijmegen, supervised by Heino Falcke. Sjoert will continue his research at the Johns Hopkins University in Baltimore, funded by a Hubble Fellowship that he received for the proposal 'Transients at the heart of galaxies'.